PHOTOCATALYTIC OXIDATION OF ORGANIC POLLUTANTS UNDER VISIBLE LIGHT IRRADIATION: FROM N-DOPED TIO$_2$ PHOTOCATALYSTS TO THE DESIGN OF A CONTINUOUS FIXED BED REACTOR

Olga Sacco

Unione Europea

Ministero dell'Istruzione, dell'Università e della Ricerca

UNIVERSITÀ DEGLI
STUDI DI SALERNO

Department of Industrial Engineering

Ph.D. Course in Chemical Engineering
(XIII Cycle-New Series)

PHOTOCATALYTIC OXIDATION OF ORGANIC POLLUTANTS UNDER VISIBLE LIGHT IRRADIATION: FROM N-DOPED TIO$_2$ PHOTOCATALYSTS TO THE DESIGN OF A CONTINUOUS FIXED BED REACTOR

Supervisor
Prof. Diana Sannino

Ph.D. student
Olga Sacco

Scientific Referees
Prof. Paolo Ciambelli
Prof. Dionysios D. Dionysiou
Ph.D Vincenzo Vaiano

Ph.D. Course Coordinator
Prof. Paolo Ciambelli

"I poeti dicono che la scienza rovina la bellezza delle stelle, riducendole solo ad ammassi di atomi di gas. Solo? Anche io mi commuovo a vedere le stelle di notte nel deserto, ma vedono di meno o di più?[..]

Acknowledgments

Publications list

1. Sacco, O. ; Stoller, M.; Vaiano, V. ; Ciambelli, P. ; Chianese, A.; Sannino, D. Photocatalytic degradation of organic dyes under visible light on n-doped TiO_2 photocatalysts **International Journal of Photoenergy** Volume 2012, 2012, Article number 626759
2. Sannino D; Vaiano V.; Sacco, O.; Ciambelli, P. Mathematical modelling of photocatalytic degradation of methylene blue under visible light irradiation **Journal of Environmental Chemical Engineering** Volume 1, Issue 1-2, 2013, Pages 56-60
3. Vaiano V.; Sacco O.; Stoller M.; Chianese A.; Ciambelli P., and Sannino D.
   Influence of the photoreactor configuration and of different light sources in the photocatalytic treatment of highly polluted wastewater **International Journal of Chemical Reactor Engineering** 2013; 11(1): 1–13doi 10.1515/ijcre-2013-0090
4. Rizzo, L. , Sannino, D. , Vaiano, V., Sacco, O., Scarpa, A., Pietrogiacomi, D. Effect of solar simulated N-doped TiO_2photocatalysis on the inactivation and antibiotic resistance of an E. coli strain in biologically treated urban wastewater
   Applied Catalysis B: Environmental Volume 144, January 2014, Pages 369-378
5. Vaiano, V.; Sacco, O.; Sannino, D.; Ciambelli, P.; Longo, S.; Venditto, V.; Guerra, G. N-doped TiO_2/s-PS aerogels for photocatalytic degradation of organic dyes in wastewater under visible light irradiation **Journal of Chemical Technology and Biotechnology** Volume 89, Issue 8, August 2014, Pages 1175-1181
6. Vaiano, V.; Sacco, O.; Sannino, D.; Ciambelli, P.; Increasing the photoactivity of N-doped TiO_2 photocatalysts using phosphors as light carriers **Chemical Engineering Transactions** Volume 39, Issue Special Issue, 2014, Pages 619-624
7. Vaiano, V.; Sacco, O.; Sannino, D.; Ciambelli, P.; Photocatalytic removal of spiramycin from wastewater under visible light with N-doped TiO_2 photocatalysts **Chemical Engineering Journal**
8. Sacco O.; Vaiano, V. ; Han C.; Sannino D; Dionysiou, D.D.; Photocatalytic removal of atrazine using N-doped TiO_2 supported on phosphors **Applied Catalysis B: Environmental** Volume 164, March 01, 2015, Pages 462-474
9. Vaiano, V.; Sacco, O.; Sannino, D.; Ciambelli, P. Process intensification in the removal of organic pollutants from wastewater using innovative photocatalysts obtained coupling ZnS-based phosphors with nitrogen doped semiconductors **Journal of Cleaner Production**

10. Vaiano, V.; Sacco, O.; Sannino, D.; Ciambelli, P Photocatalytic removal of Organic Dyes using nanostructured N-doped TiO_2 coated on glass spheres **Environmental Science and Pollution Research**

11. Sacco O.; Vaiano, V. ; Han C.; Sannino D; Dionysiou, D.D.; Long Afterglow green phosphors functionalized with Fe-N Doped TiO_2 for the photocatalytic removal of emerging contaminants **Chemical Engineering Transactions**

.

Contents

I

Index of figures

II

IV

VIII

X

Index of tables

Abstract

As a consequence of the rapid growth of population in urban areas, water use and reuse has become a major concern, leading to an urgent imperative of developing effective and affordable technologies for the treatment of water and wastewater. Traditional methods for water treatment are usually based on physical and biological processes but, unfortunately, some organic pollutants, classified as bio-recalcitrant, are not biodegradable. In this way heterogeneous photocatalysis may become an effective water treatment technology to remove organic pollutants hardly oxidised by conventional techniques.

Photocatalysis represents one of the main challenges in the field of treatment and decontamination of water and air, because it is able to work at ambient temperature and atmospheric pressure. Heterogeneous photocatalysis is a catalytic process that uses the energy associated to a light source to activate a catalyst with semiconducting properties. The most common used photocatalyst is titanium dioxide (TiO_2), which is able to oxidize a wide range of toxic organic compounds to harmless compounds such as CO_2 and H_2O. However, the following major factors limit both photocatalytic efficiency and activity of TiO_2:

a) the band gap of anatase TiO_2 is 3.2 eV, i.e. it absorbs light in the UV region, so that only a small portion (5%) of sunlight can be used for a photocatalytic process. This is a great limitation in its use as photocatalyst for the conversion of solar into chemical energy;

b) as in all semiconductors, photogenerated electron-hole couples undergo fast recombination in competition with charge transfer to adsorbed species on the catalyst surface;

c) the use of slurry reactors limits the industrial applications of photocatalysis, since the necessary separation of catalyst powders after liquid phase reactions is troublesome and expensive.

In this context, during this PhD project different routes have been explored to go beyond these limitations:

1. With respect to the use of visible light irradiation, doping with anions belonging to the p-block was investigated in recent years to sensitize TiO_2 towards visible light, either by introducing newly created mid-gap energy states, or by narrowing the band gap itself. However, the role of titania dopants such as N, C, B, S, P, I and F is still not completely understood. The insertion of dopants in the crystalline structure of TiO_2 may induce light absorption in the visible region, but also increases the rate of the undesired recombination of photogenerated charge carriers. This effect becomes relatively lower if the crystallinity of the oxide structure is higher.

Our attention was focused on nitrogen as dopant. N-doped TiO_2 photocatalysts were prepared by sol gel method, via hydrolysis of titanium tetraisopropoxide by aqueous ammonia solution. More in details, the sol-process was carried out at 0°C to limit the evaporation of ammonia due to the exothermic character of the hydrolysis reaction, and then the obtained powders were dried and calcined at 450°C. N/Ti molar ratio and calcination time conditions were optimized. All samples were characterized by BET, UV-vis absorption, Raman spectroscopy, FTIR, SEM-EDAX, TEM and XRD. The effects of the dopant amount on the structural features of the doped materials were systematically investigated in relation to their photocatalytic activity.

The photocatalytic degradation of methylene blue (MB) in aqueous suspension was employed as test reaction. MB is a highly popular test pollutant in semiconductor photocatalysis used in the assessment of such key features as novel photocatalytic materials, photoreactors and light sources.

The best photocatalytic performances in the presence of visible light irradiation have been obtained with a N/Ti molar ratio equal to 18.6 and for a calcination time of 30 minutes.

The photocatalytic behaviour of the optimized N-doped TiO_2 photocatalyst was further explored in other reactions, i.e. the degradation of spyramicin, atrazine, methyl orange and on the inactivation of E. coli.

It is also important to evidence that this optimized N-TiO_2 photocatalyst resulted also able to reduce the total chemical oxygen demand (COD) of a highly polluted wastewater such as tannery wastewater.

2. The industrial application of photocatalytic processes is greatly hindered by the insufficient quantum efficiency of the photocatalytic reactions, which results from the relatively high recombination rate of photogenerated electron-hole (e^-- h^+) pairs. Therefore, N-doped TiO_2 was coupled with other semiconductors. In particular, ZnS-based phosphors (ZSP) were chosen. The coupling with ZSP not only reduces the charge-carriers recombination rate but also enhances the photons transfer inside the photoreactor, because ZSP emits, under UVA excitation, visible light centred at 440nm, able to photoexcite N-doped titania catalyst.

Also in this case a simple sol-gel method was adopted and the amount of N-doped TiO_2 on the surface of ZSP was optimized. All samples were characterized by BET, UV-vis absorption, Raman spectroscopy, FTIR, SEM-EDAX, TEM and XRD. The effects of coupling (N-doped TiO_2/ZSP) were systematically investigated in relation to their photocatalytic activity. In particular, the photocatalytic activity of N-doped TiO_2/ZSP was firstly evaluated for the removal of MB and of atrazine under UVA light irradiation. Enhanced performance in comparison to either pure N-doped TiO_2 nanoparticles or bare ZSP was obtained. The photocatalyst N-doped TiO_2/ZSP at 30 wt % of N-dopedTiO_2 loading (30N-TiO_2/ZSP) exhibited the highest photocatalytic activity for the removal of MB and atrazine.

A study of the reaction intermediates during the photocatalytic removal of atrazine was also carried out by LC-QTOF and LC/MS/MS analyses. The degradation mainly involved dealkylation reaction and alkyl chain oxidation both in presence of 30N-TiO_2/ZSP and ZSP. It has been found that the presence of N-doped TiO_2 particles dispersed on ZSP surface led to a change of selectivity, lowering the number of intermediates formed during irradiation. It is important to underline that in the presence of ZSP support no dechlorination of aromatic structure occurred, and thus no formation of cyanuric acid was observed. This study clearly demonstrates the importance of using the ZSP as a supporting material for N-doped TiO_2 nanoparticles.

3. The development of an optimized reactor in slurry configuration was then performed. In this case, the experimental results were carried out by using different light sources, such as white LEDs, blue LEDs and UV lamps, with the aim to evaluate the process efficiency at different operating conditions. From the collected experimental data it was developed a simplified mathematical model to correlate the power input of the used light source, and the geometrical properties of the reactor and of the emitting sources spectra with the performances of the photocatalytic reaction. This simplified mathematical model may represent a valuable tool to design and optimize photocatalytic processes for wastewater treatment.

The most limitation of the photocatalytic processes in slurry reactors is the low activity of N-doped TiO_2 in powder form, mainly due to the aggregation phenomena between nanoparticles. Therefore, to understand the effect of aggregation, a dispersing agent was added to the N-doped TiO_2 suspension and the influence of particles aggregate size on the photocatalytic activity was evaluated. The control of the dispersion and aggregation of the nanoparticles resulted crucial to exploit the advantages of the N-doped TiO_2 particles in photocatalytic activity: a lower aggregate size increased the amount of MB adsorbed on the catalyst surface and enhanced the photocatalytic activity. In particular, after 120 minutes of visible light irradiation, MB degradation in the presence of dispersing agent was about

80%, markedly higher than the value (about 50%) reached without the dispersing agent.

Moreover, taking into account the problem related to the scattering and screening of the light by the catalyst and the accessibility of the catalytic surface to photons and reactants, a novel way to achieve high dispersion of the photocatalyst was also investigated. It consists in dispersing it in a light-transparent support, permitting the penetration of the radiation in the inner core of the photocatalyst. , In particular, N-doped TiO_2 was dispersed in transparent syndiotactic polystyrene monolithic aerogel (s-Ps) which, due to its high specific surface area, allows a better dispersion of the catalysts, strongly limiting the aggregation phenomena that typically occur when the catalyst is suspended in water solutions. These features increased the photocatalytic activity of the N-doped TiO_2 under visible light irradiation in comparison with the powder sample dispersed in solution.

4. One of the most important drawbacks of photocatalytic process is that photocatalysts are used in slurry reactors. With this type of reactor, photocatalysts must be recovered from the purified water after the treatment, and the cost of this separation stage may even invalidate economically this technique. With the aim to overcome this technical limitation the N-doped TiO_2 photocatalyst was immobilized on glass spheres to design a fixed bed continuous photoreactor. With respect to the methods reported in literature for the immobilization of N-doped TiO_2 (mainly carried out through sputtering technique or chemical vapour deposition), the method developed is a simple sol-gel method that uses ammonia aqueous solution as the only doping source. The effect of sol-gel synthesis temperature on the crystallization and crystallite size of N-doped TiO_2 was investigated; the best temperature for the immobilization through dip-coating process was found at -20°C.

The decolourization of MB and eriochrome black-T (EBT) aqueous solutions was tested in a traditional batch reactor to evaluate the photocatalytic activity of the immobilized photocatalyst. The optimization of N-doped TiO_2 amount on glass spheres was established. It was found that until to four dip-coating steps, the photocatalytic activity increased. Moreover, the N-doped TiO_2 immobilized on glass spheres (NdTcg) can be easily separated from the reaction mixture, and maintained excellent photocatalytic activity and durability after four cycles. Finally, NdTcg showed a high photocatalytic activity in the decolourization of MB and EBT both under UV and visible light irradiation.

The optimized NdTcg structured catalyst was used to design a continuous fixed bed photoreactor.

The geometric characteristics of the reactor were chosen to maximize the exposition of catalysts to the light source. The fluid dynamic in the packed bed reactor was also deeply studied. In particular, the inlet conditions of

liquid phase were experimentally obtained in order to have a uniform distribution of pollutant concentration along the catalytic bed in the absence of reaction. In addition, a CFD model (COMSOL Multiphysics 4.2a) was utilized to determine the shape and the dimension of the transparent support for N-doped TiO_2. A Langmuir–Hinshelwood kinetic model was applied for estimating the kinetic parameters of the catalyst, starting from experimental data collected at different contact times. In order to simplify the model of light distribution inside the reactor, instead of the traditional LVRPA, the Helmholtz equation set with the Dirichlet conditions on the boundary was used. The kinetic expression, together with the spatial photons distribution, was incorporated in the mass balance to achieve the theoretical distribution of the pollutant concentration in the reactor. The developed mathematical model allows determining the best irradiation conditions of the photoreactor to minimize the reactor volume required to achieve the complete removal of organic pollutants from liquid phase.

I Introduction

In the last century, due to the fast industrialization, a very severe problem has emerged, namely the intense water and air pollution. The progressive accumulation of organic compounds in natural waters is mostly due to the development and extension of chemical technologies for organic synthesis and processing (Segneanu et al. 2013).

Population explosion, expansion of urban areas increased adverse impacts on water resources, particularly in regions in which natural resources are still limited. Currently, water use and reuse has become a major concern. For this reason, it is an urgent imperative to develop effective and affordable technologies for wastewater treatment.

The main causes of surface water and groundwater contamination are industrial discharges (even in low quantities), excess use of pesticides, fertilizers (agrochemicals) and land filling domestic wastes. General classes of compounds of concern include: solvents, volatile organics, chlorinated volatile organics, dioxins, dibenzofurans, pesticides, PCB's, chlorophenols, asbestos, heavy metals, and arsenic compounds. Some specific compounds of interest are 4-chlorophenol, pentachlorophenol, trichloroethylene (TCE), perchloroethylene (PCE), ethylene dibromide, vinyl chloride, ethylene dichloride, methyl chloroform, p-chlorobenzene, and hexachlorocyclopentadiene. Extensive research is underway to develop advanced analytical, biochemical, and physicochemical methods for the characterization and elimination of hazardous chemical compounds from air, soil, and water.

The wastewater treatment is based upon various mechanical, biological, physical and chemical processes. In fact, this is a combination of many operations like filtration, flocculation, chemical sterilization and the elimination of particles in suspension. The biological treatment is the ideal process (natural decontamination).

The physico-chemical processes (coagulation and flocculation) use various chemical reagents (aluminum chloride or ferric chloride, polyelectrolytes, etc.) and generate large amounts of sludge. Increasing demands for water quality indicators and drastic change regulations on

wastewater disposal require the development of processes more efficient and more effective (ion exchange, ultrafiltration, reverse osmosis and chemical precipitation, electrochemical technologies). Each of these treatment methods has advantages and disadvantages.

Water resources management exercises ever more pressing demands on wastewater treatment technologies to reduce industrial negative impact on natural water sources. Thus, the new regulations and emission limits are imposed and industrial activities are required to seek new methods and technologies capable of effective removal of heavy metal pollution loads and reduction of wastewater volume, closing the water cycle, or by reusing and recycling wastewater. Advanced technologies for wastewater treatment are required to eliminate pollution and may also increase pollutant destruction or separation processes. These technologies can be applied successfully to remove pollutants that are partially removed by conventional methods, e.g. biodegradable organic compounds, suspended solids, colloidal substances, phosphorus and nitrogen compounds, heavy metals, dissolved compounds, microorganisms that thus enabling recycling of residual water (Zhou and Smith, 2002). Special attention was paid to electrochemical technologies, because they have advantages: versatility, safety, selectivity, possibility of automation, environmentally friendly and requires low investment costs (Hansen et al., 2007).

The technologies for treating wastewater containing organic compounds fall within one of the following categories:

Non-destructive procedures are based on physical processes of adsorption, removal, stripping etc. Biological destructive procedures based on biological processes use active mud. Oxidative destructive processes – based on oxidative chemical processes can fall within one of the following categories:

- Incineration;

- WO "Wet Oxidation", operating in conditions of high temperature and pressure, with the versions:

  - WAO - "Wet Air Oxidation" (wet oxidation with O_2 air oxidative agent);
  - CWAO - "Catalytic Wet Air Oxidation" (catalytic wet oxidation with O_2 air oxidative agent);
  - SWA - "Supercritical Water Oxidation" (oxidation with O_2 air oxidative agent in supercritical conditions).

- Liquid oxidation: AOPs - "Advanced Oxidation Processes", operate in conditions of room temperature and pressure and use as oxidative agents O_3, H_2O_2 and even O_2, catalysts and/ or UV radiations
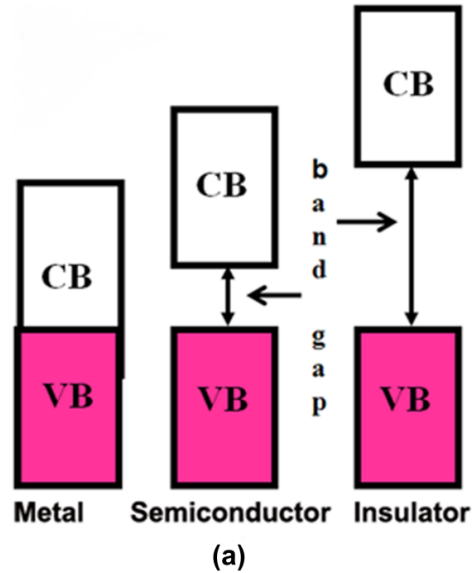
Figure 1 *VB and CB positions in metals, semiconductors, and insulators (Lazar et al., 2012).*

I.1 Advanced oxidation processes (AOPs)

Advanced oxidation processes (AOPs) are widely used for the removal of recalcitrant organic constituents from industrial and municipal wastewater. In this sense, AOPs type procedures can become very promising technologies for treating wastewater containing non-biodegradable or hardly biodegradable organic compounds with high toxicity. These procedures are based on generating highly oxidative HO radicals in the reaction medium.

- H_2O_2

H_2O_2 + UV (direct photolysis)

H_2O_2 + $Fe^{2+/3+}$ (classic, homogeneous Fenton)

H_2O_2 + Fe/support (heterogeneous Fenton)

H_2O_2 + $Fe^{2+/3+}$ + UV (VIS) (Photo-Fenton)

- O_3

O_3 (direct ozone feeding)

O$_3$ + UV (photo-ozone feeding)

O$_3$ + catalysts (catalytic ozone feeding)

- H$_2$O$_2$ + O$_3$

TiO$_2$ (heterogeneous catalysis)

TiO$_2$ + UV (photo-catalysis)

Photocatalytic water purification using semiconduxtor is a predominant advanced oxidation process (AOP) because of its efficiency and eco-friendliness. Among all AOP processes heterogeneous photocatalysis may not require any additional reagents beyond the catalyst. Photocatalysis can be defined as a "catalytic reaction involving the production of a catalyst by absorption of light" (Verhoeven, 1996). The appropriate positioning of valence (VB) and conduction (CB) bands in semiconductors (Figure 1) makes them suitable materials for the absorption of light and photocatalytic action.

I.1.1 Basic Principles

Photocatalysis is generally defined as the change in the rate of a chemical reaction or its initiation under the action of ultraviolet, visible or infrared radiation in the presence of a substance, the photocatalyst, which absorbs light and it is involved in the chemical transformation of the reaction partners.

$$A + D \xrightarrow[light \geq E_{bg}]{semiconductor} A^- + D^+$$
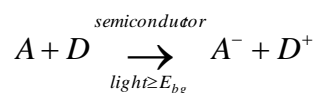
Moreover, when a solid material is used as the photocatalyst, the definition of heterogeneous photocatalysis is preferred (Schiavello, 1997). The most commonly used photocatalysts are semiconductor materials (most of them metal oxides) which, possess a void energy region (band-energy structure), where no energy levels are available (Figure 2). The void region which extends from the top of the filled valence band to the bottom of the vacant conduction band is called band gap, E$_g$.

Activation of a semiconductor photocatalyst is achieved through the absorption of a photon of ultra-band gap energy, which results in the promotion of an electron from the valence band into the conduction band, e-CB, and in the concomitant generation of a hole in the valence band, h$^+$

VB. The reaction of either the photopromoted electron with a reducible adsorbed substrate (usually oxygen in aerated system) and/or the hole with an oxidizable adsorbed species can subsequently occur.

The overall process of semiconductor-sensitized photoreactions can be summarized as follows: The probability and the rate of such charge transfer processes depend on the position of the conduction and valence band edges and on the redox potentials of the adsorbed species. For example, when a semiconductor is used as a photocatalyst in the environmental remediation, usually involving the photodecomposition or complete mineralization of organic pollutants, it should be capable to generate a valence band hole with a redox potential that is positive enough to oxidise the organic pollutant. At the same time the photogenerated electron in the conduction band should be negative enough to reduce adsorbed O_2 to superoxide radical anion (Hoffmann et al., 1995).
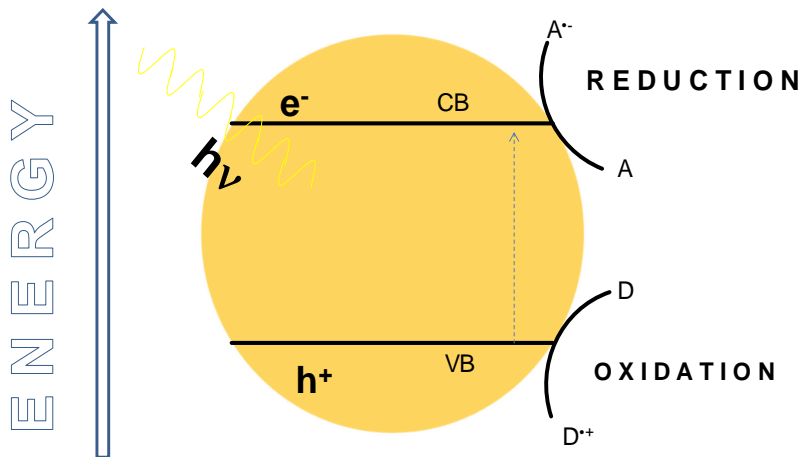
Figure 2 *Illustration of the main processes occurring on a semiconductor particle under electronic excitation*

Errore. L'origine riferimento non è stata trovata. Figure 3 shows the band gap values of different semiconductors and their position on the electrochemical scale. A substrate can successfully interact only with some semiconductors: it is necessary that the electrochemical potential value of the electron acceptor is more positive (down in the graph) than the semiconductor conduction band potential, and that the electron donor potential is more negative (up in the graph) than that of the semiconductor

valence band. A photocatalytic reaction can take place only under such conditions.

Recombination of electron-hole pairs can occur, in competition with charge transfer to adsorbed species, in the volume of the semiconductor particle or in its surface with the release of heat. This phenomenon represents the major deactivation path which could significantly decrease the overall photocatalytic efficiency.

The detrimental process of back-donation to the semiconductor after charge transfer to the adsorbed species can also occur.

The efficiency of a photocatalyst depends on the competition of different interface transfer processes involving electrons and holes and their deactivation by recombination (Fox and Dulay, 1993; Hoffmann et al., 1995; Serpone, 1997).The position of the flatband of an SC in solution follows a Nernstian pH dependence, decreasing 59mV per pH unit (Ward et al., 1983), and consequently, the ability of electrons and holes to enact redox chemistry can be controlled by changes in the pH.
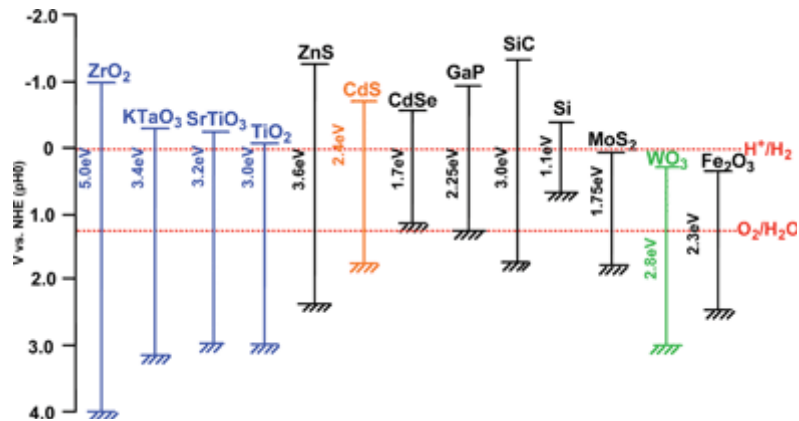
Figure 3 *Illustration of the main processes occurring on a semiconductor particle under electronic excitation (Kudo and Miseki, 2009).*

By using a semiconductor (SC), the heterogeneous photocatalytic process is a complex sequence of reactions that can be expressed by the following set of simplified equations (Linsebigler et al., 1995):

a) *Charge separation*

$$SC + h\nu \longrightarrow e^-_{CB} + h^+_{VB}$$
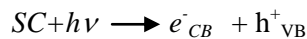
b) *Bulk/surface separation*

6

$$e^{-}_{CB} + h^{+}_{VB} \longrightarrow heat$$

c) *Surface trapping*

$$h^{+}_{VB} + \equiv\text{Ti-OH} \longrightarrow \equiv \text{Ti-O}^{\cdot} + \text{H}^{+}$$
$$e^{-}_{CB} + \equiv\text{Ti-OH} \longrightarrow \equiv \text{Ti}^{\cdot} + \text{OH}^{-}$$
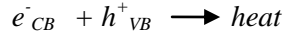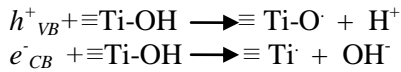
d) *Surface recombination*

$$e^{-}_{CB} \equiv\text{Ti-O} + \text{H}^{+\cdot} \longrightarrow \equiv \text{Ti-OH}$$

$$h^{+}_{VB} + \equiv\text{Ti-OH} \longrightarrow \equiv \text{Ti-O}^{\cdot} + \text{H}^{+}$$
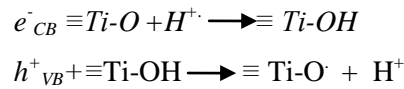
e) *Interfacial charge transfer*

$$\text{Red}_1 + \equiv\text{Ti-O}^{\cdot} \longrightarrow \text{Ox}_1 + \equiv \text{Ti-OH}$$
$$\text{Ox}_2 + \text{H}_2\text{O} + \equiv \text{Ti}^{\cdot} \longrightarrow \text{Red}_2 + \equiv \textit{Ti-OH}$$

f) *Back reaction*

$$\text{Red}_2 + \equiv\text{Ti-O}^{\cdot} \longrightarrow \text{Ox}_2 + \equiv \text{Ti-OH}$$
$$\text{Ox}_1 + \equiv \text{Ti.} \longrightarrow \text{Red}_1 + \equiv \text{Ti-OH}$$
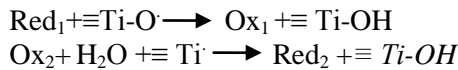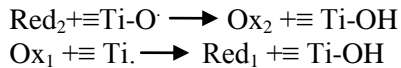
It's worth to remember that a semiconductor free of impurities is defined intrinsic. A semiconductor doped with impurities is called extrinsic.

Doping involves the addition of a different element into the semiconductor.

The visible light photoactivity of metal-doped TiO_2 can be explained by a new energy level produced in the band gap of TiO_2 by the dispersion of metal nanoparticles in the TiO_2 matrix. As shown in Figure. 1, electron can be excited from the defect state to the TiO_2 conduction band by photon with energy equals $h\nu^2$. Additional benefit of transition metal doping is the improved trapping of electrons to inhibit electron-hole recombination during irradiation. Decrease of charge carriers recombination results in enhanced photoactivity.

Many techniques have been examined to achieve this purpose. Metal and non-metal doped TiO_2 has attracted considerable attention due to its reported activity in the visible light. There are many elements for doping TiO_2 such as Fe, W, Cr, Ru, V, Mo, Nb, Au, Pt, Pd, Ag, Sb, Co, Mn, Ni, Zn, Zr or with heteroatoms such as fluorine, sulfur, carbon, phosphorus, boron, iodine, chlorine, bromine, nitrogen (Biedrzycki et al., 2014; Zaleska, 2008).

For example, for the titania doped with nitrogen (N-doped TiO_2), there are three different main opinions regarding modification mechanism of TiO_2 doped with doping: (1) Band gap narrowing; (2) Impurity energy levels; and (3) Oxygen vacancies:

1. Asashi, et al. (Asahi et al., 2001) found N 2p state hybrids with O 2p states in anatase TiO$_2$ doped with nitrogen because their energies are very close, and thus the band gap of N-doped TiO$_2$ is narrowed and able to absorb visible light;

2. Irie, et al. (Irie et al., 2003) stated that TiO$_2$ oxygen sites substituted by nitrogen atom form isolated impurity energy levels above the valence band. Irradiation with UV light excites electrons in both the VB and the impurity energy levels, but illumination with visible light only excites electrons in the impurity energy level;

3. Ihara, et al. (Ihara et al., 2003) concluded that oxygen-deficient sites formed in the grain boundaries are important to emerge vis-activity and nitrogen doped in part of oxygen-deficient sites are important as a blocker for reoxidation. The modification mechanism of anatase doped with nonmetals was also analyzed by Zhao et al. (Zhao et al., 2014). They investigated N-TiO$_2$ and concluded that TiO$_2$ doped with substitutional nitrogen has shallow acceptor states above the valence state. In contrast, TiO$_2$ doped with interstitial nitrogen has isolated impurity states in the middle of the band gap. These impurity energy levels are mainly hybridized by N 2p states and O 2p states.

I.2   Fundamental Engineering Aspects

The photocatalytic process results from the excitation by UV-visible light of a solid semiconductor, generating free electrons and holes, which lead to redox processes on the surface and the attack of adsorbed molecules. Direct attack of organic molecules on the surface, or formation of highly reactive hydroxyl radicals results, in the presence of oxygen, in the oxidation of the organic molecules, which, in most cases, leads to a complete

Mineralization hotocatalytic reactions are the result of the interaction of photons having the appropriate wavelength with a semiconductor. When the arriving light has energy equal or greater than the semiconductor band gap, radiation is absorbed and electrons are moved from the valence band to the conduction band giving rise to the formation of electron–hole pairs. These charge carriers can migrate to the catalyst surface in competition with an exothermic and normally fast recombination reaction. When they reach the semiconductor surface they may, once more recombine, or participate in successive chemical reactions (Alfano et al., 2000). The main components of

a photocatalytic process are indeed the photoreactor and the radiation sources (Augugliaro et al., 1997). For thermal and catalytic processes the parameters that affect reactors performance are:

1. the mode of operation;
2. the phases present in the reactor;
3. the flow characteristics;
4. the needs of heat exchange;
5. the composition and the operative conditions of the reacting mixture.

For selecting the type of heterogeneous photoreactor additional parameters must be considered since photons are the primary source for the occurrence of photoreaction. The selection of the construction material for the photoreactor must be generally done in order to allow the penetration of radiation into the reacting mixture. The choice of the radiation source must be made by considering that the absorbed radiation energy should be equal to or higher than the band gap.

I.2.1 *Photoreactor Geometries*

Two main features determine the design of the reactor:

• suspended or immobilised catalyst;

• source of irradiation.

The most useful reactors for the wastewater treatment are heterogeneous phototoreactors, where the photocatalysts can be present in suspended modes (slurry reactor) or immobilized on transparent support (fixed bed reactor). Most of the early photoreactors have employed a TiO_2 suspension because it offers a high surface area for the reactions. The disadvantages of the slurry photocatalysis include 1) difficulty and time consuming process of separation or filtration of the photocatalyst after the photocatalytic process; 2) particle aggregation and agglomeration at high photocatalyst concentration; and 3) difficulty of using the suspended photocatalyst in continuous processes (Sopyan et al., 1996). Various types of support have been used, made mainly of glass (plate, beads, fibreglass mat) but also paper, cotton, fibres. The source of irradiation can be either natural (solar irradiation) or artificial (lamp). The geometry of the reactor is strongly related to the source of irradiation, in particular it has to be designed so as to

collect the maximum of emitted light and reducinge the energy and investment cost.

I.2.1.1 Solar reactors

Considering the unidirectional solar irradiation, the collection of the irradiation is carried out in two ways (Milow et al., 1999): use of a fixed reactor where a large surface of the solution or suspension is exposed to the sun (Bouchy and Zahraa, 2003): trickling on a flat plate supporting a catalyst mesh, flowing through an array of pipes so as to increase the residence time, or through a flat fixed-bed or exposure within a tank such as those designed for water stations, which can be equipped with impellers designed to ensure a good mixing and aerating of the slurry, focusing with a mirror (parabolic trough (Pacheco et al., 1993)) or more elaborate system (Fresnel lenses, holographic collector) on a reactor of small dimension. When using a focusing system, the volume of fluid is reduced, which makes it easier to build, and is also a necessity as the whole system (collector + reactor) must be placed on a motorised support so as to track the sun. However, it leads to a high irradiation flux, which may reduce the quantum yield of degradation. In addition, depending on the weather, an important fraction of the sunlight can be diffuse instead of direct, which reduces the efficiency of the focusing system (Pacheco et al., 1993). An interesting compromise is the Compound Parabolic Collector (Pacheco et al., 1993) which is fixed, but ensures a partial focusing and a moderate irradiation flux on the catalyst.

I.2.1.1.1 Artificial light reactors

Artificial light sources are on the contrary multidirectional. Two main solution are:

• to reflect or focus the emitted light to a reactor (Martin et al., 1999);

• to wrap the light source with the reactor, such as in the coaxial lamp system; this has the additiona advantage that the back-scattering of light by the catalyst is not a loss as this scattered light re-enters the reactor. The main artificial sources are mercury lamps;

• low pressure lamps (254 nm) of high yield "at the plug" (up to 0.5) of low power (about 30W/m) which require quartz windows,

• fluorescent lamps (around 365 nm) (Sannino et al., 2011), i.e. low pressure lamps equipped with a fluorescent coating, with a decrease of the emitting power of about 50% (so-called black-light lamps);

10

• medium pressure lamp (UV-visible range), higher in power (about to 3 kW/m) but lower in emission yield;

• high-pressure lamp, nearly punctual, with low part of the emission in the UV range. High-pressure lamps have a high cost in energy as along as UV light is looked for. Medium-pressure lamps have a very high power which leads to a low quantum yield of degradation unless the catalyst is placed at a large enough distance to ensure a low enough irradiation flux, which would be space consuming. According to these considerations, fluorescent lamps working with conventional glass vessels are often suggested. An alternative is the distribution of light over a large area of catalyst by the use of coated optical fibres or hollow tubes (Periyathamby and Ray, 1999). The difficulty of these designs is to collect the maximum amount of light from the source and to ensure a distribution of irradiation of the catalyst along the whole of the light conductor by a careful design of the interface loss through refraction. A summary of reactors is presented below, which although not exhaustive gives an insight into the variation of designs, some of which have been the object of advanced modelling when some others are mainly of an intuitive design

I.2.1.1.2   Types of Radiation Sources

Global climate change is one of the most serious environmental problems facing this generation. Average global temperatures have risen by approximately 0.6°C (1.1°F) in the last century and this trend is expected to continue and even accelerate over the 21st century (IPCC, 2001). As the warming continues, the effects of climate change are likely to have adverse impacts on environmental and socio-economic systems throughout the world, although the extent of these impacts is highly sensitive upon the rate and the magnitude of the climate change over the next century (IPCC, 2001).

There is growing consensus in the scientific community that the warming trend is a result of rising atmospheric concentrations of greenhouse gases (GHGs) (NRC, 2001). These GHG are accumulating in the atmosphere as a result of human, or anthropogenic, activities such as fossilfuel combustion. Currently in the United States, fossil fuel energy sources (including coal, natural gas, and oil) are used to generate approximately 70% of U.S. electricity (EIA, 2004).

When fossil fuels are burned to extract energy, carbon dioxide (CO_2), one of the primary GHG is released into the atmosphere. Atmospheric concentration levels of CO_2 have been extracted from ice core samples taken in Antarctica and Greenland. These samples show that CO_2 concentration levels today are higher than those of pre-industrial times, and have followed an upward trend over the last 43 years. A 2001 report from the National Academies conclusively attributed the rising concentration of CO_2 to

anthropogenic activities (NRC, 2001). Of these anthropogenic activities, fossil fuel burning has been, and is projected to be, the most significant source of CO_2 emissions. Innovative technologies can play a major role in curbing emissions of GHG that contribute to global climate change. Solid-state lighting (SSL) is one recent example of an innovative technology, which has received considerable attention in the last several years. This emerging lighting technology has tremendous potential to become significantly more energy-efficient than lighting technologies that are currently used, such as incandescent and fluorescent lighting. Currently in the U.S., approximately 22% of the electricity generated is used for lighting. Put into a broader context, the DOE estimates that 8.3% of U.S. primary energy consumption goes to lighting (DOE, 2002). Solid-state lighting has the potential to significantly reduce the electricity needed for lighting. Estimates for lighting energy savings potential have been as optimistic as a 50% reduction by 2025, which would in turn decrease total electricity consumption by about 10% (Tsao, 2004).
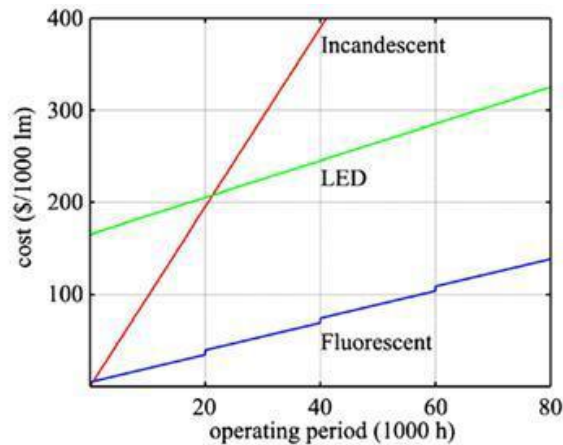
Figure 4 *Costs vs operating period for different commercial light souces (Bisegna et al. 2010)*

The use of light-emitting diodes marks great advancements (Figure 4). LEDs allow the control of spectral composition and the adjustment of light intensity .They have the ability to produce high light levels with low radiant heat output and maintain useful light output for years. LEDs do not contain electrodes and thus do not burn out like incandescent or fluorescent bulbs that must be periodically replaced. Not to mention that incandescent and fluorescent lamps consume a lot of electrical power while generating heat, which must be dispelled from closed environments such as spaceships and space stations.

12
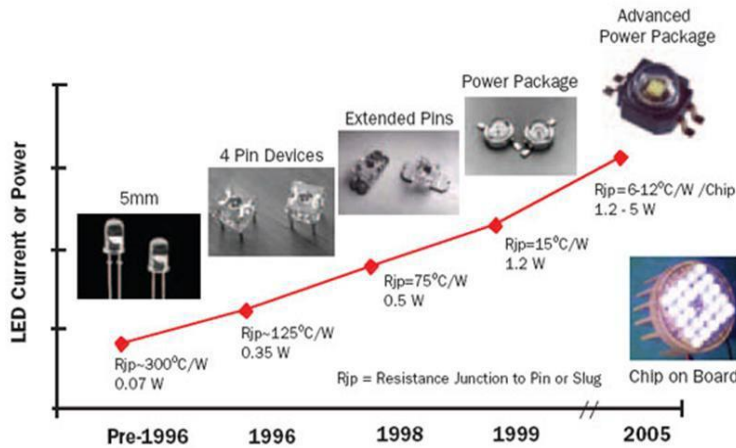
Figure 5 *LEDs evolution (Bisegna et al. 2010)*

I.2.1.1.3   LED development

LED is a unique type of semiconductor diode **Errore. L'origine riferimento non è stata trovata.**. It consists of a chip of semiconductor material doped with impurities to create a p–n junction. Current flows easily from the p-side (anode), to the n-side (cathode), but not in the reverse direction. Electrons and holes flow into the junction from electrodes with different voltages. When an electron meets a hole, it falls into a lower energy level, and releases energy in the form of a photon. The color (wavelength) of the light emitted depends on the band gap energy of the materials forming the p–n junction. The materials used for an LED have a direct band gap with energies corresponding to near-infrared, visible or near-ultraviolet light. The key structure of an LED consists of the die (or light-emitting semiconductor material), a lead frame where the die is placed, and the encapsulation which protects the die. LED development began with infrared and red devicesmade with gallium arsenide. Advances inmaterials science have made possible the production of devices with ever-shorter wavelengths, producing light in a variety of colors (Margolin J. et al. 2005) reported that the first known light-emitting solid state diode was made in 1907 by H. J. Round. No practical use of Round's diode was made for several decades until the invention of the first practical LED by Nick Holonyak, Jr in 1962. His LEDs became commercially available in late 1960s. TheseGaAsPLEDs combine three primary elements: gallium, arsenic and phosphorus to provide a 655 nm red light with brightness levels of approximately 1– 10 mcd at 20 mA. Asthe luminous intensitywas low, these LEDs were only used in a few applications, primarily as indicators.   Following GaAsP, GaP (gallium phosphide) red LEDs were developed. These devices exhibit very high

quantum efficiencies at low currents. As LED technology progressed through the 1970s, additional colors and wavelengths became available. The most common materials were GaP green and red, GaAsP orange, and high efficiency red and GaAsP yellow. The trend towards more practical applications (such as in calculators, digital watches, and test equipment) also began to develop.AstheLEDmaterials technologybecamemoreadvanced, the light output was increased, and LEDs became bright enough to be used for illumination. In 1980s a new material, GaAlAs (gallium aluminum arsenide) was developed followed by a rapid growth in the use of LEDs. GaAlAs technology provides superior performance over previously available LEDs. The voltage requirement is lower, which results in a total power savings. LEDs could be easily pulsed or multiplexed and thus are suitable for variable message and outdoor signs. Along this development period, LEDs were also designed into bar code scanners, fiber optic data transmission systems, and medical equipment. During this time, the improvements in crystal growth and optics design allow yellow, green and orange LEDs only minor improvement in brightness and efficiency. The basic structure of the material remained relatively unchanged.

As laser diodes with output in the visible spectrum started to commercialize in late 1980s, LED designers used similar techniques to produce high-brightness and high reliability LEDs. This led to the development of InGaAlP (indium gallium aluminium phosphide) visible light LEDs. Via adjusting the energy band gap InGaAlP material can have different color output. Thus, green, yellow, orange and red LEDs could all be produced using the same basic technology. Also, light output degradation of InGaAlP material is significantly improved. Shuji Nakamura at Nichia Chemical Industries of Japan introduced blue LEDs in 1993 (Grampp and Landgraf, 2002). Blue LEDs have always been difficult to manufacture because of their high photon energies (>2.5 eV) and relatively low eye sensitivity. Also, the technology to fabricate these LEDs is very different and less advanced than standard LED materials. But blue is one of the primary colors (the other two being red and green). Properly combining the red, green, and blue light is essential to produce white and full-color. This process requires sophisticated software and hardware design to implement. In addition, the brightness level is low and the overall light output of each RGB die being used degrades at a different rate resulting in an eventual color unbalance. The blue LEDs available today consist of GaN (gallium nitride) and SiC (silicon carbide) construction. The blue LED that becomes available in production quantities has result in an entire generation of new application that include telecommunications products, automotive applications, traffic control devices, and full-color message boards. Even LED TVs can soon become commercially available. Compare to incandescent light's 1000-h and fluorescent light's 8000-h life span, LEDs have a very significantly longer life of 100,000 h. In addition to their long life, LEDs have many advantages

14

over conventional light source. These advantages include small size, specific wavelength, low thermal output, adjustable light intensity and quality, as well as high photoelectric conversion efficiency. Such advantages make LEDs perfect for supporting plant growth in controlled environment such as plant tissue culture room and growth chamber.

I.2.1.2   Slurry photoreactors

Reactors with suspended catalyst have been the object of fundamental studies (e.g.(Li Puma and Brucato, 2007; Martin et al., 1999)) with the aim of either getting true kinetic data or allowing large reactors to be designed. Several designs have been studied or suggested. Suspended catalyst has often been used as a flow in an annular space (Alfano et al., 2000; Martin et al., 1999) around a linear lamp but a thorough study has been dedicated to a falling film reactor (Li Puma and Yue, 1998), where a thin film runs freely on the outer wall within the annular space. If the reaction is fast enough, a radial concentration gradient in the reactants will take place, this can be reduced by creating a turbulent flow by the presence of baffles of various design. A completely different design is the fountain reactor (Li Puma and Yue, 2001) where a nearly planar horizontal film is exposed to artificial or solar irradiation. These reactors are meant for water treatment where conversion in the reactor is usually very low so that they are coupled with a tank with a continuous recirculation of the fluid. Mass balance for the whole reactor has to take this situation into account although in the case of a low conversion and good stirring of the tank, the reactor is formally analogous to a batch reactor.

I.2.1.3   Liquid-phase fixed-bed reactors

Another design for cylindrical reactors is a fixed-bed reactor where the catalyst is fixed onto a support so as to avoid a separation process. The support can be packed Rashing rings (Alexiadis et al., 2001), fibre mesh whereas an intermediate design between suspended and fixed catalyst uses freely suspended glass beads as catalyst support. Other reactors use large sized supports such as the inner or outer wall of an annular reactor (Alfano et al., 2000). Confinement of the catalyst onto a practically two-dimensional surface requires a good mixing of the fluid phase in the annular space. Creating a turbulent flow by the use of baffles or foils (Sczechowski et al., 1995), of a catalyst-coated ridged helix, or by inducing a helicoidal swirl is then important. An original solution to this problem is also a vortex reactor where the rotating inner wall induces instability of the flow due to centrifugal forces and the buildingup of successive vortex cells within the annular space as shown in a detailed study (Donaldson et al., 2013). Improving the contact between fluid and catalyst can also be obtained by allowing the fluid to pass through a catalyst loaded mesh on successive flat

or conical supports around the lamp (De Lasa et al., 2005) Basically these reactors are built around a single lamp and large reactors can be obtained by a parallel array of elementary reactors. The design can be improved by using an array of light sources in a large tank. Hydrodynamics of such a system is much more complicated than in the case of cylindrical symmetry. Design of the reactor can be helped by the use of fluid dynamics simulation. Such a study, which is very demanding in computational equipment, has been demonstrated on a structure consisting of a cylindrical tank equipped with seven catalyst-coated hollow tubes acting as light conductors (Periyathamby and Ray, 1999). As a homogeneous "dark" reaction can also take place, it can be of interest to accommodate successive periods of irradiation and thermal evolution by a special design of the reactor (Sczechowski et al., 1995).

I.2.1.3.1   Drawbacks of TiO_2 in powder form

Titanium dioxide is conventionally available in the form of powder. It can be applied to wastewater either in the form of powderthat is suspended form or can be supported over a suitable sub-strate (Alexiadis et al., 2001). Although when used in the form of powder, it showsgreater surface area and efficiency yet it suffers from the followingdrawbacks:

- Low light utilization efficiency of suspended photocatalyst. This is attributed to the attenuation loss suffered by light rays. It has beenreported that less than 1% of UV light or about 20% of visible light actually penetrates at a depth of 0.5 m under the water surface;
- Post-treatment recovery is both time and money consuming. This is because catalyst requires long settling time and efficient solid-liquid (phase) separation techniques (Pozzo et al., 1997). It also leads to loss of catalyst;
- Unfavorable human health problems are also associated with themobility of the powder form (Nohynek and Dufour, 2012).

To overcome the above mentioned drawbacks, continuous efforts are being made to coat TiO_2 on various substrates. Immobilization of TiO_2 has the following advantages;
- Relatively high quantum utilization efficiency as compared to powder TiO_2 photocatalyst (Vaiano et al., 2014c);
- Easy of post-treatment recovery that would reduce the opera-tional cost when used for large scale practical applications;
- Minimizing catalyst loss;

16

- Availability of longer contact time of the photocatalyst with pol-lutants to be degraded.Immobilization has its own sets of drawbacks too, such as:
    - Reduction in the surface area available for reaction
    - Need of various suitable techniques involving well-defined pro-cedures and equipments, unlike powder form of TiO_2 which isavailable in "ready to be used form."

Overall, the advantages of immobilizing TiO_2 outweighs theabove said disadvantages and thus has attracted researchers allover the globe to focus on devising simple yet efficient proceduresto coat TiO_2 on suitable substrateer the globe to focus on devising simple yet efficient proceduresto coat TiO_2 on suitable substrate

I.2.1.3.2 Different supports available

Some of the various supports that have been reported in the literature (Singh et al., 2013)are glass materials, inorganic carbon fabrics, ITO glass, synthetic fabrics, plastics, natural fabrics, polymers, fly ash, vycor glass, hollow glass spheres, polyeth-ylene sheets, reactor walls, fiber glass, silica gel, fabric or wool,micro-porous cellulose membranes, quartz optical fibers, aluminaclays, ceramic membranes and monoliths, stainless steel, zeolites,anodized iron, glass plates, raschig rings, films and fabrics. In fact, the exhaustive nature of the above list indicates that a variety of substrates have been tried for supporting titania. For a researcher, the possible deterrent for not trying a material as a substrate could be the non-adherence of TiO_2 on the support.

I.2.2   Modeling of Photocatalytic Reactors

The modeling of photocatalytic reactors requires a complex analysis of the radiation field in the photoreactor (Cassano et al., 1995). This analysis, linked to the modeling of the fluid-dynamics and the reaction kinetics, results in integro-differential equations which almost invariably require demanding numerical computations. Further advances of photocatalytic oxidation on an industrial scale will be facilitated by the availability of simpler mathematical models that retain the essential elements of a rigorous model and that can be easily used for scale-up and design.

Figure 5 shows a schematic representation of the modeling of a photocatalytic reactor. The development of a reactor model requires the inclusion of a number of sub-models. These are a radiation emission model, a radiation absorption-scattering model, a kinetic model and a fluid-dynamic

model.
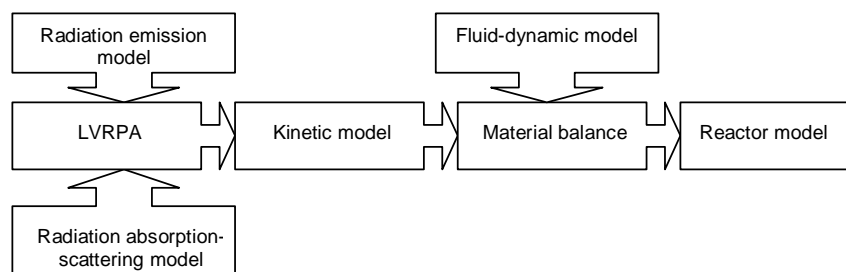
Figure 5 *Schematic representation of the modeling of a photocatalytic reactor*

The central aspect of the modeling procedure is the calculation of the Local Volumetric Rate of Photon Absorption (LVRPA) at each point of the reaction space, which requires solving the radiative transfer equation (RTE) in the reaction space. Due to the complex nature of radiation scattering, this results in a set of integro-differential equations, which require demanding numerical computational efforts. In practice, combining a simplified radiation emission model of the light source with a simplified radiation absorption-scattering model in the reaction space and performing a radiation balance in the reaction space can simplify the RTE.

The above scheme assumes that the "useful photons" of a given photocatalytic reactor, i.e. those photons with energy higher than the band-gap of the semiconductor photocatalyst, are absorbed by the solid photocatalytic particles only. This assumption removes the interdependence of the progress of the reaction and the attenuation of the radiation because the absorbing species do not undergo changes in concentration. Consequently, the incident radiation flux becomes a function of the reactor position only and can be obtained independently of the information provided by the material balance equation.

Once the LVRPA has been calculated, this is normally substituted into the kinetic equation and into the material balance equation which when solved with suitable boundary conditions, yields the concentration of a generic substrate at the reactor outlet.

Three approaches have been proposed in the literature for the calculation of the LVRPA: 1) The "rigorous approach" which involves the mathematical solution of the RTE, although its integro-differential nature makes this approach considerably complex (Cassano et al., 1995); 2) The "numerical approach" which involves the Monte Carlo simulation of the radiation field in the photoreactor, a simple but also a computationally demanding procedure (Changrani and Raupp, 1999); and 3) the "simplified approach" which models the radiation field in the photoreactor using two-flux (Brucato and Rizzuti, 1997), radiation absorption-scattering models. The two and six-

flux models yield a sensible representation of the LVRPA in the reaction space and allow a considerable simplification of the mathematical model. Finally the scattering properties of the photocatalyst, and the geometrical configuration of the photoreactor, determine in large extent the degree of complexity of a mathematical model (Li Puma, 2005).

I.3   Aim of the Work

For industrial applications of photocatalytic processes aimed to the removal of pollutants from water and wastewater, a good solution for a final scale-up is the choice of a photocatlytic system able to work both with UV light and visible light. The optimal design needs, firstly, the formulation of a photocatalyst able to work under visible light irradiation. Recently, many efforts have been made to modify titanium dioxide with non metals. Among all non metals dopants, nitrogen seems to be the most promising dopant since it makes titania active under visible light irradiation. So, starting from this consideration, the synthesis of N-doped TiO_2 was developed through a simple sol-gel method carried out using ammonia as nitrogen source. The synthesis conditions have been studied in order to maximize the photocatalytic activity under visible light. The effectiveness of the formulated N-doped TiO_2 has been tested in the removal of organic dyes, emerging contaminats and in the inactivation of E.coli. To increase the photoactivity, the N-doped TiO_2 was coupled with other semiconductors, such as ZnS-based phosphors.

The optimized photocatlyst was afterwards deposited on glass supports to avoid the drawback related to the separation of a catalyst in powder form after the reaction. Finally, with the structured catalyst, a continuous photocatalytic reactor for water and wastewater treatment was designed and developed.

II Sol-gel synthesis and characterisation techniques

For the synthesise of TiO_2 materials for photocatalytic applications different strategies such as sol-gel, micelle and inverse micelle, hydrothermal, solvothermal, direct oxidation, chemical vapour deposition, flame spray pyrolysis electrodeposition, sonochemical and microwave methods have been proposed by Chen and Mao (Chen and Mao, 2007). Among all these techniques, the sol-gel method is the most commonly used due to its relatively low cost and great flexibility. This technique has been chosen for the preparation of home-made doped TiO_2 samples, which have been investigated during this PhD thesis.

II.1 Sol-gel process

Nowadays, the sol − gel process is used to prepare various types of materials. Matijevic and co-workers (Matijevic et al. 1993) have employed these concepts to produce an enormous range of colloidal powders with controlled size and morphologies, including oxides (TiO_2, α-Fe_2O_3, Fe_3O_4, $BaTiO_3$, CeO_2), hydroxides ($AIOOH$, $FeOOH$, $Cr(OH)_3$), carbonates ($Cd(OH)CO_3$, $Ce_2O(CO_3)_2$, $Ce(III)/YHCO_3$), sulfides (CdS, ZnS), metals ($Fe(III)$, Ni, Co), and various mixed phases or composites (Ni, Co, Sr ferrites), sulfides (Zn, CdS), (Pb, CdS), and coated particles (Fe_3O_4 with $Al(OH)_3$ or $Cr(OH)_3$).

The controlled hydrolysis of alkoxides has also been used to produce submicrometer TiO_2 (Barringer et al.1982), doped TiO_2 (Fegley et al.1984).

The sol-gel method is based on inorganic polymerization reactions, involving four basic steps: hydrolysis, polycondensation, drying and thermal decomposition of precursors.

The hydrolysis reaction, through the addition of water replaces alkoxide groups (OR) with hydroxyl groups (OH). Subsequent condensation reactions involving the M-OH groups produce M-O-M bonds plus the by-products

water or alcohol. Additionally, because water and alkoxides are immiscible, the use of a mutual solvent such as an alcohol is necessary. With the presence of this homogenizing agent, i.e. the alcohol, hydrolysis is facilitated due to the miscibility of the alkoxide and water (Figure 6) (Brinker and Scherer, 1985).

Several parameters, such as type of precursor, type of solvent, water content, pH, concentration of precursor and temperature, can influence the structure of the initial gel, and, in turn, the properties of the resulting materials, including the crystal structure, particle size, shape and crystallinity (Yin and Shen, 2001).
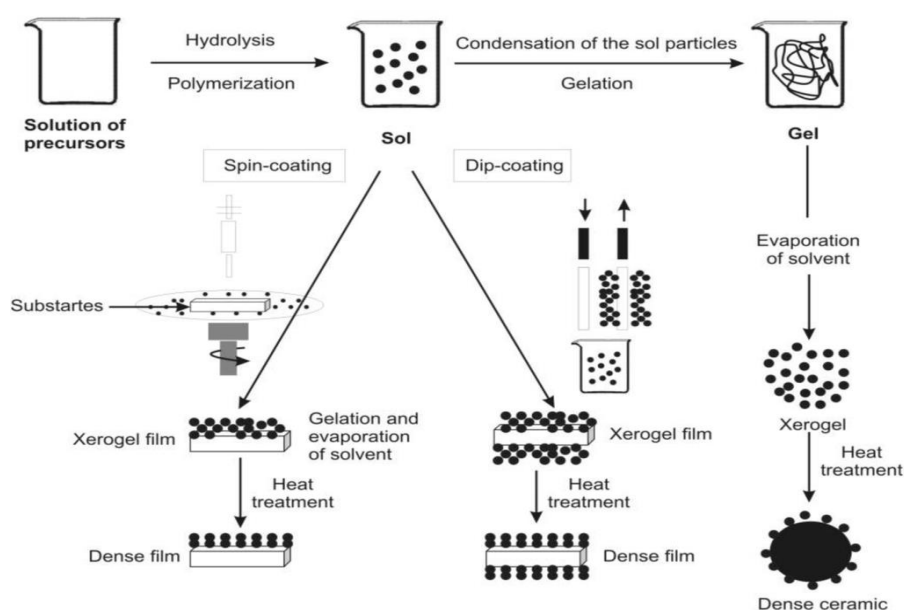
Figure 6 *Schematic overview of the sol-gel process* (*Larry et al.1990*)

II.1.1   XRD powder diffraction

Materials are made of atoms. Knowledge of how atoms are arranged into crystal structures and microstructures is the foundation on which we build our understanding of the synthesis, structure and properties of materials. There are many techniques for measuring chemical compositions of materials, and methods based on inner-shell electron spectroscopies are covered in this book. The larger emphasis of the book is on measuring spatial arrangements of atoms in the range from 10^{-8} to 10^{-4} cm, bridging from the unit cell of the crystal to the microstructure of the material. There

are many different methods for measuring structure across this wide range of distances, but the more powerful experimental techniques involve diffraction.

To date, most of our knowledge about the spatial arrangements of atoms in materials has been gained from diffraction experiments. In a diffraction experiment, an incident wave is directed into a material and a detector is typically moved about to record the directions and intensities of the outgoing diffracted waves "Coherent scattering" preserves the precision of wave periodicity. Constructive or destructive interference then occurs along different directions as scattered waves are emitted by atoms of different types and positions. There is a profound geometrical relationship between the directions of waves that interfere constructively, which comprise the "diffraction pattern," and the crystal structure of the material. The diffraction pattern is a spectrum of real space periodicities in a material. Atomic periodicities with long repeat distances cause diffraction at small angles, while short repeat distances (as from small interplanar spacings) cause diffraction at high angles.

It is not hard to appreciate that diffraction experiments are useful for determining the crystal structures of materials. Much more information about a material is contained in its diffraction pattern, however. Crystals with precise periodicities over long distances have sharp and clear diffraction peaks. Crystals with defects (such as impurities, dislocations, planar faults, internal strains, or small precipitates) are less precisely periodic in their atomic arrangements, but they still have distinct diffraction peaks. Their diffraction peaks are broadened, distorted, and weakened, however, and "diffraction lineshape analysis" is an important method for studying crystal defects. Diffraction experiments are also used to study the structure of amorphous materials, even though their diffraction patterns lack sharp diffraction peaks. In a diffraction experiment, the incident waves must have wavelengths comparable to the spacings between atoms. Three types of waves have proved useful for these experiments. X-ray diffraction (XRD), conceived by von Laue and the Braggs, was the first. The oscillating electric field of an incident x-ray moves the atomic electrons and their accelerations generate an outgoing wave. In electron diffraction, originating with Davisson and Germer, the charge of the incident electron interacts with the positively-charged core of the atom, generating an outgoing electron wavefunction.

In neutron diffraction, pioneered by Shull, the incident neutron wavefunction interacts with nuclei or unpaired electron spins. These three diffraction processes involve very different physical mechanisms, so they often provide complementary information about atomic arrangements in materials. Nobel prizes in physics (1914, 1915, 1937, 1994) attest to their importance. As much as possible, we will emphasize the similarities of these three diffraction methods, with the first similarity being Bragg's law
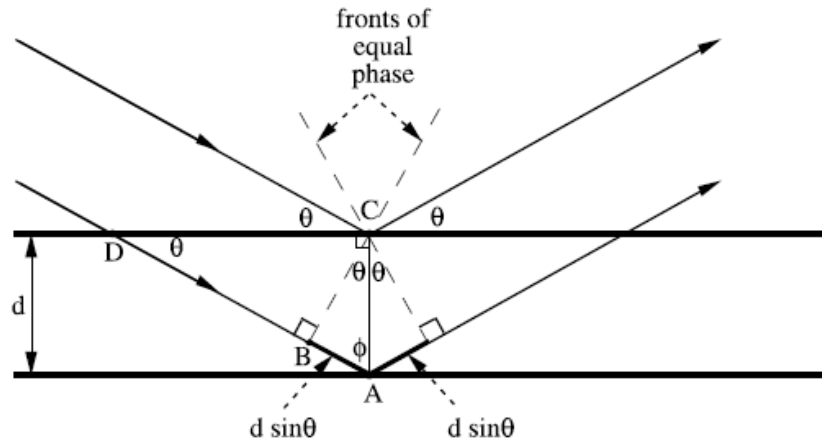
Figure 7 *Geometry for interference of a wave scattered from two planesseparated by a spacing, d. The dashed lines are parallel to the crests or troughs of the incident and diffracted wavefronts. The important path length difference for the two rays is the sum of the two dark segments*

II.1.1.1 Bragg's Law

Figure 7 is the construction needed to derive Bragg's law. The angle of incidence of the two parallel rays is θ . You can prove that the small angle in the little triangle is equal to θ by showing that the two right triangles, ABC and ACD, are similar. (Hint: Look at the shared angle of $\varphi = \pi/2 - \theta$).

The interplanar spacing, d, sets the difference in path length for the ray scattered from the top plane and the ray scattered from the bottom plane. Figure 7 shows that this difference in path lengths is 2d sin θ . Constructive wave interference (and hence strong diffraction) occurs when the difference in path length for the top and bottom rays is equal to one wavelength, λ:

2d sin $\theta = \lambda$.   Eq.1

The right hand side is sometimes multiplied by an integer, n, since this condition also provides constructive interference. Our convention, however, sets n = 1. When there is a path length difference of nλ between adjacent

24

planes, we change d (even though this new d may not correspond to a real interatomic distance). For example, when our diffracting planes are (100) cube faces, and

$$2d_{100} \sin \theta = 2\lambda \qquad \text{Eq.2}$$

.

then we speak of a (200) diffraction from planes separated by $d_{200} = (d_{100})/2$. A diffraction pattern from a material typically contains many distinct peaks, each corresponding to a different interplanar spacing, d. For cubic crystals with lattice parameter a_0, the interplanar spacings, d_{hkl}, of planes labeled by Miller indices (hkl) are:

$$d_{hkl} = \frac{a_0}{\sqrt{h^2 + k^2 + l^2}} \qquad \text{Eq.3}$$

(as can be proved by the definition of Miller indices and the 3D Pythagorean theorem). From Bragg's law (Eq.1) we find that the (hkl) diffraction peak occurs at the measured angle $2\theta_{hkl}$:

$$2\vartheta_{hkl} = 2\arcsin\left(\frac{\lambda\sqrt{h^2 + k^2 + l^2}}{2a_0}\right) \qquad \text{Eq.4}$$

There are often many individual crystals of random orientation in the sample, so all possible Bragg diffractions can be observed in the "powder pattern." There is a convention for labeling, or "indexing," the different Bragg peaks in a powder diffraction pattern using the numbers (hkl). An example of an indexed diffraction pattern. The intensities of the different diffraction peaks vary widely, and are zero for some combinations of h, k, and l. For this example of polycrystalline silicon, notice the absence of all combinations of h, k, and l that are mixtures of even and odd integers, and the absence of all even integer combinations whose sum is not divisible by 4. One important use of x-ray powder diffractometry is for identifying unknown crystals in a sample. The idea is to match the positions and the intensities of the peaks in the observed diffraction pattern to a known pattern of peaks from a standard sample or from a calculation. There should be a one-to-one correspondence between the observed peaks and the indexed peaks in the candidate diffraction pattern. For a simple diffraction pattern, it is usually possible to guess the crystal structure with the help of the charts in. This tentative indexing still needs to be checked. To do so, the θ -angles of the diffraction peaks are obtained, and used with (Eq.1) to obtain the interplanar spacing for each diffraction peak. For cubic crystals it is then

possible to use (Eq.3) to convert each interplanar spacing into a lattice parameter, a_0. (Non-cubic crystals usually require an iterative refinement of lattice parameters and angles.) The indexing is consistent if all peaks provide the same lattice parameter(s).

For crystals of low symmetry and with more than several atoms per unit cell, it becomes increasingly impractical to index a diffraction pattern by hand. An old and reliable approach is "fingerprinting." The International Centre for Diffraction Data, ICDD, maintains a database of diffraction patterns from hundreds of thousands of inorganic and organic materials. For each material the data fields include the observed interplanar spacings for all observed diffraction peaks, their relative intensities, and their hkl indexing. Software packages are available to identify peaks in the experimental diffraction pattern, and then search the ICDD database to find candidate materials. Computerized searches for pattern matches are particularly valuable when the sample contains a mixture of unknown crystalline phases. The task of indexing a diffraction pattern is helped with information about chemical compositions and candidate crystal structures. For example, candidate phases can be identified with handbooks of phase diagrams, and their diffraction patterns found in the ICDD database.

When the sample contains multiple phases, there can be ambiguity in assigning a diffraction peak to a specific diffraction pattern, and there can be overlaps of peaks from different patterns. A computerized match of full patterns often proves helpful in such cases. Nevertheless, sometimes it is easy to distinguish individual diffraction patterns. The diffraction pattern in was measured to determine if the surface of a glass-forming alloy had crystallized. The amorphous phase has two very broad peaks centered at $2\theta = 38°$ and $74°$. Sharp diffraction peaks from crystalline phases are easily distinguished. Although this crystalline diffraction pattern has not been indexed, the measurement was useful for showing that the solidification conditions were inadequate for obtaining a fully amorphous solid.

Another approach to structure determination by powder diffractometry is to calculate diffraction patterns from candidate crystal structures, and compare them to the measured diffraction patterns. Central to calculating a diffraction which are characteristic of each crystal structure.
Simple diffraction patterns can be calculated with a hand calculator, but structure factors for materials with more complicated unit cells require computer software. The most straightforward software packages take input files of atom positions, atom types, and x-ray wavelength, and return calculated positions and intensities of powder diffraction peaks. In an important extension of this approach, some features of the crystal structure, e.g., lattice parameters, are treated as adjustable parameters.
These parameters are adjusted or "refined" as the software finds the best fit between the calculated and measured diffraction patterns.

26

II.1.2 UV-vis Diffuse Reflectance Spectroscopy

Diffuse Reflectance Spectroscopy is based on the interaction between a UV or visible beam and a powdered sample, from which the beam can be reflected in all directions.

Only the fraction of beam which is scattered within a sample and returned to the surface is considered to be a diffuse reflection. All the reflected radiation can thus be collected within an integrating sphere, enhancing the signal-to noise ratio.

The internal walls of the sphere are usually covered with barium sulfide, a compound that ensures a reflectivity greater than 0.98 in the UV-vis light region. Moreover the reflectance spectrum of a reference standard ($BaSO_4$) should always be recorded prior to that of any other sample.

It's clear that the raw diffuse reflectance spectrum is different from its equivalent absorption due to the multiple surface reflections of the powder grain. At the same time photoabsorption is one of the most significant steps in photocatalysis and the estimation of the number (or flux) of absorbed photons is an important fundamental experiment, considering the first law of photochemistry, i.e. light must be absorbed by a chemical substance in order to promote a photochemical reaction. However, it's still rather difficult to get accurate expressions of photoabsorption spectra of solid materials.

In the literature on photocatalysis, a photoabsorption spectrum, i.e. a plot of the absorption extent as a function of wavelength, is usually reported in terms of absorbance units or Kubelka–Munk function. The former, i.e. absorbance, is traditionally defined as $\log(I_0/I)$, where I_0 and I are the intensities of incident and transmitted light, respectively. Otherwise when photoabsorption is measured in a reflection mode, I can be considered the reflection intensity, while I_0 represents the reflection of a 'standard material', such as $BaSO_4$, which can reflect all the incident light, i.e. 100% reflection. In this regard the Kubelka-Munk (KM) function, usually employed for samples diluted with a medium of less photoabsorption, is otherwise defined as follows:

$$F(R_\infty) = \frac{(1 - R_\infty)^2}{2R_\infty} = \frac{\alpha}{s}$$ Eq.5

In photocatalysis, especially when dealing with doped materials, extremely important is to estimate the optical absorption edge energy of a semiconductor material. The optical absorption edge energy is the minimum photon energy required to promote electrons from the highest occupied molecular orbital (HOMO) to the lowest unoccupied molecular orbital (LUMO). Two basic types of electronic transitions are distinguished, i.e. direct and indirect.Direct transitions demand only the excitation of electrons by photons, while indirect transitions require additionally concerted

27

vibrations and energy from the crystal lattice (phonons). The electron energy near the absorption edge in the case of semiconductors is given by:

$$\alpha = \frac{(h\nu - E_g)^{\eta}}{h\nu} \qquad\qquad \text{Eq.6}$$

where α is the absorption coefficient, $h\nu$ is the energy of the incident photon and E_g is the optical absorption edge energy. The variable η depends on the type of the optical transition caused by photon absorption. In crystalline semiconductors η can assume the following values:

- 1/2 when the transition is direct-allowed
- 3/2 when the transition is direct-forbidden
- 2 when the transition is indirect-allowed
- 3 when the transition is indirect-forbidden

In the case of amorphous, homogeneous semiconductors η is 2 independently of the type of transition. In case of TiO_2, $\eta = 2$ is usually considered.

Experimental diffuse reflectance data cannot be used directly to measure absorption coefficients (α) because of scattering contributions to the reflectance spectra. Scattering coefficient s, however, depends weakly on energy and $F(R_\infty)$ can be considered to be proportional to the absorption coefficient within the narrow range of energy containing the absorption edge features. In such way, the determination of the absorption edge energy can be estimated from the $(F(R_\infty) \cdot h\nu)1/\eta$ versus $h\nu$ plot. In particular the experimental band gap value can be obtained from the x-intercept of the straight tangent line to this plot.

II.1.3 *Surface area and pore structure evaluation by gas adsorption*

Surface area and porosity are important parameters in powdered materials. The most widely used techniques for estimating surface area are based on physical adsorption of gas molecules on a solid surface.

Generally gas adsorption on solid surfaces and in the pore spaces is a complex phenomenon involving mass and energy interaction and phase changes. Depending upon the strength of the interaction, all adsorption processes can be divided into the two categories of chemical or physical adsorption. The former, also called irreversible or chemisorption, is characterized mainly by large interaction potentials, which lead to high heats

of adsorption often approaching the values of chemical bonds. This fact, coupled with other spectroscopic, electron spin resonance, and magnetic susceptibility measurements, confirms that chemisorption involves true chemical bonding of the gas or vapour with the surface. Because chemisorption occurs through chemical bonding, it is often found to occur at temperatures above the adsorbates' critical temperature. Strong bonding to the surface is necessary, in the presence of higher thermal energies, if adsorption has to occur at all. Also, as it is true for most chemical reactions, chemisorption is usually associated with an activation energy. In addition, chemisorption is necessarily restricted to, at most, a single layer of chemically bound adsorbate at the surface. Another important factor relating to chemisorption is that the adsorbed molecules are localized on the surface. Because of the formation of a chemical bond between an adsorbate molecule and a specific site on the surface, the adsorbate is not free to migrate along the surface. This fact often enables the number of active sites on catalysts to be determined by simply measuring the quantity of chemisorbed gas. The second category, reversible or physical adsorption, exhibits characteristics that makes it most suitable for surface area determinations as indicated by the following:

- Physical adsorption is accompanied by low heats of adsorption with no violent or disruptive structural changes occurring on the surface during the adsorption measurements.

- Unlike chemisorption, physical adsorption may lead to surface coverage by more than one layer of adsorbate. Thus, pores can be filled by the adsorbate for pore volume measurements.

- At elevate temperatures physical adsorption does not occur or is sufficiently slight that relatively clean surfaces can be prepared on which to make accurate surface area measurements.

- Physical adsorption equilibrium is achieved rapidly since no activation energy is required as in chemisorption. An exception here is adsorption in small pores, where diffusion can limit the adsorption rate.

· Physical adsorption is fully reversible, enabling both the adsorption and desorption processes to be studied.
· Physical adsorbed molecules are not restrained to specific sites and are free to cover the entire surface. For this reason surface areas, rather than the number of sites, can be calculated.

The kinetics and thermodynamics of adsorption have been extensively studied, but, when surface area and pore structure are the subject of interest, it's essential to establish the meaning of an adsorption (desorption) isotherm. This is a measure of the molar quantity of gas n (or standard volume V_a, or general quantity q) taken up, or released, at a constant temperature T by an initially clean solid surface as a function of gas pressure P. In order to increase the amount of physisorbed molecules (usually nitrogen) most frequently the test is conducted at a cryogenic temperature, usually that
of liquid nitrogen (LN_2) at its boiling point (77.35 K at 1 atm pressure). Convention has established that the quantity of gas adsorbed is expressed as its volume at standard temperature and pressure conditions (0°C and 760 torr and denoted by STP), while the pressure is expressed as a relative pressure, which is the actual gas pressure P divided by the vapor pressure P_0 of the adsorbing gas at the temperature of the test. Plots of V_a as the ordinate against P/P_0 as the abscissa reveal much about the structure of the adsorbing material (called the adsorbent) simply from their shape. The theory mainly used in order to get essential information (such as surface area and pore distribution) from experimental adsorption isotherm is known as BET theory from the surnames of its creators, Brunauer, Emmett and Teller.50 This is an extension to multilayer adsorption of the Langmuir model (related to monolayer molecular adsorption) and the resulting BET equation is expressed as follows:

$$V_\alpha = \frac{V_m C P}{(P_0 - P)\left[1 + (C-1)\dfrac{P}{P_0}\right]}$$

Eq.6

where:

$V\alpha$ = volume of adsorbed gas at pressure P.
V_m = monolayer volume.
P = gas pressure.
P_0 = saturation gas pressure

The value of parameter C, fairly constant for a given class of materials, e.g. oxides and metals, in simplest terms is given by the following equation:

$$C \propto \exp\frac{(q_1 - q_L)}{RT}$$

Eq.7

where:

30

q_l = heat of adsorption of the first layer.
q_L = heat of liquefaction of the adsorptive.
R = gas constant.
T = absolute temperature.

Small values of the C parameter stand for a higher affinity between molecules than between the molecules and the adsorbing species, resulting in lower wettability. On the contrary, high C values describe the typical isotherm, characterized, firstly, by a monolayer adsorption and then by the multilayer one, layer by layer.

Equation 6 can also be written in the linear form:

$$\frac{P}{V_\alpha(P_0 - P)} = \frac{1}{V_m C} + \frac{C-1}{V_m C}\left(\frac{P}{P_0}\right)$$ Eq.8

Isotherm data for most solids when using nitrogen as the adsorptive and plotting them in according to equation (Eq.8) yield a straight line within the range $0.05 < P/P_0 < 0.35$.

From the slope and intercept values of the BET linear plot it is possible to calculate both the amount of adsorbate corresponding to the first monolayer, V_m, and the C parameter can be calculated. Assuming that the surface occupied by a N_2 molecule is 16.2·10-20 m^2, once calculated V_m, it's easy to obtain the Specific Surface Area (SSA) of the adsorbing material, by the following equation:

$$SSA = \frac{V_m N_A S_{N_2}}{22.414 g}$$ Eq.9

where:

N_A = Avogadro number (6.023·10^{23} molecules mol^{-1}).
S_{N2} = surface occupied by a N_2 molecule adsorbed on the monolayer.
22.414 = volume (dm^3) occupied by 1 mole of gas under standard conditions.
g = sample quantity (g).

Moreover, the C value is most frequently between 50 and 300, when using nitrogen at 77 K. A high or negative C value is indicative of micropores and their measurement cannot be analysed by this BET model without further modification

II.1.4 Electron microscopy

Since its invention, the electron microscope has been a valuable tool in the development of scientific theory and it contributed greatly to biology, medicine and material sciences. This wide spread use of electron microscopes is based on the fact that they permit the observation and characterization of materials on a nanometer (nm) to micrometer (μm) scale. The basic theory for electron microscopy are here shortly presented, focusing on the two basic types of Ems; SEM (Scanning Electron Microscope) and TEM (Transmission Electron Microscope).

Electron Microscopes are scientific instruments that use a beam of highly energetic electrons to examine objects on a very fine scale. This examination can yield information about the topography (surface features of an object), morphology (shape and size of the particles making up the object), composition (the elements and compounds that the object is composed of and the relative amounts of them) and crystallographic information (how the atoms are arranged in the object). Electron Microscopes were developed due to the limitations of Light Microscopes which are limited by the physics of light to 500x or 1000x magnification with a resolution of 0.2 mm. In the early 1930's this theoretical limit had been reached and there was a scientific desire to see the fine details of the interior structures of organic cells (nucleus, mitochondria...etc.). This required 10.000x plus magnification which was just not possible using Light Microscopes.

The Transmission Electron Microscope (TEM) was the first type of Electron Microscope to be developed and is patterned exactly on the Light Transmission Microscope except that a focused beam of electrons is used instead of light to "see through" the specimen. It was developed by Max Knoll and Ernst Ruska in Germany in 1931. The first Scanning Electron Microscope (SEM) debuted in 1942, with the first commercial instruments around 1965. Its late development was due to the electronics involved in "scanning" the beam of electrons across the sample. Electron Microscopes (EMs) function exactly as their optical counterparts except that they use a focused beam of electrons instead of light to "image" the specimen and gain information as to its structure and composition.

II.1.4.1 Electron-matter interactions

When an electron beam interacts with the atoms in a sample, individual incident electrons undergo two types of scattering - elastic and inelastic. In the former, only the trajectory changes and the kinetic energy and velocity remain constant. In the case of inelastic scattering, some incident electrons will actually collide with and displace different kind of electrons from the

specimen, thus loosing their kinetic energy. Figure 8 summarizes the main secondary signals (with different relative intensity) that can be produced due to electron–matter interactions.

By considering the large amount of information obtained by this kind of interaction it's essential try to amplify each single signal by using different kinds of instrumentation. In this regard the first main difference between SEM and TEM, mainly concerning the sample location in the microscope, can be outlined. In particular SEM studies the information related to secondary and backscattered electrons, detected on the same side with respect to the incident electrons beam. In this case the sample holder is located at the end of microscope's column (Figure 9a). On the contrary TEM deals with transmitted, elastically or inelastically scattered electrons, detected on the opposite side with respect to the incident electrons beam. In this case the sample holder is located in the middle of the microscope's column (Figure 9b).
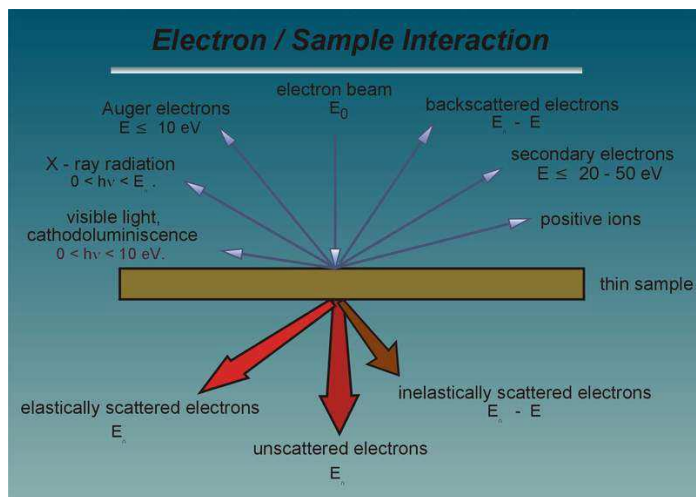
Figure 8 *Signals generated when a high-energy beam of electrons interacts with a thin specimen.*

Both SEM and TEM instruments must work under ultra high vacuum conditions (10^{-7}-10^{-8} Pa) in order to avoid any kind of collision between the electrons beam and atoms, which are not those contained in the investigated sample. Moreover there are essential instrumental components which are common to SEM and TEM systems: electron guns, which can be divided into thermoionic and field-emission types, and metal apertures and magnetic lenses necessary to confine and focus the electron beam toward the specimen (thanks to the application of a proper potential).

33
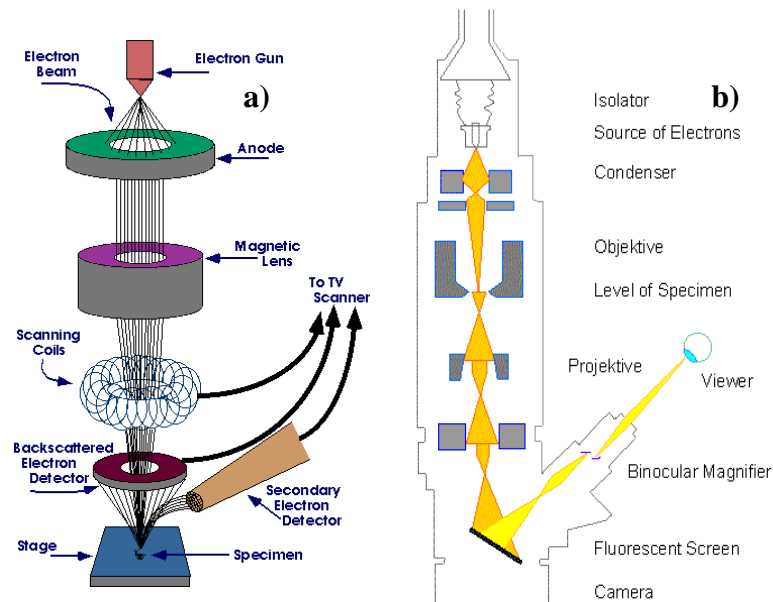
Figure 9 *General scheme of a) SEM and b) TEM instrumentations.*

II.1.4.2 Electrons exploited in Trasmission Electron

Microscopy (TEM)

TEM exploits three different interactions of electron beam-specimen: unscattered electrons (transmitted beam), elastically scattered electrons (diffracted beam) and inelastically scattered electrons. When incident electrons are transmitted through the thin specimen without any interaction occurring inside the specimen, then the beam of these electrons is called transmitted. The transmission of unscattered electrons is inversely proportional to the specimen thickness. Areas of the specimen that are thicker will have fewer transmitted unscattered electrons and so will appear darker; conversely the thinner areas will have more transmitted and thus will appear lighter. Another part of the incident electrons, are scattered (deflected from their originalpath) by atoms in the specimen in an elastic fashion (without loss of energy). These diffracted electrons according to Bragg's law are then transmitted through the remaining portions of the specimen. In this case a diffraction pattern and the related information about orientation, atomic arrangements and phases present in the examined area can be obtained. There are essentially three different imaging modes in TEM, which

can be selected by changing proper apertures of the back focal plane (after the objective lens) (Figure 10):

1. Bright field mode: the aperture selects only transmitted electrons. In this case, factors such as mass and thickness of the sample influence the formation of the image.

2. Dark field mode: in this case only diffracted electrons, which gave strong interaction with the sample, are selected. The image obtained can give information about the presence of defects or different phases of the specimen.

3. High resolution (HR-TEM): in this case both transmitted and diffracted electrons are selected. Using proper corrections for spherical aberration, special high resolution TEMs can generate images with a resolution below 0.1 nm; it's thus possible observe reticular planes and get crystallographic information of the examined sample. By considering that for TEM analysis the analyzed electrons have to pass through the sample, the specimens have to be rather thin, less than 100 nm.
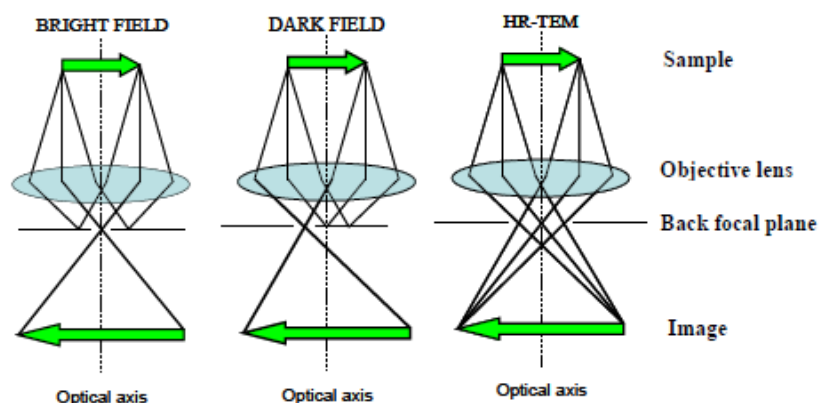
Figure 10 *Generalized description of the three main imaging modes in TEM.*

II.1.5 The Raman spectroscopy

The Raman spectroscopy measures the vibrational motions of a molecule like the infrared spectroscopy. The physical method of observing the vibrations is, however, different from the infrared spectroscopy. In Raman spectroscopy one measures the light scattering while the infrared spectroscopy is based on absorption of photonsThe Raman phenomenon was detected in 1928 by the Indian physicist Sir Chandrasekhara Venkata Raman and Kariamanikkam Srinivasa Krishnan.12 Independently of this work, the

phenomenon was also reported by Grigory Landsberg and Leonid Mandelstam. However, the phenomenen was predicted theoretically even earlier by using the classical model. After the end of 1920's the method was forgotten for several decades because the signal is very weak. Raman spectrocopy experienced a renaissance in the 1960's when the lasers were invented and started to be used as light sources in spectroscopy. The basics of the Raman scattering can be explained using classical physics but a more comprehensiv theory requires quantum mechanical treatise. Both the classical and quantum mechanical formulations are schetched below.

When light interacts with matter, the photons which make up the light may be absorbed or scattered, or may not interact with the material and may pass straight through it. If the energy of an incident photon corresponds to the energy gap between the ground state of a molecule and an excited state, the photon may be absorbed and the molecule promoted to the higher energy excited state. It is this change which is measured in absorption spectroscopy by the detection of the loss of that energy of radiation from the light. However, it is also possible for the photon to interact with the molecule and scatter from it. In this case there is no need for the photon to have an energy which matches the difference between two energy levels of the molecule. The scattered photons can be observed by collecting light at an angle to the incident light beam, and provided there is no absorption from any electronic transitions which have similar energies to that of the incident light, the efficiency increases as the fourth power of the frequency of the incident light. Scattering is a commonly used technique. For example, it is widely used for measuring particle size and size distribution down to sizes less than 1 mm. One everyday illustration of this is that the sky is blue because the higher energy blue light is scattered from molecules and particles in the atmosphere more efficiently than the lower energy red light. However, the main scattering technique used for molecular identification is Raman scattering. The process of absorption is used in a wide range of spectroscopic techniques. For example it is used in acoustic spectroscopy where there is a very small energy difference between the ground and excited states and in X-ray absorption spectroscopy where there is a very large difference. In between these extremes are many of the common techniques such as NMR, EPR, infrared absorption, electronic absorption and fluorescence emission, and vacuum ultraviolet (UV) spectroscopy. Radiation is often characterized by its wavelength (l). However, in spectroscopy, because we are interested in the interaction of radiation with states of the
molecule being examined and this being usually discussed in terms of energy, it is often useful to use frequency (n) or wavenumber (v) scales, which are linearly related with energy

$$\lambda = \frac{c}{v} \hspace{6cm} Eq.10$$

$$v = \frac{\Delta E}{h} \qquad\qquad\qquad\qquad \text{Eq.11}$$

$$\varpi = \frac{1}{\lambda} \qquad\qquad\qquad\qquad \text{Eq.12}$$

It is clear from Equations 10-12 that the energy is proportional to the reciprocal of wavelength and therefore the highest energy region is on the left in Figure 11 and the longest wavelength on the right. The way in which radiation is employed in infrared and Raman spectroscopies is different. In infrared spectroscopy, infrared energy covering a range of frequencies is directed onto the sample. Absorption occurs where the frequency of the incident radiation matches that of a vibration so that the molecule is promoted to a vibrational excited state. The loss of this frequency ofradiation from the beam after it passes through the sample is then detected. In contrast, Raman spectroscopy uses a single frequency of radiation to irradiate the sample and it is the radiation scattered from the molecule, one vibrational unit of energy different from the incident beam, which is detected. Thus, unlike infrared absorption, Raman scattering does not require matching of the incident radiation to the energy difference between the ground and excited states. In Raman scattering, the light interacts with the molecule and distorts (polarizes) the cloud of electrons round the nuclei to form a short-lived called a 'virtual state'.

Gamma X-rays	UV-visible	Near IR	Mid-IR	Far IR	Micro-radio
	--	
10^{-11}	10^{-7}	10^{-6}	10^{-5}	10^{-4}	10 m
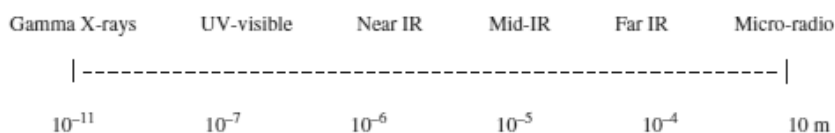
Figure 11 *The electromagnetic spectrum on the wavelength scale in metres.*

This state is not stable and the photon is quickly re-radiated. The energy changes we detect in vibrational spectroscopy are those required to cause nuclear motion. If only electron cloud distortion is involved in scattering, the photons will be scattered with very small frequency changes, as the electrons are comparatively light. This scattering process is regarded as elastic scattering and is the dominant process. For molecules it is called Rayleigh scattering. However, if nuclear motion is induced during the scattering process, energy will be transferred either from the incident photon to the molecule or from the molecule to the scattered photon. In these cases the process is inelastic and the energy of the scattered photon is different from

that of the incident photon by one vibrational unit. This is Raman scattering. It is inherently a weak process in that only one in every $10^6 - 10^8$ photons which scatter is Raman scattered. In itself this does not make the process insensitive since with modern lasers and microscopes, very high power densities can be delivered to very small samples but it is does follow that other processes such as sample degradation and fluorescence can readily occur.

Figure 12 shows the basic processes which occur for one vibration. At room temperature, most molecules, but not all, are present in the lowest energy vibrational level. Since the virtual states are not real states of the molecule but are created when the laser interacts with the electrons and causes polarization, the energy of these states is determined by the frequency of the light source used. The Rayleigh process will be the most intense process since most photons scatter this way. It does not involve any energy change and consequently the light returns to the same energy state. The Raman scattering process from the ground vibrational state m leads to absorption of energy by the molecule and its promotion to a higher energy excited vibrational state (n). This is called Stokes scattering.
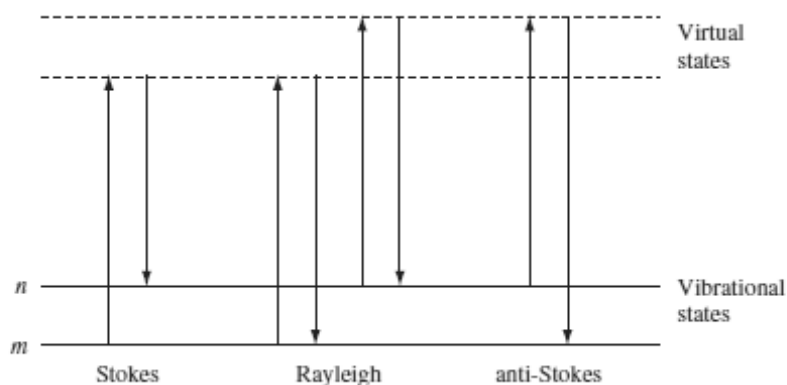
Figure 12 *Diagram of the Rayleigh and Raman scattering processes. The lowest energy vibrational state m is shown at the foot with states of increasing energy above it. Both the low energy (upward arrows) and the scattered energy (downward arrows) have much larger energies than the energy of a vibration.*

However, due to thermal energy, some molecules may be present in an excited state such as n in Figure 12. Scattering from these states to the ground state m is called anti-Stokes scattering and involves transfer of energy to the scattered photon. The relative intensities of the two processes depend on the population of the various states of the molecule. The populations can be worked out from the Boltzmann equation but at room

38

temperature, the number of molecules expected to be in an excited vibrational state other than any really low-energy ones will be small. Thus, compared to Stokes scattering, anti-Stokes scattering will be weak and will become weaker as the frequency of the vibration increases, due to decreased population of the excited vibrational states. Further, anti-Stokes scattering will increase relative to Stokes scattering as the temperature rises.

Figure 13 shows a typical spectrum of Stokes and anti-Stokes scattering from cyclohexane separated by the intense Rayleigh scattering which should be offscale close to the point where there is no energy shift. However there is practically no signal close to the frequency of the exciting line along the x-axis. This is because filters in front of the spectrometer remove almost all light within about 200 cm^{-1} of the exciting line. Some breakthrough of the laser light can be seen where there is no energy shift at all. Usually, Raman
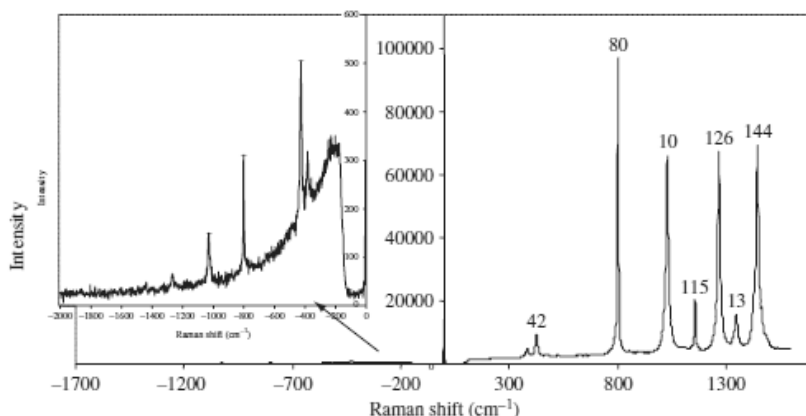
Figure 13 *Stokes and anti-Stokes scattering for cyclohexane. To show the weak anti- Stokes spectrum, the y-axis has been extended in the inset.*

scattering is recorded only on the low-energy side to give Stokes scattering but occasionally anti-Stokes scattering is preferred. For example, where there is fluorescence interference, this will occur at a lower energy than the excitation frequency and consequently anti-Stokes scattering can be used to avoid interference. The difference in intensities of Raman bands in Stokes and anti-Stokes scattering can also be used to measure temperature Figure 12 illustrates one key difference between infrared absorption and Raman scattering. As described above, infrared absorption would involve direct excitation of the molecule from state m to state n by a photon of exactly the energy difference between them. In contrast, Raman scattering uses much higher energy radiation and measures the difference in energy between n and m by subtracting the energy of the scattered photon from that of the incident beam (the two vertical arrows in each case). The cyclohexane spectrum in Figure 13 shows that there is more than one vibration which gives effective

Raman scattering (i.e. is Raman active). However, there is a basic selection rule which is required to understand this pattern. Intense Raman scattering occurs from vibrations which cause a change in the polarizability of the electron cloud round the molecule. Usually, symmetric vibrations cause the largest changes and give the greatest scattering. This contrasts with infrared absorption where the most intense absorption is caused by a change in dipole and hence asymmetric vibrations which cause this are the most intense. As will be seen later, not all vibrations of a molecule need, or in some cases can, be both infrared and Raman active and the two techniques usually give quite different intensity patterns. As a result the two are often complementary and, used together, give a better view of the vibrational structure of a molecule.
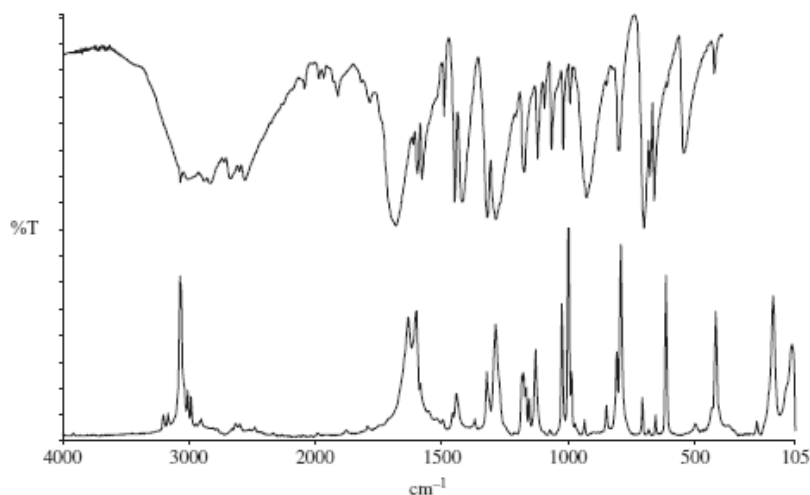
Figure 14 *Infrared and Raman spectra of benzoic acid. The top trace is infrared absorption given in % transmission (%T) so that the lower the transmission value the greater the absorption. The lower trace is Raman scattering and the higher the peak the greater the scattering.*

One specific class of molecule provides an additional selection rule. In a centrosymmetric molecule, no band can be active in both Raman scattering and infrared absorption. This is sometimes called the mutual exclusion rule. In a centrosymmetric molecule, reflection of any point through the centre will reach an identical point on the other side (C_2H_4 is centrosymmetric, CH_4 is not). This distinction is useful particularly for small molecules where a comparison of the spectra obtained from infrared absorption and Raman scattering can be used to differentiate cis and trans forms of a molecule in molecules such as a simple azo dye or a transition metal complex.

40

Figure 14 shows a comparison of the infrared and Raman spectra for benzoic acid. The x-axis is given in wavenumbers for which the unit is cm^{-1}. Wavenumbers are not recommended SI units but the practice of spectroscopy is universally carried out using these and this is unlikely to change. For infrared absorption each peak represents an energy of radiation absorbed by the molecule. The y-axis gives the amount of the light absorbed and is usually shown with the maximum absorbance as the lowest point on the trace. Raman scattering is presented only as the Stokes spectrum and is given as a shift in energy from the energy of the laser beam. This is obtained by subtracting the scattered energy from the laser energy. In this way the difference in energy corresponding to the ground and excited vibrational states (n and m in Figure 12) is obtained. This energy difference is what is measured directly by infrared. The scattering is measured as light detected by the spectrometer and the maximum amount of light detected is the highest point on the trace

Strictly speaking, Raman scattering should be expressed as a shift in energy from that of the exciting radiation and should be referred to as Δcm^{-1} but it is often expressed simply as cm^{-1}. This practice is followed in this book for simplicity. Although different energy ranges are possible, the information of interest to most users is in the 3600-400 cm^{-1} (2.8–12 micron) range in infrared spectroscopy and down to 200 cm^{-1} in Raman spectroscopy since this includes most modes which are characteristic of a molecule. In some applications, much larger or smaller energy changes are studied and modern Raman equipment can cope with much wider ranges. One specific advantage of Raman scattering is that shifts from the laser line of 50 cm^{-1} or lower can easily be recorded with the correct equipment. Many modern machines for reasons of cost and simplicity are not configured in asuitable way to measure shifts below 100-200 cm^{-1}. The intensities of the bands in the Raman spectrum are dependent on the nature of the vibration being studied and on instrumentation and sampling factors. Modern instruments should be calibrated to remove the instrument factors but this is not always the case; these factors are dealt with in the next chapter. Sampling has a large effect on the absolute intensities, bandwidths observed and band positions. Again these will be dealt with later. This chapter will concentrate on the effect on Raman scattering of the set of vibrations present in a molecule and set out a step-by-step approach to interpretation based on simple selection rules.

II.1.6 *Infrared spectroscopy (FTIR)*

Infrared spectroscopy is certainly one of the most important analytical techniques available to today's scientists. One of the great advantages of infrared spectroscopy is that virtually any sample in virtually any state may

be studied. Liquids, solutions, pastes, powders, films, fibres, gases and surfaces can all be examined with a judicious choice of sampling technique. As a consequence of the improved instrumentation, a variety of new sensitive techniques have now been developed in order to examine formerly intractable samples. Infrared spectrometers have been commercially available since the 1940s. At that time, the instruments relied on prisms to act as dispersive elements, but by the mid 1950s, diffraction gratings had been introduced into dispersive machines. The most significant advances in infrared spectroscopy, however, have come about as a result of the introduction of Fourier-transform spectrometers. This type of instrument employs an interferometer and exploits the wellestablished mathematical process of Fourier-transformation. Fourier-transform infrared (FTIR) spectroscopy has dramatically improved the quality of infrared spectra and minimized the time required to obtain data. In addition, with constant improvements to computers, infrared spectroscopy has made further great strides. Infrared spectroscopy is a technique based on the vibrations of the atoms of a molecule. An infrared spectrum is commonly obtained by passing infrared radiation through a sample and determining what fraction of the incident radiation is absorbed at a particular energy. The energy at which any peak in an absorption spectrum appears corresponds to the frequency of a vibration of a part of a sample molecule. In this introductory chapter, the basic ideas and definitions associated with infrared spectroscopy will be described. The vibrations of molecules will be looked at here, as these are crucial to the interpretation of infrared spectra. Once this chapter has been completed, some idea about the information to be gained from infrared spectroscopy should have been gained. The following chapter will aid in an understanding of how an infrared spectrometer produces a spectrum. After working through that chapter, it should be possible to record a spectrum and in order to do this a decision on an appropriate sampling technique needs to be made. The sampling procedure depends very much on the type of sample to be examined, for instance, whether it is a solid, liquid or gas.

The interactions of infrared radiation with matter may be understood in terms of changes in molecular dipoles associated with vibrations and rotations. In order to begin with a basic model, a molecule can be looked upon as a system of masses joined by bonds with spring-like properties. Taking first the simple case of diatomic molecules, such molecules have three degrees of translational freedom and two degrees of rotational freedom. The atoms in the molecules can also move relative to one other, that is, bond lengths can vary or one atom can move out of its present plane. This is a description of stretching and bending movements that are collectively referred to as vibrations. For a diatomic molecule, only one vibration that corresponds to the stretching and compression of the bond is possible. This accounts for one degree of vibrational freedom.

Polyatomic molecules containing many (N) atoms will have 3N degrees of freedom. Looking first at the case of molecules containing three atoms, two groups of triatomic molecules may be distinguished, i.e. linear and non-linear.Two simple examples of linear and non-linear triatomics are represented by CO_2. and H_2O, respectively . Both CO_2 and H_2O have three degrees of translational freedom. Water has three degrees of rotational freedom, but the linear molecule carbon dioxide has only two since no detectable energy is involved in rotation around the O=C=O axis. Subtracting these from 3N, there are 3N−5 degrees of freedom for CO_2 (or any linear molecule) and 3N−6 for water (or any non-linear molecule). N in both examples is three, and so CO_2 has four vibrational modes and water has three.

Whereas a diatomic molecule has only one mode of vibration which corresponds to a stretching motion, a non-linear B−A−B type triatomic molecule has three modes, two of which correspond to stretching motions, with the remainder corresponding to a bending motion. A linear type triatomic has four modes, two of which have the same frequency, and are said to be degenerate. Two other concepts are also used to explain the frequency of vibrational modes. These are the stiffness of the bond and the masses of the atoms at each end of the bond. The stiffness of the bond can be characterized by a proportionality constant termed the force constant, k (derived from Hooke's law). The reduced mass, μ, provides a useful way of simplifying our calculations by combining the individual atomic masses, and may be expressed as follows:

$$\frac{1}{\mu} = \left(\frac{1}{m_1}\right) + \left(\frac{1}{m_2}\right)$$
Eq.13

where m_1 and m_2 are the masses of the atoms at the ends of the bond. A practical alternative way of expressing the reduced mass is:

$$\mu = \frac{m_1 m_2}{\left(m_1 + m_2\right)}$$
Eq.14

The equation relating the force constant, the reduced mass and the frequency of absorption is:

$$v = \frac{1}{2\pi}\sqrt{\frac{k}{\mu}}$$
Eq.15

This equation may be modified so that direct use of the wavenumber values for bond vibrational frequencies can be made, namely:

$$\bar{v} = \frac{1}{2\pi c}\sqrt{\frac{k}{\mu}}$$
Eq.16

where c is the speed of light

43

A molecule can only absorb radiation when the incoming infrared radiation is of the same frequency as one of the fundamental modes of vibration of the molecule. This means that the vibrational motion of a small part of the molecule is increased while the rest of the molecule is left unaffected.

Vibrations can involve either a change in bond length (stretching) or bond angle (bending). Some bonds can stretch in-phase (symmetrical stretching) or out-of-phase (asymmetric stretching). If a molecule has different terminal atoms such as HCN, ClCN or ONCl, then the two stretching modes are no longer symmetric and asymmetric vibrations of similar bonds, but will have varying proportions of the stretching motion of each group. In other words, the amount of coupling will vary.

II.1.7 Dynamic light scattering (DLS)

Dynamic light scattering (DLS), also known as photon correlation spectroscopy (PCS) and quasi-elastic light scattering (QELS), provides many advantages as a particle size analysis method. DLS is a noninvasive technique that measures a large population of particles in a very short time period, with no manipulation of the surrounding medium. Modern DLS instruments, notably the Zetasizer Nano system (Malvern Instruments, Southborough, MA), can measure particle sizes as small as 0.6 nm and as large as 6 μm across a wide range of sample concentrations. Because of the sensitivity to trace amounts of aggregates and the ability to resolve multiple particle sizes, DLS is ideally suited for macromolecular applications necessitating low sample concentration and volume, such as the development of stable food, drug, and surfactant formulations and in the screening of protein samples for crystallization trials.

Particles and macromolecules in solution undergo Brownian motion. Brownian motion arises from collisions between the particles and the solvent molecules. As a consequence of this particle motion, light scattered from the particle ensemble will fluctuate with time. In DLS, these fluctuations are measured across very short time intervals to produce a correlation curve, from which the particle diffusion coefficient (and subsequently the particle size) is extracted. In contrast to separation techniques, where particles are separated and then counted, in the DLS technique, all of the size information for the ensemble of particles is contained within a single correlation curve. As such, particle size resolution requires a deconvolution of the data contained in the measured correlation curve. While standard algorithms exist for transforming the correlation curve to a particle size distribution, an understanding of the precision and accuracy of the distribution necessitates a solid understanding of the underlying principles behind the DLS technique itself. This article presents a brief overview of the DLS technique, along

with common algorithms used to deconvolute the size distribution from the measured correlation curve.

II.1.7.1 Dynamic light scattering

Light scattering is a consequence of the interaction of light with the electric field of a particle or small molecule. This interaction induces a dipole in the particle electric field that oscillates with the same frequency as that of the incident light. Inherent to the oscillating dipole is the acceleration of charge, which leads to the release of energy in the form of scattered light. For a collection of solution particles illuminated by a light source such as a laser, the scattering intensity measured by a detector located at some point in space will be dependent on the relative positions of the particles within the scattering volume. The scattering volume is defined as the crossover section of the light source and the detector optics.
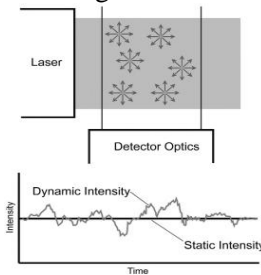
Figure 15 S*chematic detailing the scattering volume and subsequent static anddynamic light scattering intensities*
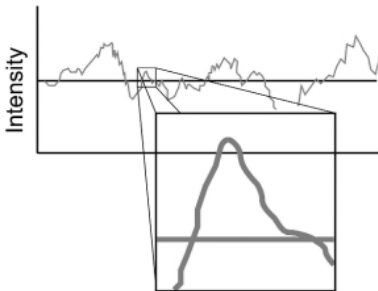
Figure 16 *Intensity time trace showing the lack of discontinuity expected for arandom signal when viewed across a short time interval*

The position dependence of the scattering intensity arises from constructive and destruction interference of the scattered light waves. If the particles are static, or frozen in space, then one would expect to observe a scattering intensity that is constant with time, as described in Figure 15. In practice, however, the particles are diffusing according to Brownian motion, and the scattering intensity fluctuates about an average value equivalent to the static

intensity. As detailed in Figure 15, these fluctuations are known as the dynamic intensity. Across a long time interval, the dynamic signal appears to be representative of random fluctuations about a mean value. When viewed on a much smaller time scale, however (Figure 16), it is evident that the intensity trace is in fact not random, but rather comprises a series of continuous data points. This absence of discontinuity is a consequence of the physical confinement of the particles in a position very near to the position occupied a very short time earlier. In other words, on short time scales, the particles have had insufficient time to move very far from their initial positions, and as such, the intensity signals are very similar. The net result is an intensity trace that is smooth, rather than discontinuous.
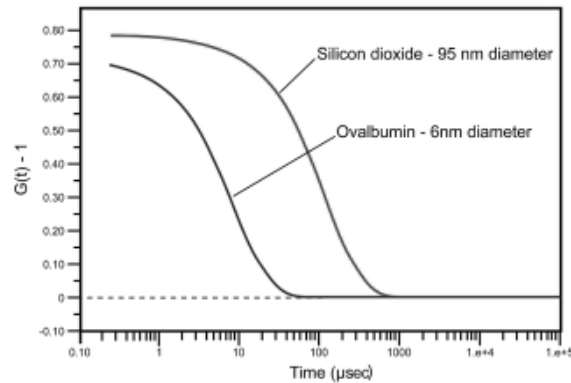
Figure 17 *Intensity correlation curves for ovalbumin and silicon dioxide, measured with a Zetasizer Nano ZS static, dynamic, and electrophoretic light scattering instrument.*

Correlation is a second-order statistical technique for measuring the degree of nonrandomness in an apparently random data set. When applied to a time-dependent intensity trace, as measured with DLS instrumentation, thecorrelation coefficients, G(τ), arecalculated as shown in Eq.17, where t is the initial (start) time and τ is the delay time.

$$G(\tau) = \int_0^\infty I(t)I(t+\tau)dt \qquad \text{Eq.17}$$

$$G_k(\tau_k) = \sum_{i=0} I(t_i)I(t_i+\tau_k) \qquad \text{Eq.18}$$

Typically, the correlation coefficients are normalized, such that G(∞) = 1. For monochromatic laser light, this normalization imposes an upper correlation curve limit of 2 for G(t_o) and a lower baseline limit of 1 for G(∞).

In practice, however, the upper limit can only be achieved for carefully optimized optical systems. Typical experimental upper limits are approx. In DLS instrumentation, the correlation summations are performed using an integrated digital correlator, which is a logic board comprising operational amplifiers that continually add and multiply short time scale fluctuations in the measured scattering intensity to generate the correlation curve for the sample. Examples of correlation curves measured for two submicron particles are given in Figure 17. For the smaller and hence faster diffusing protein, the measured correlation curve has decayed to baseline within 100 µsec, while the larger and slower diffusing silicon dioxide particle requires nearly 1000 µsec before correlation in the signal is completely lost

II.1.7.2 Hydrodynamic size

All of the information regarding themotion or diffusion of the particles in thebsolution is embodied within the measured correlation curve. For monodisperse samples, consisting of a single particle size group, the correlation curve can be fit to a single exponential form as given in Eq.19, where B is the baseline, A is the amplitude, and D is the diffusion coefficient. The scattering vector (q) is defined by Eq.20, where ñ is the solvent refractive index, λ_o is the vacuum wavelength of the laser, and θ is the scattering angle.

$$G(\tau) = \int_{0}^{\infty} I(t)I(t+\tau)dt = B + Ae^{-2q^2D\tau} \qquad \text{Eq.19}$$

$$q = \frac{4\pi n}{\lambda_0}\sin\left(\frac{\vartheta}{2}\right) \qquad \text{Eq.20}$$

The hydrodynamic radius is defined as the radius of a hard sphere that diffuses at the same rate as the particle under examination. The hydrodynamic radius is calculated using the particle diffusion coefficient and the Stokes- Einstein equation given in Eq. 20, where k is the Boltzmann constant, T is the absolute temperature, and η is the solvent viscosity of the correlation curve is the fittin procedure recommended by the International Standards Organization (ISO).

$$R_H = \frac{kT}{6\pi\eta D} \qquad \text{Eq.21}$$

The hydrodynamic size extracted using this method is an average value, weighted by the particle scattering intensity. Because of the intensity weighting, the Cumulant size is defined as the Z average or intensity average.
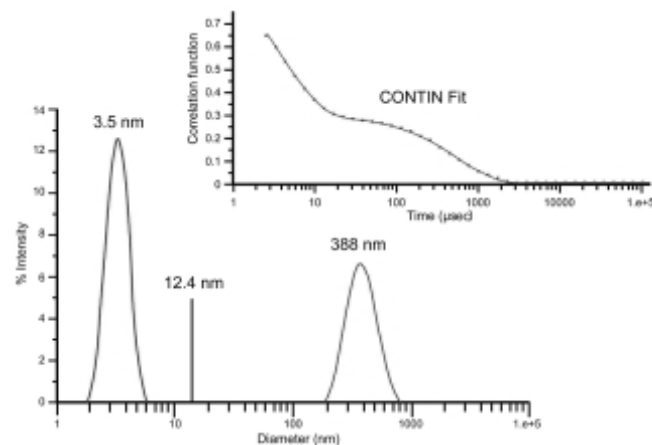
Figure 18 *Correlation curve and CONTIN distribution for 10-mg/mL lysozyme in 100 mMNaCl at 69 °C, measured with a Zetasizer Nano ZS static, dynamic, and electrophoretic light scattering system. The Z average of 12.4 nm is indicated by the solid line in the distribution results.*

While the Cumulant algorithm and the Z average are useful for describing general solution characteristics, for multimodal solutions, consisting of multiple particle size groups, the Z average can be misleading. For multimodal solutions, it is more appropriate to fit the correlation curve to a multiple exponential form, using common algorithms such as CONTIN or Non Negative Least Squares (NNLS). Consider, for example, the correlation curve shown in Figure 18. This correlation curve, measured for a 10- mg/mL lysozyme sample in 100 mM NaCl at 69 °C, clearly exhibits two exponential decays, one for the fast-moving monomer at 3.5 nm and one for the slow-moving aggregate at 388 nm. The size distribution shown in Figure 18 was derived using the CONTIN algorithm. When the single exponential Cumulant algorithm is used, a Z average of 12.4 nm is indicated, which is clearly inconsistent with the distribution results.

II.1.7.3 Thermal analysis (TG-MS)

The performances of samples as a function of temperature were determined by Air flow thermal analysis (TG-MS). The apparatus used were a TGAQ500 thermogravimetric analyzer (TA Instruments) and a SDTQ600 simultaneous DSC/TGA (TA Instruments). Both analyzers can be coupled to a Pfieffer Vacuum Benchtop Thermostar mass spectrometer (MS).
TGAQ500 measures weight changes in a material as a function of temperature. The system works in a temperature range of 20-1000 °C, and weight variation resolution is 0.1 µg . The sample, loaded in a crucible made

of platinum and connected to the balance arm by a small hook, is progressively heated in the oven. A thermocouple controls the oven temperature and a second thermocouple reads the sample temperature. Sample pan loading and furnace movement are totally automated and there is a touch screen data display to change operating parameters. Typically measurements are carried out with 20 mg of sample in chromatographic air flow (60 Ncc/min) with a heating rate of 10 °C/min in the temperature range of 20- 800 °C.

The results are displayed as TG curves showing the mass variations as functions of temperature or time, and DTG curves showing the conversion rate (mass loss percentage per unit time) as functions of temperature or time.

Figure 19 contains the typical trends of the TG and DTG curves. SDTQ600 provides a simultaneous measurement of weight change (TGA) and heat flow (DSC) on the same sample from ambient to 1500 °C. It features a proven horizontal dual beam design with automatic beam growth compensation, and the ability to analyze two TGA samples simultaneously. DSC heat flow data is dynamically normalized using the instantaneous sample weight at any given temperature. The sample is loaded in a crucible made of alumina and heated in the horizontal oven. There are two thermocouples to control the oven temperature and the sample temperature. Measurements are carried out with about 30 mg of sample in chromatographic air flow (100 Ncc/min) with a heating rate of 10 °C/min in the temperature range of 20- 800 °C
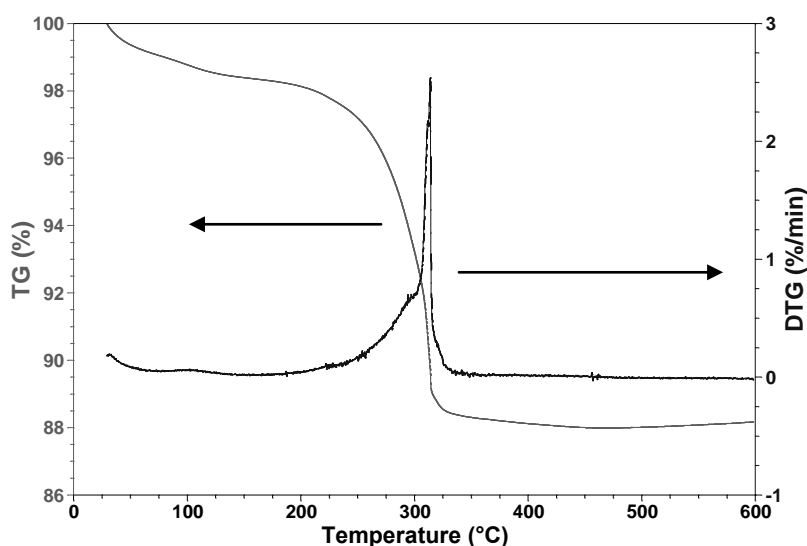
Figure 19 *TG and DTG curves*

Pfieffer Vacuum Benchtop Thermostar mass spectrometer can measure the gas evolved from thermal analyzers up to 300 AMU. The evolved gases

49

are introduced into a heated quartz capillary, which is extremely fine, in order to produce the necessary high vacuum, when the evolved gases enter the mass spectrometer. The heated capillary is necessary in order to prevent condensation of the hot gases on cold surfaces. The analysis of gases is performed by a very high sensitive quadrupole mass detector. The necessary high vacuum is obtained through 2 stages of vacuum pumps that are integrated into a compact housing. First stage is a rotary pump; second stage is a turbo molecular pump.

Both systems, the Mass Spectrometer and the Thermal Balance, are connected to a common PC for data acquisition.

III Nitrogen doped TiO$_2$ photocatalysts: synthesis characterization and optimization

For doping titania with nitrogen, a preliminary investigation has the aim to find the optimal amount of N/Ti ratio, starting from synthesis with different amount of ammonia with respect to the TiO$_2$ precursor (titanium tetraisopropoxide). The obtained samples were characterized to analyze the structure and the ability of absorbing visible light.

III.1 Optimitation of N/Ti ratio: samples preparation and characterization

N-doped TiO$_2$ photocatalysts were prepared by sol-gel method, according to the modified synthetic procedure developed by Sato (Sato et al. 1986). Different amounts (25 ml, 50 ml, 75 ml and 100 ml) of ammonia aqueous solution at 30 wt %, supplied by Carlo Erba, were added to 25 ml of 97 wt% titanium tetraisopropoxide (TTIP by Sigma Aldrich) at 0°C while the solution was vigorously stirred, leading to the formation of a white precipitate. The precipitate was carefully washed with water and centrifuged to be separated. Finally, the obtained powders were dried and calcined at 450°C for 30 minutes to get TiO$_2$ in the anatase phase. In Table 1, a list of doped and undoped titania are respectively reported.

Table 1 *List of catalysts with their nitrogen nominal content*

Catalyst	TTIP volume (mL)	NH₃ solution volume (mL)	N/Ti molar ratio
TiO_2	25	0	-
N_1	25	25	4.6
N_2	25	50	9.3
N_3	25	75	13.9
N_4	25	100	18.6

To characterize the samples studied in this work the following techniques were used:

- UV-vis reflectance spectra (UV-vis);
- Micro Raman spectroscopy;
- Fourier Transform Infrared (FTIR) spectroscopy;
- N_2 adsorption at -196 °C to obtain specific surface area and po characteristics;

III.1.1 UV-vis spectra

UV–vis reflectance spectra (UV-vis DRS) of catalysts were recorded by a Perkin-Elmer spectrometer Lambda 35 using a RSA-PE-20 reflectance spectroscopy accessory (Labsphere Inc., North Sutton, NH). All spectra were obtained using an 88 sample positioning holder, giving total reflectance relative to a calibrated standard SRS-010-99 (Labsphere Inc., North Sutton, NH). The reflectance data were reported as the $F(R\infty)$ value from Kubelka-Munk theory vs the wavelength. Band gap determinations were made by plotting $[F(R\infty)*h\nu]^2$ vs $h\nu$ (eV) and calculating the x intercept of a line passing through $0.5 < F(R\infty) < 0.8$.

The reflectance measurements (Figure 20) of N-doped TiO_2 showed that the absorption onset shifted from 380 to 480 nm determining a decrease of band-gap values from 3.3 eV (the typical band-gap of undoped TiO_2) to 2.5 eV, which is an unexpected value for the only anatase phase. This change in band-gap is therefore attributed to the presence of nitrogen in the crystal structure phase. This result confirms the ability of photocatalysts to absorb visible light.

Table 2 *Band-gap estimation from UV-Vis DRS.*

Catalyst	Bandgap energy (eV)
TiO$_2$	3.3
N_1	2.6
N_2	2.6
N_3	2.5
N_4	2.5
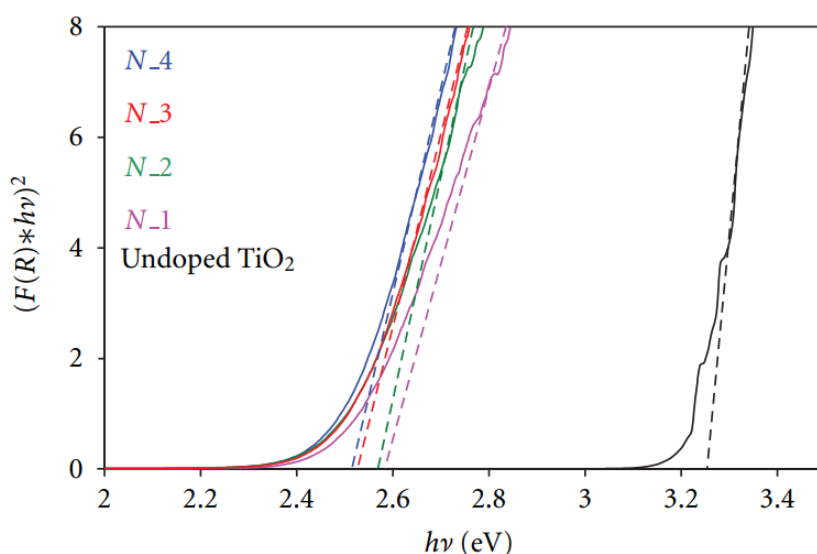
Figure 20 *Band-gap estimation from UV-Vis DRS.*

III.1.2 Micro-Raman spectroscopy

Laser Raman spectra were obtained at room temperature with a Dispersive MicroRaman (Invia, Renishaw), equipped with 785nm diode-laser, in the range 100-2500 cm^{-1} Raman shift

Among the three natural phases including rutile and brookite, anatase phase is retained to be the more active in photocatalysis. Anatase has tetragonal structure of space group D$^{19}_{4h}$ with two formulas per unit cell and thus has six Raman active modes (A$_{1g}$ + 2B$_{1g}$ + 3E$_g$) (Ohsaka et al.1978) (Figure 21). In fact, the Raman modes at 141, 194, 394, 515 and 636 cm^{-1} are all assigned to the anatase phase and, correspondingly, could be assigned to E$_g$, E$_g$, B$_{1g}$, A$_{1g}$ (or B$_{1g}$) and E$_g$ modes in anatase phase, respectively. Bands related to nitrogen species on N-doped TiO$_2$ samples are not

detectable. For all doped photocatalysts the signal from 141 cm^{-1} moves to 144cm^{-1}. It has been reported that the blue shift is related to changes of the oxygen stoichiometry instead of any internal stress or grain size effects (Parker and Siegel, 1990). The defect in oxygen stoichiometry may be due to the presence of nitrogen.
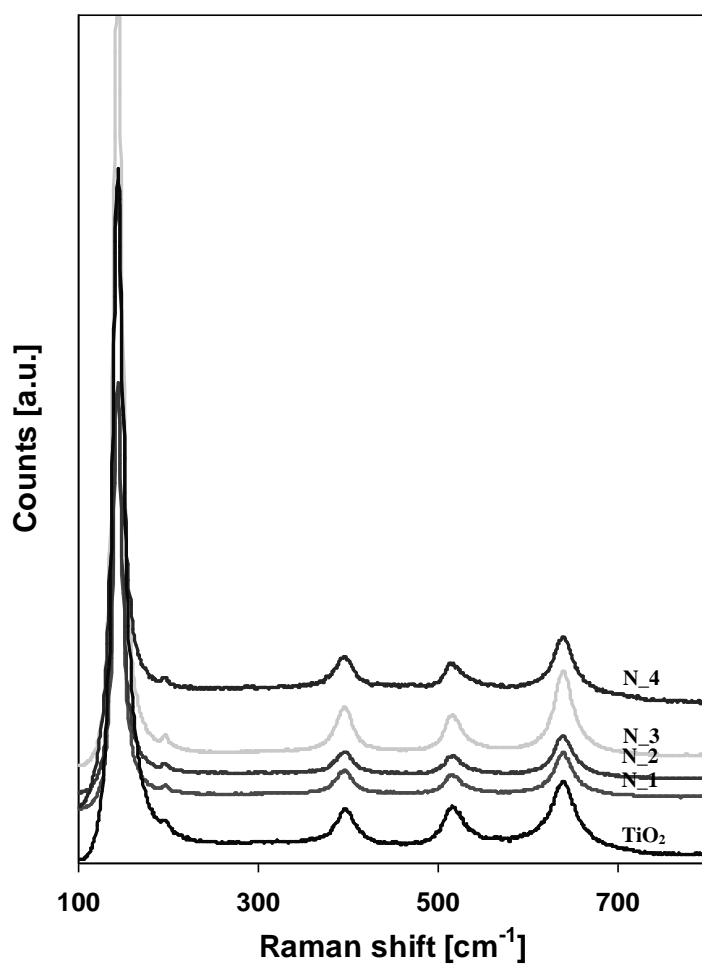
Figure 21 *Raman spectra of undoped TiO$_2$, N_1; N _2; N _3; N _4*

III.1.3 Fourier Transform Infrared (FTIR) spectroscopy

FTIR measurements were carried out by a spectrometer (Perkin- Elmer 2000), equipped with a MCT detector, operating at a resolution of 4 cm^{-1}. The powdered samples were pelletted (pressure, 2×104 kg cm^{-2}) in self-supporting disks of ca. 10 mg cm^{-2}, and put in an IR cell that allowed heating in presence of helium atmosphere
The FTIR spectra analysis of Ndoped TiO$_2$ samples and undoped TiO$_2$ are shown in Figure 22. Undoped sol-gel TiO$_2$ shows bands in the range 3900-900 cm^{-1} related to the presence of water, according to 1633 cm^{-1} stretching
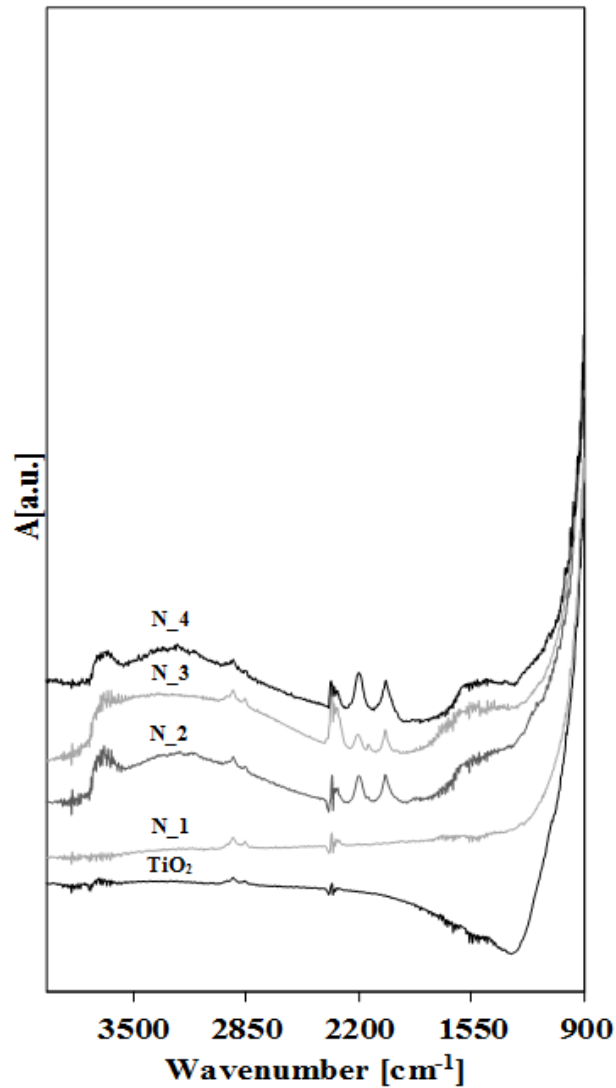
Figure 22 *FTIR spectra of undoped TiO₂, N_1; N _2; N _3; N _4*

band, and to OH vibrations at 3769, 3720-24, 3731-33 cm^{-1} (isolated, bridged and vicinal groups).

Low absorptions at 2850-3060 are typical of titania samples (Figure 22). All doped samples show new bands at 2050-53, 2166, 2214-17, 2345 cm^{-1} and a composite peak with three maxima at 2350, 2360, 2364 cm^{-1}; these peaks can be attributed to the N atoms embedded in the TiO_2 network, or present in its surface. Moreover, these bands could be attributed to several N

58

forms. At 2056 cm^{-1} a N bounded by a triple bond vibrates, and so the band at 2046 cm^{-1} could be likely due to the presence of this kind of surface specie. Peaks at 2166 and 2214-17 cm^{-1} resemble the absorptions of isocianate species bonded to Ti, such as 2M-N=C=O (2147cm^{-1}, 2210 cm^{-1} (Blyholder, 1998) while the composite bands around 2360 cm^{-1} are indicative of NO$^+$, whose presence was detected by a different characterization technique on N-TiO$_2$ photocatalysts. The presence of three maxima in the absorption band could be related to the occurring of different kind of nitrosil ions, interstistial and substitutional, as revealed by XPS measurements (Di Valentin et al., 2007). A wide band in the range 3050-3600 cm^{-1} could indicate the presence of different surface NH terminal groups. From this broad signal emerges a band, around 3170 cm^{-1} assignable to NH stretching of –NH$_2$ groups, confirmed by the presence of 1467 and 1571 cm^{-1} bands. Other contributions at higher wavenumbers can be ascribed to OH groups and it must be observed for the sample N_4 and N_3 in particular bridged OH, vibrating at lower frequencies (3688 cm^{-1}). In addition to the water bending at 1630 cm^{-1}, a band at 1388 cm^{-1} is found, probably due to an NO vibration.

So a more complex picture of the surface emerges from FT-IR analysis, beyond the nitrosyl groups presence, where ammino and isocianate groups (coming from the not complete removal of the precursor organic part), appear responsible for the higher basicity of N-doped TiO$_2$, with respect to the more acid undoped TiO$_2$. Further N-species are likely located as terminal groups linked to Ti, while bridged OH are already present and stabilized on the surface

III.1.4 XRD measurements

XRD analysis for all exhibited strong diffraction peaks at 25° and 48° indicating that TiO$_2$ is mainly in anatase phase (Figure 23). However, a broad and weak diffraction peak at 27° could indicate that only a minor fraction of TiO$_2$ is rutile (Francisco and Mastelaro, 2002).
The averaged anatase grain sizes were determined according to the Scherrer's equation D = kλ/β cos θ, where D is the grain size; k is a constant (shape factor, about 0.9); λ is the X-ray wavelength; β is the full width at half maximum of the diffraction line and θ is the diffraction angle corresponding to (101) diffraction planes (Sannino et al., 2013a). The crystallites size values are reported in Table 3.
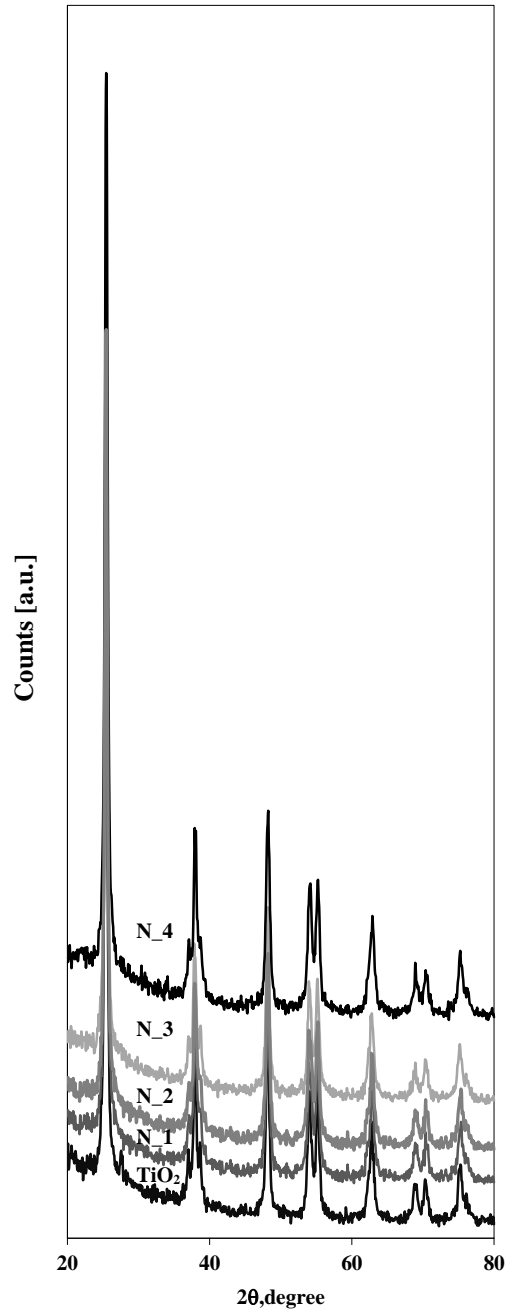
Figure 23 *XRD spectra of undoped TiO2, N_1; N _2; N _3; N _4*

The doped catalysts showed a very similar value with respect to (1 0 1) plane (between 15 and 16 nm), without relevant changes associated with the addition of nitrogen.

Table 3 *Crystallites size from XRD analysis*

Catalyst	Crystallites size (nm)
TiO$_2$	7
N_1	16
N_2	15
N_3	16
N_4	15

III.1.5 Specific surface area (BET)

Specific surface area (BET) was evaluated from dynamic N$_2$ adsorption measurement at -196°C, performed by a Costech Sorptometer 1040 after pretreatment at 150°C for 30 min in He flow.

Type IV isotherm according to the International Union for Pure and Applied Chemistry (IUPAC) classification (Rouquerol et al., 1994) was found for all the photocatalysts, confirming the mesoporous character the undoped titania and for all home made doped titania. As consequence, in Table 4 the specific surface area of all samples evaluated by BET method is reported. The undoped titania sample showed values 171 m^2 g^{-1}. The specific surface area doped photocatalysts were found to be similar 80 m^2 g^{-1} and not influenced by ammonia content

Table 4 *Specific surface area (BET)*

Catalyst	Crystallites size (nm)
TiO$_2$	171
N_1	75
N_2	80
N_3	75
N_4	80

III.1.6 Discussion

From the preliminary results of characterization of doped samples it seems that the N/Ti ratio doesn't influence the chemical- physical

properties of photocatalysts, so the only parameter that could influence the chemical- physical properties is the synthesis procedure.

- The modality of addition of reagents

- Syntesis temperature

- Time of mixing

- Temperature of calcination

- Time of calcination

For understand the influence of this parameter different proced of synthesis was followed until to obtain a standard synthesis method.

III.2 Optimitation of samples preparation

- Different amounts (25 ml, 50 ml, 75 ml and 100 ml) of ammonia aqueous solution at 30 wt %, supplied by Carlo Erba, were added to 25 ml of 97 wt% titanium tetraisopropoxide (TTIP by Sigma Aldrich) drop to drop at 0°C while the solution was vigorously stirred for 10 min, leading to the formation of a white precipitate. The precipitate was carefully washed with water and centrifuged to be separated.

- 25 ml of 97 wt% titanium tetraisopropoxide was frozen (TTIP by Sigma Aldrich) and added to different amounts (25 ml, 50 ml, 75 ml and 100 ml) of ammonia aqueous solution at 30 wt %, supplied by Carlo Erba at 0°C until to obtained the complete dissolution of TTIP and the formation of a white precipitate. The precipitate was carefully washed with water and centrifuged to be separated.

Finally, the obtained powders were dried and calcined at 450°C for 30 minutes to get TiO_2 in the anatase phase. In Table 1, a list of doped and undoped titania are respectively reported.
The method of synthesis was repeated three times and all catalysts was characterized by Uv-vis and specific surface area was evaluated.
From the first method of synthesis, chemical- physical characterizations have dimostarted that the sample is not repeatable.
The second method of synthesis showed that the best result was obtained for the samples N_4 where the band-gap and specif surface area for the all batch of synthesis was the same. So, for increase thethe activity of catalysts the time of catalcination was also optimizated.

Table 5 *Specific surface area (BET).*

Catalyst	1th	2nd	3th
N_1	45	25	4.6
N_2	18	24	15
N_3	20	23	27
N_4	30	30	30

Finally, the obtained powders were dried and calcined at 450°C at different times (10, 20, 30, 40 min) to get an optimized visible photoactive TiO$_2$ (Figure 24). The obtained samples were yellow in colour.
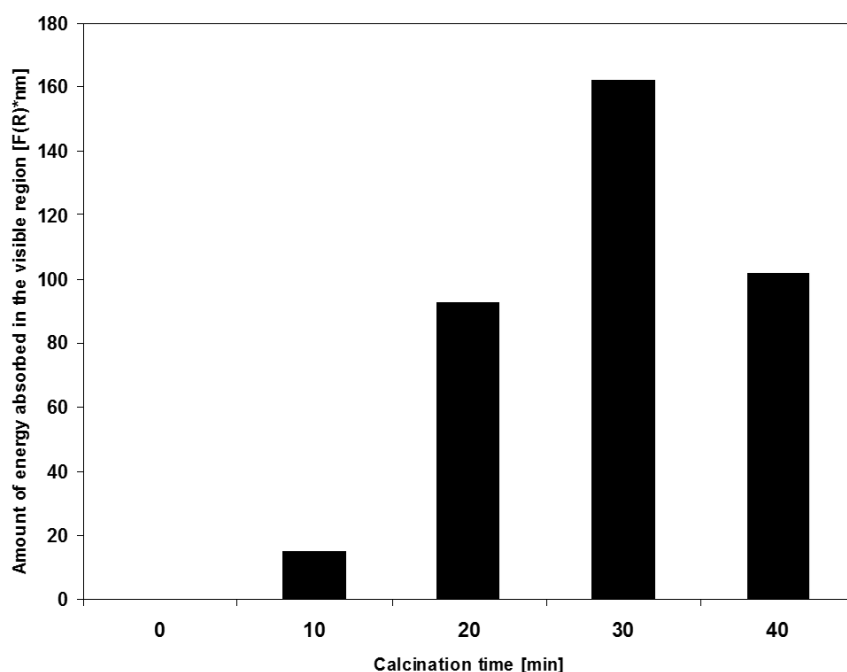
Figure 24 *Amount of energy absorbed in visible region by N_4 catalyst as a function of calcination time.*

III.2.1 Termogravimetric analyses

Thermogravimetric analysis (TG-DTG) of samples was carried out in air flow with a thermo balance (SDT Q600, TA Instruments) in the range 20-1000°C at 10°C min^{-1} heating rate. Samples were analyzed without pretreatment, with a fast start of temperature program, to avoid dehydration in the anhydrous air stream.Thermogravimetric results of N_4 photocatalysts

samples are shown in Figure 25. For all the samples, a first main weight loss takes place below 180°C, associated with hydration water desorption. The second step (present as a shoulder) that occurred up to about 390°C, is related to the removal of OH- surface groups of titania (Sannino et al., 2011).

On N_4 sample (Figure 25), the weight loss starting at about 380°C could be due to the oxidation reaction of NH_3 or NH_2 which are bonded coordinately onto Lewis acid site with the oxygen released from amorphous grain-boundaries by forming oxygen deficient sites (Ihara et al., 2003). The amount of this loss is 0.16 wt %.
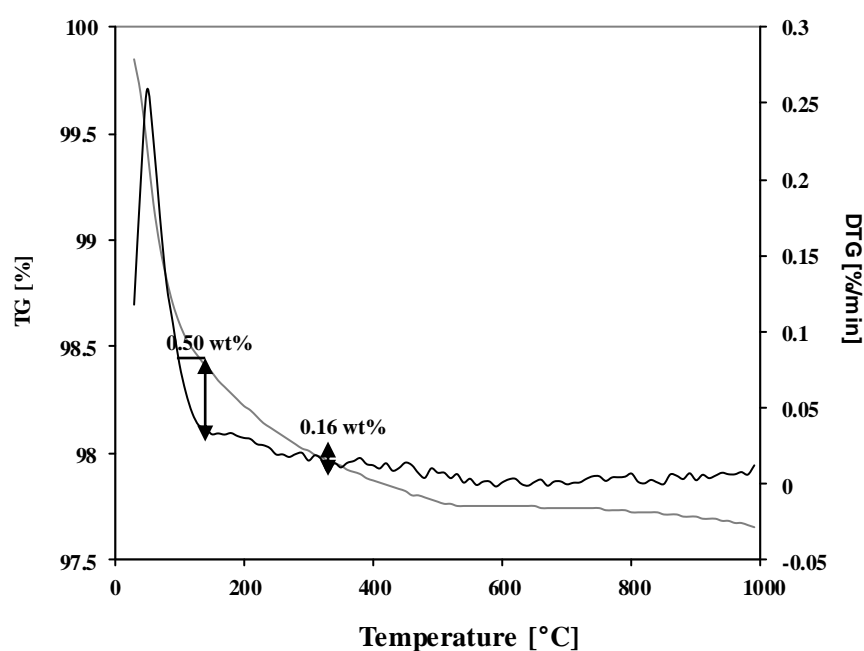
Figure 25 *TG analysis of N_4 photocatalyst*

III.2.2 Point of zero charge (PZC)

Mass titration method was used to estimate the acidity of sample powders. The PZC, which describes the acidity of oxide materials, may be measured using potentiometric titration, mass titration, or measurement of the wetting angles. The mass titration method of PZC characterization was initially proposed by Noh and Schwarz (Noh and Schwarz, 1989). In this work, the mass titration studies were performed using procedures described

elsewhere (Noh and Schwarz, 1989). Shorter stabilization times after each powder addition (2 hours in this study) were used to minimize possible dissolution of sample powders.
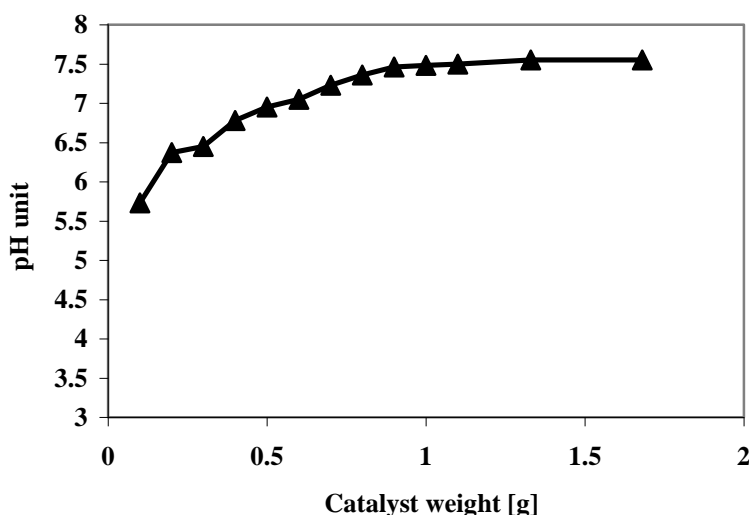
Figure 26 *PZC of N_4 sample*

According to the method used, the trend of pH as a function of photocatalyst powder addiction is plotted in Figure 26.
The value of PZC of N_4 is 7.6, more basic with respect to the values of PZC of 6.2 reported in literature for pure anatase titania (Ciambelli et al., 2005), according to its amphoteric character. This basic character can be ascribed to the presence of surface nitrogen groups in the doped titania whose nature could be supposed to be an NH specie (Sorrentino et al., 2001).

III.2.3 TEM

A JEM-2010F (JEOL) transmission electron microscope with field emission gun at 200 kV was used to obtain information on particle size and particle structure.The TEM images shows with a higher resolution, 100nm and 20nm (Figure 27). In this case, it is interesting to observe that N_4 titania have a pseudo spherical crystallites.
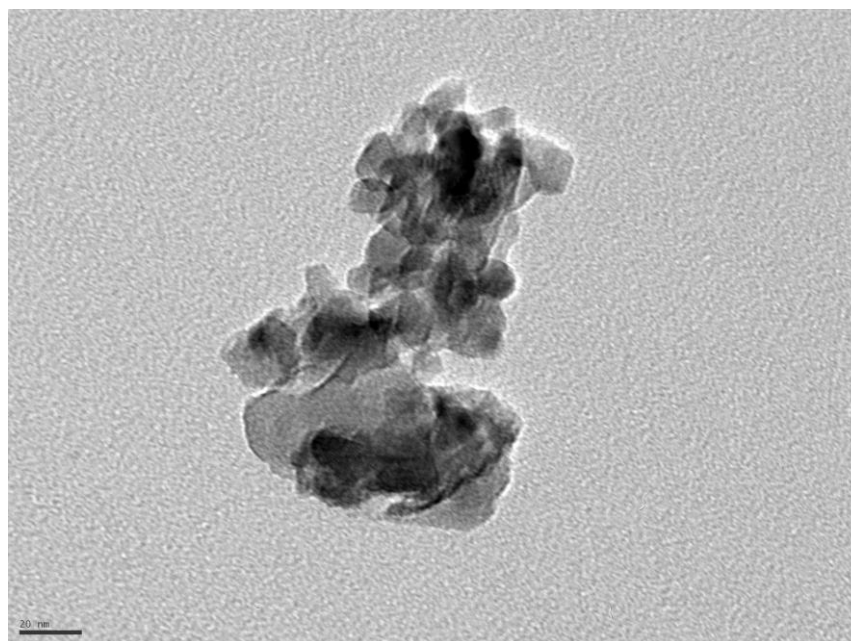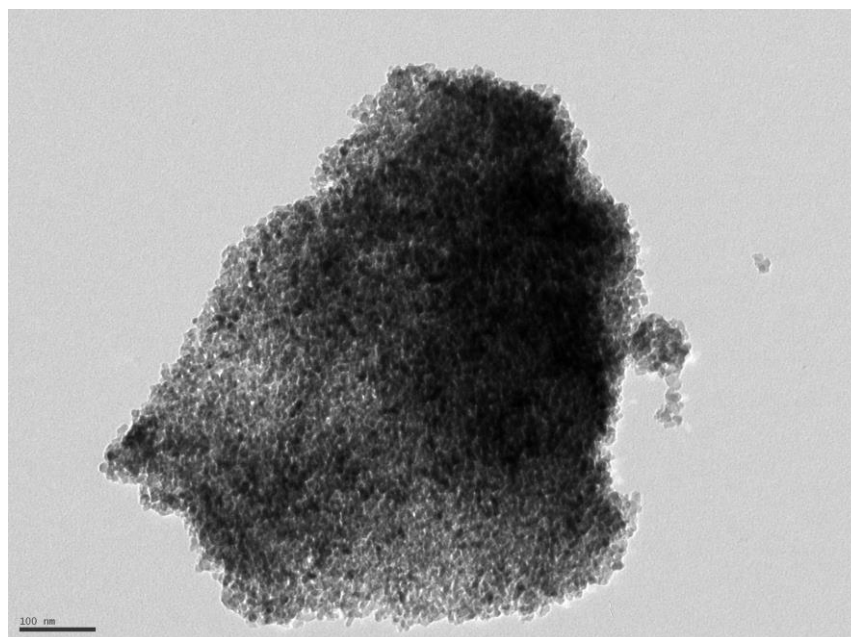
Figure 27 TEM imagine of N_4

IV Experimental Results: Photocatalytic tests on

N-doped TiO$_2$

IV.1 Photocatalytic Degradation of Organic Dyes under visible

light irradiation

Industrial effluents are foremost causes of environmental pollution because effluents coming from dyeing industries are highly colored with a large amount of suspended organic solid. Presently, more than 10.000 of different commercial dyes, for example methylene blue (MB), and pigments exists and about 7 x 105 tones are produced annually world wide (Azhar et al., 2005). Raw disposal of this dyed water into the receiving water body either causes damage to aquatic life. Dyes are widely used in industries such as textile, rubber, paper, plastic, cosmetic etc. Among these various industries, textile ranks first in usage of dyes for coloration of fibers. Due to low biodegradation of dyes, a convectional biological treatment process is not very effective in treating a dyes wastewater. It is usually treated with either by physical or chemical processes. In this context, photocatalysis stands out to be one probable methodology that can be effectively exploited for the complete mineralization of various dye pollutants present in liquid media. The heterogeneous photocatalytic oxidation process developed in the 1970s is of special interest especially when solar light is used. These processes are all characterized by the same chemical features such as production of hydroxyl radicals (OH) and superoxide anion (O$_2$), which are generated when a semiconductor catalyst absorbs radiation when it is in contact with water and oxygen.

IV.1.1 Photocatalytic Activity Tests under Visible Light

In a typical activity test a defined amount of photocatalyst was suspended in 100 mL of MB solution. The suspension was left in dark condition for 2 hours to reach the adsorption equilibrium, and then photocatalytic reaction was initiated under visible light up to 3 h. The experiments wereperformed with a pyrex cylindrical photoreactor (ID = 2.5 cm) equipped with an air distributor device (Qair = 150 cm^3/min (STP)), a magnetic stirrer to maintain the photocatalyst suspended in the aqueous solution, and a temperature controller. The photoreactor was irradiated by a strip composed by 30 white light LEDs (nominal power: 6 W) with wavelength emission in the range 400–800 nm or by a similar number of blue light LEDs (nominal power: 6 W) with wavelength emission in the range 400–550 nm. The LEDs strip was positioned around the reactor so that the light source uniformly illuminated the reaction volume. The curve inside Figure 28 represents the emission spectrum of white LEDs, while the fraction of curve coloured in blue evidence the spectrum emission of blue LEDs. On the left side of the same figure a schematic picture of the photocatalytic reactor is presented. Slurry samples were collected at fixed time intervals, and centrifuged for 20 minutes at 4000 rpm for removing photocatalyst particles.
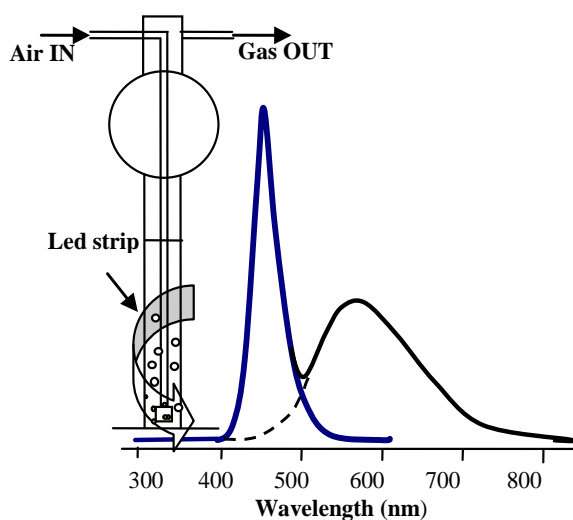
Figure 28 *Emission spectrum of the light sources and schematic picture of the photoreactor.*

The behaviour of MB decolourisation under visible light generated by white LEDs is represented in (Figure 29) for undoped TiO$_2$ and doped TiO$_2$ with different nitrogen content. In dark conditions a decrease of MB concentration was observed during the first hour of the test and it was unchanged in the second hour, indicating that the adsorption equilibrium of dye on catalyst surface was reached. The curves show that N-TiO$_2$ catalysts have different amounts of MB adsorbed in dark. To explain this last result, the specific area was estimated (Table 1); for the sample N_1 and N_3 it was 75 m^2/g, while for N_2 and N_4 it was 80 m^2/g. As expected, the amount of organic dye adsorbed increases the higher is the specific surface area, fairly accordingly to the differences in the area values, as shown in Figure 29.
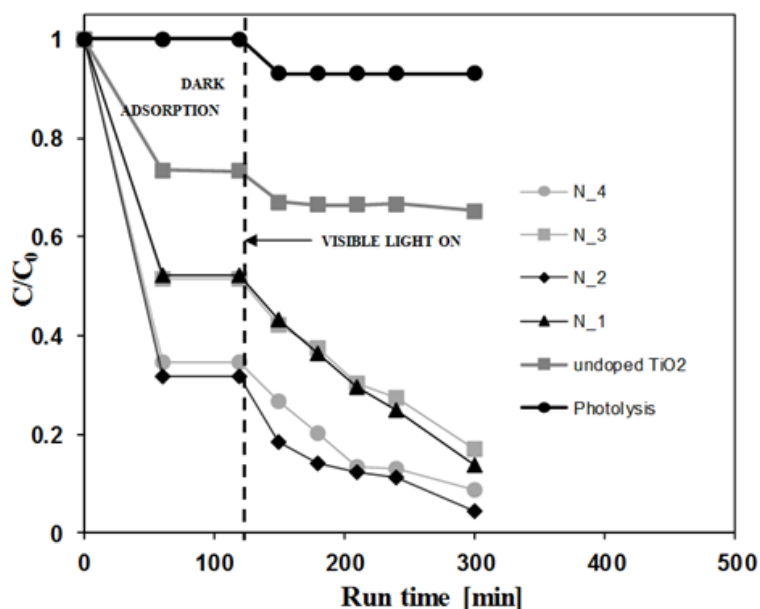
Figure 29 *Decolorization of MB under visible light generated by white LEDs; catalyst weight: 0.3g; initial MB concentration: 7.5 ppm*
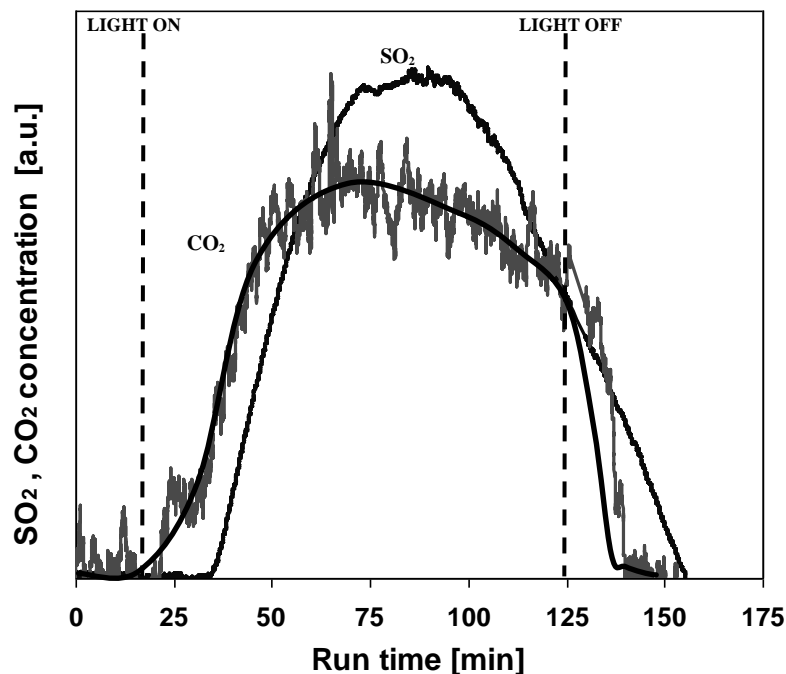
Figure 30 *Gas analysis phase during visible irradiation of MB solution*

After the dark period, the solution was irradiated with visible light and the reaction started to occur. Figure 29 shows that undoped TiO_2 is slightly effective for MB decolourization, the C/C_0 reduction being about 8%, a value similar to that of photolysis reaction (7%). On the contrary, all the N-doped TiO_2 photocatalysts exhibited higher photocatalytic activity under visible light irradiation. The order of decolourisation activity of N-doped TiO_2 after 180 min was as following: N_2 > N_4 > N_3 ~ N_1. The final value of MB conversion depends on dye concentration after the dark period.The decolourization of MB does not necessary correspond to the oxidation and mineralization of the molecule; in fact the reduced form of MB (LMB, leuco) which is colourless, can be produced in the presence of light (Emeline et al., 2008). The lack of coincidence among the best performing samples with respect to either discolourization or mineralization, can be the result of different routes followed by MB during irradiation.

$$h^+ + OH^- \longrightarrow OH\bullet \hspace{4cm} R1$$

$$MB + OH\bullet \longrightarrow INTERMEDIATES \longrightarrow CO_2 \qquad\qquad R2$$

$$MB + e^- \longrightarrow MB\bullet^- \qquad\qquad R3$$

$$2MB\bullet^- \longrightarrow MB + LMB \qquad\qquad R4$$

$$LMB + OH\bullet \longrightarrow INTERMEDIATES \longrightarrow CO_2 \qquad\qquad R5$$
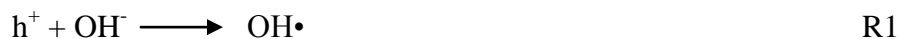
The MB molecule can be transformed into LMB through reduction by electrons in the conduction band (R4) or oxidized by interactions with the valence band holes or native OH species, starting with a de-methylation step to be finally mineralized (R2). For long reaction times also LMB can be further degradated and mineralized.The analysis of gases coming from the photoreactor showed the presence of CO_2 and SO_2 during the visible light irradiation, confirming the occurring of MB mineralization (Figure 30). In fact, a significant TOC reduction was obtained. Its final value increased up to 97 % by increasing the doping level (Figure 31). In this case, the order of activity was the following: N_4 > N_3 > N_2 >>N_1.
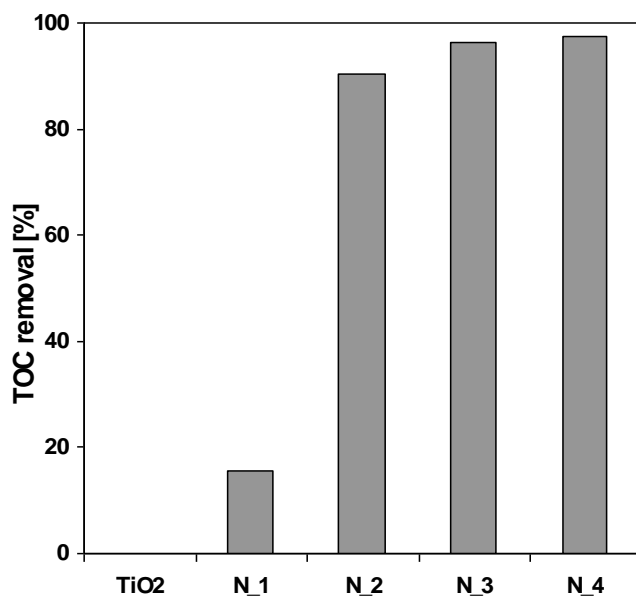
Figure 31 *TOC removal after 180 min of irradiation time ; catalyst weight: 0.3g; initial MB concentration:7.5 ppm*

71

The photocatalyzed decolorization process can be described by a first order kinetic equation (Eq.22) with respect to the concentration of MB (Yogi et al., 2009).

$$-\ln\frac{C}{C_0^*} = k_i \cdot t \qquad\qquad\qquad \text{Eq.22}$$

Where:

C = concentration of MB at any given time;

C_0^* = concentration of MB after dark adsorption:

T = irradiation time;

ki = apparent kinetic constant.

The obtained results are plotted in Figure 32.

The order of kinetic constants of N-doped TiO_2 after 150 min of light irradiation is: k2 > k4 > k3 ~ k1.
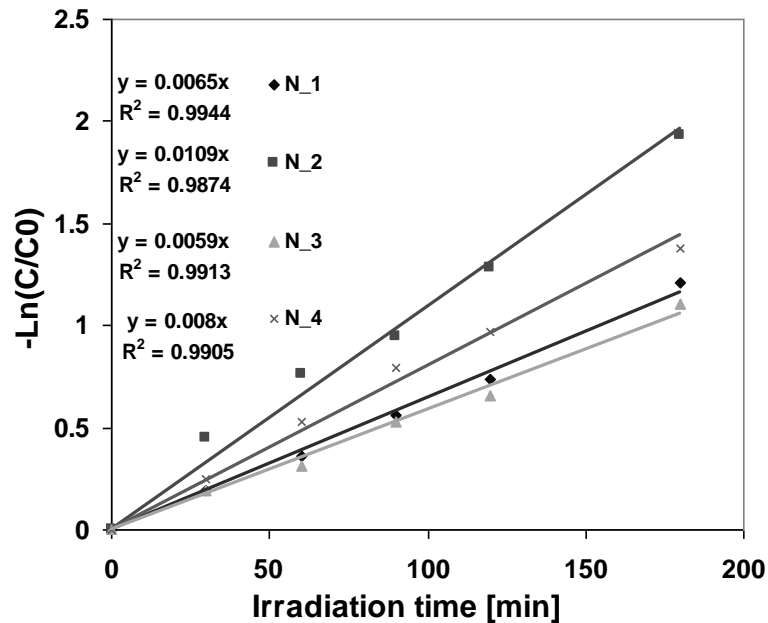
Figure 32 *Evaluation of decolorization kinetic*

Many reports suggest that the amount of catalyst plays a major role in the degradation of organic compounds or dyes in photocatalytic systems. To avoid the use of a catalyst excess, it is necessary to identify the optimum

loading for an efficient removal of dye or organic compound. So it is necessary to optimize the amount of catalyst with respect to the highest photocatalytic activity. To study the effect of the amount of catalysts, different quantities of powder between 0.05 and 1.5g were used. The initial concentration of MB dye (7.5 ppm) was kept the same in all these experiments. Figure 33 shows the effect of the amount of catalyst on the conversion of MB in the presence of white LEDs. The progress of the conversion is linear up to 0.3g, while for further increase of catalyst amount, the conversion stabilizes. These data indicate that 0.3g of powders are completely exposed to the radiation. This phenomenon may be explained considering that with an increase of catalyst loading in the aqueous medium, the light penetration through the solution becomes difficult. Therefore 0.3g of photocatalyst loading is considered to be an optimal value.
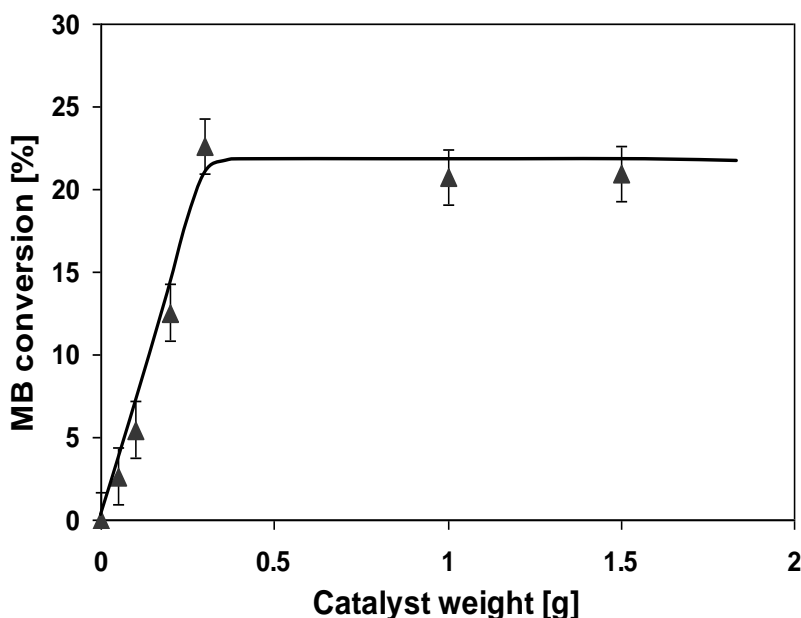
Figure 33 *Evaluation of decolorization after 30 minute with different amount of N_4 catalyst.*

Also the dye concentration plays a key role in the photocatalytic degradation. The effect of MB initial concentration on the photocatalytic activity was checked in the range between 4 and 95 ppm with N_4 catalyst and optimal catalyst loading (0.3g in 100ml of solution). The trend of the curves was similar and it is shown in Figure 34. After 120 minutes of dark adsorption, the photocatalytic test started. At fixed reaction times, the increase of MB initial concentration determined a decrease of the photocatalytic activity. This could be due to the increase of colour intensity

of the solution that reduces the light penetration into the aqueous medium, meaning that the path length of photons inside the solution decreases. After 180 minutes of irradiation the final value of the decolorization was 100% in the case of 4 ppm and 15% in the case of 95 ppm MB initial concentration. The same effect was observed by Matthews during the photocatalytic degradation of MB with TiO_2 catalysts (Matthews, 1989).
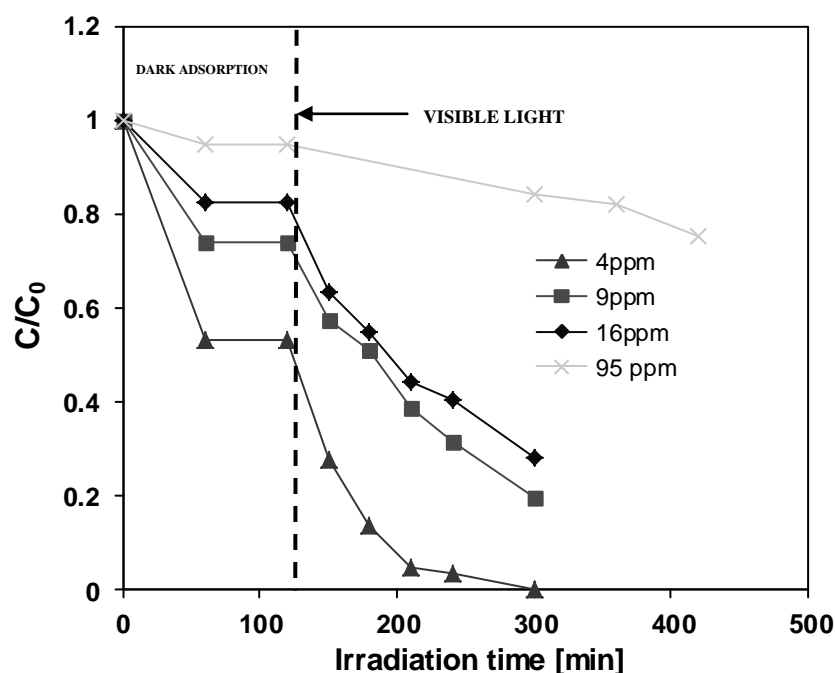
Figure 34 *Evaluation of decolorization with different initial concentration of MB; catalyst: N_4*

Moreover, the efficiency of the system was also evaluated with blue LEDs as source of visible light and methyl orange (MO) as organic dye. Figure 35 shows the comparison between the obtained results in presence of white and blue LEDs. As expected from the evaluation of N_4 band-gap energy (2.5 eV), only a fraction of radiation is used in the decolorization process. In fact, the curves related to the MB concentration during the irradiation time showed a similar trend because the range of radiation used by the photocatalyst was that one having an emission wavelength lower than 440nm. Similar results were obtained for methyl orange (MO).
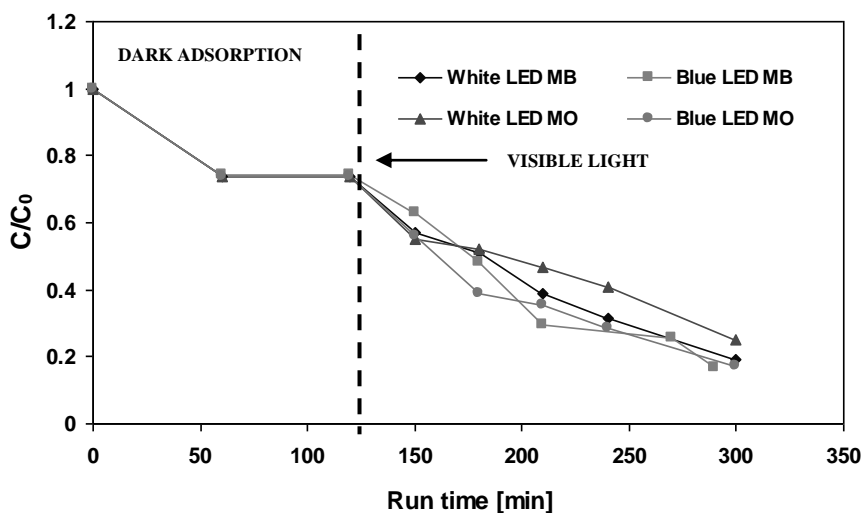
Figure 35 *Evaluation of decolorization with different dyes and different light source; initial MB and MO concentration:9 ppm*
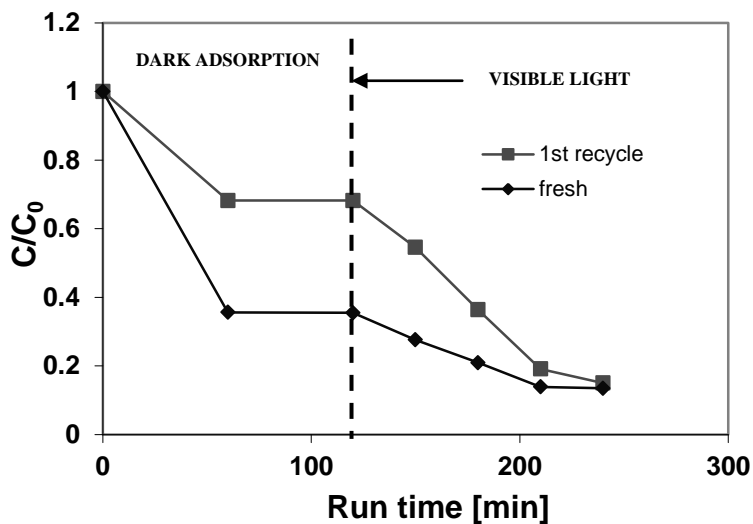
Figure 36 *Evaluation of decolorization performances obtained on N_4 photocatalyst after one recycling experiment. Initial MB concentration 7.5ppm.*

recycling experiments (Figure 36). In the first cycle, the amount of MB adsorbed was lower than that one obtained with fresh catalyst because, using the same catalyst coming from the first test, a certain quantity of dye is already adsorbed. The rate of dye removal depends on the initial concentration in solution, so it is higher, the higher is residual MB after dark adsorption. However, it must be noted that the photocatalytic activity remained high and the level of final MB removal was the same at the end of the test, indicating that no deactivation occurred and the dye concentration decreased continuously under visible light irradiation.

IV.2 Photocatalytic removal of spiramycin from wastewater

under visible light with N-doped TiO$_2$ photocatalysts

Pharmaceutical active compounds (PACs) have attracted much attention in recent years due to their adverse effects towards natural organisms and potential effects on human beings. Most treatment plants filter and chlorinate sewage to remove disease-causing microbes and excess organic matter, but do nothing to clean the water from pharmaceuticals, which can not be removed with traditional treatment processes. When treatment plants release treated water into streams, they pump drug-tainted water directly into the aquatic habitat. Thus PACs are constantly released into aquatic environments. In fact, several studies carried out in the past few years, have demonstrated the presence of PACs in groundwater, surface water and even in drinking water (Jones et al., 2005a). As a consequence, waters must be treated for human consumption or used for different activities such as irrigation (Jones et al., 2005b). Advanced oxidation processes (AOPs), such as ozonation, Fenton, photo-Fenton oxidation, and heterogeneous photocatalysis, have shown great efficiency in recent years as possible future complementary methods to conventional water treatment. Among these AOPs, TiO$_2$ photocatalysis is gradually developed as an affordable, effective, environmentally friendly, reusable, and sustainable technology for water treatment. Several studies have demonstrated that ultraviolet (UV) and visible light is able to decompose pharmaceuticals by direct photolysis or indirect photolysis through an AOP. Indeed, Amoxicillin [(Dimitrakopoulou et al., 2012) nitroimidazoles (Prados-Joya et al., 2011), oxytetracycline (Zhao et al., 2013), and sulfamethoxazole(Xekoukoulotakis et al., 2011), are degraded by UV or visible light treatments .

Among antibiotics, spiramycin (SP) (Figure 37), which belongs to the group of macrolide antibiotics, is produced by fermentation. SPM is a macrolide antibiotic used to treat infections of the oropharynx, respiratory system, genito-urinary tract, as well as cryptosporidiosis and

76

toxoplasmosis(Shi et al., 2004). Similarly to the other antiibiotics, there is a need to remove SP from water and AOPs are recommended for this purpose.

SP degradation has been reported under UV light irradiation in presence of TiO$_2$ (Liu et al., 2012), but no one has studied photocatalytic degradation of SP under visible light irradiation.

However, to reach this goal, it is necessary to modify titanium dioxide in order to make it able to exploit visible light wavelength. This feature can be realized by doping TiO$_2$ crystal lattice with various elements. Among such modified materials, N–doped TiO$_2$ has achieved promising success under visible light, exhibiting stable characteristics and performance in water treatment applications (Rizzo et al., 2013b; Sacco et al., 2012).The use of visible light would represent, then, a more economical alternative. For this reason the objective of this study is to explore the possibility of using blue LEDs as source of visible light for the photocatalytic degradation of SP. The effect of various parameters, such as SP concentration and type of light sources was investigated.
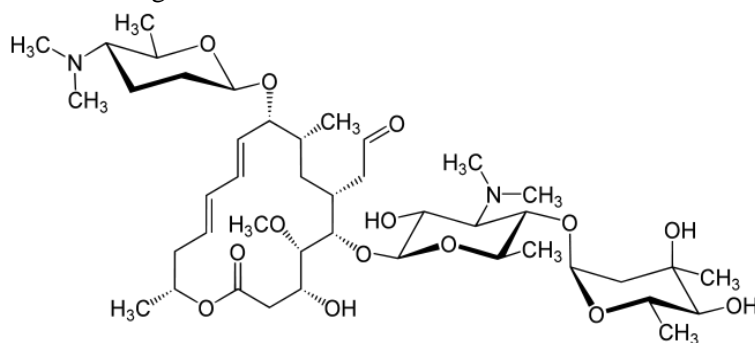
Figure 37 *Chemical structure of SP*

IV.2.1 Photocatalytic Activity Tests under Visible Light

Aqueous solutions containing SP were prepared using weighted fractions of pills dissolved in bidistilled water, to get a more realistic drug-tainted wastewater. The experiments were realized using a pyrex cylindrical photoreactor (ID= 2.5 cm) equipped with an air distributor device (Q$_{air}$=250 cm^3/min (STP)), magnetic stirrer to maintain the photocatalyst suspended in the aqueous solution and temperature controller. The photoreactor was irradiated with a strip composed by 25 blue LEDs (BL strip) (provided by NEW ORALIGHT; light intensity 32mW cm^{-2}) with wavelength emission in the range 400–550 nm (Prados-Joya et al., 2011) or with four Black Light UV tubes (provided by Philips; nominal power: 32 W) with wavelength maximum emission around at 365nm. The light sources were positioned around the external surface of the photoreactor (Figure 38).

Figure 38 *Experimental set up apparatus (1) flow meter; (2) magnetic stirrer; (3) photoreactor; (4) CO$_2$ analyzer, (5) personal computer for data acquisition.*

In a typical photocatalytic test, 3 g/L of photocatalyst was suspended in 100 mL solution. The system was left in dark condition for 2 hours to reach SP adsorption equilibrium on catalyst surface, and then photocatalytic reaction was initiated under visible or UV light up to 7 h. Samples were taken during the tests and centrifuged for removing powders from the SP solution. The analysis of gas phase coming from the photoreactor was performed by means of a continuous CO, CO$_2$, non-dispersive infrared analyser (ABB Advance Optima). The photocatalytic activity was tested in terms of the reduction of total organic carbon (TOC) that is a parameter able to analyze SP mineralization. TOC of solution has been measured from CO$_2$ obtained by catalytic combustion at T=680 °C. CO$_2$ produced in gas-phase was monitored by continuous analyzers, measuring CO, CO$_2$ (Uras 14, ABB) and O$_2$ (Magnos 106, ABB) gaseous concentrations (Jones et al., 2005a).The natural pH of solution was equal to about 6 and the temperature was controlled being in the range 20-30°C. Finally, the performances of N_4 photocatalyst in presence of visible light were tested in the photocatalytic treatment of a real pharmaceutical wastewater containing SP with an initial TOC content of about 20 mg /L. Preliminary experiments were carried out to in order to verify that SP was degraded by heterogeneous photocatalytic process. In the absence of N-TiO$_2$, no significant decrease in TOC was observed during the 7h of illumination both with UV light and visible light irradiation (Figure 39). In particular, TOC removal was less than 10% in the

case of visible light irradiation and 19% in the case of UV light irradiation. So, photolysis phenomena occur but in a limited extent.
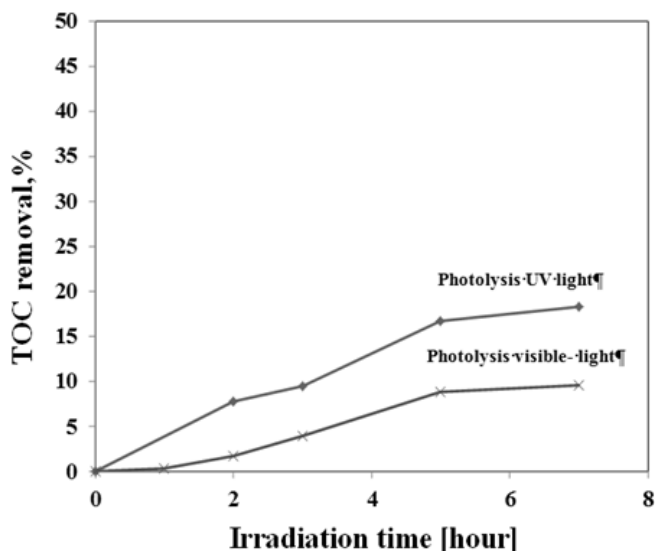
Figure 39 *Comparison between photolysis under visible light and UV light*

The TOC profiles as function of irradiation time obtained in the presence and in the absence of N-TiO$_2$ under the irradiation realized by UV lamps are reported in Figure 40. In dark conditions, a decrease of TOC was observed during the first hour of the test and it was unchanged in the second hour, indicating that the adsorption equilibrium of SP on catalyst surface was reached. After the dark period, the solution was irradiated with UV light and the reaction started to occur. It can be seen that TOC value was lower when UV light was applied in the presence N-TiO$_2$ photocatalyst. In fact, a final TOC removal reached a value of about 48%, so remarkably improved in comparison to photolysis alone.The analysis of gases coming from the photoreactor showed the presence of only CO$_2$ during the UV light irradiation, confirming the occurring of the mineralization of SP (Figure 41). It is important to underline that no formation of CO$_2$ was detected in absence of light irradiation. This last experimental result shows that the TOC reduction obtained in dark conditions was due to only adsorption of SP on N-TiO$_2$ surface.
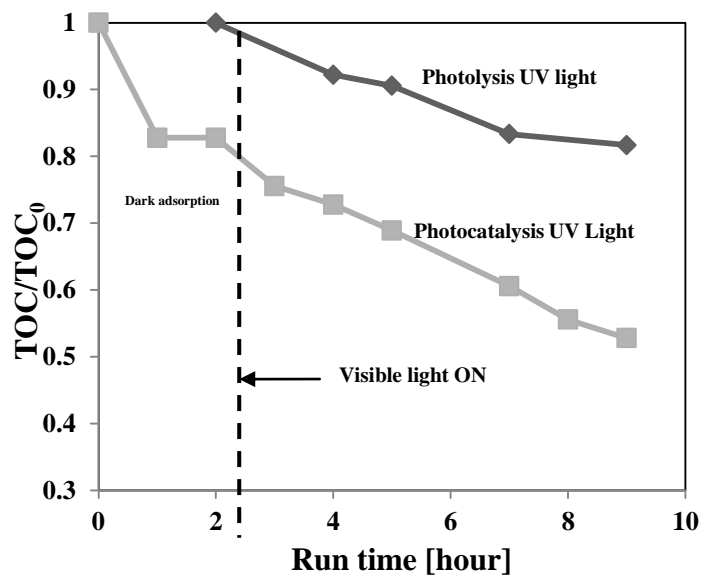
Figure 40 *Comparison between photolysis and photocatalysis (N-TiO$_2$ dosage: 3g/L) using UV light sources*
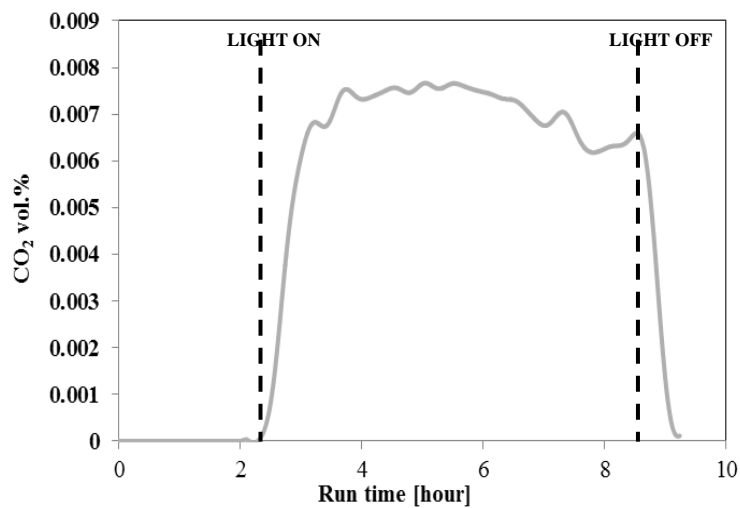
Figure 41 *Gas phase analysis during photocatalysis in presence of UV irradiation.*

Through a comparison between the amount of carbon consumed during the photocatalytic reaction (as assessed by TOC analysis) and the amount of carbon released as CO$_2$, the total carbon mass balance was closed to about 95±5%, evidencing that SP is selectively converted to CO$_2$. It is possible to affirm that total mineralization of SP was obtained in presence of photocatalyst.It was also performed visible light driven photocatalytic removal of SP over the N-TiO$_2$ using the light emitted by BL and results are presented in Figure 42. It is observed that SP photolysis shows a progressive removal of TOC up to a value lower than 10% after 7 h of irradiation. In contrast, the presence of N-TiO$_2$ showed higher removal rate with a final TOC removal of 45 % after 6 h of irradiation. This enhanced photocatalytic ability in presence of visible light is ascribed to nitrogen insertion in the crystalline structure of titania**.**
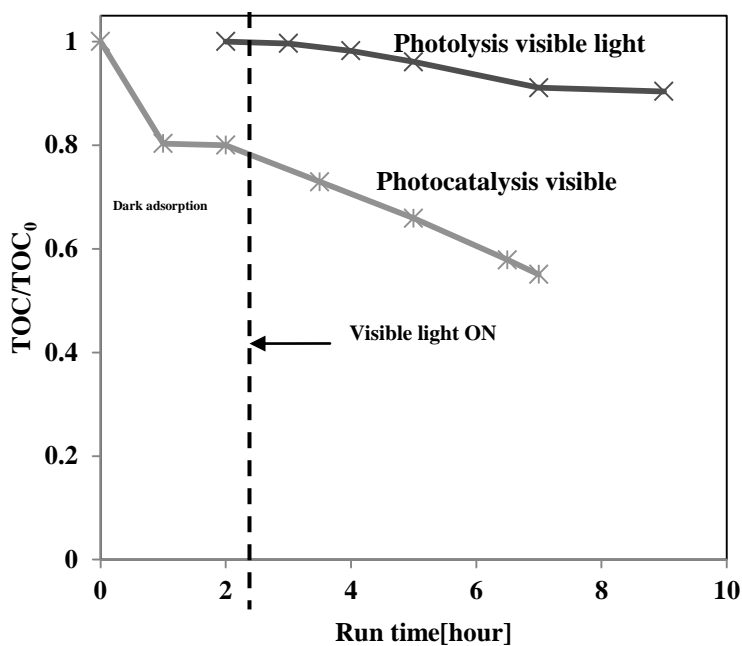
Figure 42 *Comparison between photolysis and photocatalysis (N-TiO$_2$ dosage : 3g/L) using visible light (blue LEDs)sources*

IV.3 Effect of solar simulated N-doped TiO$_2$ photocatalysis on the inactivation and antibiotic resistance of an E. coli strain in biologically treated urban wastewater

The large use of antibiotics (for human, veterinary and aquaculture purposes) brings about their continuous release into the environment and possible development of antibiotic resistance in bacterial populations, which make antibiotics ineffective in the treatment of several diseases (Schwartz et al., 2003). Conventional urban wastewater treatment plants (UWWTPs), typically based on biological processes, are among the hotspots of antibiotics (Michael et al., 2013) and antibiotic resistant bacteria (ARB) (Michael et al., 2013) spread into the environment. The release of ARB from UWWTPs effluents to receiving surface waters may be due to either: (i) absence of disinfection process or (ii) inability of conventional disinfection processes (e.g., chlorination and UV radiation) to effectively control ARB spread (Munir et al., 2011). Accordingly, alternative/new disinfection methods, such as advanced oxidation processes (AOPs), should be investigated to evaluate the effect on antibiotic resistance in wastewater. AOPs include different processes (e.g., Fenton, photo-Fenton, TiO$_2$ photocatalysis, UV/O$_3$, UV/H$_2$O$_2$ etc.) which have in common the capacity of producing highly oxidising molecules (hydroxyl radicals) able to successfully remove a wide range of contaminants (Alrousan et al., 2012). TiO$_2$ photocatalysis has recently emerged as interesting water disinfection option, because: (i) it does not result in the formation of toxic disinfection by-products compared to chemical disinfectants (Malato et al., 2009) and (ii) it can be operated with solar radiation thus saving money for energy (Rengifo-Herrera et al., 2009). In particular the N-doped TiO$_2$ was used in inactivation of the selected antibiotic resistant E. coli strain was evaluated under solar simulated radiation (250W lamp) and different photocatalysts loadings (0.025-0.5 g L-1). Antibiotic resistance to ciprofloxacin (CIP), cefuroxime (CEF), tetracycline (TET) and vancomycin (VAN), before and after photocatalytic treatment, was evaluated by Kirby-Bauer method.

IV.3.1.1 Wastewater sample

Wastewater samples were taken from a large UWWTP (250000 equivalent inhabitants) located in southern Italy, in the effluent of the biological process (activated sludge), just upstream of the disinfection unit (chlorination). Samples were collected in sterilized 1L amber glass bottles. The average values of some parameters in the effluent of biological process

are: pH 7.9, BOD$_5$ 10.0 mg/L, COD 23.3 mg/L, TSS 32.5 mg/ L, redox potential 63.6 mV, conductivity 1105 μS/cm.

IV.3.1.2 Inoculum and sample preparation

Multi drug resistant E. coli strain was selected according to the procedure published in our previous work (Rizzo et al., 2013a) and inoculated to autoclaved (15 min at 121°C) wastewater samples. The selected E. coli strain was unfrozen and transferred in 10 mL physiological solution to achieve 107 CFU 1001/mL (0.5 McFarland). The physiological solution was finally added to 500 mL wastewater sample.

IV.3.2 Photocatalytic tests

Photocatalytic experiments were carried out in 2.2 L cylindrical glass reactor (13.0 cm in diameter) filled in with 500 mL wastewater sample (5.0 cm water height). The reactor was placed in a water bath to keep the temperature constant (roughly 30°C) during the experiments and continuously stirred. Solar radiation was simulated by a wide spectrum 250 W lamp equipped with a UV filter (Procomat, Italy), fixed at 40 cm from the upper water level in the reactor. A spectrometer model HR-2000 from Ocean Optics (Florida, USA), equipped with cosine corrector with Spectralon diffusing material, was used to measure irradiance spectra of UV lamp (Figure 43).
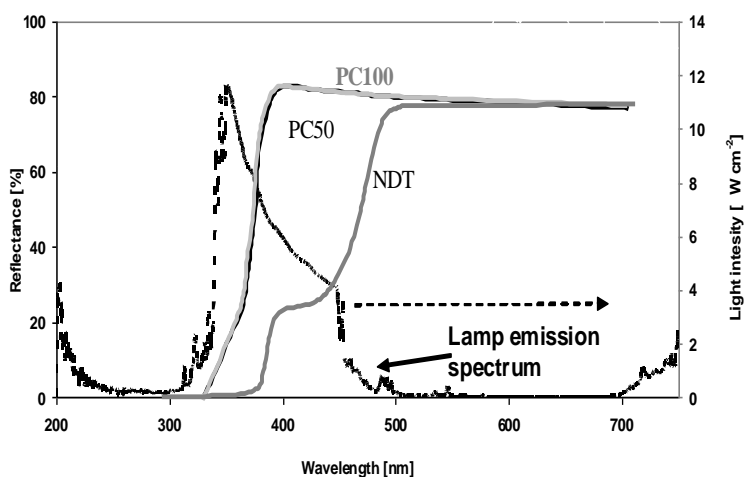
Figure 43 *Comparison between UV-Vis spectra of PC50, PC100 and NDT photocatalysts and emission spectrum of lamp*

In photocatalytic experiments, N-TiO$_2$ powder was compared with Millennium PC50 and PC100 commercially available TiO$_2$ powders. A suitable amount of TiO$_2$ powder was added to the autoclaved wastewater sample and sonicated for 5 min, than the inoculum was added. The effect of the photocatalyst loading on E. coli strain was investigated in the range 0.025-0.5 g /L for 10 min irradiation time. Control tests without any photocatalyst addition were also performed. As the photocatalyst dose was optimized, inactivation kinetic (60 min total irradiation time) was investigated.

IV.3.2.1 Bacterial count

Bacterial count was performed by spread plate method. Briefly, small amounts of wastewater samples were diluted according to the expected number of colonies, 100 μL were spread on TBX agar medium (Sigma Aldrich) and incubated at 44 °C for 24 h. Measurements were carried out in triplicates and average values and standard deviation were plotted as CFU 1001/mL.

IV.3.2.2 Antibiotic resistance assay

Antibiotic resistance of bacterial colonies before and after photocatalytic treatment was tested by Kirby–Bauer method. Briefly, the colonies survived to photocatalytic treatment and growth on TBX agar medium were collected from (4-5 colonies randomly selected from each one agar/irradiation time) and transferred in 10 mL physiological solutions, respectively, to achieve 107 CFU 1001/mL (0.5 McFarland). Then bacterial suspensions were spread on Mueller Hinton agar (Biolife, Italy) using a sterile cotton swab. Antibiotic discs of CIP (5 mg), CEF (30 mg), TET (30 mg) and VAN (30 mg) (all from Biolife) were placed on the surface of each inoculated plate. After 24 h of incubation at 37°C, the diameters of antibiotic inhibition of growth were measured. The procedure was duplicated and the average values plotted.

IV.3.3 Optimization of N-doped TiO$_2$ loading for the inactivation

tests

The effect of N-TiO$_2$ loading on *E. coli* strain inactivation was investigated in the range 0.025-0.5 g /L after 10 min irradiation time (Figure 44). Although solar light or simulated solar light has a bactericidal effect, the addition of photocatalyst results in a faster microorganisms inactivation (Malato et al., 2009); in our experiments, simulated solar radiation alone
84

resulted in a significantly lower initial inactivation rate (1.25 $\times$ 10^5 CFU 1001/mLmin) compared to photocatalytic tests (Figure 44).
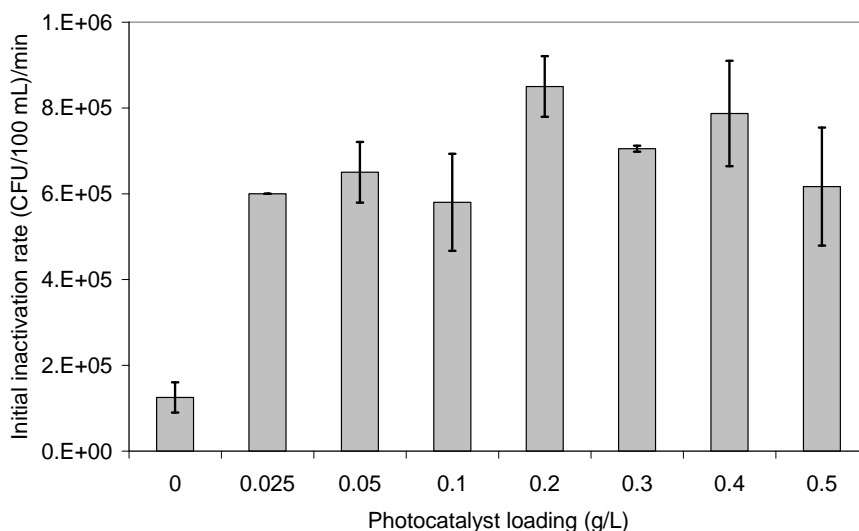
Figure 44 *Initial inactivation rate as a function of N-TiO$_2$ loading*

In particular, the higher initial inactivation rate (8.5 $\times$ 10^5 CFU 1001/mL min) was observed for 0.2 g/L photocatalyst loading. The increase in the rate, at low catalyst loading from 0.025 to 0.2 g /L, suggests that the addition of more titania particles improved the number of the photoactive sites in the solution. At concentrations higher than 0.2 g/L, the decrease of *E. coli* strain inactivation may be due to the aggregation of free TiO$_2$ particles (increased N-TiO$_2$ particle size) that results in a decrease in the number of surface active sites (Chen et al., 2007a). Further, the excessive opacity and screening effect due to the higher TiO$_2$ loading act as shield, and consequently hinder the light penetration. Therefore, there is loss of available surface area for light-harvesting which results in a reduction of the catalytic activity (Lea and Adesina, 1998).The effect of photocatalyst loading has been investigated in several works available in scientific literature and very different results were observed, the optimal photocatalyst loading mainly depending on the photoreactor design and the light intensity (Malato et al., 2009). For instance, when using solar photo-reactors with compound parabolic collectors technology, the optimal catalyst concentration of TiO$_2$ P25 was found to be 0.05 g/L (Fernandez et al., 2005); but 0.01 g/L of TiO$_2$ P25 (400W sodium lamp located 10 cm from the reaction vessel) were enough to successfully inactivate *E. coli*, *P. aeruginosa*, and *Staphylococcus aureus*, within 40 min. Moreover, some studies on the *E. coli* inactivation with N-

doped TiO_2 have been reported but different results were observed. Liu et al. (Liu et al., 2006) observed a high efficiency with a total inactivation (initial bacterial density 10^9 CFU/mL) after 120 min irradiation under solar light (10 mW cm^{-2}). In contrast, a comparatively poor efficiency (just 50% *E. coli* inactivation after 120 min irradiation, initial bacterial density 10^6 CFU/mL) was observed in a subsequent study under simulated solar light (total intensity: 550 W/m^2; UV intensity 20-30 W/m^2; concentration of TiO_2 powders of 1 g /L) (Rengifo-Herrera and Pulgarin, 2010).

IV.3.4 Comparison among catalysts

N-TiO_2 catalyst was found to be the most effective catalyst to inactivate the antibiotic resistant *E. coli* strain for all investigated catalysts loadings (Figure 45).
The higher inactivation rate (89.47%) after 10 min irradiation time was observed at 0.2 g/ L catalyst loading. PC100 was found to be more effective than PC50 for the lower investigated catalysts loadings, but PC50 and P100 were less effective as catalyst loading was increased up to 0.5 g /L, likely due to photons transfer limitations at higher titania concentration, as previously discussed. It could be argued that the tendency to the aggregation, and consequently the size of aggregates of titania nanoparticles may influence the ability of the different titanias to inactivate bacterial colonies. The size of the aggregates is dependent mainly on the specific surface area of titania, surface characteristics and concentration (Jassby et al., 2011). Accordingly, the decreasing trend in the inactivation ability observed at higher concentration could be also related to an increased TiO_2 aggregates size in the solution. In the Figure 45, the values of the particle size and the suspension pH were also included. In the case of PC100 there is a fairly agreement among the changing of aggregate size and the variation of inactivation percentage. The higher activity of PC50 may be due to the lower aggregates size for photocatalyst loading less than 0.3 g/ L.
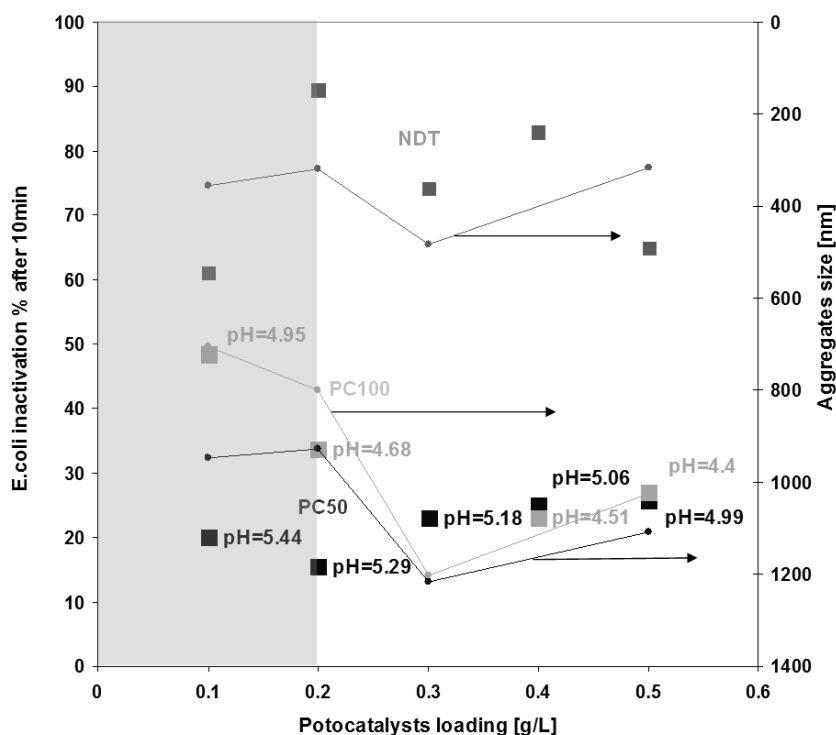
Figure 45 *E. coli inactivation (■) and aggregates size (●) as a function of photocatalysts loading with pH value of the suspension for each photocatalyst loading*

For higher titania loading, the inactivation percentage is similar for PC50 and PC100. Surprisingly, the average aggregate size is similar for both titania showing that the larger aggregates play a negative effect on the inactivation. Accordingly, the decrease in the percentage of inactivated *E. Coli* for NDT is not significant, and this agrees with the presence of aggregates of lower size whose dimensions do not change significantly as catalyst loading was changed (Figure 45). For all the samples, no pH effect was observed.

IV.3.4.1 Particles size analysis in aqueous phase

Particle size (PS) and particle size distribution (PSD) were measured by dynamic laser scattering (DLS) using a Nanosizer (NanoZS Malvern Instrument, UK) equipped with a He-Ne laser operating at 5.0 mW and 633 nm that measures the hydrodynamic diameter of the particles. PVP microparticles were dispersed in distilled water. DLS analysis was performed setting temperature at 25°C.

Weighted average size of titania aggregates is reported in Figure 45 as function of TiO_2 concentration in aqueous phase. For N-TiO_2 aggregates, size ranges between 318 and 482 nm. For PC50 and PC100 bigger sizes were found within the ranges 928-1216 nm and 706-1204 nm, respectively. For the both latter titanias, a tendency to an increased size as titania concentration was increased can be observed.

IV.3.4.2 Inactivation kinetic

The optimum photocatalyst loading (0.2 g/ L) for N-TiO_2 was used to investigate the inactivation kinetic of antibiotic resistant *E. coli* strain. A total inactivation took place after 60 min irradiation.
The obtained results are comparable with the inactivation rate observed by Liu et al. (Liu et al., 2006) in *E. coli* suspensions: total inactivation (10^9 CFU/mL initial *E. coli* density) was achieved after 120 min of irradiation (average light intensity $10mW/cm^2$).

IV.4 Effect of photocatalytic process on antibiotic resistance

Figure 46 shows the results of antibiotic resistance of *E. coli* strain to the target antibiotics investigated (CIP, CEF, TET and VAN) according to Kirby-Bauer test. The larger the inhibition diameter, the lower is the resistance. The average value of inhibition diameter for CIP before photocatalytic treatment (t = 0) is 12.5 mm. Compared to the corresponding clinical breakpoints values for *E. coli*, from EUCAST database (EUCAST) (susceptible (S) $\geq$ 22 mm; 22 < intermediary (I) $\leq$ 19 mm; resistant (R) < 19 mm), the *E. coli* strain used in this work is resistant to CIP. Moreover, solar photocatalytic process with N-TiO_2 affected its resistance to some extent, because a decreasing trend ($p < \alpha = 0.05$; $p = 0.0311$) as irradiation time increased can be observed (Figure 13). The average value of inhibition diameter for CEF before photocatalytic treatment (t = 0) is 25.3 mm. Compared to the corresponding clinical breakpoints values for *E. coli* from EUCAST database (S $\geq$ 18 mm; R < 18 mm), the *E. coli* strain is susceptible to CEF, and photocatalytic treatment affected its sensitivity to some extent, because a decreasing trend ($p < \alpha = 0.05$; $p = 0.0018$), as irradiation time increased, was observed (Figure 46). The average value of inhibition diameter for TET and VAN before photocatalytic treatment (t = 0) is the same (10 mm), b   ut unfortunately no comparison can be made with EUCAST database because any clinical breakpoint data is available for *E. coli* and these antibiotics, respectively. However, solar photocatalytic treatment with N-TiO_2 did not significantly affect resistance of *E. coli* strain to both antibiotics as irradiation time increased
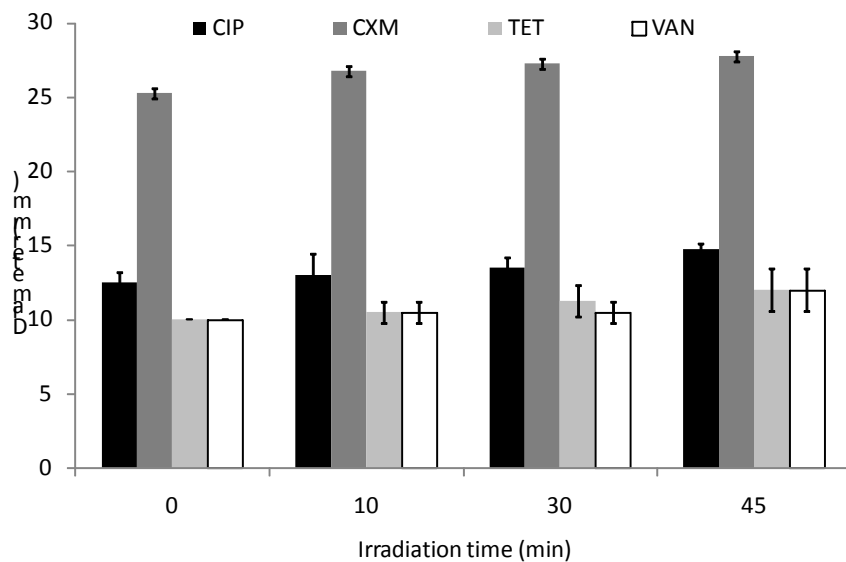
Figure 46 *Antibiotic resistance of E. coli strain to the target antibiotics investigated (CIP, CEF, TET and VAN) according to Kirby-Bauer test*

V Mathematical modelling of photocatalytic degradation of model solution

V.1 Mathematical modelling of photocatalytic degradation of

MB under visible light irradiation

In the last years, photocatalytic oxidation with TiO_2 in presence of visible light has been gaining industrial and academic attention.

Most studies on organic compound decomposition with TiO_2/UV investigated some factors that might influence the degradation rate of the organic compounds and proposed some kinetic models to explain their results. In addition they used traditional UV lamps to irradiate the photocatalysts (Barka et al., 2010). Nowadays, LEDs are replacing traditional UV lamps in many applications, owing to the much higher efficiency in light-electricity conversion, since the light emission by LEDs is induced by the recombination of electrons and holes excess(Chen et al., 2007b). Further advantages of LEDs derive from the small dimensions, robustness, and the long lasting (hundred thousands of hours compared to thousands of hours in the case of classical lamps) (Tayade et al., 2009). On the other hand, only few papers regarding the mathematical modelling of the photocatalytic degradation of MB under visible light were developed. This last issue is important to properly design a photocatalytic reactor, effective in the treatment of organic dyes in very different operating conditions. For this reason, this work has been focused on the developing of a lumped mathematical model for photocatalytic degradation of MB using an N-doped TiO_2 catalyst active with visible light (Asahi et al., 2001; Morikawa et al., 2001). The effects of many operating factors such as initial MB concentration, N-doped TiO_2 dosage, and visible light intensity were

investigated and used to verify the ability of the model to predict the experimental results.

V.1.1 Photocatalytic tests

In a typical activity test a defined amount of photocatalyst was suspended in 100 mL of MB solution. The suspension was left in dark condition for 2 hours to reach the adsorption equilibrium, checking the achieving of stable value of MB concentration, and then photocatalytic reaction was initiated under visible light up to 3h. The experiments were performed with a pyrex cylindrical photoreactor (ID= 2.5 cm) equipped with an air distributor device (Qair=150cm^3/min (STP)), a magnetic stirrer to maintain the photocatalyst suspended in the aqueous solution, and a temperature controller. The photoreactor was irradiated by a strip composed by 30 white light LEDs (nominal power: 6W) whose emission spectrum is shown in Figure 47.
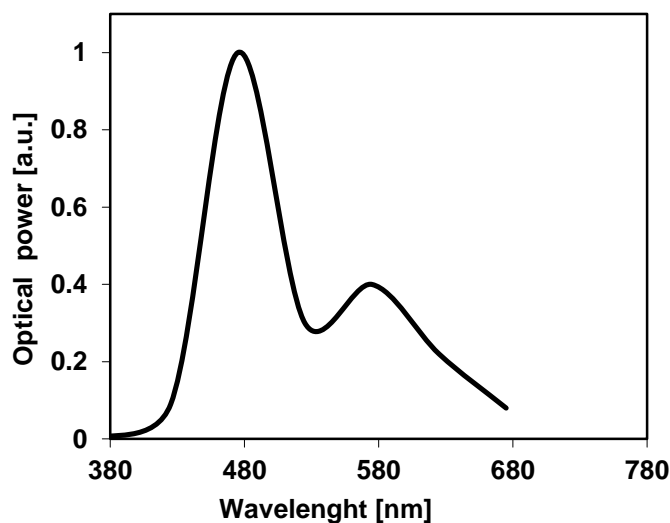
Figure 47 *Emission spectrum of the white LEDs*

The LEDs strip was positioned around the reactor so that the light source uniformly illuminated the reaction volume. Slurry samples were collected at fixed time intervals, and centrifuged for 20minutes at 4000rpm for removing photocatalyst particles. The centrifuged samples were analysed to determine

92

the change of MB concentration, measured with a Perkin Elmer UV-Vis spectrophotometer at $\lambda = 663$ nm. A standard calibration curve was obtained for different MB concentration, and allowed to convert absorbance to concentration (mg/L) units. The gas flowrates were measured and controlled by mass flow controllers (Brooks Instruments). The gas composition was continuously measured by an online quadrupole mass detector (Trace MS,ThermoQuest) and a continuous CO-CO_2 NDIR analyzer (Uras10, Hartmann & Braun)

V.1.2 Experimental photocatalytic tests

A typical trend found during photocatalytic oxidation of MB tests is reported in (Figure 48).
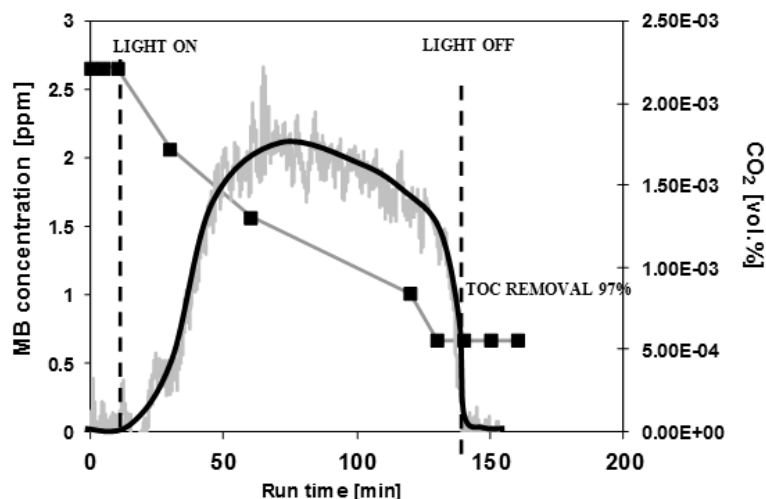
Figure 48 *Decolorization of MB under visible light generated by white LEDs; catalyst weight: 0.3g; initial MB concentration: 7.5ppm and gas analysis of CO_2 during visible irradiation of MB solution*

The initial concentration of MB was 7.5 ppm.
Before the light switching on, an air stream was fluxed through the reactor in the dark at ambient temperature. In dark conditions a decrease of MB concentration was observed during the first hour of the test reaching the value of 2.7 ppm and it was unchanged in the second hour, indicating that the adsorption equilibrium of dye on catalyst surface was reached (Houas et al., 2001). The analysis of the gaseous phase evidenced that no formation of CO_2 was observed. This demonstrates that the disappearance of MB from the solution is due to the ability of the catalyst to adsorb the dye on its surface.

As shown in Figure 48, when LEDs were switched on, the MB concentration decreased. After 130 minutes of irradiation the overall conversion of MB was 91% and TOC removal was 97% (Figure 48)

The analysis of gaseous stream coming from the photoreactor during the irradiation revealed the presence of CO_2 and SO_2. The CO_2 observed in the gas phase was due to the oxidation of MB which started at high reaction rate after few minutes of irradiation. Through a comparison between the amount of carbon consumed during the reaction (as assessed by the analysis of MB concentration in liquid phase) and the amount of carbon released as CO_2, the total carbon mass balance was closed to about 100%. This allowed affirming that the MB is selectively converted to CO_2 according to reaction (R).

$$C_{16}H_{18}ClN_3S + \frac{43}{2}O_2 = 16CO_2 + 9H_2O + SO_2 + N_2 + Cl_2$$

The hypothesis of absence of nitrate was confirmed by colorimetric tests, and the absence of HCl was verified by monitoring the pH of the solution during the photocatalytic test. In fact, this last one was in the range 6-7 during the overall test.
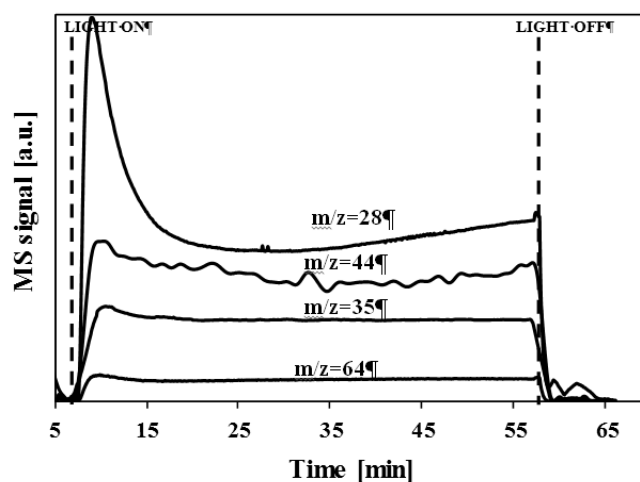
Figure 49 *Outlet reactor concentration (a.u.) of chlorine (m/z) 35, nitrogen (m/z) 28, carbon dioxide (m/z) 44, and sulphur dioxide (m/z) 64, as a function of run time. Initial cyclohexane concentration 10 ppm; incident light intensity 32mW/cm².*

When the LED$_S$ modules were switched on, the analysis of products in the outlet stream disclosed the presence of nitrogen and chlorine, as identified respectably from the characteristic fragments m/z 28 (fragment is reported in Figure 49) and 35, respectively (fragment is reported in Figure 49). No presence of carbon monoxide was disclosed. No deactivation of the catalyst was observed during photocatalytic tests.

94

V.1.3 Adsorption of methylene blue in dark conditions

Considering that the adsorption equilibrium was reached after 2 hours (Houas et al., 2001) of run time, the behaviour of the amount of MB adsorbed on catalyst (C^*) as a function of the concentration of MB in solution (C_0) is similar to a Langmuir adsorption isotherm (Figure 50 insert).

Thus, for the adsorption of MB on the active surface (Francisco and Mastelaro, 2002), it is possible to write:
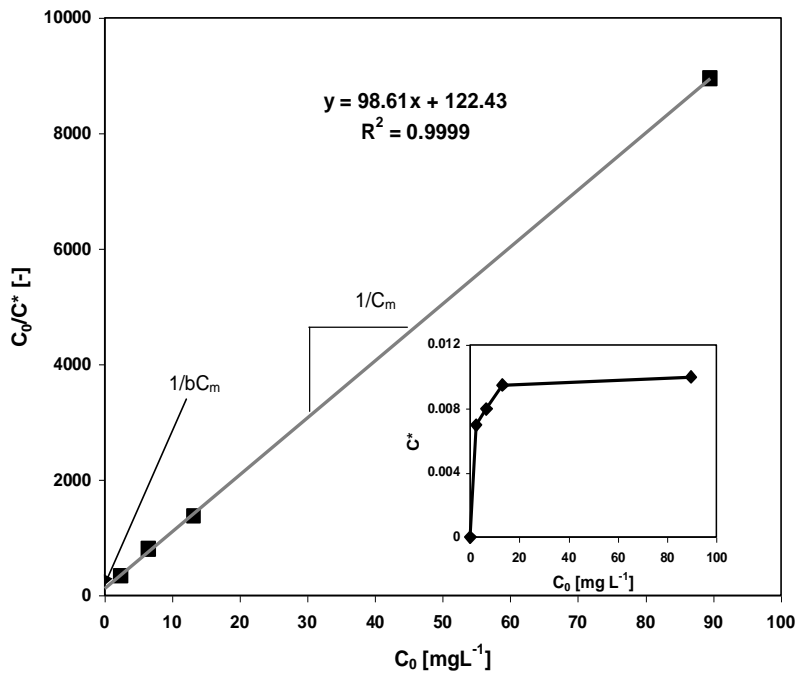
Figure 50 *Evaluation of MB adsorption constant and amount of MB adsorbed on N-doped TiO$_2$ (inset)*

$$C^* = \frac{b \cdot C_0}{1 + b \cdot C_0}$$

Eq. 23

Where:

C^*: amount of MB adsorbed on catalyst [g $_{MB}$/g$_{TD}$]

C_m: maximum absorbable value of C^*

C_0: concentration of MB in solution after dark adsorption [mg/ L]

b: adsorption constant of MB [L /mg]

The Langmuir isotherm can be rearranged to give:

$$\frac{C_0}{C^*} = \frac{1}{b \cdot C_m} + \frac{1}{C_m} \cdot C_0 \qquad \text{Eq.24}$$

Accordingly, a plot of C_0/C^* as a function of C_0 produces a straight line with: slope=$1/C_m$ and intercept=$1/bC_m$ (Figure 50).
The value of b was calculated from the Eq.24 utilizing the data reported in Figure 4 and it was equal to 0.82 [L /mg].

V.1.4 Mathematical modelling

The mathematical model has been realized considering that in the batch reactor under white LEDs irradiation, occur mainly the catalytic oxidation of MB (R).
MB mass balance can be written as:

$$V \cdot \frac{dC(t)}{dt} = r(C, I) \cdot W_{TD}$$

$$\text{Eq.25}$$

Where:
   V: solution volume, [L]
   $C_1(t)$: MB concentration, [g/ L]
   -r: reaction rate, [g /L min]
   WTD: catalyst amount, [g]
   I= light intensity reaching the photocatalyst surface [mW/ cm^2].
   The initial conditions are:
   t=0   C=Cin
   The kinetic expressions employed in the model is the following

$$-r = K_1 \frac{b \cdot C}{1 + bC} \cdot \frac{I \cdot \alpha}{1 + I \cdot \alpha} \qquad \text{Eq.26}$$

Where:
   K_1=kinetic constant [mg /g min]
   α= light absorption coefficient [cm^2 /mW]
   I= light intensity reaching the photocatalyst surface [mW /cm^2].

Equation 26 is similar to the Langmuir-Hinshelwood rate law used by other studies (Welte et al., 2008). In the hypothesis of keeping the reactant concentration constant, the dependence of reaction rate on photonic flux (Eq. 27) is the same reported in literature (Herney-Ramirez et al., 2010b), which

96

presented a simple approach for the design of photocatalytic reactors, considering that photons can be treated as immaterial reactants. This expression allows taking into account that only a fraction of light intensity reaching the photocatalyst particle, is absorbed by itself. This effect was evaluated utilizing the parameter α.

Moreover, it is important to consider that the availability of active sites increases with the catalyst concentration in the suspension, but the light penetration decreases with the catalyst concentration in the suspension due to screening effect (Sivalingam et al., 2003a).This suggests that only a part of the light intensity entering in the reactor, will be reach the photocatalyst particles. To consider this screening effect, a first order correlation, similar to Lambert-Beer law, for the effective light energy received by the TiO_2 particles was used:

$$I = I_0 * e^{-k_I [TiO_2]} \qquad\qquad Eq.27$$

Where:

k_I= the specific extinction coefficient per unit catalyst mass [L /mg]
I= light intensity reaching the photocatalyst surface [mW /cm^2].
I_0= nominal light intensity [mW/ cm^2]
[TiO_2]= catalysts dosage [mg /L].

The Eq. 25, coupled with the Eq. 26, together with the initial condition, was solved by the Eulero iterative method. Primary goal of the simulation by mathematical model is to identify the constants K_1, α, and K_I by fitting experimental data reported in Figure 51 as a function of irradiation time. The fitting procedure was realized by using the least squares approach obtaining the value of K_1: 0.46 [mg/ g min], α:0.000925 [cm^2 /mW] and K_I: 0.012 [L/ mg]
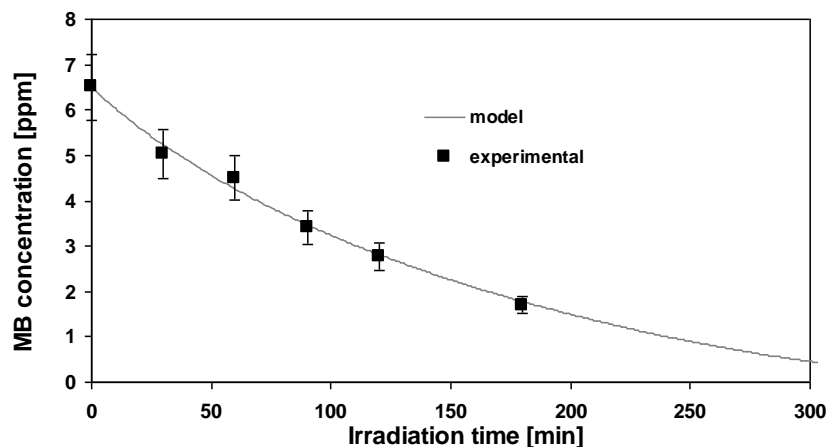
Figure 51 *Comparison between model calculation and experimental data to find the model constant. Catalyst weight: 0.3g; light intensity: 32 mW cm^{-2}.*
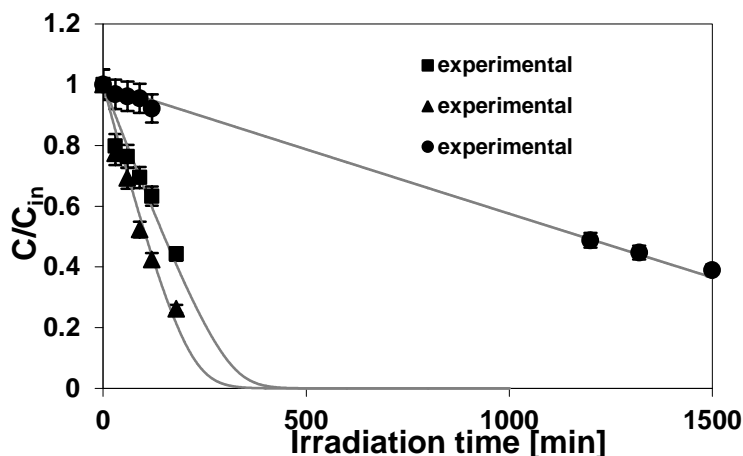
Figure 52 *Experimental and predicted data as a function of MB initial concentration; catalyst weight: 0.3g; light intensity: 32 mW/cm^2.*

After obtaining the model parameters, another series of experiments in which the initial MB concentration was varied from 6.5 to 95mg/L were carried out in order to analyse the ability the model to predict the experimental data. The obtained results are shown in Figure 52. In this series of experiments, the incident light intensity (I_0) and N-TiO$_2$ dosage are kept constant equal to 0.3g and 32mW cm^{-2}, respectively .At fixed reaction times,

the increase of MB initial concentration determined a decrease of the photocatalytic activity. This could be due to the increase of colour intensity of the solution that reduces the light penetration into the aqueous medium, meaning that the path length of photons inside the solution decreases (Sacco et al., 2012). The calculated values in all case are in good agreement with the experimental data. It is important to note that for the higher concentration (90ppm), the model is also able to predict correctly the experimental data obtained after 24 and 25hours of irradiation time, as reported in Figure 52.

Figure 53 shows the effect of the amount of N-TiO$_2$ catalyst, on the conversion of MB in the presence of white LEDs. At fixed irradiation time, the MB concentration decreased by increasing the N-TiO$_2$ amount as shown by the experimental results. For a content of catalyst equal to 0.3g, the complete decolourization was obtained after about 250minutes. For a catalyst amount of 1 and 1.5g, the total conversion of MB was achieved quickly and in particular after 80 and 50 minutes respectively.
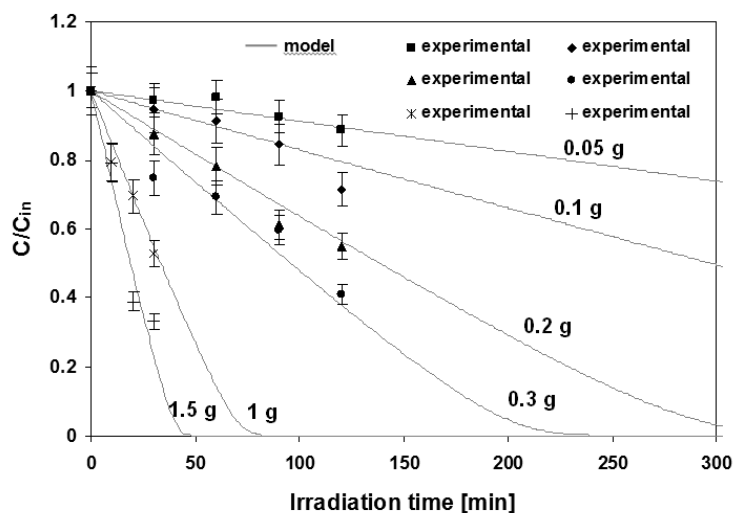
Figure 53 *Experimental and predicted data as a function of catalyst weight; initial MB concentration: 10 ppm; light intensity: 32 mW/cm^2*

Also by changing the catalyst dosage in the solution, the transient predicted results obtained by the mathematical model agree with the experimental results using the same set of parameters determined by the fitting procedure with the data reported in Figure 51.

The next series of experiments were carried out increasing the incident light intensity from 8 to 32mW/cm^2 (Figure 53). As expected, the decolourization reaction rate increased with the LEDs light intensity. Finally, also in this case, the experimental results of MB decolourization were satisfactorily predicted by the model developed in this study.

V.2 Mathematical modelling of photocatalytic degradation of

MB under visible light irradiation

V.2.1 Photocatalytic tests

Aqueous solutions containing SP were prepared using weighted fractions of pills dissolved in bidistilled water, to get a more realistic drug-tainted wastewater.

The experiments were realized using a pyrex cylindrical photoreactor (ID= 2.5 cm) equipped with an air distributor device (Qair=250 cm^3/min (STP)), magnetic stirrer to maintain the photocatalyst suspended in the aqueous solution and temperature controller. The photoreactor was irradiated with a strip composed by 25 blue LEDs (BL strip) (provided by NEW ORALIGHT; light intensity 32mW /cm^2) with wavelength emission in the range 400–550 nm (Prados-Joya et al., 2011) or with four Black Light UV tubes (provided by Philips; nominal power: 32 W) with wavelength maximum emission around at 365nm. The light sources were positioned around the external surface of the photoreactor (Chapter IV).

V.2.2 Adsorption in dark condition of SP

For the evaluation of SP adsorption on the active surface (Shi et al., 2004), the following equation was used:

$$TOC^* = \frac{b \cdot TOC_d}{1 + b \cdot TOC_d}$$

Eq. 27

Where:
TOC*: amount of SP adsorbed on catalyst in dark conditions [g /g]
TOCm: maximum absorbable value of TOC*
TOCd: concentration of SP in solution after dark adsorption [mg/ L]
b: adsorption equilibrium constant [L /mg]
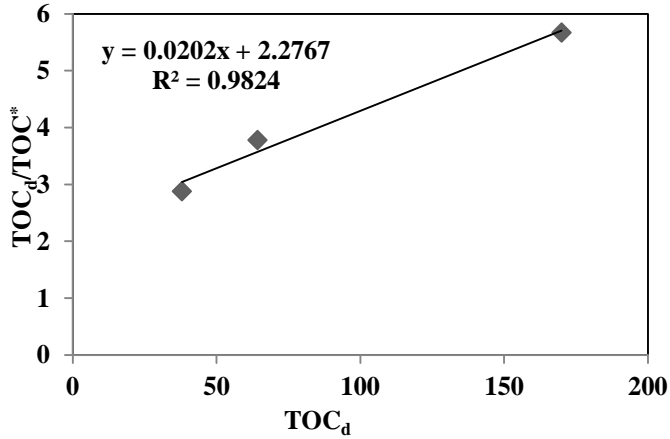
Figure 54 *Evaluation of SP adsorption constant*

Eq.27 can be rearranged to give:

$$\frac{TOC_d}{TOC^*} = \frac{1}{b \cdot TOC_m} + \frac{1}{TOC_m} \cdot TOC_d$$ Eq.28

Accordingly, a plot of TOC_d/TOC^* as a function of TOC_d produces a straight line with: slope=$1/TOC_m$ and intercept=$1/b*TOC_m$ (Figure 54).
The value of b was calculated from Eq. 28 utilizing the data reported in Figure 28 and it was equal to 0.0089 [L/ mg].

V.2.3 *Evaluation of rate constant*

The mathematical model has been realized considering that in the batch reactor under blue LEDs irradiation, occur mainly the total oxidation of SP to CO_2. Mass balance on SP concentration (expressed as TOC) can be written as:

$$V \cdot \frac{dTOC(t)}{dt} = r(TOC, I) \cdot W_{Nt}$$ Eq.29

Where:
TOC(t) :TOC at given reaction time, [g /L]
-r: reaction rate, [g /L h]

W_{Nt}: amount of catalyst effectively irradiated (Zhao et al., 2013) [g]
The initial conditions are:
t=0 $TOC=TOC_0$

The kinetic expressions are well described with the classic Langmuir-Hinshelwood (L-H) mechanism in terms of mineralization of SP as in the following:

$$-r = K \cdot \frac{b \cdot TOC}{1+b \cdot TOC} \cdot \frac{I \cdot \alpha}{1+I \cdot \alpha} \qquad \text{Eq. 30}$$

Where:
K=kinetic constant [mg/ g h]
α= light absorption coefficient [cm^2 /mW]
I= light intensity reaching the photocatalyst surface [mW/ cm^2].

Eq. 30 is similar to the Langmuir-Hinshelwood rate law used in other studies regarding the mathematical modelling of methylene blue degradation(Xekoukoulotakis et al., 2011).
This equation takes into account also the influence of light intensity. In fact, only a fraction of nominal radiation reaching the photocatalyst particles is absorbed by itself. This effect was considered utilizing the parameter α. This parameter depends only on the reactor configuration and light sources and not on the liquid medium; its value is equal to 0.000925 [cm^2 /mW] and it is the same used in a previous work (Xekoukoulotakis et al., 2011). Moreover, it is important to consider that the light penetration inside the reactor core depends on type of pollutant (in this case SP) and on the catalyst concentration (Xekoukoulotakis et al., 2011). This suggests that only a part of the light intensity entering in the reactor, will be reach the photocatalyst particles. To consider this screening effect, a first order correlation (similar to Lambert-Beer law) for the effective light energy received by the N-TiO_2 particles (Xekoukoulotakis et al., 2011) was used:

$$I = I_0 \cdot e^{-[N-TiO_2] \cdot k_I} \qquad \text{Eq.31}$$

Where:
k_I= specific extinction coefficient per unit catalyst mass [L /mg]
I= light intensity reaching the photocatalyst surface [mW /cm^2].
I_0= nominal light intensity= 32 mW /cm^2
[N-TiO_2]= catalysts dosage [mg /L].
Eq. 29, coupled with Eq. 30, together with the initial condition, was solved with Euler iterative method to identify the constants K and k_I by fitting experimental data reported in Figure 55 as a function of irradiation time
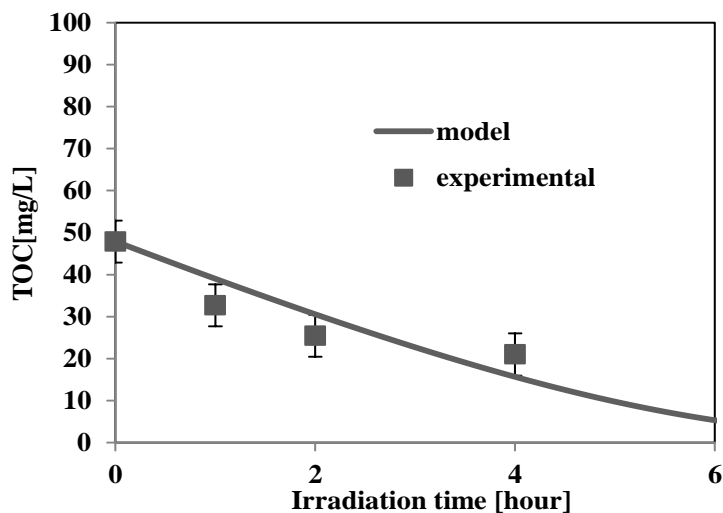
Figure 55 *Comparison between model calculation and experimental data to find the reaction constant*

. The fitting procedure was realized by using the least squares approach obtaining the value of K: 6.04 [mg/ g- h], and k_I: 0.349 [L /mg]. After obtaining the model parameters, the experimental data obtained with different initial TOC were fitted to analyse the ability of the model to predict the experimental data. The obtained results are shown in Figure 56.
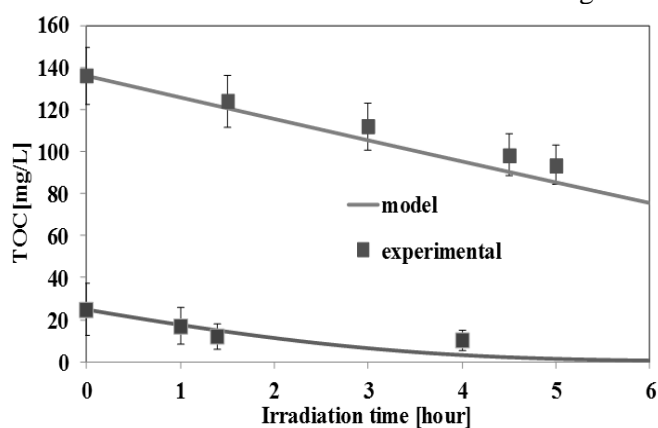
Figure 56 *Experimental and predicted data as a function of initial TOC_0*

In this series of experiments, the incident light intensity (I_0) and N-TiO$_2$ dosage are kept constant. The calculated values in both cases are in good

103

agreement with the experimental data. It is important to note that also for the higher TOC_0 (170 ppm), this system is able to predict the mineralization trend with a single value of kinetic constant. This last result is in contrast with literature works about kinetic degradation of antibiotics in liquid phase that report different values for mineralization constant(Palma et al., 2010a).

VI Photocatalytic degradation of highly polluted wastewater

The wastewater generated from the factory of has many kinds of high concentration complex organic constituents, but the conventional method such as coagulation is not useful for removal of total organic carbon (TOC) and chemical oxygen demand (COD) . Alternative technology has been developed to help solving the problem. Advanced oxidation processes (AOPs) are frequently used to oxidize complex organic constituents found in wastewaters which are difficult to be degraded biologically into simpler end products .

VI.1 Experimental set up apparatus and photocatalytic tests

conditions

Tannery wastewater is produced during the fabrication of leather articles and is characterized by high organic matter content composed by a variety of different chemicals added at different stages of the process. As a consequence, this wastewater stream is polluted by organic matter, heavy metals, toxic chemicals, chloride, lime, dissolved and suspended salts among other pollutants.

In general, wastewater treatment requires complex procedures in order to recover the water by the pollution elimination, and in recent years conventional and innovative treatment processes have been applied to a wide range of wastewater streams. Among the conventional processes carried out to treat such wastewater, i.e. biological, oxidation membrane and chemical processes, difficulties or disadvantages were found (Stoller and Chianese, 2006). Physical and chemical methods are considered very expensive in

terms of energy and reagents consumption, and give rise to excessive sludge production (Churchley, 1994).

The photocatalytic degradation has been discussed as a promising technology for the wastewater treatment in the scientific literature since 1976, and efforts focused on the use of heterogeneous photocatalysis by using oxide semiconductors as catalyst (Carey et al., 1976). Titanium dioxide, TiO_2, is characterized by chemical stability, no intrinsic toxicity or cheapness, and represents one of the most important worldwide used oxides in several fields of photochemistry (environmental remediation, photoelectrolysis of water, dye-sensitized solar cells) (Anpo, 2004). The efficiency increases if the particle size of the catalyst is in the nanometric range, and this result can be reached only by paying particular attention during the photocatalyst synthesis process .

The relative high value of its band-gap energy; equal to 3.0-3.3eV, has as a consequence that TiO_2 is capable to absorb mainly a small fraction of the solar spectrum emission in the UV range. This aspect implies that wastewater treatment by titania photocatalysis cannot be carried out in presence of light sources emitting in the visible region, but only under UV radiation, resulting usually in an unappealing application from an economic point of view. In order to overcome this constraint, doped TiO_2 photocatalysts were developed to increase sensitivity to visible light. Nitrogen doped TiO_2 seems to be, among the second generation titania photocatalysts, the most promising ones. The doping can be performed by the application of various techniques such as sputtering, treating of TiO_2 powders in ammonia atmosphere with urea hydrolyzing organic or inorganic titanium compounds (Asahi et al., 2001).

The aim of this work is to investigate the performances of photodegradation using home-made nitrogen doped TiO_2 nanoparticles on a tannery wastewater stream under different light sources and different photoreactor configurations. The obtained results are compared to those obtained by using a commercial titania powder (Degussa P25). Moreover, a simplified mathematical model capable to correlate the power input of the used light source to the degradation of the wastewater, measured in term of chemical oxygen demand ("COD") reduction, was developed. The mathematical model was validated, presenting it as a useful engineering tool for the optimization of process design.

VI.1.1 Photocatalytic tests

The photocatalytic activity of the samples was tested in terms of the reduction of chemical oxygen demand (COD) of a wastewater tannery collected after preliminary depollution treatments, ie. screening,

homogeneization, neutralization, with an initial COD content of 2000mg/L. In a typical photocatalytic test, 3 g/L of photocatalyst was suspended in 200mL solution. The photocatalytic reaction was performed under visible or UV light for 6 h.

The experiments were realized in two photoreactor configurations: the first one was a pyrex photoreactor (I.D.= 10 cm; height=6.3 cm) equipped with an air distributor device positioned at bottom of the reactor (Q_{air} =150 cm^3/min (STP)), a magnetic stirrer to maintain the photocatalyst suspended in the solution and with a thermocouple to monitor the temperature during irradiation. The reactor was irradiated by different light sources: a UV lamp (provided by Philips), two blue LEDs (BL) (provided by Vollong Electronics Co., Limited) or two white LEDs (WL) (provided by Vollong Electronics Co., Limited) whose characteristics are reported in Table 1. The position of light sources was 15 cm above the upper surface of the batch reactor. Moreover the photoreactor was covered with reflecting aluminium foils in order to assure that only its upper surface was irradiated. Experimental set up is represented in Figure 57(configuration A).
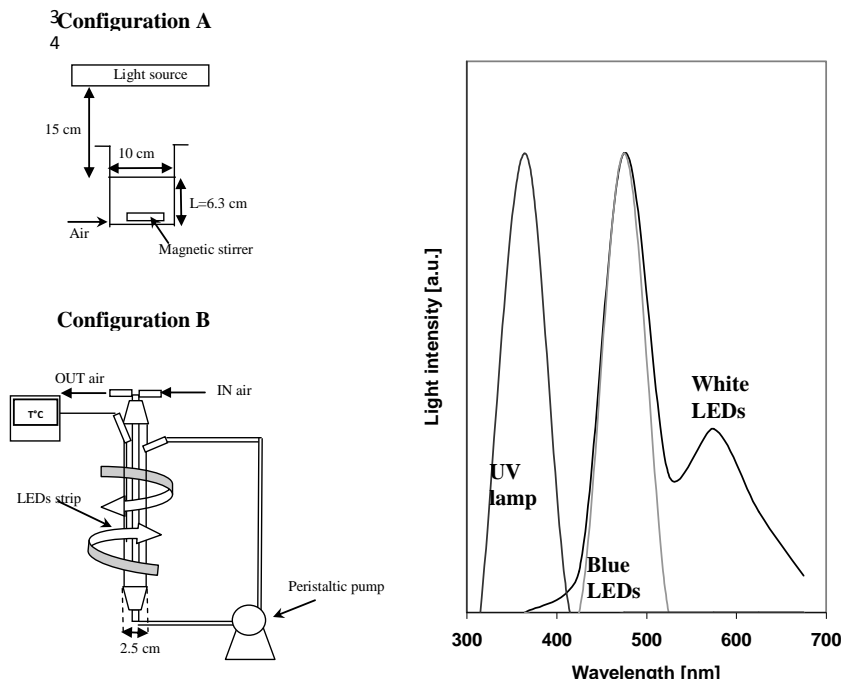
Figure 57 *Reactor configurations (A and B) and emission spectrum of the different light sources*

To increase the efficiency of the process a second configuration of the photoreactor was realized. In this case the pyrex photoreactor I. D. was reduced from 10 to 2.5 cm. Experimental set up is represented in Figure 57 (configuration B). Also in this case, the photoreactor was equipped with an air distributor device (Q_{air} =150 cm^3/min (STP)). In this case the continuous mixing of the wastewater and of the photocatalyst was realized by external recirculation of wastewater through the use of a peristaltic pump. Thermocouple was inserted inside the reactor to monitor the temperature during irradiation. In the configuration B, the photoreactor was irradiated with a strip composed by 25 white light LEDs (WL strip) (provided by NEW ORALIGHT) with wavelength emission in the range 400–800nm or by 25 blue light LEDs (BL strip) (provided by NEW ORALIGHT) with wavelength emission in the range 400–550 nm (Table 6). The strips of LEDs were positioned around and in contact to the external surface of the photoreactor. Table 7 and Figure 57 report, in detail, the emission characteristics of all the used light sources.

Liquid samples were collected at fixed time intervals, and centrifuged for 20 minutes at 4000 rpm to allow the removal of photocatalysts particles. The centrifuged samples were analysed to determine the change of COD by using the analytical spectrophotometrical procedure developed by Dr.Hach-Lange (Lasa100), using kit cells in the range of COD 1.000-10.000 and 100-2.000 mg /L.

Table 6 *Characteristics of light sources.*

Light source	Type	Nominal Power [W]	η, %
UV lamp	UV lamp, λ=365nm	32	25
BL strip	Blue light LED strip	5	50
WL strip	White light LED strip	5	50
BL	Blue light LED	20	50
WL	White light LED	6	50

Table 7 *Spectral emission of light sources as a function of wavelength [λ]*

λ [nm]	Relative emission intensity (Y)		
	UV	WL and WL strip	BL and BL strip
365	1.000	0	0
425	0	0.09	0
475	0	1	1.000
525	0	0.3	0
575	0	0.4	0
625	0	0.22	0
675	0	0.08	0

The photocatalytic plate reactor was realised in steel with a quartz window (reactor volume: 0.7 L).

VI.1.2 Experimental results

In order to verify that wastewater was degraded by heterogeneous photocatalytic process, blank experiments were performed. A control test was carried out in the absence of photocatalysts and in presence of UV or visible light. No COD removal was detected during these tests, indicating the necessity of the catalyst for realizing the degradation of the tannery wastewater.
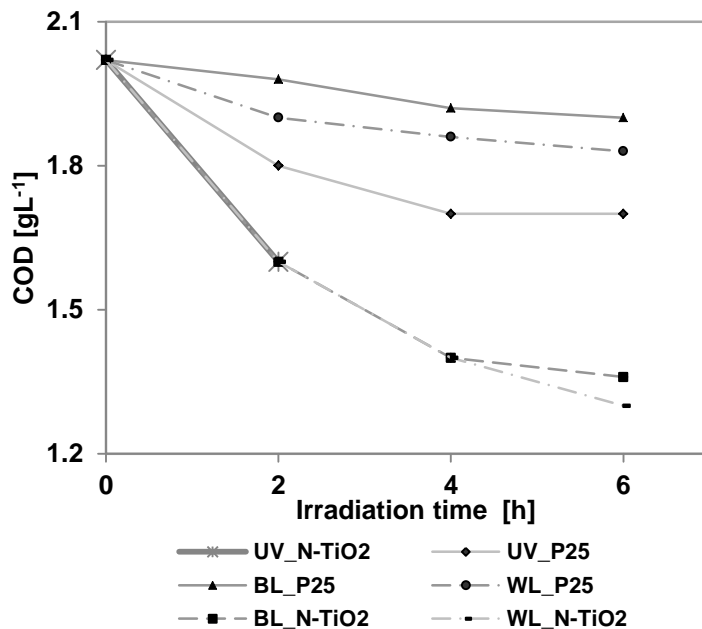
Figure 58 *Comparison of photocatalytic results using different light sources in the configuration A; catalyst dosage: 3g/L.*

The COD profiles as function of irradiation time obtained on P25 and N-TiO$_2$ in the configuration A under the irradiation realized by UV lamp, WL, and BL are shown in Figure 58. The catalyst P25 showed interesting removal activity of COD only with UV lamp as expected from its absorption properties. In contrast, N-TiO$_2$ catalyst has evidenced a different trend, giving rise to a significant activity in presence of all the light sources used. During the first 4h of irradiation, the COD removal on N-TiO$_2$ reached a

value of about 40% and remained constant after 6h in presence of WL. This result may be an indication of catalyst deactivation that could be due to the scarce irradiation of the overall wastewater treated volume, caused by the photonic transfer limitation from the external sources towards the bottom of the photoreactor in the configuration A. With the aim to verify these hypotheses, the reactor configuration B was employed for further tests, to profit of its reduced diameter and higher irradiation of the wastewater obtained by changing the position of light sources realizing their envelope around the photoreactor B external surface. Figure 59 shows the comparison of the photocatalytic tests carried out in the two photoreactor configurations in presence of white LEDs, at the same initial COD, catalyst dosage and reaction temperature. With the configuration B, the COD removal was about 70% after 5h of irradiation while when configuration A was used, COD removal was lower and equal to 35 %. The use of WL strip allows to cover a larger area reducing the dispersion of the radiation in the external environment, thus increasing the radiation useful in the process of photodegradation.
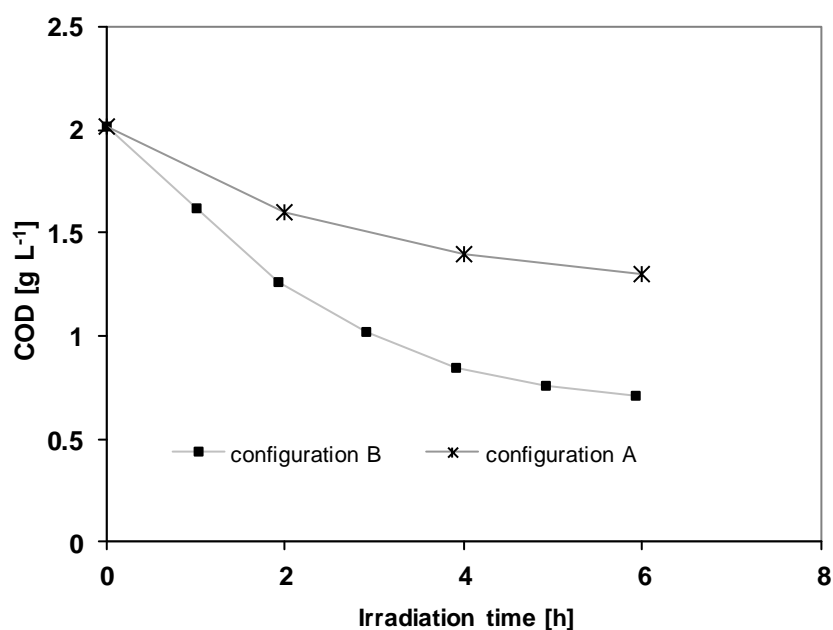
Figure 59 *Comparison between photoreactor configuration A and configuration B using white LEDs and N-TiO$_2$ catalyst; catalyst dosage: 3g/L*

VI.1.3 Mathematical modelling

Experimental data obtained from photocatalytic tests with configuration B and over N-TiO$_2$ photocatalyst, were used to develop a simplified model to permit a correlation between the used light source and the obtained COD reduction, taking into account i) lamp electrical nominal power, ii) electricity into light conversion efficiency (η), iii) the radiation optical pathlength and iv) illumination angle, and finally v) system geometry. Mass balance on pollutants overall concentration (expressed as COD) can be written as:

$$\frac{dCOD}{dt} = r(\alpha_{photons}, COD) \cdot \left(\frac{W_{cat}}{V} \right)$$

Eq.32

V: solution volume, [L]

COD(t) : COD as a function of irradiation time, [gO$_2$ L^{-1}]

-r: reaction rate, [gO$_2$ mol$_{photons}$ g$_{cat}$$^{-1}$ h^{-1}]

W$_{cat}$: amount of catalyst effectively irradiated, [g] [51]

The initial conditions are:

t=0   COD=COD$_0$

The kinetic expressions employed in the model is the following

$$r = k \cdot \alpha_{photons} \cdot COD$$

Eq.33

a$_{photons}$= moles of photons absorbed by catalyst per hour, [mol$_{photons}$ h^{-1}]

k = model constant, [L g$_{cat}$$^{-1}$]

To assess $\alpha_{photons}$ parameter, was firstly evaluated the energy of the single photon (E) emitted as a function of wavelength considering the sources emission spectrum and relative emission intensity (Y) (Table 7):

$$E = \sum_{\lambda_i} Y_i \cdot h \cdot \frac{c}{\lambda_i}$$

Eq.34

Where:

E=energy of single photon [J]

h= Planck constant 6.62 10^{-34} [J s]

c= light velocity, 300000 [km s^{-1}]

λ_i= wavelength, [km]

Y_i= relative emission intensity at λ_t [−].

The number of moles of photons per hour entering into reactor was a function of lamp electrical nominal power and source efficiency η (data furnished by the provider of each light source), reported in Table 6, and also of the fraction of photoreactor surface (S) exposed to light, evaluated as the ratio between the photoreactor surface exposed to light source and the entire surface covered by the emitted photons. The last one depends on illumination angle, and on the distance between the light source and the photoreactor surface. So, the number of moles of photons N that reach the reactor surface can be estimated through the following relationship:

$$N_{photons} = \frac{P \cdot \eta \cdot S}{E \cdot N_{Avogsdro}}$$ Eq.35

Where:

$N_{photons}$= moles of photons per hour entering into reactor [mol h^{-1}]

P= electrical nominal power, [J h^{-1}]

η= efficiency of light source [-]

$N_{Avogadro}$=number of Avogadro, [$6.02214129 \times 10^{23}$ mol^{-1}]

S= fraction of photoreactor surface exposed to light [-].

For evaluating S and the number of photons effective for the degradation of the organic matrix, the irradiation geometry was schematized. For configuration B, thanks to the LEDs strip flexibility, about 90% of surface was irradiated (S=0.9). Different situation is observed on the contrary for configuration A (Figure 59) where only the upper surface of photoreactor was irradiated. Considering that the diameter of the reactor was 10 cm, the photoreactor surface exposed to light (S_r) is equal to 78.5 cm^2.Thus, knowing the height at which the LEDs have been positioned during the test, equal to 15cm, and the illumination angle of light sources, respectively, equal to 50° for white LEDs and 70° for blue LEDs (data furnished by the provider), it was possible to evaluate the entire surface covered by the emitted photons (S_{tot}) through the following equation:

$$S_{tot} = \pi \cdot \left(H \cdot tg(\beta)\right)^2$$ Eq.36

Where:

β= half of illumination angle of light sources; equal to 25° for WL and 35° for BL.

H= height at which the LEDs have been positioned equal to15 cm.

112

The value of S_{tot} was 153 and 346 cm^2 for WL and BL, respectively. Finally, it was possible to estimate, in a simple way, the value of $S=S_r/S_{tot}$ that was 0.5 for WL and 0.2 for BL. Not all photons emitted by the lamps that reach the photoreactor, are useful to activate the photocatalyst. To consider this aspect, UV-Vis reflectance spectra of catalysts were used to estimate the absorbance (A) of photocatalyst as function of wavelength *f[A]* (Table 8), according to the following equation:

f[A] = 1-R(λ)   Eq.37

Where:

R= reflectance value of the catalyst (from UV-Vis DRS spectra) as a function of wavelength.

f[A]= absorbance of catalyst as a function of wavelength

Thus, it is possible to evaluate $\alpha_{photons}$ according to the following relationship:

$$\alpha_{photons} = N_{photons} \cdot f[A] \cdot I^*$$ Eq.38

Where I* is the ratio between the average light intensity inside the core of the reactor and the light intensity entering into the reactor. This value is almost equal to 1 for configuration B in which the LEDs are positioned around and in contact to the photoreactor walls. On the contrary I* is a number lower than 1 for configuration A because in this case the irradiation is realized only on the upper surface. So an extinction of the light occurred due to the height of the reactor and the light absorption properties of the wastewater. For this reason, from the absorbance profile of tannery wastewater obtained by UV-vis DRS (Figure 60),

Table 8 *Light absorbance of photocatalyst*

Wavelenght [nm]	Absorbance N-TiO$_2$	Absorbance P25
365	0.781	0.551
425	0.554	0.001
475	0.435	0.017
525	0.251	0.042
575	0.180	0.065
625	0.128	0.082
675	0.088	0.099

the absorbance profile was estimated inside the tannery wastewater as a function of the reactor height (equal to 6.3cm). This has been realized estimating the parameter σ through Lambert-Beer law knowing the value of

absorbance of the wastewater corresponding to the emission wavelength of different light sources used in the model (Table 7).

$$A_i = \varepsilon_i \cdot c \cdot l \underset{=}{} \sigma_i \cdot l$$

Eq.39
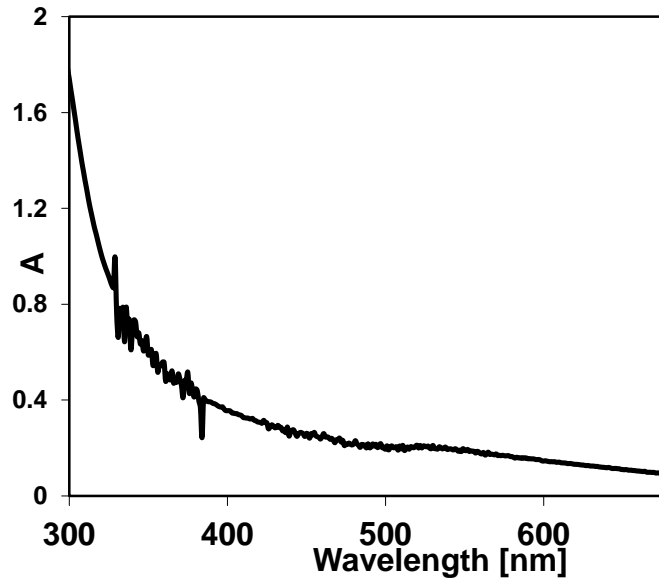
Figure 60 *Absorbance spectrum of tannery wastewater*

Where:

A= absorbance at wavelength λ_i.

l=optical path equal to (1cm)

ε_i = molar extinction coefficient at λ_i [L number of molecules $^{-1}$cm^{-1}].

c=concentration of the species in the wastewater [number of molecules L^{-1}].

$$\sigma_i = \varepsilon_i \cdot c$$

Eq.40

These values then were used for calculating the average intensity of transmitted light in the height of reactor (configuration A) according to the following relationship.

114

$$I^* = \frac{\int_0^L \sum_{\lambda_i} e^{-\sigma_i \cdot x} \cdot dx}{L} \qquad \text{Eq.41}$$

Where:

I^*= ratio between the light intensity entering into the reactor and the average light intensity inside the core of the reactor due to the tannery wastewater.

L= reactor height (configuration A) equal to 6.3 cm.

These values are reported in Figure 62 for BL and WL.
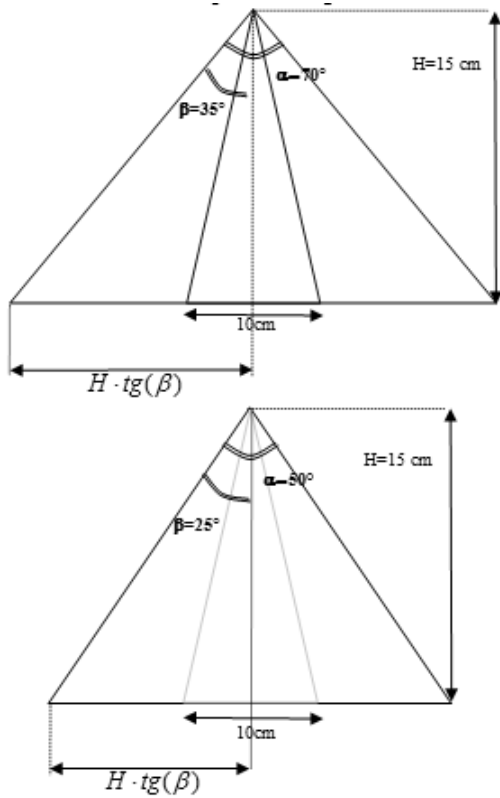
Figure 61 *Geometric schematization of light flux upper the photoreactor (configuration A)*

However, it must take into account that the product *f[A] I*, present* in the equation 41, considers both the attenuation of light due to the wastewater

115

and that one caused by the light absorption of catalyst particles. Finally, αphotons values were calculated and reported in Table 5, showing that changing the reactor configuration from A to B, the value of αphotons increases because the fraction of photoreactor surface exposed to light increases.
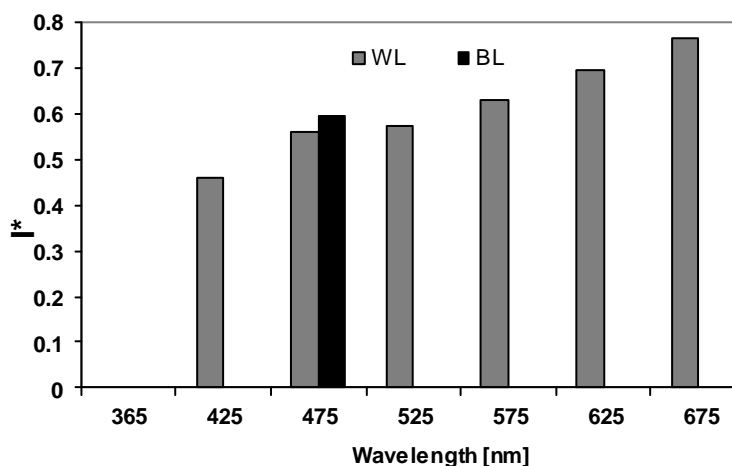
Figure 62 *Calculated I^* for WL and BL.*

The estimated $\alpha_{photons}$ were introduced into the kinetic expression. The Eq. 32, together with the initial condition, was solved by the Euler iterative method. Primary goal of the simulation by mathematical model is to identify the constants k, by fitting experimental data reported in Figure 7 as a function of irradiation time. The fitting procedure was realized by using the least squares approach obtaining the value of k equal to 3.296 L g_{cat}^{-1}. This value of k was then used to interpret all the curves obtained both with reactor configuration A and configuration B. In the Figure 63 the experimental results under irradiation with WL strip carried out for 5h of irradiation are reported. After 1h of irradiation the COD removal was about 20% reaching a final value of about 70%. In the same figure, the trend of model as a function of irradiation time was compared to the experimental values after the fitting procedure.Figure 63 shows the effect of the dosage of N-TiO$_2$ catalyst on the reduction of COD, in the presence of WL strip. The final COD value was lower than that one recorded when a catalyst dosage of 3g/L was used. Also by changing the catalyst dosage, the transient predicted results obtained by the mathematical model agree with the experimental results using the same k determined by the fitting procedure with the data reported in Figure 63.

116
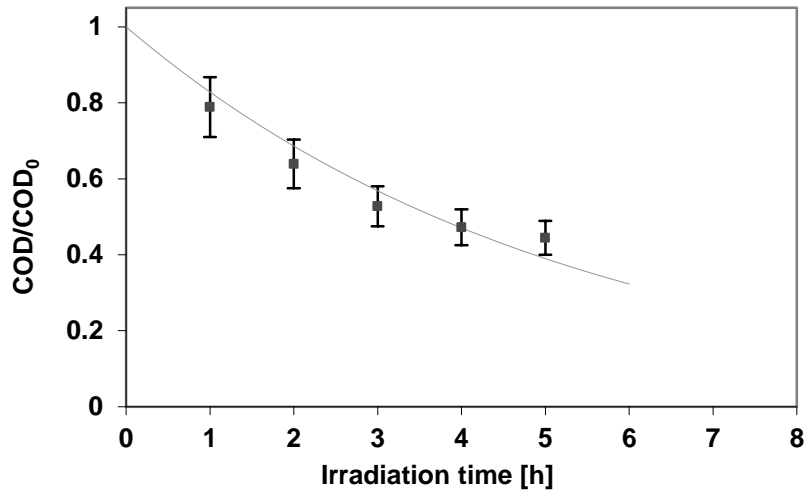
Figure 63 *Comparison between model calculation and experimental data to evaluate the model constant; catalyst: N-TiO$_2$; configuration B; catalyst dosage: 3g/L; light source: WL strip*
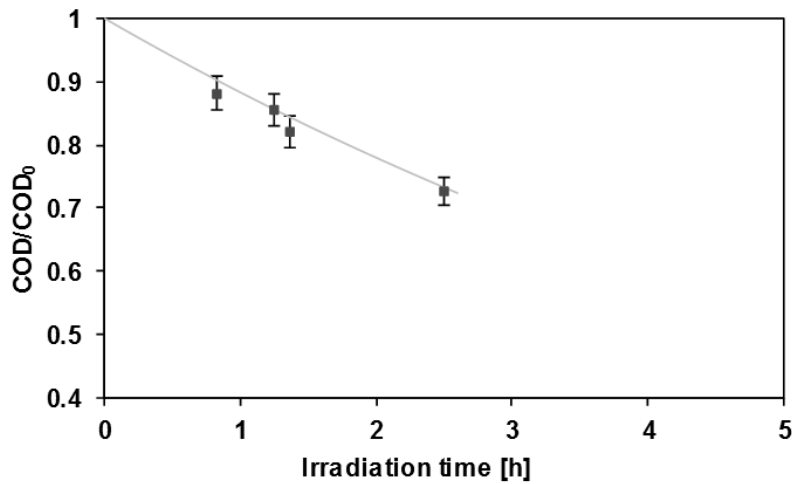
Figure 64 *Comparison between model calculation and experimental data with a catalyst dosage of 1.5g/L; catalyst: N-TiO$_2$; configuration B; light source: WL strip.*

Also with configuration A, the predicted results obtained by the mathematical model agree with the experimental data both using WL and BL (Figure 64 and Figure 65).

117
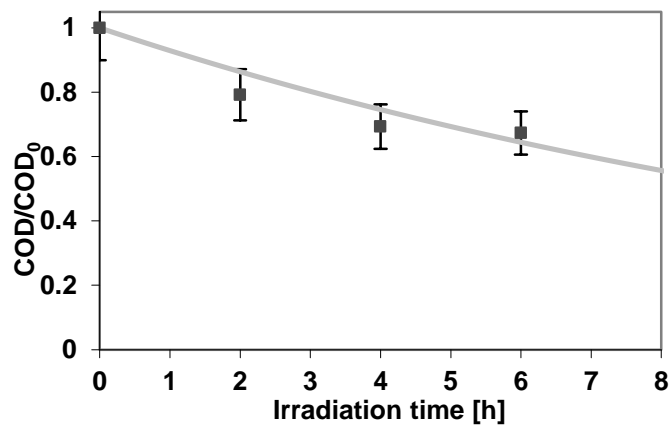
Figure 65 *Comparison between model calculation and experimental data with a catalyst dosage of 3 g/L; catalyst: N-TiO₂; configuration A; light source: BL*
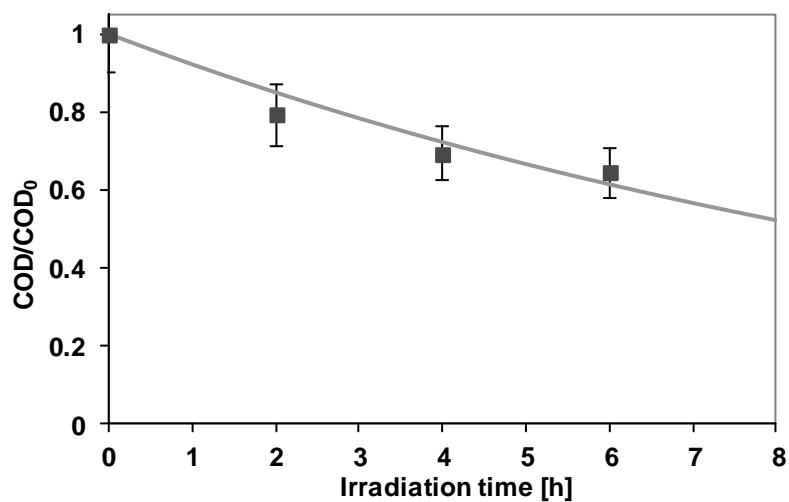
Figure 66 *Comparison between model calculation and experimental data with a catalyst dosage of 3 g/L; catalyst: N-TiO₂; configuration A; light source: WL.*
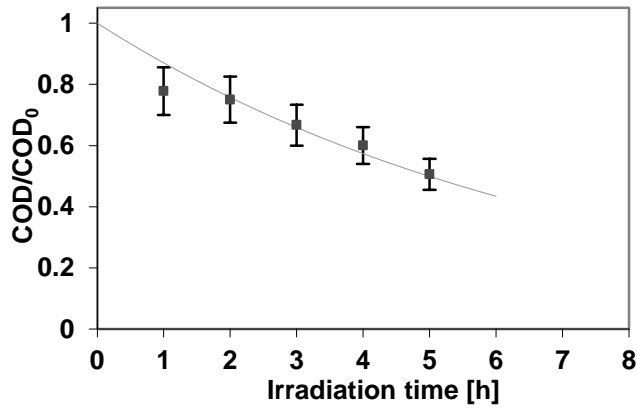
Figure 67 *Comparison between model calculation and experimental data with a catalyst dosage of 3 g/L; catalyst: N-TiO₂; configuration B; light source: BL strip.*
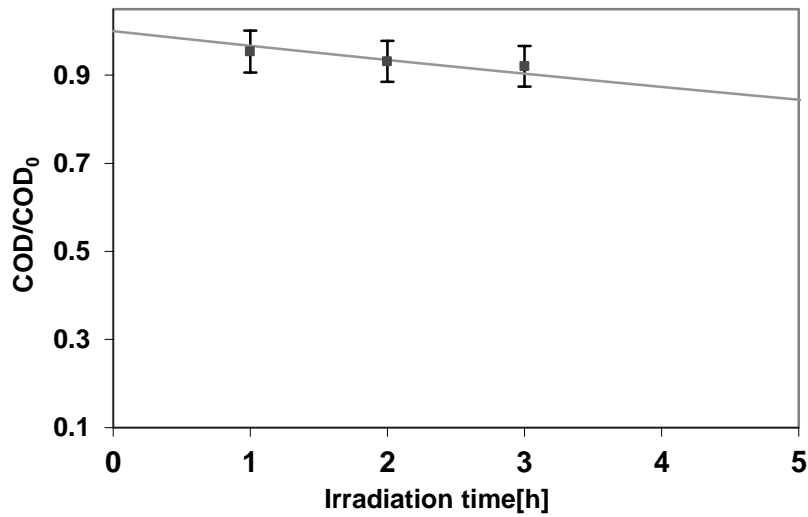
Figure 68 *Comparison between model calculation and experimental data with a catalyst dosage of 3 g/L; catalyst: N-TiO₂; configuration B; light source: UV lamp.*

119

The effect of the different light sources, in the configuration B, (BL strip in Figure 66 and UV lamp in Figure 67) with N-TiO$_2$ catalyst was evaluated. Also in this case, the model well fits the experimental data. The efficiency of degradation of organic matter present in tannery wastewater by means commercial P25 and N-doped titania nanoparticles under UV or visible light irradiation has been investigated. From the experimental results, it was evinced that P25 was active only in presence of UV light. In contrast, N-doped titania was effectiveness in the treatment of the wastewater and showed remarkably photoactivity also in presence of visible light emitted by LEDs. The efficiency of the process was increased disposing the light source around the photoreactor. In this case, in presence N-doped TiO$_2$, a COD reduction of about 70 % was reached after 5 hours of irradiation. Considering the light absorption properties of the photocatalyst and the emission characteristics of the light sources, a simplified mathematical model was developed representing a valuable tool to design and optimize photocatalytic processes for wastewater treatment using visible light sources.

VII   Limitations of the photocatalytic process in slurry reactors

The most limitation regards photocatalytic processes in slurry reactor is the low activity of commercial TiO_2 samples mainly due to the aggregation phenomena between nanoparticles. Another limitation is instead due to the effective transfer of the light towards the overall amount of photocatalyst.

However, the key parameter for a successful implementation of photocatalytic processes at large scale is the reduction of reaction time.

VII.1 Effect of aggregates size on photocatalytic activity of N-TiO₂ particles in aqueous suspensions in presence of visible light irradiation

Photocatalytic nanoparticles are being studied for a wide range of applications including gaseous streams (Hajaghazadeh et al., 2014; Murcia et al., 2013; Rizzo et al., 2013b) and water treatment (Augugliaro et al., 2012; Vaiano et al., 2014e), solar power (Pagliaro et al., 2008; Palmisano et al., 2009), and self-cleaning surfaces (Lam et al., 2009; Sannino et al., 2013e). TiO_2 nanoparticles, arguably the most commonly used engineered nanomaterials, are found in numerous industrial products and applications(de Caprariis et al., 2012; Jassby et al., 2012).

Evaluation of the photocatalytic activity of semiconductors in liquid phase reactions is often performed in slurry reactors. These reactors contain the photocatalyst as a dispersed solid phase and are irradiated with either internal or external light sources. The expected industrial applicability of photocatalytic slurry reactors is limited due to the required separation of the

solid catalyst from the liquid medium after the reaction. However, the generally short diffusion lengths which prevent external mass transfer limitation in these reactors, is beneficial for conversion of low pollutant concentrations, and therefore these reactors are still considered feasible in water cleaning.

However an important aspect to consider is that photocatalyst nanoparticles have strong tendency to agglomerate, due to their large surface area. The formation of large agglomerates from small primary particles can significantly influence optical properties, such as available photoactive surface area. The change in agglomerate size has a significant effect on the propagation of light and especially on the scattering properties.

The agglomeration phenomenon is generally due to the Van der Waals attraction forces between nanoparticles which can be counterbalanced by electrostatic and steric stabilization (Othman et al., 2012).
Stabilization induced by steric hindrance can be achieved by the adsorption of an organic substance on the surface of the nanoparticles to prevent that the nanoparticles are physically close enough to one another and cause agglomeration (Greenwood and Kendall, 1999).

Once introduced into an aqueous system, TiO_2 nanoparticles encounter conditions of ionic strength and pH that may alter nanoparticle surface chemistry, leading to changes in stability with respect to their aggregation.

There are three different mechanisms of nanoparticle cluster break up which are rupture, erosion and fragmentation. Rupture occurs when large agglomerate is broken up into numerous agglomerates of either the same or different size which can be subsequently broken up further. Erosion, on the other hand, occurs when small fragments are gradually sheared off and detached from the outer surface of large agglomerates. The smaller fragments are either primary particles or aggregates that cannot be broken up further under the effect of hydrodynamic stresses. Finally, shattering occurs when the energy level provided is very high, in which the agglomerate disintegrate into numerous small fragments of either aggregates or primary particles in a single event (Othman et al., 2012).

Sato et al. (Sato et al., 2008) focused on the effects of ultrasonic irradiation on slurry viscosity and aggregate size of commercial nanocrystalline TiO_2 aqueous suspensions containing polyelectrolyte dispersants and compared the results with those obtained via ball milling and bead milling. Fazio et al. (Fazio et al., 2008), on the other hand, studied the effect of dispersant nature, concentration, and the effect of ultrasonication time on colloidal behavior of dilute commercial and synthesized (sol-gel)-nanosized TiO_2 powder in aqueous suspensions. However, all of these studies mainly focused on preparing disperse and stable TiO_2 aqueous suspensions. As a consequence, there are few information about the correlation between the photocatalytic activity and TiO_2 agglomeration phenomena. In fact, the role that aggregates size may play in the

photocatalytic removal of organic pollutants from liquid phase, is up to now subject, in our knowledge, of few papers (Jassby et al., 2012; Rizzo et al., 2014; Sacco et al., 2012; Vaiano et al., 2014d). The size of the aggregates is mainly dependent on the specific surface area exposed by the titania, surface characteristics and amount (Jassby et al., 2012). Accordingly, a decreasing trend in the degradation ability at higher N-doped TiO_2 catalyst loading has been observed, not only related to the specific surface area, strictly connected to the crystallites size, but also to the increase of nanoparticles aggregate size in the solution (Rizzo et al., 2014; Sacco et al., 2012). Starting from this evaluation, one possible solution to increase the photocatalytic activity could be the enhancing of the nanoparticles dispersion, and thus the minimization of agglomeration phenomena inside the aqueous solution. Therefore, in this work the influence of aggregates size of N-doped TiO_2 on the photocatalytic activity in aqueous solution has been studied in presence of visible light irradiation.

VII.1.1 Photocatalytic activity test

The experiments were realized using a Pyrex cylindrical photoreactor (ID= 2.5 cm) equipped with an air distributor device (Q_{air}=150cm^3 min^{-1} (STP)), magnetic stirrer to maintain the photocatalyst suspended in the aqueous solution and temperature controller. The photoreactor was irradiated with a strip composed by 25 blue LEDs (provided by NEW ORALIGHT; light intensity: 32mW cm^{-2}) with wavelength emission in the range 400–550 nm (Sacco et al., 2012). The photocatalytic activity was evaluated comparing the decolourization process of MB in 100 mL of 5 mg L^{-1} MB aqueous solution.

The suspension was left in dark condition for 30 minutes to reach the MB adsorption equilibrium, and then visible light photodecomposition was performed for 2 h. Slurry samples were collected at fixed time intervals, and centrifuged for 20 minutes at 4000 rpm to separate photocatalyst particles from the solutions. The supernatant solutions were analyzed to determine the change of MB concentration, measured with a Perkin Elmer UV-Vis spectrophotometer at λ=663 nm. A standard calibration curve was attained for different MB concentration, and allowed to convert absorbance to concentration (mg L^{-1}) units.

VII.1.2 Selection of dispersing agent

Starting from literature studies in which organic compounds with aromatic character are studied for dispersion and stability of undoped TiO_2 nanoparticles in aqueous medium (Sentein et al., 2009), the aromatic based

compound azulene was chosen as dispersing agent.. because of its very low toxicity compared to benzene and naphthalene (Abinaya Subbaiyan, 2013).

VII.1.3 Particles size analysis in aqueous phase

VII.1.3.1 Effect of dispersing agent (AZ) on N-TiO$_2$ suspension

Particle size (PS) and particle size distribution (PSD) were measured by dynamic laser scattering (DLS) using a Nanosizer (NanoZS Malvern Instrument, UK) equipped with a He-Ne laser operating at 5.0 mW and 633 nm that measures the hydrodynamic diameter of the particles. Catalyst particles were dispersed in distilled water. DLS analysis was performed setting temperature at 25°C. The value used is Dv50 that is the median particle size based on a volumetric particle size distribution,

To determine the particle size in the range, 0.02-3000 μm, Malvern Mastersizer-S (Malvern Instruments Ltd., U. K.) light scattering was used.
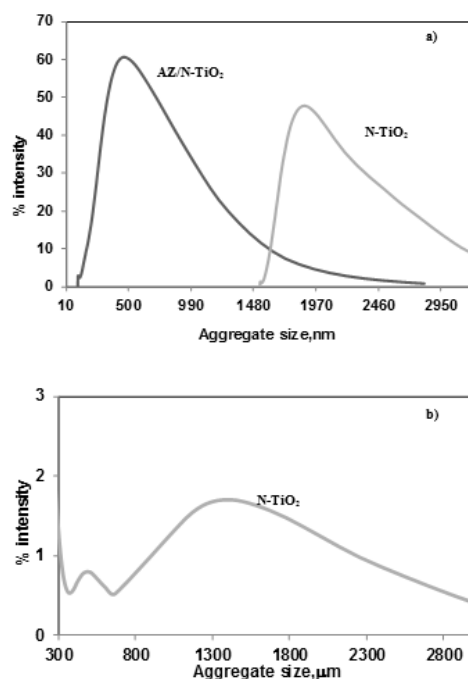
Figure 69 *a) Aggregate size distribution of N-TiO$_2$ with and without azulene in range 10-3000 nm; b) Aggregate size distribution of N-TiO$_2$ without azulene in range 300-3000 μm*

Figures 69a and 69b, respectively, show the particle size distribution of the N-TiO$_2$ suspensions with and without the dispersing agent. The particle size distribution of the TiO$_2$ nanoparticles suspension prepared without dispersing agent shows a trimodal distribution indicating that the nanoparticles generate agglomerates with size agglomerate mainly in three size ranges of approximately 1480–3000 nm (Figure 69a), 300–553 µm and 553-3000 µm (Figure 69b). When the dispersing agent was added in the aqueous solution, with a concentration of 10 mg L^{-1}, N-TiO$_2$ particle size distribution becomes monomodal (Figure 69a), ranging between 100 and 2000 nm.

This data implies that smaller fragments were sheared off from large agglomerates, and as a result, the volume of smaller aggregate increased.

VII.1.3.1.1   Effect of amount of AZ

Figure 70 shows the effect of amount of AZ on Dv50 when the amount of photocatalyst was equal to 3g L^{-1}. For all the tested AZ concentrations, aggregates size distribution was monomodal.
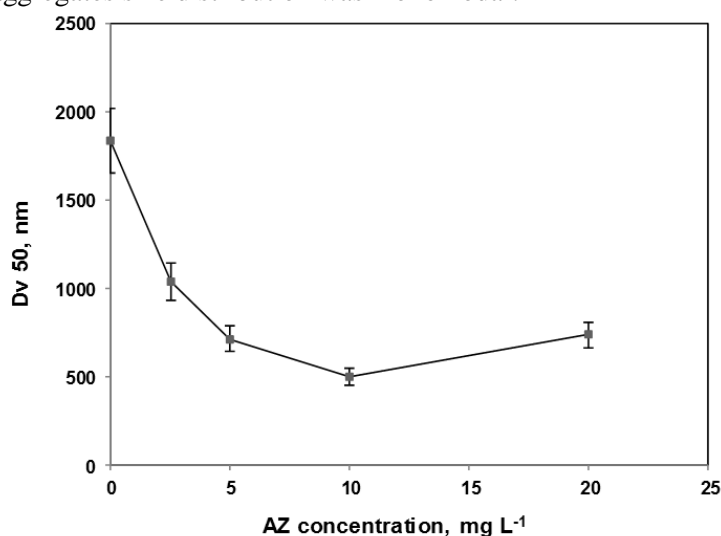
Figure 70 *Effect of concentration of AZ (2.5-20 mg L^{-1}) on the Dv 50 size of N-TiO$_2$ suspensions; N-TiO$_2$ dosage: 3g L^{-1}.*

For this reason, Dv50 parameter can represent, with a very good approximation, the average aggregates size of N-TiO$_2$ particles in aqueous medium.

It can be seen from Figure 70 that below 10 mg L^{-1}, Dv50 was relatively high (about 1042 nm at 2.5 mg L^{-1} and 717 nm at 5 mg L^{-1}), most likely due

to lack of dispersant to prevent that the nanoparticles from being agglomerated.

The amount of AZ required to produce the smallest average aggregate size (500 nm) was found to be 10 mg L^{-1}.

When the amount of dispersant was increased up to 20 mg L^{-1}, an increase in average aggregate sizes (739 nm) occurred, probably due to the agglomeration caused by the presence of AZ in solution, in a similar way that observed for other organic dispersants (Fazio et al., 2008).

VII.1.3.1.2   Effect of amount of N-TiO$_2$

Figure 71 shows the effect of amount of N-TiO$_2$ photocatalyst on Dv 50 when the concentration of AZ in aqueous solution was equal to 10 mg L^{-1}.
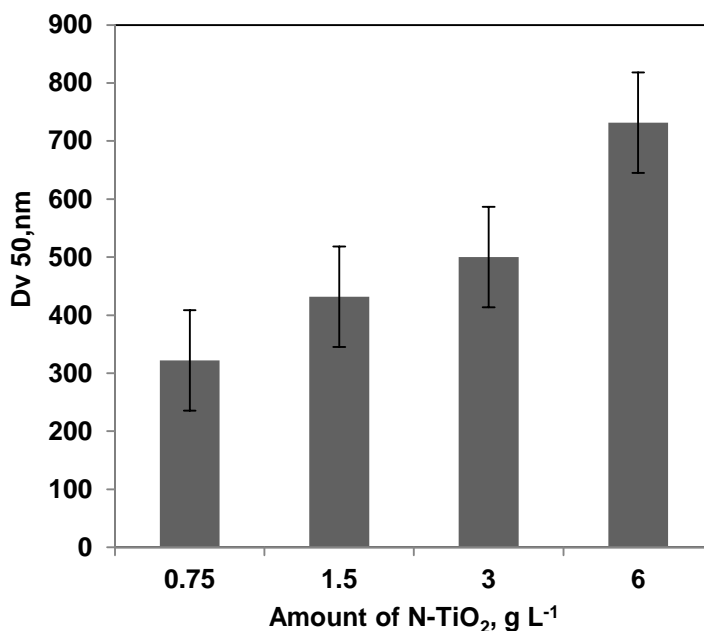
Figure 71 *Effect of amount of N-TiO$_2$ (0.75-6 g L^{-1}) on the Dv 50 size of N-TiO$_2$ suspensions in bidistilled water solution with AZ concentration of 10 mg L^{-1}.*

From 0.75 g L^{-1} up 3 g L^{-1}, Dv50 increased from 322 to 500 nm. However, between 1.5 and 3 g L^{-1}, the increase of Dv50 is not dramatically and included in the experimental error bands. On the contrary, when the amount of N-TiO$_2$ is 6 g L^{-1}, a marked increase of Dv50 (731.5 nm) was achieved.

126

VII.1.3.2 FTIR analysis

FTIR measurements were carried out by a spectrometer (Bruker IFS 66). Samples were diluted at 1 wt % in KBr.
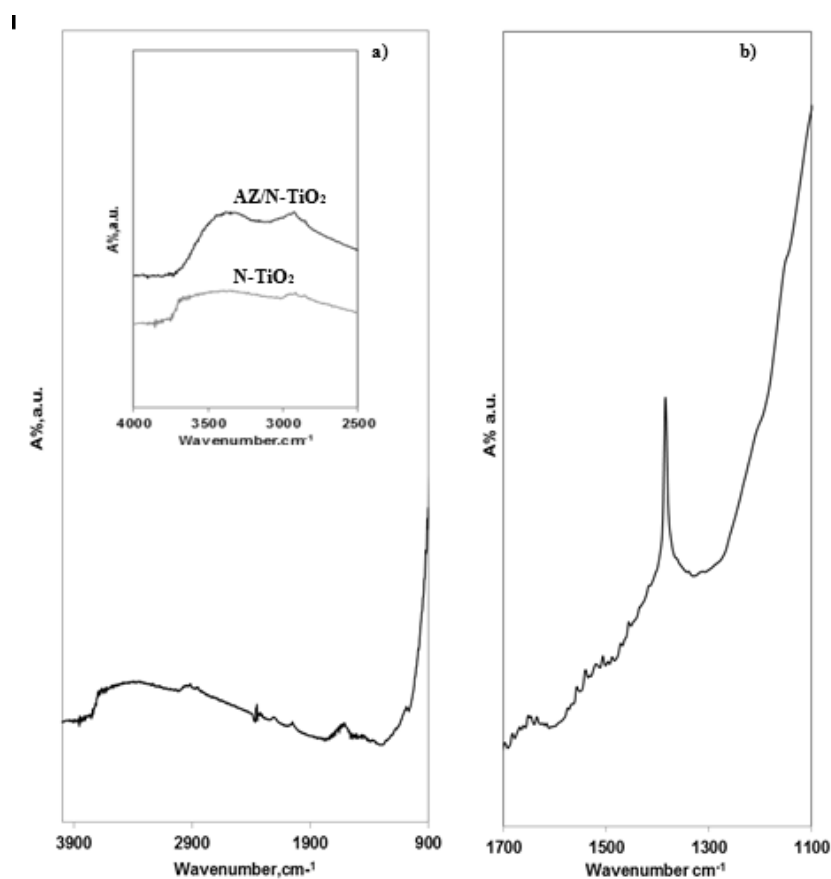
Figure 72 *a) FTIR spectra of N-TiO$_2$ b) The FTIR difference spectra of AZ/N-TiO$_2$*

The mixture was ground and a transparent disk of 100 mg was prepared with a press in vacuum. Disks are introduced into the proper chamber and the scan is carried out at room temperature. The infrared spectrum includes all the radiation of wavelengths ranging from 0.1 to 1000 µm.
FTIR analysis was done on N-TiO$_2$ nanoparticles before and after adsorption of 10 mg L^{-1} of AZ aqueous solution (AZ/N-TiO$_2$).

The FTIR spectra of N-TiO$_2$ and AZ/N-TiO$_2$ is reported Figure 72a. N-TiO$_2$ and AZ/N-TiO$_2$ showed a wide band in the range 3900-3750 cm^{-1} assigned to OH stretching of adsorbed water, and around 3769-3731 cm^{-1} due to the OH vibrations of hydroxyls group bonded to the titania in

127

different coordination to the surface as isolated, bridged and vicinal groups. Moreover a broad band around 3170 cm^{-1} is assignable to NH stretching of ammino groups. In the range 3000-2500 cm^{-1}, absorptions at 2869, 2930, 2989 cm^{-1} are typical of N-titania samples, N-TiO$_2$ evidenced moreover bands at about 2050, 2166, 2345 cm^{-1} and a composite peak which have been attributed to N atoms, both embedded into the TiO$_2$ network and present as terminal group on the titania surface (Rizzo et al., 2014). FTIR difference spectra between AZ/N-TiO$_2$ and bare N-TiO$_2$ (Figure 72b) shows bands in the ranges 1506-1568 cm^{-1} (Socrates, 2004), 1434-1488 cm^{-1} (Socrates, 2004) and at 1384 cm^{-1} (Wang et al., 2003). All these contributions are assigned to aromatic C=C ring stretching vibrations (Wang et al., 2003).In particular the signal at 1384 cm^{-1} is probably due to azulene monomer (Nie et al., 2007). The band around 1650 cm^{-1} can be assigned to the O$^{..}$C$^{..}$O stretch of bound carboxylate groups (Porel et al., 2012) while the absorptions around 1475-1440 cm^{-1} suggests the presence of aliphatic ethers, that could be confirmed by the bands at 1156 and 1190 cm^{-1}. So the formation of an interaction adsorbed AZ and N-TiO$_2$ surface could be hypothesized. The seven ring members of AZ structure open, giving rise to ester and ether bonds with the titania surface.

This interaction caused the disappearing of the OH vibrations of hydroxyls group, inasmuch as for AZ/N-TiO$_2$ sample these bands are not present (Figure 72b).

This indicates that the hydroxyls group of titania are probably involved in a bond with the oxidized form of AZ. In addition, the observation of the increase of signals at 2939 and 2977 cm^{-1}, shows the vibrations of aliphatic –CH groups while a wide and weak absorption due to the CH stretching of aromatic ring is visible. These results suggest the occurring of ring opening reaction at the highly reactive seven members ring and the formation aliphatic or partially unsaturated branches bearing carboxylic groups that may react with the hydroxyls forming ester bonds with the titania surface (Figure 73).
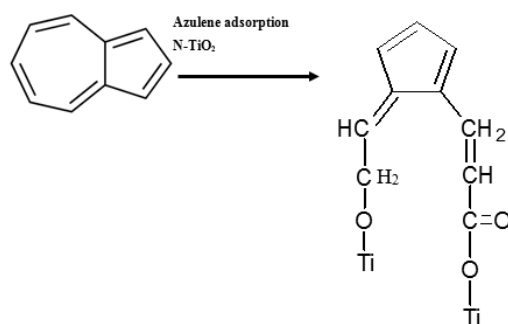
Figure 73 *Hypotesis of the interaction of azulene with N-TiO$_2$ surface*

128

VII.1.3.3 Thermogravimetric analyses

Thermogravimetric analysis (TG-DTG) of samples was carried out in air flow (100 cm^3/min STP) with a thermo balance (SDT Q600, TA Instruments) in the range 20-1000°C at 10°C min^{-1} heating rate. The thermo balance is connected online with quadrupole mass detector (Quadstar 422, Pfeiffer Vacuum). Thermogravimetric results of N-TiO$_2$ photocatalysts sample after adsorption of AZ solution at 10 mg L^{-1} (N-TiO$_2$/ AZ) are shown in Figure 74. The first step of weight loss that occurred up to about 220°C, is related to the removal of adsorbed water and to the OH$^-$ surface groups of titania (Figure 74a) (Sannino et al., 2011).
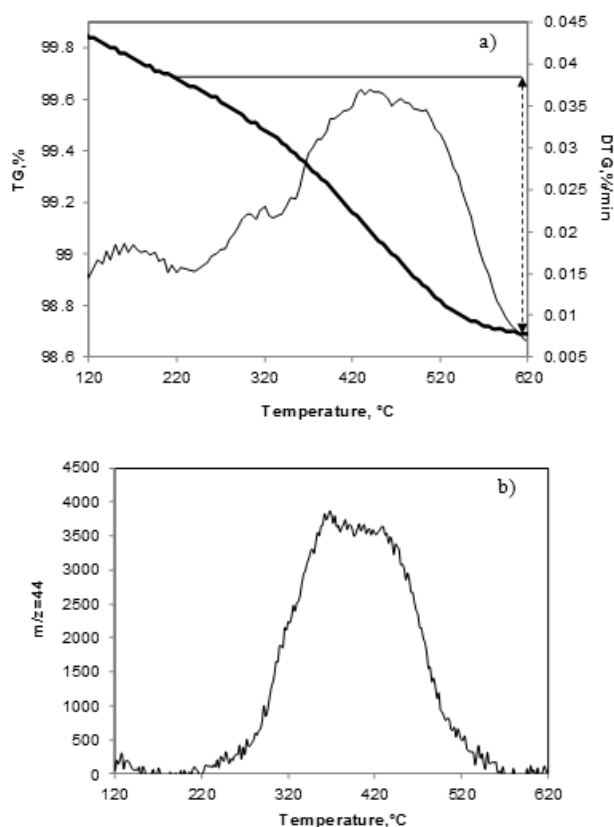
Figure 74 *a) TG analysis of AZ/N-TiO$_2$ sample; b) MS result of AZ/N-TiO$_2$ sample*

The second step that take place from 220°C up to 620°C, is due to the oxidation of AZ adsorbed on N-TiO$_2$ surface, as confirmed by the presence of the mass fragment m/z=44 associated to CO$_2$ (Figure 74b). This oxidation step occurred in a temperature range higher than sublimation temperature of

129

pure AZ (97°C). This result indicates a possible interaction between organic groups of AZ with N-TiO$_2$ surface. The amount estimable from the oxidation of AZ is about 0.03 g$_{AZ}$/g$_{N-TiO2}$.

This result indicates that, starting form 10 mg L^{-1} AZ aqueous solution and 3 g L^{-1} N-TiO$_2$ dosage, all the AZ present in solution is adsorbed on catalyst surface. Moreover, thermogravimetric results support the findings obtained from FTIR spectra (Figure 74b) confirming the interaction between AZ molecule with N-TiO$_2$ surface.

VII.1.4 Photocatalytic activity results

VII.1.4.1 Effect of AZ on MB dark adsorption

The behavior of MB adsorption in dark conditions is represented in Figure 75a for N-TiO$_2$ dispersed in aqueous solution with and without AZ.

An increase of MB amount adsorbed was observed after 5 minutes of the test and it was the same during the 30 minutes indicating that the adsorption equilibrium of dye on catalyst surface was reached. The amount of MB adsorbed on the surface of N-TiO$_2$ increases of about 14% when the dispersing agent (AZ) is present in the aqueous solution. It is important also to underline that the presence of AZ doesn't influence the adsorption kinetic of MB on the surface of N-TiO$_2$. This effect could be due to a higher affinity induced by the presence of coordinated AZ, or to an increased exposed surface area of the titania.

VII.1.4.2 Effect of dispersing agent (AZ) on photocatalytic activity

After the dark period, the solution was irradiated with visible light and the results are shown in the Figure 75b.
The MB photolysis reaction (not shown) was found at about 7% in a previous work (Sacco et al., 2012). A similar value was found also when in the aqueous solution was present AZ at a concentration of 10 mg L^{-1} Figure 75b .On the contrary, N-TiO$_2$ with and without AZ exhibited a significant photocatalytic activity under visible light irradiation. In particular after 120 minutes of visible light irradiation, MB decolorization in presence of dispersing agent (AZ) was about 80%, higher than the value (about 60%) reached without AZ. Since the aggregates size in presence of AZ was smaller that that one obtained without dispersing agent, the previous result can show the relevance of the aggregates size on both adsorption properties and in the photocatalytic activity.

130

VII.1.4.3 Effect of AZ concentration

The effect of AZ concentration using 3 g L^{-1} N-TiO$_2$ in the photocatalytic decoulorization of MB was studied.
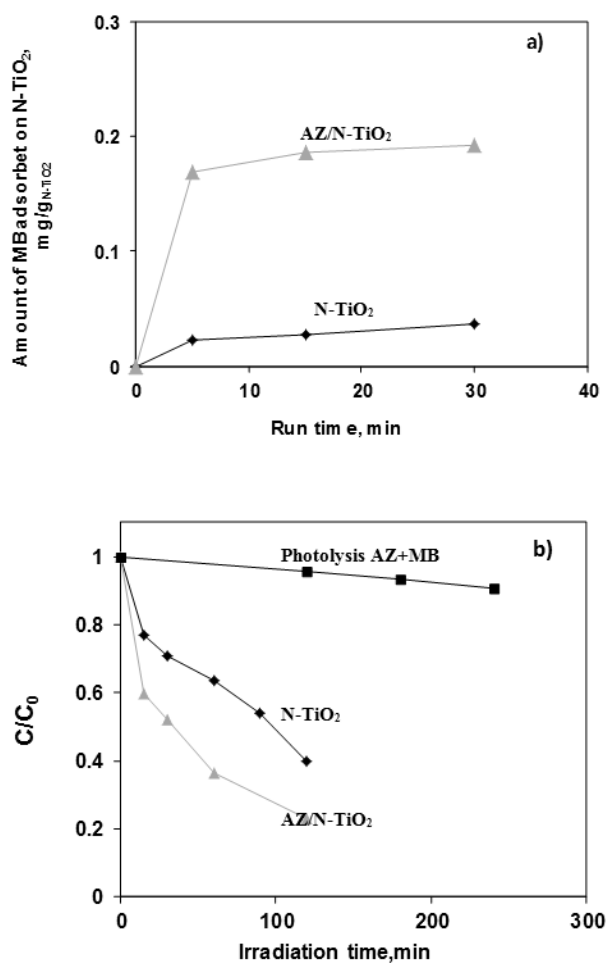
Figure 75 *a) Dark adsorption of MB on 3 g L^{-1} of N-TiO$_2$ with and without AZ; b) Photocatalytic decolourization of MB using 3g L^{-1} of N-TiO$_2$ with and without AZ and photolysis of MB in presence of AZ.*

After the dark period, the visible light was turn on and the obtained results are show in Figure 76. It was found that N-TiO$_2$ has low effectiveness in the

MB decolourization when the Dv50 was in the range 717-739 nm, obtained with an AZ concentration of 5 and 20 mg L^{-1}. On the contrary, when Dv50 was about equal to 500 nm (corresponding to an AZ concentration of 10 mg L^{-1}), N-TiO$_2$ exhibited the highest photocatalytic activity. In particular after 120 minutes of visible light irradiation, MB degradation was about 80%.

Since the similarity of Dv50 obtained when AZ concentration was equal to 5 and 20 mg L^{-1}, the very lower activity obtained in the latter case could be due to the presence to an higher residual AZ in the aqueous solution, due to the lower amount absorbable by N-TiO$_2$ surface, or to the slight higher size of the aggregates in solution. In this case AZ could act as competitive pollutant with MB leading to a lower decolourization activity. However, the amount of MB adsorbed on surface of N-TiO$_2$, when the AZ concentration is 5, 10 and 20 mg L^{-1}, is equal to 5, 5.1 and 4.9 mg$_{MB}$/g$_{N-TiO2}$ respectively. This data indicated that the presence of AZ in aqueous solution doesn't influence the MB adsorbed on N-TiO$_2$ surface. So, the aggregate size seems to play a more relevant effect on the photocatalytic activity.
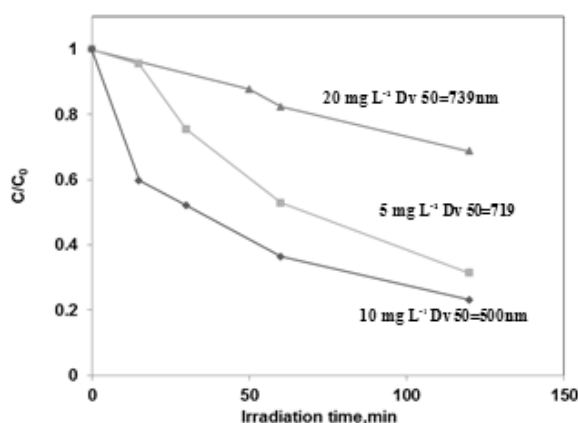
Figure 76 *Photocatalytic decolourization of MB using 3g L^{-1} of N-TiO$_2$ with different AZ concentration*

VII.1.4.4 Effect of N-TiO$_2$ catalyst amount

To study the effect of the amount of catalyst, different dosages of powder, between 0.05 and 6 g L^{-1}, were used.

The initial concentration of MB (5 mg L^{-1}) and AZ (10 mg L^{-1}) were kept the same in all these experiments. Figure 77 shows the effect of the amount of catalyst on MB decolourization in the presence of visible light. Decolourization activity increased up to 3 g L^{-1}, while for further increase of catalyst amount (6 g L^{-1}) the photocatalytic activity decreased. Since the Dv50 for 1.5 and 3 g L^{-1} is about the same (431 and 500 nm respectively) the

highest photocatalytic activity, found for 3 g L^{-1}, indicates that up to this photocatalyst loading, the overall photoactive surface of N-TiO$_2$ powders is exposed to the visible irradiation.
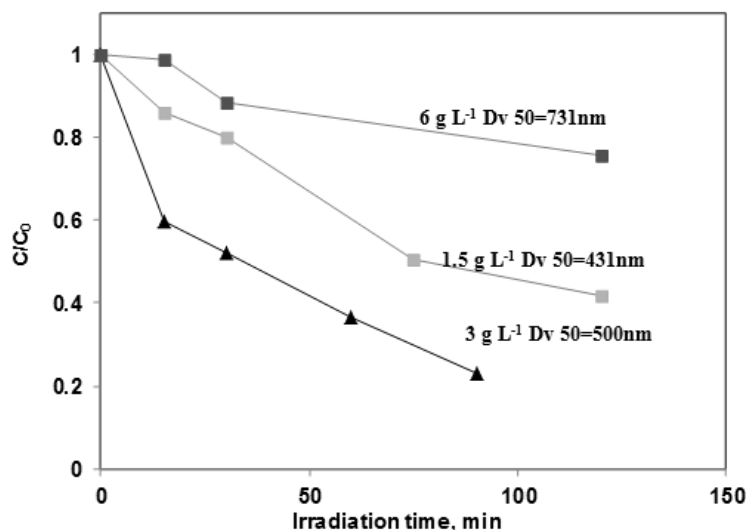
Figure 77 *Photocatalytic decolourization of MB (AZ concentration 10 mg L^{-1}) using different amount of N-TiO$_2$ (1.5 - 6g L^{-1})*

When the N-TiO$_2$ loading is increased to 6 g L^{-1}, the photocatalytic activity is influenced by not only the aggregation phenomenon, but it is also necessary to consider that with an increase of catalyst loading, in the aqueous medium, the light penetration through the solution becomes difficult (Sacco et al., 2012), causing a decrease of photocatalytic activity.

The effect of photocatalysts aggregate size on photocatalytic performances was investigated. The photoreactivity of N-TiO$_2$ catalysts was assessed in batch experiments under visible light irradiation using methylene blue as model pollutant. The control of the dispersion and aggregation of the nanoparticles resulted crucial to exploit the advantages of the nanometer-sized N-TiO$_2$ particles in photocatalytic activity. When the photocatalysts particles are suspended in bidistilled water, the aggregate distribution is trimodal with aggregates size ranging between 1480–3000 nm, 300–553 μm and 553-3000 μm, after sonication. The trend of aggregate size distribution is different if in the aqueous solution is present an organic compound acting as dispersing agent. In particular, azulene was found to yield lower size of aggregates. In this case, in fact, the range of particle distribution becomes monomodal, in particular between 100 and 2000 nm, after sonication. The different aggregate size distribution influenced the amount of MB adsorbed on catalyst surface and increased the photocatalytic activity. In particular, after 120 minutes of visible light irradiation, MB degradation in the presence

133

of dispersing agent was about 80%, relevantly higher than the value (about 50%) reached without dispersing agent.

The influence of several parameters such as catalyst dosage and dispersing agent concentration were also presented.

The optimal dispersant concentration was found to be 10 mg L^{-1} correspondent to a mean photocatalyst aggregates size is equal to 500nm.

The experimental results confirmed the relevance of N-TiO$_2$ dispersion on the photocatalytic activity, which so appears as a very relevant parameter in the photocatalytic reactions carried out in slurry reactors.

VII.2 N-doped TiO$_2$/s-PS aerogels for photocatalytic degradation

of organic dyes in wastewater under visible light irradiation

Even if the aggregation phenomena using dispeding agent are minimized, two obvious problems arise from the powder dispersion in a slurry reactor: scattering and screening of the light by structured support and the accessibility of the catalytic surface to the photons and the reactants (Murcia et al., 2013).

So, to permit the penetration of the radiation in the inner core of the photocatalyst, a promising alternative is to fix the photocatalyst on a light-transparent support (Miranda-García et al., 2010). It is essential therefore to fasten the catalyst on the support and at the same time to minimize both the phenomena of aggregation between the particles of the semiconductor, and to guarantee a high dispersion of the photocatalyst on the overall geometric surface of support.

Various substrates have been tried for supporting TiO$_2$ photocatalysts. Polymeric substrates are very promising and economics (Singh et al., 2013). Several advantages are related to the use of polymeric structured support, such as flexible nature, chemical resistance, mechanical stability, low density, high durability and easy availability. If the catalyst is dispersed in a transparent solid structure, a good dispersion could be achieved avoiding the aggregation phenomena between the particles of the semiconductor minimizing also light scattering phenomena. Among all, monolithic aerogels based on semicrystalline thermoplastic polymers (Daniel et al., 2013) offer the opportunity to be tested as economic, recyclable and easy to handle support for photocatalysts. In particular, monolithic aerogels based on thermoplastic polymers that exhibit nanoporous-crystalline phases, such as syndiotactic polystyrenes (s-PS) (Daniel et al., 2005) or poly(2,6-diphenyl-1,4-phenylene oxide) (PPO) (Longo et al., 2013), due to their high specific surface area, present very high solubility of many organic compounds and moreover, are particularly suitable to be used in combination with photocatalysts. In addition, the use of monolithic aerogels involves the

further advantage to remove the risk of contamination or inhalation of micro and nanoparticles (Shi et al., 2013).

VII.2.1. N-doped TiO$_2$ nanocomposite aerogels preparation

Nt was dispersed in chloroform at a temperature of 100°C and the dispersion was constantly under stirring. After two hours, s-PS was added to the dispersion. The mixture so obtained was sonicated for three hours, at a temperature of 80°C to prevent the polymer gelation. After cooling this dispersion, a uniform gel was achieved. The corresponding aerogels were obtained by extraction with supercritical carbon dioxide. In the final obtained sample, the s-PS/Nt weight ratio was 95/5. The final sample is named Nt-sPS (Figure 78). The obtained sample, s-PS/Nt has cylindrical shape with diameter equal to 0.6 cm and height equal to 3 cm.
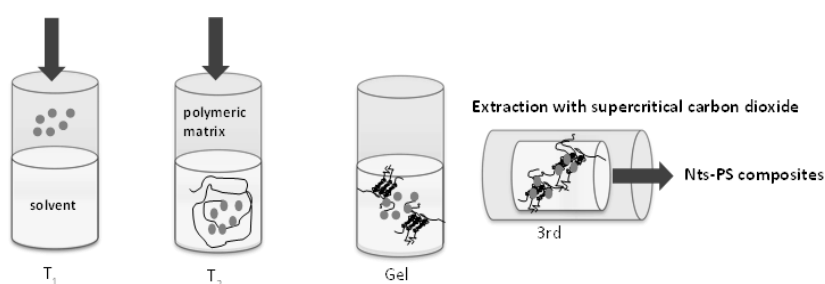
Figure 78 *Nt-sPS composites step of synthesis*

The Nt-sPS aerogels retain the cylindrical shape of the starting gel (whose solvent content is of 95 wt%) while their volume is reduced of nearly 15%, and hence present a porosity close to 80%. In this respect it is worth adding that the analogous s-PS aerogels, in the absence of nanoparticles, maintain unaltered the volume of the starting gels, with a finally porosity close to 95%.

VII.2.2 Photocatalytic activity tests

Methylene blue (MB) was used as a model dye .The experiments were carried out with initial concentration of MB equal to 7.5 ppm, at ambient temperature and pressure. In the case of Nt dispersed in the solution, a catalyst dosage of 0.13g L^{-1} was used. In the case of Nt-sPS, the amount was equal to 2.93 g L^{-1} (corresponding to a Nt dosage equal to 0.13 g L^{-1}). The total volume of MB solution was 75 mL in all the tests. The experiments were realized using a pyrex cylindrical photoreactor (I.D.= 2.5 cm;

135

height=25 cm) equipped with an air distributor device (Q_{air} =150 cm^3 min^{-1} (STP)). The continuous mixing of the wastewater was realized by external recirculation of wastewater through the use of a peristaltic pump. Thermocouple was inserted inside the reactor, to monitor the temperature during irradiation (30±2 °C). The photoreactor was irradiated with a strip composed by 25 white light LEDs (5 W nominal power; provided by NEW ORALIGHT), with wavelength emission in the range 400–800 nm (Vincenzo Vaiano, 2014) with main emission peak at 475 nm. The WL strip was positioned around and in contact to the external surface of the photoreactor (incident light intensity: 32mW cm^{-2}). The schematic picture of photoreactor is presented in a previous work [43]. The system was left in dark for 2 hours to reach MB adsorption equilibrium, and then photocatalytic reaction was initiated under visible light up to 4.5 h. The samples were analysed to determine the change of MB concentration, measured with a Perkin Elmer UV-Vis spectrophotometer at λ=663 nm. A standard calibration curve was obtained for different MB concentration, and allowed to convert absorbance to concentration (mg L^{-1}) units.

VII.2.3. Samples characterization

Laser Raman spectra were obtained at room temperature with a Dispersive MicroRaman (Invia, Renishaw), equipped with 785 nm diode-laser, in the range 100-2500 cm^{-1}. Scanning Electron Microscope (SEM) (Assing, mod. LEO 420) was used to characterize the morphology of Nt-sPS at an accelerating voltage of 20 kVThe Raman spectra of Nt and Nt-sPS are shown in Figure 79.
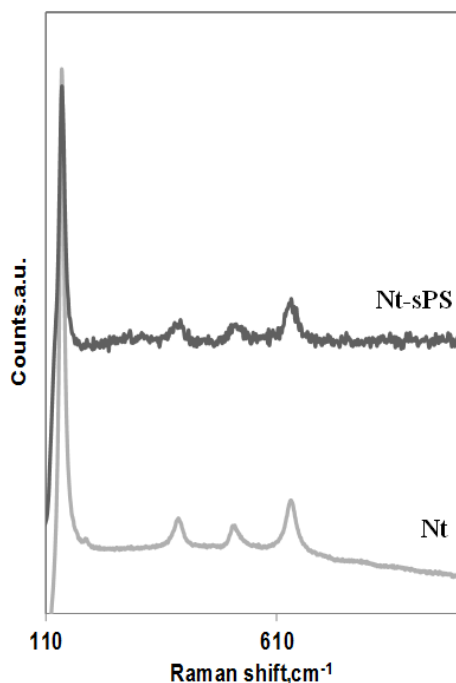
Figure 79 *Raman spectra of Nt and Nts-PS*

The Nt sample showed bands at 144, 396, 514, 637 cm^{-1} and a weak shoulder at 195 cm^{-1}, due to the Raman-active fundamental modes of anatase (Ciambelli et al., 2008). From the observation of the Raman spectra of Nt-sPS, it was clear the presence of same bands of Nt without any shift in their positions. This indicated that the dispersion of Nt inside aerogels matrix doesn't cause modification in the crystalline structure of Nt catalyst.Wide-angle X-ray diffraction (WAXD) patterns with nickel filtered Cu-Kα radiation were obtained, with an automatic Bruker D8 Advance diffractometer, in reflection. The intensities of the WAXD patterns were not corrected for polarization and Lorentz factors, to allow an easier comparison with most literature data.The X-ray diffraction pattern of Nt-sPS aerogel, as well as those of a pure s-PS aerogel and of pristine Nt are reported in Figure 80. The results obtained from X-ray diffraction analysis of Nt showed the presence of signals typical of the titanium dioxide in the anatase form. Furthermore, the average crystallites size of Nt catalyst was calculated according the Scherrer equation on diffraction plane (101) and the obtained values is 15 nm. Nt-sPS evidenced the signals typical of s-PS structure and an additional one (at about 25.3 degree) due to titanium dioxide in the anatase form.

.

137
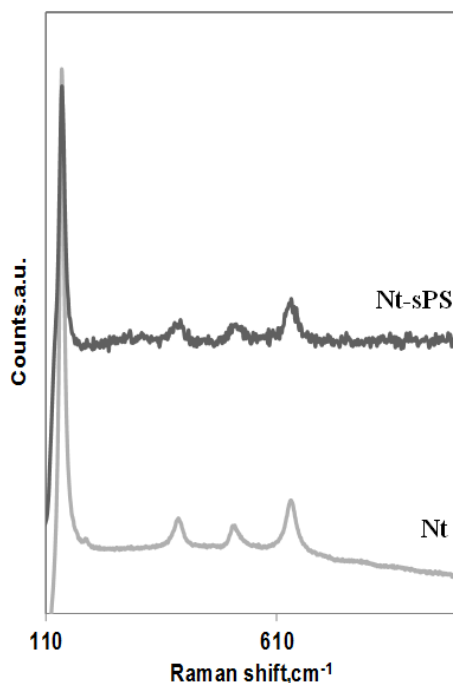
Figure 80 *XRD spectra of (a) s-PS (b) Nt-sPS and (c) Nt*

The average crystallites size of Nt remains essentially unaltered after the inclusion in the s-PS aerogel. The pattern of Nt-sPS (Figure 80b) also shows the diffraction peaks of the nanoporous delta form of s-PS (Figure 80a), whose degree of crystallinity (≈45%) is essentially not altered by the presence of the filler in the aerogel. Specific surface area of the samples (BET) was evaluated from dynamic N_2 adsorption measurement at -196 °C, performed by a Costech Sorptometer 1040 after pretreatment at 150 °C for 30 min in He flow for Nt catalyst and at room temperature overnight for s-PS and Nt-sPS .

Table 9 *BET values for Nt, s-PS and Nt-sPS*

Samples	BET (m^2g^{-1})
Nt	30
s-PS	260
Nt-sPS	222

The specific surface areas (SSA) of the samples used in the present work are reported in Table 9. For Nt sample, SSA is equal to 30 m^2g^{-1} and for s-PS is equal to 260 m^2g^{-1}. The presence of Nt in the s-PS aerogels determines a decrease of the specific surface area to a value of 222 m^2g^{-1}. The high surface areas of the s-PS aerogels is strictly depending on the nature of the polymer crystalline phase, varying from 20-40 m^2g^{-1} for the dense α, β and γ forms to 240-320 m^2g^{-1} for the nanoporous delta and epsilon forms (Daniel et al., 2009). Because the delta crystalline phase and its crystallinity remain essentially unaltered as a consequence of composite aerogel preparation, the insertion of the Nt catalysts is to be found in the pores of highest dimension and the reduction of SSA can be prevailingly attributed to the observed reduction of the overall porosity from 95% down to 80%. In fact, the amount of Nt present takes into account only of 1.5 m^2g^{-1}, evaluated from the SSA of pure Nt powders and considering its percentage in the composite aerogel. Moreover, a further confirmation that the reduction of the overall porosity is likely responsible of the decrease of SSA with respect to that one of s-PS aerogels in delta form, can be drawn from the proportional evaluation of the percentage of specific surface area exposed by the Nt-sPS aerogel, subtracted of the contribution of Nt, with respect to the s-PS aerogel alone. This calculated percentage is close to the value of 80%, so almost coincident to the value of the overall porosity found. So, the micro- and meso-pores structure remains unaltered, and the slight decrease of the specific surface area of composite Nt-sPS can be ascribed to the matrix shrinkage of the polymeric aerogel. The morphology of Nt-sPS aerogels was revealed by SEM analysis (Figure 81). The aerogels material Nt-sPS exhibited highly porous structure. However, Nt particles could not be easily distinguished from the fibrillar morphology of the polymer (Figure 81). Few small aggregates of Nt particles are observable in the same figure and the overall network appears homogeneous.
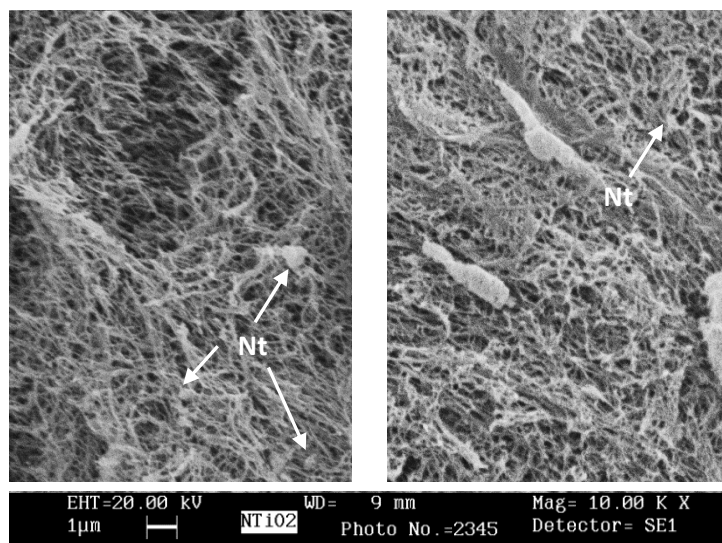
Figure 81 *SEM image of Nt-sPS aerogel*

VII.2.4 Photocatalytic activity results

VII.2.4.1 Influence of N-doped TiO_2 in polymeric structure

In Figure 82 the comparison of the photocatalytic activity obtained with the polymer sPs and Nt-sPS is shown. Firstly, it was evaluated the decolourization of MB due to the dark adsorption for 2h (Figure 82a). Both aereogels s-PS and Nt-sPS have an initial step of adsorption corresponding to 10 and 12% of MB decolourization respectively. The adsorption phenomenon, which happens in absence of visible light irradiation, is related to the very high specific surface area of s-PS and Nt-sPS samples. The slight increase of the amount of MB adsorbed for Nt-sPS with respect to s-PS is due to the presence of photocatalyst particles dispersed in the s-PS structure. After the dark period, the solution was irradiated with visible light and the reaction started to occur causing a decrease of MB concentration in liquid phase (Figure 82a). In particular, starting from the MB level reached after equilibrium adsorption, under visible light irradiation (Figure 82b), s-PS aereogels were only slightly effective for MB decolourization, leading to a C/C_0 reduction of about 8%, a value similar to that one obtained with photolysis reaction (7%).

140
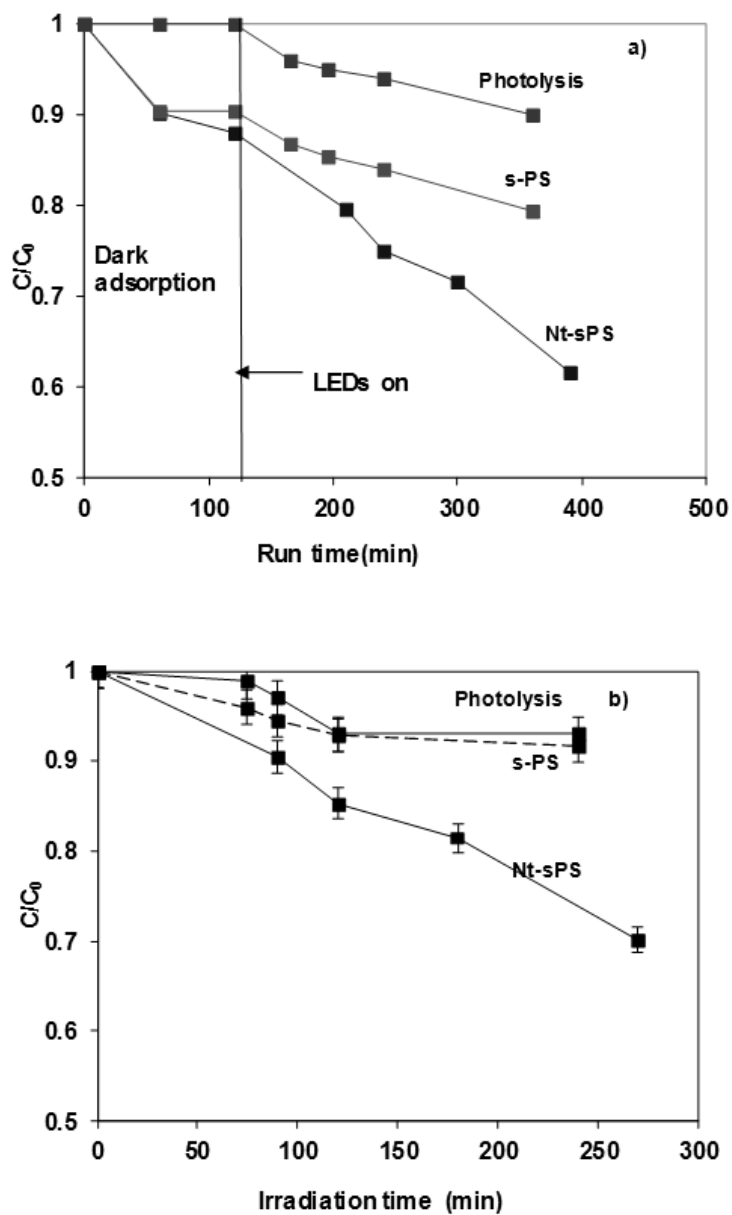
Figure 82 *Comparison between the photocatalytic activity of s-PS aerogel and the photocatalyst dispersed in the polymeric substrate (Nt-sPS) as a function of run time (a) and as a function of irradiation time (b)*

This is further confirmed by the similarity of the slopes of irradiated curves of photolysis and in the presence of s-PS, that clearly suggests that on s-PS the combination of MB adsorption and photolysis occurs. On the contrary, Nt-sPS sample exhibited higher photocatalytic activity under visible light irradiation up to a conversion of 30 % after 270 min of irradiation. This data indicates that the photocatalytic activity is exclusively promoted by the presence of Nt catalyst dispersed in the polymeric matrix.

VII.2.4.2 Comparison between Nt and Nt-sPS

Figure 83 shows the comparison between the photocatalytic activities of Nt dispersed as powder in the solution and structured Nt-sPS.
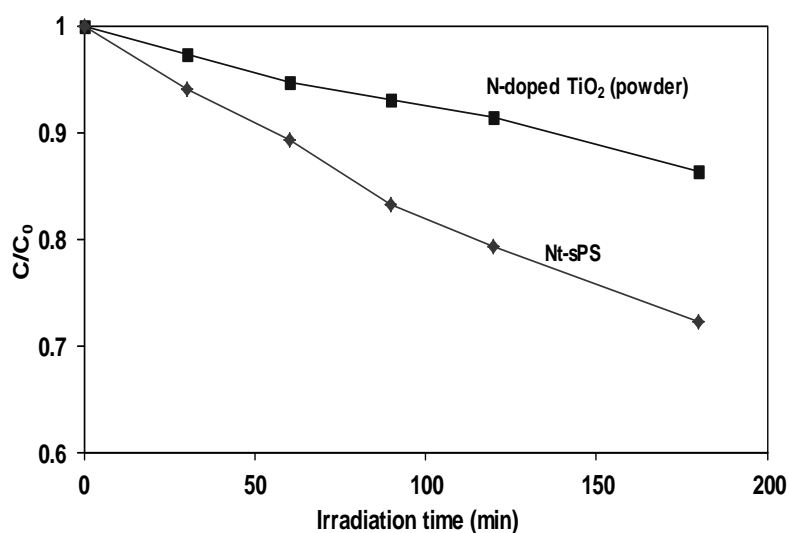
Figure 83 *Comparison of photocatalytic activity of structured photocatalyst (Nt-sPS) with respect to powdered catalyst*

Nt dispersed in the solution lead to a MB decolourization of 16 % after 180 minutes of illumination.The photoactivity of Nt-sPS sample has been increased surprisingly up to a conversion of 30% after 180 min of illumination. This unexpected behavior can be understood if it's considered preliminarily the main parameters that influence the titania based photocatalyst performances in the aqueous phase.It can be guessed that, in a slurry photoreactor, the photoactivity depends on the catalysts particle size, which is not referred to the size of the primary nanoparticles, instead have to be attributed to the size of aggregates of titania nanoparticles, that occur between the primary crystallites owing to electrostatic and hydrogen bonding interactions among the functional groups present at the external surface. This may strongly influences the ability of system in decolourization of MB. In

fact, it could be stressed that, apart from the main characteristics, such as specific surface area of titania, surface characteristics and pollutant concentration, the aggregates size can play an important role. This aspect has been investigated in our previous papers (Rizzo et al., 2013b; Sacco et al., 2012). Accordingly, the increase in decolourization ability observed for Nt-sPs could be due to sizes of Nt aggregates in the aerogels being smaller than in the water dispersions. This last hypothesis is confirmed by the following relationship (Daniel et al., 2009) between the reaction rate and particle sizes of photocatalysts.

$$r_{30} = -0.114 \cdot \ln(D) + 0.652 \qquad\qquad \text{Eq. 42}$$

Where :

r_{30} = reaction rate after 30 minute of irradiation, mg L^{-1} min^{-1}

D=aggregate size, μm

Known the MB decolourization rate after 30 minutes of irradiation for Nt and Nt-sPS, it was found that the ratio between the aggregates size of Nt powder suspended in aqueous solution and aggregates size of Nt dispersed in the s-Ps aerogel was equal to about 7.Consequently, the role of the aerogel structure is also to minimize the aggregation phenomena between the particles of the semiconductor and then, promoting the activity of MB decolourization with respect the same photocatalysts dispersed in powder form in reaction medium.

VII.2.4.3 Influence of MB initial concentration

The effect of MB initial concentration on the photocatalytic activity was checked and the results are shown in Figure 84. After 2h of dark adsorption, the photocatalytic tests started. Increasing the MB initial concentration, the adsorbed amount was increased, leading to a decolourization of MB of 12% with an initial concentration equal to 7.5ppm and 39% with an initial concentration of 15 ppm. The adsorption of MB presents a strong dependency on dye initial concentration. The reason that an increase of the initial concentration led to increase the amount absorbed is attributed to the enhancement of the driving forces (concentration gradient) with the increase in the initial dye concentration. After 270 and 290 minutes of irradiation, the final value of MB decolourization was 39% with an initial concentration equal to 7.5 ppm and 56 % with an initial concentration of 15 ppm.
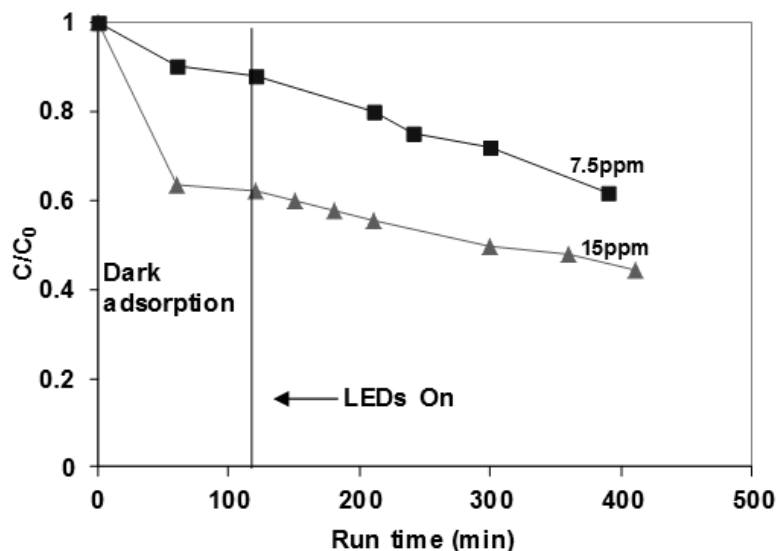
Figure 84 *Evaluation of solution decolourization with different initial MB concentration.*

VII.2.4.4 Influence of surface-volume ratio

To verify the homogeneous dispersion of catalyst inside the aerogel, the influence of the surface-volume ratio (S/V) exposed to the irradiation was also evaluated according to Eq. 43.

$$\frac{S}{V} = \frac{2 \cdot \pi \cdot r \cdot H + 2n \cdot \pi \cdot r^2}{\pi \cdot r^2 \cdot H}$$
Eq.43

S= lateral surface of Nt-sPS, cm^2

V=volume of Nt-sPS, cm^3

n= number of Nt-sPS in cylindrical shape

H= height of Nt-sPS, cm

r = radius of Nt-sPS, cm

For evaluating this influence, the initial cylindrical shape was cut in two different cylindrical pieces having a diameter and a height equal to 0.6 and 1.5 cm. Figure 84 shows that by increasing S/V ratio, photocatalytic activity increases, reaching a higher final conversion (35 %) with S/V ratio equal to 9.3 cm^{-1}.The obtained result confirms that Nt particles were dispersed also inside the core of cylindrical shape.
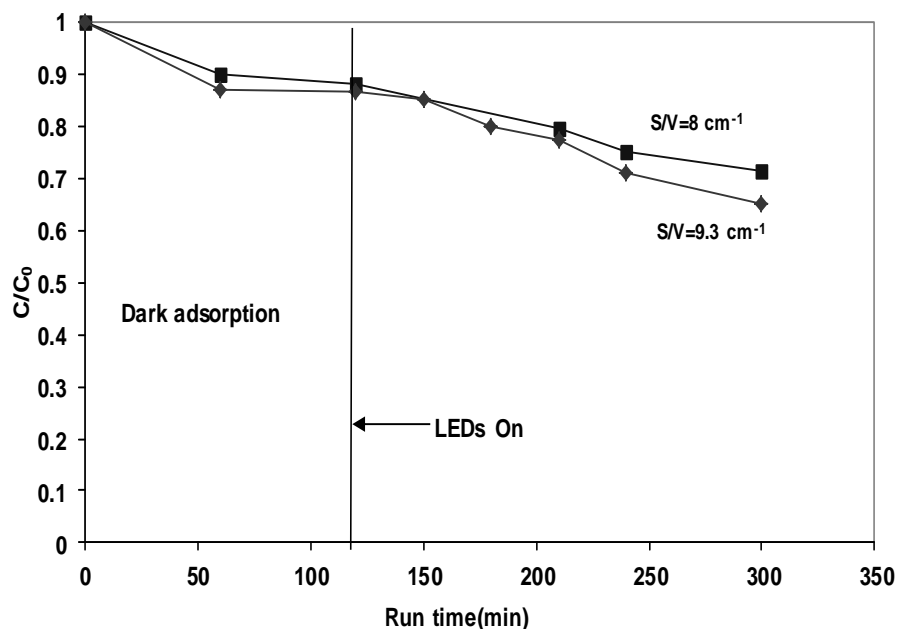
Figure 85 *Influence of different surface-volume ratio (S/V) on photocatalytic activity*

VII.2.4.5 Nt-sPS stability

With the aim to investigate Nt-sPS stability, photocatalytic performance of the five recycle is studied with the same sample and experimental conditions. From the Figure 86, it can be seen that the MB decolourization of the second and fifth time is about 63% and 68% respectively after 180 minutes of irradiation. Compared the second time and fifth time, the decolurization rate decreases by 3% indicating that photocatalytic rate of Nt-sPS doesn't declines dramatically with the recycle numbers increase. Finally the photocatalytic stability of Nt-sPS was evaluated subjecting the sample to a cycle of 500 hours of visible irradiation and monitoring the weight change of the sample over time. There were no variations of the sample weight, indicating that the polymeric support has a high stability in the presence of the photocatalyst Nt-sPS dispersed therein.
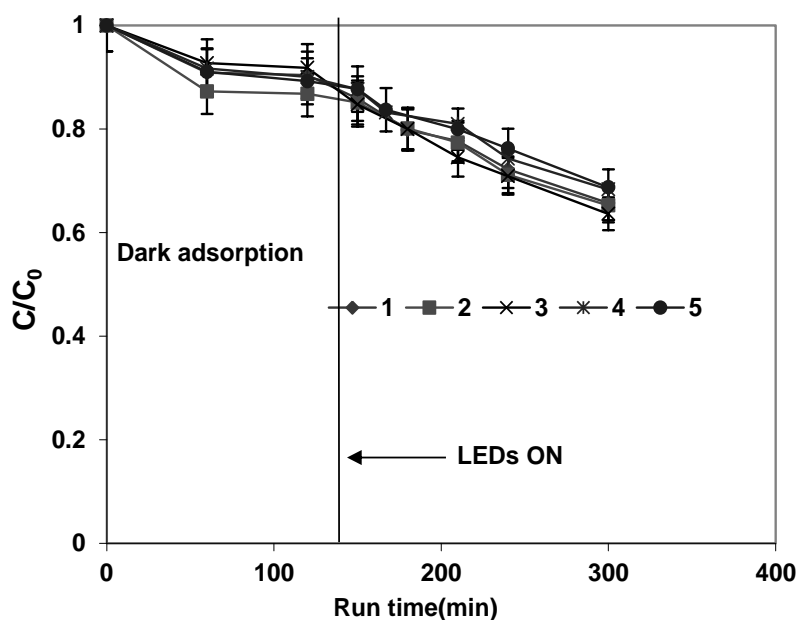
Figure 86 *Evaluation of MB decolourization performances obtained on Nt-sPS after 5 recycling experiments.*

The modified TiO_2 photocatalyst (N-doped TiO_2), highly effective in visible light, was successfully dispersed in polymer aereogels s-PS. The efficiency of structured photocatalyst was evaluated in the degradation of a recalcitrant contaminant like methylene blue from wastewater in different operating conditions. It was verified, not only the successful structuring of the visible light absorbing TiO_2, but also further beneficial effects. In particular, the advantages of dispersing the photocatalyst in the polymeric structure is the minimization of the aggregation degree between the particles of N-doped TiO_2 and minimization of light scattering phenomena because of the transparence to radiation of s-PS aereogels. These features increased the photocatalytic activity of the N-doped TiO_2 under visible light irradiation in comparison with the powder sample dispersed in solution.

VII.3 Increasing the photoactivity of N-doped TiO$_2$ photocatalysts using phosphors as light carriers

The practical applications of the photocatalytic process are greatly hindered by the insufficient quantum efficiency of photocatalytic reactions which result from the relatively high recombination rate of photogenerated electron (e$^-$)–hole (h$^+$) pairs. Therefore, the major challenge in this area is to improve the photoactivity by minimizing the charge recombination. For this purpose, a variety of strategies have been utilized to promote the photoinduced charge carrier separation (Labiadh et al., 2014). This can be achieved by coupling TiO$_2$ with another semiconductor (Kim et al., 2009). Once both semiconductors are excited by light, e$^-$ accumulate at the low lying conduction band of one semiconductor while h$^+$ accumulate at the valence band of the other material. These processes of charge separation are very fast and the efficiency of reduction or oxidation of the adsorbed organics remarkably increases (Labiadh et al., 2014). TiO$_2$/CdS (Huang et al., 2011), TiO$_2$/CdSe (Harris and Kamat, 2009), TiO$_2$/PbS (Ma et al., 2011), TiO$_2$/PbSe (Acharya et al., 2009) or TiO$_2$/Cu-doped ZnS (Labiadh et al., 2014) heterojunctions have been widely studied in recent years in the photocatalytic removal of contaminants. In the case of TiO$_2$/Cu-doped ZnS, the enhanced photocatalytic activity is attributed to the ability of Cu-doped ZnS to generate hydroxyl radicals once associated to TiO$_2$ (Labiadh et al., 2014).

In addition, the photocatalytic reaction rate can be enhanced by doping TiO$_2$ with some metal and non-metal elements (Antoniadou et al., 2013; Han et al., 2011; Rizzo et al., 2013b; Sacco et al., 2012; Sannino et al., 2013d; Vaiano et al., 2014a; Vaiano et al., 2014b), increasing the specific surface area (Sato, 1986), and improving photocatalytic reactor design (Palma et al., 2010a; Vaiano et al., 2014e). The key parameter is the photon distribution inside the reactor that should be uniform to effectively irradiate the photocatalysts (Palma et al., 2010a; Sannino et al., 2013a; Sannino et al., 2013b). Sannino et al. (Ciambelli et al., 2011b; Sannino et al., 2013a) reported a significant improvement of VO$_x$/TiO$_2$ photocatalytic activity in the selective partial oxidation of ethanol to acetaldehyde by the simultaneous irradiation with light emitting phosphorescent particles (phosphors) and UVA-LEDs as external light source.

VII.3.1 Preparation of N-doped TiO$_2$ supported on phosphors

Reagents used for the preparation of the photocatalysts are: titanium (IV) isopropoxide (TTIP, >97 wt %, Sigma Aldrich), ammonia aqueous solutions

147

(30 wt %), and blue phosphors (provided by DB-Chemic, model RL-UV-B-Y, excitation wavelength: 365 nm, emission wavelength: 440 nm). The crystal structure of blue phosphors is zinc sulphide (ZnS), which emits visible light when activated with UV light (Ciambelli et al., 2011b; Sannino et al., 2013a).

TTIP and ammonia were used as $N\text{-}TiO_2$ precursors. $N\text{-}TiO_2/ZSP$ samples were prepared by sol-gel method starting from 5 g of ZSP dispersed in a volume of TTIP ranging from 3 to 17 mL and with the addition of a volume of ammonia aqueous solution at 30 wt% in a way to have a molar ratio N/Ti equal to 18.6 (Sacco et al., 2012). The addition of ammonia aqueous solution was carried out at 0 °C, and the temperature was kept at 0°C while the solution was stirred vigorously, leading to the formation of a white precipitate. The precipitate was washed with water and then centrifuged. Finally, the obtained powders were heated in air up to 450 °C and maintained at this temperature for 30 min.

Table 10 *Crystallite size, SSA(BET) and optical band gap energy of ZSP, N-TiO₂, 15N-TiO₂/ZSP 30N-TiO₂/ZSP and 50N-TiO₂/ZSP photocatalyst*

Catalyst	Nominal TiO_2 amount (wt%)	TiO_2 average crystallites size (1 0 1) (nm)	S.S.A (m^2/g)	Optical band gap energy (eV)
ZSP	0	-	0.1	3.1
$N\text{-}TiO_2$	100	17	30	2.5
15 N-TiO_2/ZSP	15	9	15	3.0
30 N-TiO_2/ZSP	30	11	22	2.9
50 N-TiO_2/ZSP	50	13	29	2.6

The nominal content of $N\text{-}TiO_2$ on ZSP surface was varied in the range of 15-50 wt% to determine an optimal loading of $N\text{-}TiO_2$. The types of photocatalysts synthesized in this study and their properties are reported in Table 10. The Brunauer, Emmett and Teller (BET) surface area of the samples was measured from dynamic N_2 adsorption measurement at -196 °C, performed by a Costech Sorptometer 1042 after pretreatment at 150 °C for 30 min in He flow. XRD measurements were carried out using an X-ray micro diffractometer Rigaku D-max-RAPID, using Cu-K radiation. Raman spectra were obtained at room temperature with a Dispersive MicroRaman (Invia, Renishaw) equipped with 514 nm diode-laser in the range of 100-2500 cm^{-1} Raman shift. The morphology and particle size were examined

using a scanning electron microscope (SEM, Philips XL 30 ESEM-FEG). In addition, energy dispersive X-ray spectroscopy (EDX) installed in ESEM was employed to observe the Ti, Zn and S distribution on the catalysts surface. A JEM-2010F (JEOL) transmission electron microscope (TEM) with field emission gun at 200 kV was used to obtain information on particle size and particle structure.

VII.3.1.1 Light absorption

The synthesized catalysts were characterized by several techniques. UV–vis reflectance spectra of the catalysts were recorded by a Perkin-Elmer spectrophotometer Lambda 35 using a RSA-PE-20 reflectance spectroscopy accessory (Labsphere Inc., North Sutton, NH). All spectra were obtained using an $8°$ sample positioning holder, giving total reflectance relative to a calibrated standard SRS-010-99 (Labsphere Inc., North Sutton, NH). The optical band-gap of each catalyst sample was determined by plotting $[F(R_\infty)*h\nu]^2$ ($F(R_\infty)$) vs $h\nu$ (eV) and calculating the x intercept of a line passing through $0.5 < F(R_\infty) < 0.8$. As reported in literature, the determination of the band gap from the measurement of the diffuse reflectance of a powder sample is a standard technique (Karvaly and Hevesi, 1971). The disk of powder sample has to be sufficiently thick that all the light that reaches the powder sample is absorbed or scattered before reaching the back surface of the sample; typically a thickness of 1-3 mm is required.

UV-vis reflectance spectra of the photocatalysts (Figure 87a) showed that the absorption onset shifted from about 410 nm (for ZSP alone) to 480 nm (for unsupported N-TiO$_2$). The data obtained from UV-vis reflectance spectra were used for evaluating the optical band-gap energy of ZSP and N-TiO$_2$/ZSP by plotting $[F(R\infty) \times h\nu]^2$ vs $h\nu$ (Figure 87b). As shown in Fig. 1b, the increase of N-TiO$_2$ loading resulted in a decrease of optical band-gap from 3.1 (band-gap of ZPS) to 2.6 eV (which is an unexpected value for undoped TiO$_2$). Unsupported N-TiO$_2$ was characterized in our previous works (Rizzo et al., 2013b; Sacco et al., 2012; Sannino et al., 2013d). In particular, the optical band-gap was 2.5 eV. This value of optical band-gap is in agreement with other studies (Franco et al., 2012; Guo et al., 2011).

The change in optical band-gap is therefore attributed to the presence of N-TiO$_2$ on ZSP surface, confirming the ability of photocatalysts to absorb visible light. These results are reported in Table 10. It is interesting to note that the comparison of optical band-gap evaluation for similar materials have to be performed in the same range of $h\nu$. However, when two semiconductors with specific optical band-gaps are present, the evaluation could be performed in different $h\nu$ ranges. In particular, for the 30N-TiO$_2$/ZSP, the optical band-gap value in the common range $(0.5 < F(R\infty) < 0.8)$ is equal to 2.9 eV, very near to the optical band-gap of ZnS. While, changing the range $(0.015 < F(R\infty) < 0.026)$, the obtained values are close to

the optical band-gap value of N-TiO_2. These results show an additive effect of the two specific band edges on the core–shell catalyst. In the case of 15N-TiO_2/ZSP and 50N-TiO_2/ZSP catalysts, this effect could not be observed, due to the prevalence of the absorption of the phosphors support in the case of 15N-TiO_2/ZSP, and due to the prevalence of N-TiO_2 absorption in the case of 50N-TiO_2/ZSP.
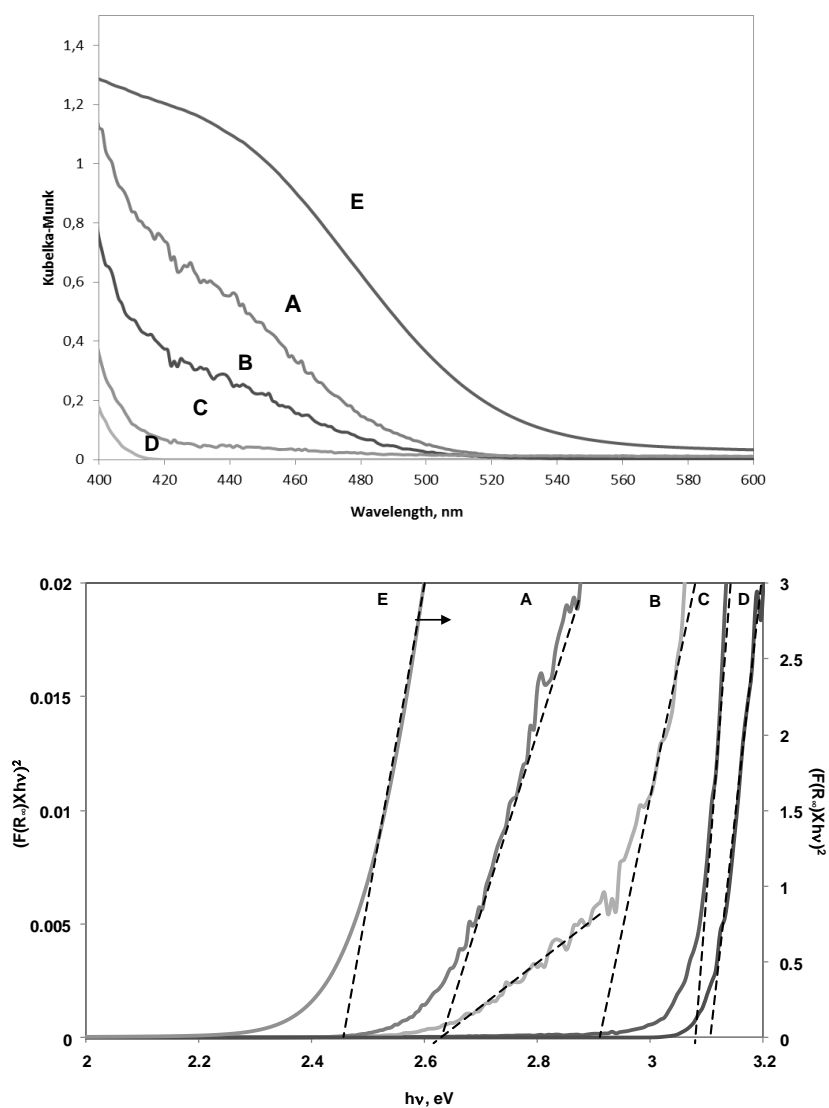
Figure 87 *UV-VIS DRS spectra (a) and band gap calculation (b) for A) 50N-TiO_2/ZSP, B) 30N-TiO_2/ZSP, C) 15N-TiO_2/ZSP, D) ZSP and E) N-TiO_2 photocatalyst.*

150

VII.3.1.2 XRD measurements

The crystal phases of N-TiO$_2$/ZSP catalysts were determined by XRD analysis (Figure 88). From the XRD spectra and the corresponding characteristic 2θ values of N-TiO$_2$/ZSP samples ((Figure 88a) and by comparing them with the spectra of bare ZnS-based phosphors and unsupported N-TiO$_2$ powder (Figure 88b), an anatase-TiO$_2$ peak is observed at about 25.5° for all N-TiO$_2$/ZSP catalysts. Moreover ZnS-based phosphors have not undergone changes of its initial cubic face centered crystallographic structure after deposition of N-TiO$_2$ (Sannino et al., 2013a).
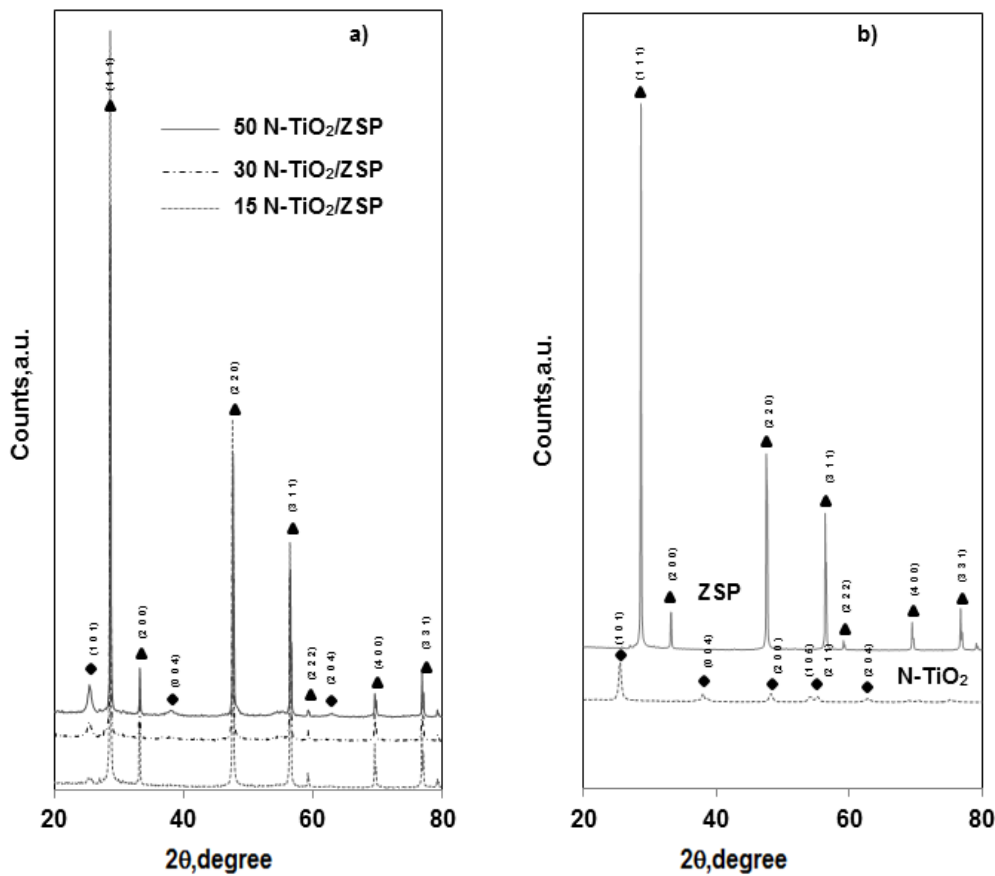
Figure 88 *a) XRD patterns of 15 N-TiO$_2$/ZSP; 30 N-TiO$_2$/ZSP; 50 N-TiO$_2$/ZSP samples; b) XRD patterns spectra of ZSP and N-TiO$_2$ samples. Legend:triangle=ZSP (Sphalerite cubic phase); diamond= N-TiO$_2$ (anatase)*

It is also possible to observe that with the increase of $N\text{-}TiO_2$ loading from 15 to 50 wt%, the intensity of the diffraction peak corresponding to anatase phase also increased.

The average size of $N\text{-}TiO_2$ crystallites in the pure powder and when supported on ZSP was calculated using the Scherrer equation on diffraction plane (1 0 1). The obtained results are reported in Table 10. The $N\text{-}TiO_2$ average crystallite size was 17 nm, according to previous characterized values (Sacco et al., 2012). On $N\text{-}TiO_2/ZnS$, the crystallite size was found smaller, with the primary particle size ranging between 9 to 13 nm. In particular, the size of the primary nanocrystallites increased with the increase of $N\text{-}TiO_2$ loading on ZSP surface. The size of crystallites of $N\text{-}TiO_2$ in the $N\text{-}TiO_2/ZnS$ composite prepared with the sol-gel method is in agreement with experimental results reported in the literature where for similar $ZnS–TiO_2$ composite the average crystallite size of TiO_2 in the $ZnS–TiO_2$ composite was lower than that of bare TiO_2 (Sannino et al., 2013d). These results could underline the influence of support on the crystalline arrangement of $N\text{-}TiO_2$.

VII.3.1.3 BET surface area measurements

The specific surface areas (SSAs) of all the samples analyzed by BET method are reported in Table 10. The SSAs of $N\text{-}TiO_2$ catalyst and bare ZSP sample were very different, being 30 and 0.1 $m^2\ g^{-1}$, respectively. It is interesting to note that the SSA of $N\text{-}TiO_2/ZSP$ samples increased by increasing the $N\text{-}TiO_2$ loading on the surface of ZSP. Thus, since ZSP has a specific surface area of about 0.1 $m^2\,g^{-1}$, the increase of SSA is attributed to the progressive increase of $N\text{-}TiO_2$ amount on ZSP surface. Since the pure $N\text{-}TiO_2$ powder has a specific surface area of 30 $m^2 g^{-1}$ and a crystallite size of 17 nm, and only the 50 % of the composite sample is $N\text{-}TiO_2$, the specific surface area should be attributed to the preparation method that leads to smaller size $N\text{-}TiO_2$ primary nanoparticles, as shown in Table 10.

VII.3.1.4 Raman spectra

Raman spectroscopy is an effective method to study the structure of $N\text{-}TiO_2/ZSP$ materials because it is extremely sensitive to crystalline phases of TiO_2 owing to its strong scattering properties (Gao et al., 1998; Yu et al., 2006). Figure 89 shows the Raman spectra of $N\text{-}TiO_2/ZSP$ Figure 89a in comparison with the spectrum of unsupported $N\text{-}TiO_2$ and bare ZSP Figure 89b. The spectrum of bare ZSP displayed a strong signal at 352 cm^{-1} and less intense bands at 182, 220, 404, 425, 456, 619, 643, and 674 cm^{-1} due to the Raman active fundamental modes of ZnS (Nilsen, 1969).

152

15N-TiO$_2$/ZSP, 30N-TiO$_2$/ZSP and 50N-TiO$_2$/ZSP samples showed bands at 144, 396, 514, 637 (Figure 89) and a weak shoulder at 195 cm^{-1} due to the Raman-active fundamental modes of anatase (Alemany et al., 1995). From the observation of the Raman spectra of N-TiO$_2$/ZSP samples, it was clear that the band of ZSP at 350 cm^{-1} decreased with the increase of titania loading, indicating a progressive coverage of phosphors surface by N-TiO$_2$. This latter issue can be investigated using the method proposed by Quincy et al. (Quincy et al., 1987). In Figure 90 the ratios (R) between the maximum intensity of the ZSP peaks at about 350 cm^{-1} and the maximum intensity of titania peak at 144 cm^{-1} are reported. The R value decreased with increasing the loading of N-TiO$_2$ in the range of 15-30 wt% on the surface of ZSP. For 50N-TiO$_2$/ZSP, R was about zero indicating that almost complete coverage of ZSP surface was achieved. This result was confirmed by the value of SSA for the same sample which was about 30 m^2 g^{-1}. This value was very close to that of the N-TiO$_2$ itself with small crystallites size, as previously underlined.
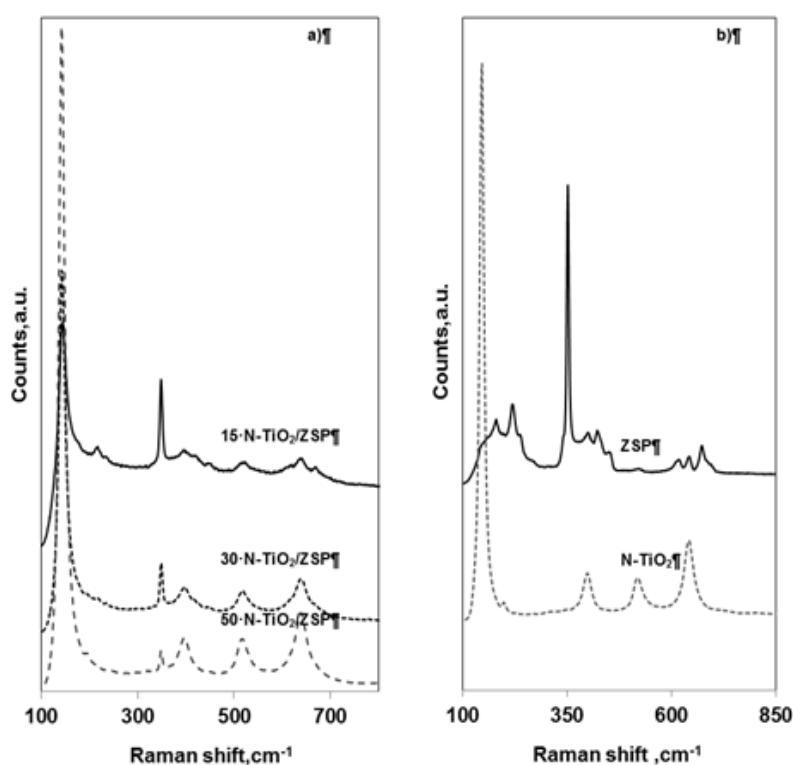
Figure 89 *a) Raman spectra of 15 N-TiO$_2$/ZSP; 30 N-TiO$_2$/ZSP; 50 N-TiO$_2$/ZSP samples ; b) Raman spectra of ZSP and N-TiO$_2$ samples*
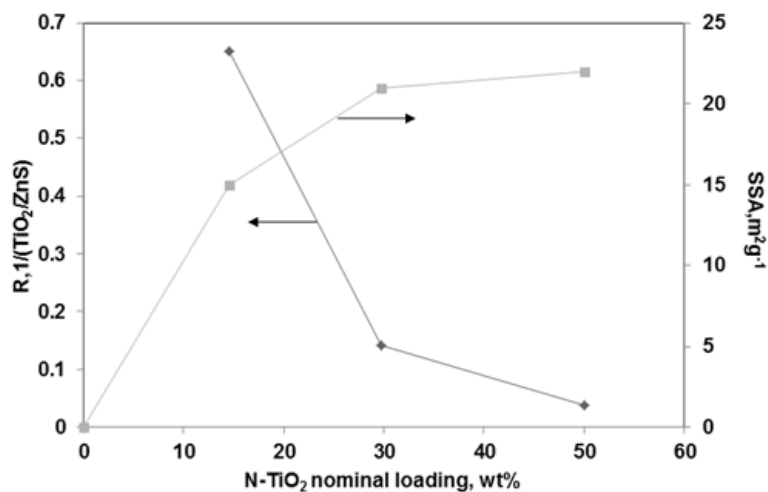
Figure 90 *Ratio between the maximum intensity of the phosphors peaks at about 350 cm^{-1} and the maximum intensity of titania peak at 144 cm^{-1} and SSA (BET) trend function of N-TiO$_2$ nominal loading*

VII.3.1.5 SEM/EDX

Figure 90 shows the low-magnification SEM image of ZSP particles and of N-TiO$_2$/ZSP catalysts. The morphology of ZSP (Figure 91a) was for most of the particles approximately spherical, or pseudo-cubical, with an average diameter of 5 μm. A smooth exposed surface of ZSP can be observed in the image. All composite samples show a similar morphology, but with an increased roughness on the surface which is attributed to the deposition of the N-TiO$_2$ on the surface. In the picture (Figure 90) isles of nanoparticles of N-TiO$_2$ are visible in some parts. From these observations it could be concluded that N-TiO$_2$ particles were rather uniformly deposited on the surface of micro-size ZSP (Figure 90).

The atomic composition was analyzed by EDX (Figure 92). For ZSP, it was confirmed that Zn and S were the prevalent elements with a Zn:S atomic ratio of 51:48. The molar ratio of Zn and S obtained from EDX analysis showed that S was less than Zn, but however close to the stoichiometric ratio in ZnS. In the case of N-TiO$_2$/ZSP samples, the amount of Zn and S decreased while the amount of Ti increased at higher loading of N-TiO$_2$ on the surface of ZSP as shown in Figure 93.

VII.3.1.6 TEM

To further characterize the nature of the N-TiO$_2$ supported on the surface of ZSP, TEM analysis was performed. TEM images with resolution of 5 μm are reported in Figure 92 a,b,c,d. The ZSP particles appear black due to their size (Figure 92a). When N-TiO$_2$ is present on ZSP surface, a thin layer of nanoparticles can be observed (Figure 91b,c,d) and it was evidenced by a yellow color. When N-TiO$_2$ was deposited on the surface of ZSP, a uniform coverage with small agglomerate was formed for the sample 15N-TiO$_2$/ZSP (Figure 92b). The nanoparticles seem to be well dispersed on the ZPS surface, and the thickness clearly increases passing from 15 to 30 wt. % of N-TiO$_2$ supported. For 50N-TiO$_2$/ZPS composite, it is not easy to observe the thickness of the layer, probably due to its high compactness. However, due to the high amount of N-TiO$_2$, some ZPS particles appear to possess a certain adherence. Moreover, it is possible to observe the formation of N-TiO$_2$ nanoparticles islands for the sample 50N-TiO$_2$/ZSP (Figure 92 d).

Figure 92 also shows TEM images with a higher resolution, 50 nm (Figure 92 e, f, g, h). In this case, it is interesting to observe that the pseudo spherical crystallites of unsupported N-TiO$_2$ (Figure 92 e) do not change when supported on the surface of ZSP (15N-TiO$_2$/ZSP, Figure 92g). By increasing the loading of N-TiO$_2$ (30N-TiO$_2$/ZSP, Figure 92 f) a part of the layer shows an increased density of nanoparticles. Moreover, passing from 15N-TiO$_2$/ZSP (Figure 92 f) to 30N-TiO$_2$/ZSP, an increase in N-TiO$_2$ size was observed in the latter catalyst (Figure 92g). For the sample 50N-TiO$_2$/ZSP (Figure 92 h), an increased nanoparticle density and size, and also a change in N-TiO$_2$ crystallite shape was observed. The almost rare appearance of elongated particles could be an indication of a possible interaction between ZSP and N-TiO$_2$.
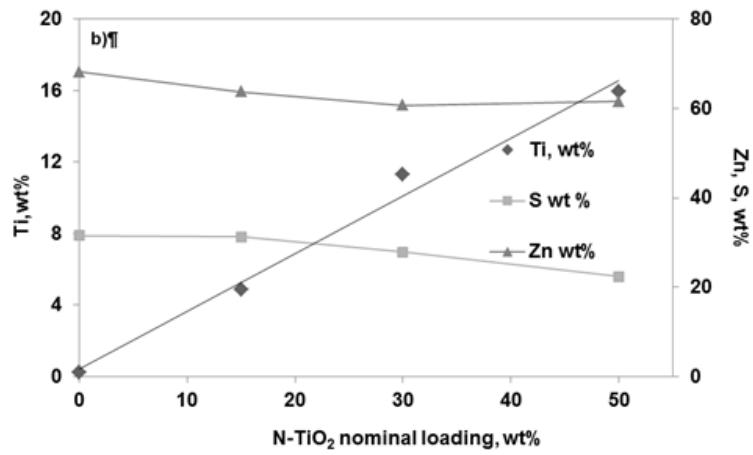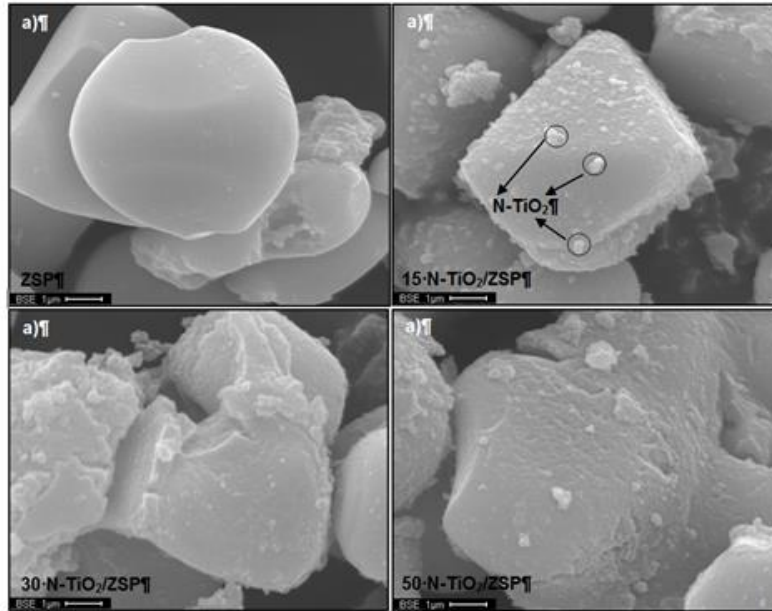
Figure 91 *a) SEM images and b)EDAX analysis of the samples ZSP; 15 N-TiO$_2$/ZSP; 30 N-TiO$_2$/ZSP; 50 N-TiO$_2$/ZSP*
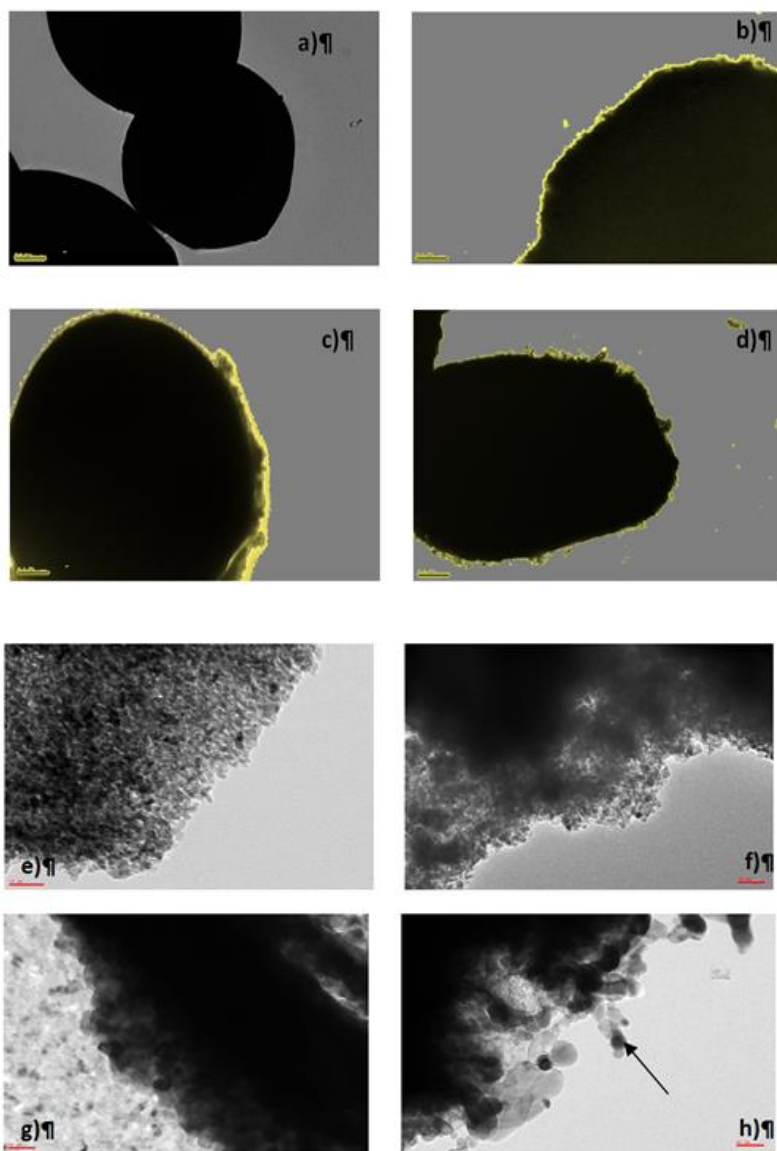
Figure 92 *TEM images: a)ZSP; b)15 N-TiO$_2$/ZSP; c) 30 N-TiO$_2$/ZSP; d)50 N-TiO$_2$/ZSP (scale bar equals 5 µm) and e) N-TiO$_2$; f)15 N-TiO$_2$/ZSP; g) 30 N-TiO$_2$/ZSP; h)50 N-TiO$_2$/ZSP (scale bar equals 50 nm).*

VII.3.1.7 Agglomerate size analysis

The size of N-TiO$_2$/ZSP agglomerates was estimated by direct observation of the SEM images obtained at 800 X magnification. Manual

157

technique of evaluation of size distribution of the agglomerates involves the use of a square grid (40 X 40 mm in size) with inscribed circles of different diameters that are used to evaluate the size of the agglomerates.

The determination of the agglomerate average size of the different samples was accomplished by counting agglomerates and using the following equation (Murcia et al., 2012)

$$\bar{d}(\mu m) = \sum d_i \cdot f_i$$

Eq.44

Where d_i is the size of counted agglomerates and f_i is the agglomerates size distribution estimated by:

$$f_i = \frac{n_i}{\sum n_i}$$

Eq.45

Where n_i is the number of agglomerates of size d_i.

The size of ZSP and the agglomeration of N-TiO$_2$/ZSP particles have been investigated using SEM images with magnification of 800x. As shown in Figure 93, the deposition of N-TiO$_2$ on ZSP surface determined a change of particle agglomeration. For the lower amount of N-TiO$_2$ on ZSP, it is possible to observe small agglomerates (Figure 93 7a and b), while by increasing the load of N-TiO$_2$, the number and the size of the agglomerates tend to increase (Figure 93 7c and d). In particular, the size distribution of the agglomerates, evaluated from the direct observation of SEM images, is reported in Figure 94. The average agglomerate size was about 5 μm for the samples ZSP, 15N-TiO$_2$/ZSP and 30N-TiO$_2$/ZSP and increased up to a value of about 10 μm for the sample 50N-TiO$_2$/ZSP.
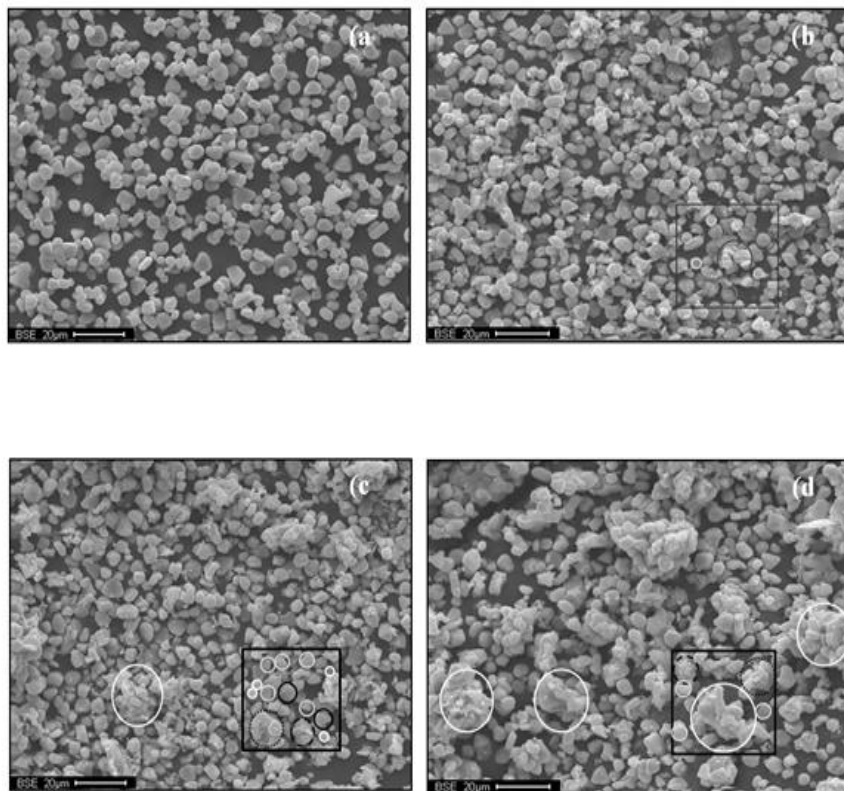
Figure 93 *SEM imagines of a) ZSP; b) 15 N-TiO₂/ZSP; c) 30 N-TiO₂/ZSP; d) 50 N-TiO₂/ZSP*
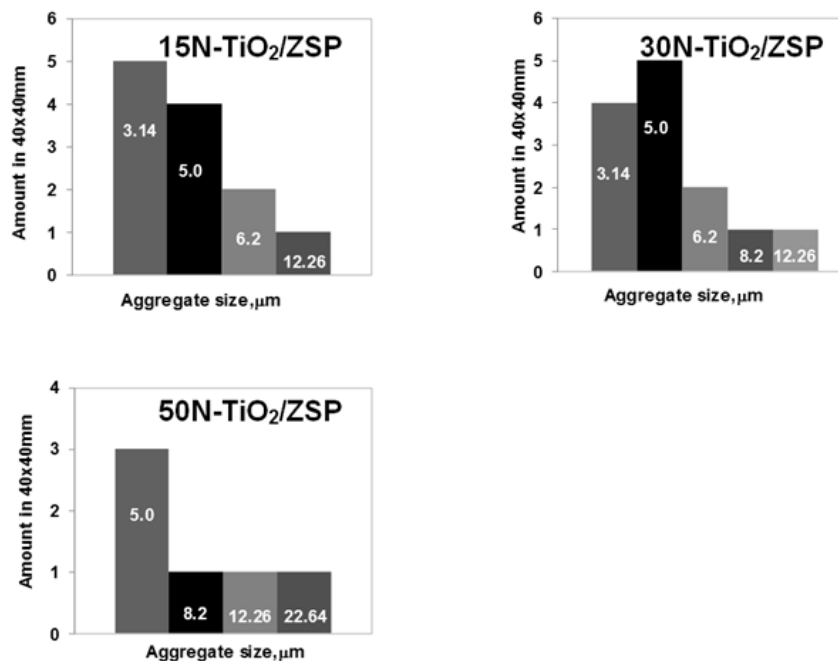
Figure 94 *Aggregate size evaluation from SEM images.*

VII.4 Photocatalytic activity tests

The evaluation of the photocatalytic activity was carried out by following the reaction of decolourization of MB. In a typical photocatalytic test, the suspension is composed by 0.3g of N-doped TiO_2 mixed with different amounts of ZSP. The total solution volume was 100mL and MB or MO concentration was 7.5 ppm. The suspension was left in dark condition for 2 hours to reach the adsorption equilibrium, and then light irradiation was performed for 3h. The experiments were realized using a pyrex cylindrical photoreactor equipped with an air distributor device, magnetic stirrer to maintain the photocatalyst suspended in the aqueous solution, temperature controller and four UV lamps (nominal power: 32 W) with wavelength emission centred at 365nm. Slurry samples were collected at fixed time and analysed to determine the change of dye concentration, measured with a Perkin Elmer UV-Vis spectrophotometer at 663 nm for MB concentration and at 464 nm for MO concentration. TOC of solution has been measured from CO_2 obtained by catalytic combustion at T=680 °C. CO_2 produced in gas-phase was monitored by continuous analyzers, measuring CO, CO_2 (Uras

14, ABB) and O_2 (Magnos 106, ABB) gaseous concentrations. The analysis of gas phase coming from the photoreactor was performed by means of a continuous CO, CO_2, and SO_2 non-dispersive infrared analyser (ABB Advance Optima).

The behaviour of MB decolourization is represented in Figure 95a for N-TiO_2 compared to the physical mixture of the same photocatalyst with light emitting phosphorescent particles ZSP. In dark conditions both photocatalysts showed a decrease of MB concentration was observed during the first hour of the test and it was the same in the second hour indicating
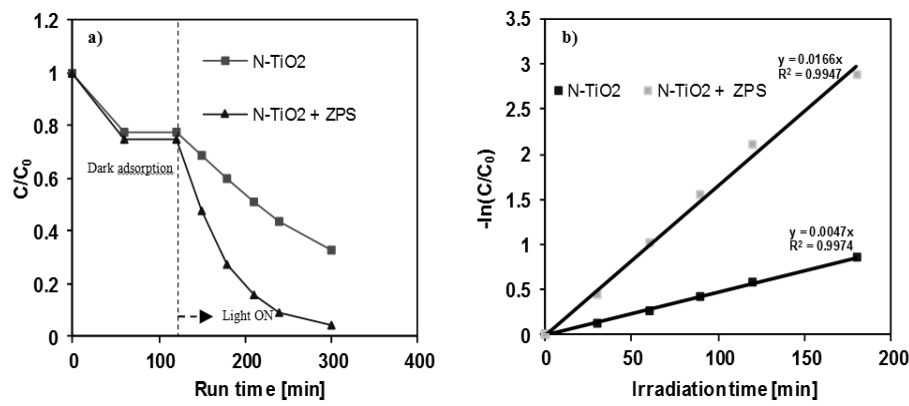
Figure 95 *(a) Decolourization of MB. (b)Evaluation of decolourization kinetic*

that the adsorption equilibrium of dye on catalyst surface was reached. In dark conditions both systems showed a decrease of MB concentration during the first hour of the test and it was the same in the second hour indicating that the adsorption equilibrium of dye on catalyst surface was reached. After the dark period, the solution was irradiated with UV lamps (Figure 95a). The results obtained with N-doped TiO_2 photocatalyst showed a decolourization activity lower than that one obtained when N- doped TiO_2 photocatalyst was mixed with ZSP with a total TOC removal. The presence of light carriers increased the effective activity in decolourization process of MB and in the removal of organic carbon, showing the presence of a limitation on in the photonic distribution and the overcoming of the the photons transfer limitations that occur for only N-dopedTiO_2.

The decolourization process on photocatalysts is described by a first order kinetic equation (Eq.46) with respect to the concentration of MB.

$$-\ln \frac{C}{C_0^*} = k_i \cdot t$$

Eq.46

Where:
C=concentration of MB at any given time;

C_0^* =concentration of MB after dark adsorption:

t= irradiation time;

k_i=apparent kinetic constant.
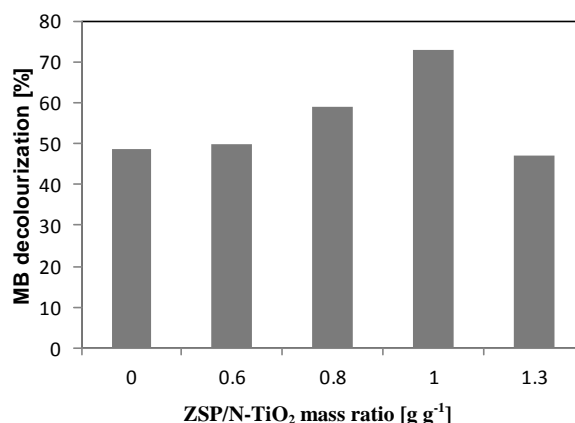
Figure 96 *Evaluation of the effect of different amount of ZPS in physical combination with the similar amount of N-TiO$_2$ (0.3 g) on the decolourization of MB after one hour*

The obtained results are plotted in Figure 95b showing that in presence of ZSP, apparent kinetic constant remarkably increased. For evaluating the effect of amount of ZSP in the MB decolourization process, 0.3 g of N-TiO$_2$ was physically mixed with different amount of phosphors (Figure 96). Increasing the dosage of ZSP from 0.6 to 1g g^{-1}, the MB decolourization after one hour of irradiation increased. With a further increase of ZSP loading in the aqueous medium, the MB decolourization activity strongly decreased, indicating that the light penetration through the solution becomes difficult. Therefore 1g g^{-1} of phosphor loading was found as the optimal value. However, the separation among the catalyst surface and the light emitted by the microcarriers remained high, since physically separated by the mere physical mixture with N-doped TiO$_2$.

Thus, the photocatalyst N-doped TiO$_2$ was supported on the surface of ZSP to get core-shell photocatalysts (Sannino et al., 2013c), to permit a higher capture of the ZPS emitted photons. The amount of N-doped TiO$_2$, however, have to be modulated, since it could be easily argued that a total coverage of ZSP by N-doped TiO$_2$ does not lead to the UV excitation of the covered phosphors (so no emission is possible), while a few amount of N-TiO$_2$ coating on ZSP will not give the desired photoactivity. So, the core-shell photocatalysts have to be able to absorb the UV light needed by the

photoreaction in the proximity of the external light source (UV lamps), but leave a residual phosphors free surface able to harvest, and release, after UV light excitation, the further radiation at 440 nm useful to proceed with the photoreaction when the photocatalysts are in darker zones of the reactor.
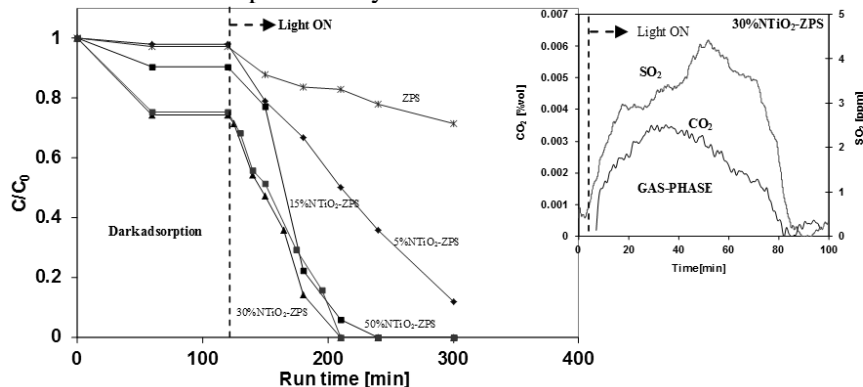
Figure 97 *Comparison of core-shell photocatalysts performances by varying the extent of N-doped TiO₂ shell (indicated by the different weight percentages of N-doped TiO₂) in photocatalytic decolourization of MB and gas-phase analysis of 30%NTiO₂-ZSP*

Figure 97 shows the comparison of the core-shell photocatalysts ($NTiO_2$–ZSP) in decolourization of MB. In all cases the equivalent amount of nominal N-TiO_2 is equal to 3 g L^{-1}. As it is possible to observe, the performances of $NTiO_2$–ZSP in the decolourization of MB were dramatically enhanced for all the samples. In particular, for the sample 30%$NTiO_2$-ZSP, the total MB decolourization was obtained after 90 minutes from the light on of the irradiation. In this case, the analysis of gaseous stream coming from the photoreactor during the irradiation revealed the presence of CO_2 and SO_2 (Figure 97). The CO_2 observed in the gas phase was due to the oxidation of MB which started at high reaction rate after few minutes of irradiation. Through a comparison between the amount of carbon consumed during the reaction (as assessed by the analysis of TOC in liquid phase) and the amount of carbon released as CO_2 in the gaseous phase, the total carbon mass balance was closed to about 100%. This allowed affirming that the MB is selectively converted to CO_2. The effect of MB initial concentration on the photocatalytic activity was evaluated with two different initial MB concentrations: 7.5 and 95 ppm and in presence of the most active photocatalyst, 30%$NTiO_2$-ZSP, (Figure 98a). At fixed reaction times, the increase of MB initial concentration determined a decrease of the photocatalytic activity. This could be due both to the higher mass of dye to remove, but also to the increase of colour intensity of the solution, that reduces the light penetration into the aqueous medium, meaning that the path

163

length of photons inside the solution decreases, however also in this case, the core-shell photocatalyst is able to assure the total MB decolourization after about 1000 minutes of irradiation. Finally, the efficiency of 30%NTiO$_2$-ZSP was also evaluated in decolourization of (MO) (Figure 98b) showing that it is able to remove also dyes different from MB.
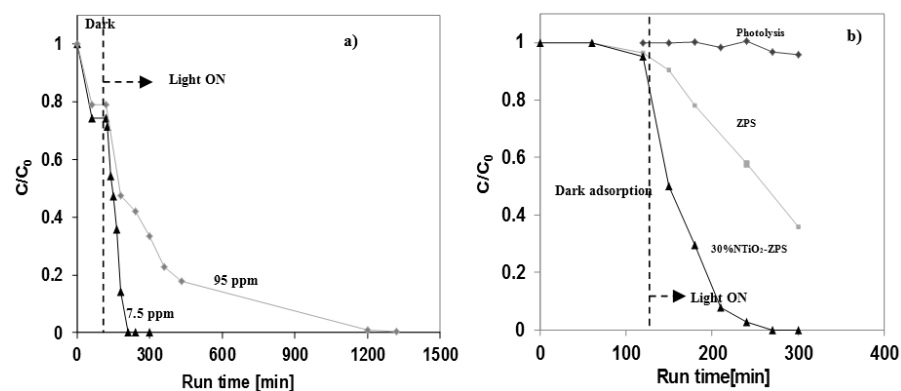
Figure 98 *a) Evaluation of decolourization with different initial concentration of MB; photocatalyst: 30%NTiO$_2$-ZSP; b) Evaluation of MO decolourization); photocatalysts 30%NTiO$_2$-ZSP*

So, Core-shell photocatalysts based on N-doped TiO$_2$ coating on ZSP were successfully synthetized. The optimal load of N-doped TiO$_2$ on the phosphors was individuated at 30 wt%, yielding in the right combination of the need of ZSP to absorb the UV light to be excited by the external light source (UV lamps), and the presence of a suitable amount of active N-doped TiO$_2$ photocatalytic phase, so developing the ability to proceed with the photoreaction when the photocatalysts are in darker zones of the reactor. Core-shell photocatalysts demonstrated remarkably activity in the decolourization of organic dyes and in the removal of total organic carbon, overcoming photons transfer limitations that typically are present in the photoreactors used for wastewater treatment.

VII.5 Photocatalytic removal of atrazine using N-doped TiO$_2$ supported on phosphors

VII.5.1 Evaluation of photocatalytic activity

The stock solution of atrazine was prepared by dissolving the solid pesticides in an appropriate amount of MilliQ-grade water. A Pyrex glass (I.D. =5 cm) petri dish was used as the reactor. The glass reactor was sealed with Parafilm and cooled with a fan to prevent evaporation and maintain a constant temperature (T = 27 ± 1 °C). The loading of each photocatalyst in the reaction solution was 0.5 g L^{-1} and the initial concentration of atrazine was 2.5 mg L^{-1}.

The total volume of solution in the reactor was 15 mL. UVA-365 nm radiation was simulated by two 15 W lamps fixed at 38 mm (light intensity: 2.47 ± 0.16 mW cm^{-2}) from the upper water level in the reactor. The reactor was left in dark condition for adsorption test and under UVA illumination for removal test. Throughout the experiments, samples were taken at various time intervals. All the withdrawn samples had a volume of 100 μL and filtered with 0.45 μm pore size filters to remove the catalysts powders.

VII.5.2 Analytical method

VII.5.2.1 High performance liquid chromatography (HPLC)

All analyses were performed using an Agilent 1100 Series liquid chromatography. The evaluation was carried out using a C8 column (150 mm×4.6 mm i.d., 5μm, Agilent), and a mobile phase consisting of 40% HPLC grade water and 60% HPLC grade acetonitrile (Tedia) (acetonitrile/H$_2$O=60:40 (v/v)) with a flow rate of 0.4 mL min^{-1} and detection wavelength λ=223 nm. The injected sample volume was 20 μl and the column temperature was maintained at 20 °C.

VII.5.2.2 Intermediates identification

Intermediate identification was carried out using a combination of liquid chomatography/quadrupole time-of-flight (LC/Q-TOF) to obtain molecular weight and formula information and liquid chromatography/mass spectrometry/mass spectrometry (LC/MS/MS) to determine further structural information. LC/Q-TOF analysis has been performed with an Agilent

G6540A quadrupole time-of-flight mass spectrometer. Nitrogen was used as the auxiliary gas with a temperature of 300 °C and nitrogen flow rate was 7 L min^{-1}. The temperature of the sheath gas was 250 °C with a flow rate of 8 L min^{-1}.

LC/MS/MS data were acquired using the same instrument in MS/MS mode. For both Q-TOF and MS/MS modes, the same LC separation method was used. The mobile phase consisted of 95% solvent A and 5% solvent B. Solvent A was 0.1% formic acid in water, and Solvent B was 0.1% formic acid in acetonitrile. The flow rate was 0.2 mL min^{-1} and the method runtime was 5 min. The column used was an Agilent Eclipse XDB-C18 column (2.1 mm × 50 mm, 3.5 micron).

VII.5.3 Photocatalytic activity of N-TiO$_2$/ZSP catalysts

VII.5.3.1 Influence of N-TiO$_2$ loading

The photocatalytic activity of N-TiO$_2$/ZSP samples was investigated under UVA light irradiation.
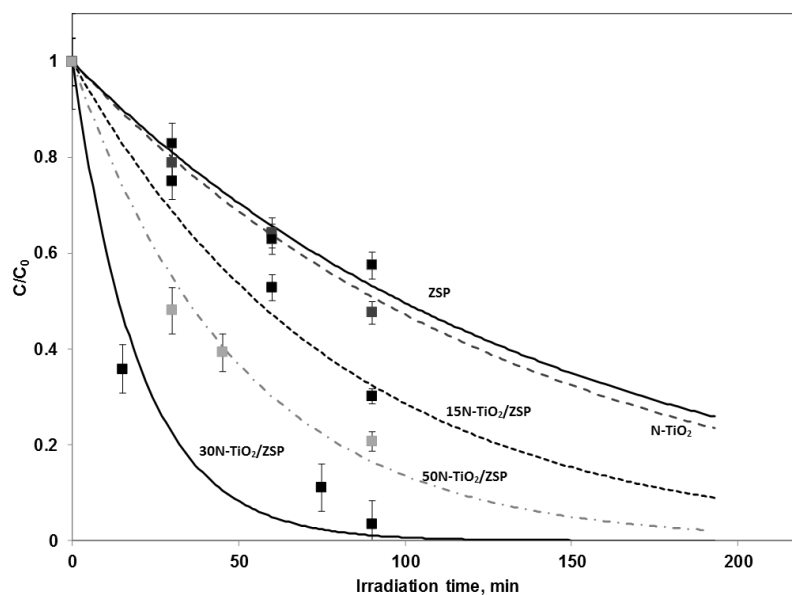
Figure 99 *Behavior of atrazine experimental concentration (■) and predicted data(-) as function of irradiation time for the different photocatalysts*

Figure 99 shows the experimental data of the removal of atrazine at initial pH equal to 5.8 and photocatalysts dosage equal to 0.5 g L^{-1}. 15N-TiO$_2$/ZSP, 30N-TiO$_2$/ZSP and 50N-TiO$_2$/ZSP samples showed significant

166

photocatalytic activity, obtaining an atrazine removal of 54, 94 and 78 %, respectively. On the other hand, with only ZSP and N-TiO$_2$, atrazine degradation degree was lower, in particular equal to 41 and 45 %, respectively. It is important to note that phosphors alone evidenced photoactivity very similar to N-TiO$_2$. This behavior has been attributed to the ability of ZnS, in the presence of water and UVA irradiation, to photogenerate surface SH group and OH radicals (Kim and Kang, 2012). As a confirmation of the general mechanism of photoxidation induced by the presence of water on the surface of ZnS, it must be remarked that when the same kind of phosphors are used in the gas phase photoreactions, no photoactivity was observed, and this could be justified by the low amount of water employed for the tests (Ciambelli et al., 2011a).

With regard to the effect of N-TiO$_2$ loading, it appears that 30N-TiO$_2$/ZSP photocatalyst showed the highest photoactivity. It showed a rapid initial decrease in the pesticide concentration with irradiation time lower than 15 min with almost complete disappearance of atrazine after about 90 min (Figure 99). The photoreactivity of 30N-TiO$_2$/ZSP was enhanced because the surface of ZSP not covered by N-TiO$_2$ nanoparticles, was able to transform 365 nm radiation into 440 nm emission, able as well to photoexcite N-TiO$_2$ itself. The obtained result evidenced that by supporting N-TiO$_2$ photocatalyst on ZSP surface allows a dramatic enhance in the removal of atrazine, confirming that a shorter light pathlength is beneficial for the photoreaction.

VII.5.3.2 Evaluation of apparent degradation kinetic constant

The evaluation of apparent kinetic constant has been realized considering that in the batch reactor under UVA irradiation, the removal of atrazine follows the pseudo-first order kinetics.

Atrazine mass balance can be written as:

$$\frac{dC(t)}{dt} = -k \cdot C \cdot a \qquad\qquad \text{Eq.47}$$

Where:

C (t) : atrazine concentration, mg L^{-1}
k: apparent kinetic constant, L g^{-1} min^{-1}
a: N-TiO$_2$ dosage, g L^{-1}

The initial condition is:
t=0 $\qquad\qquad\qquad$ C=2.5 mg L^{-1}

The equation 47, together with the initial condition, was solved by the Euler iterative method. Primary goal of the simulation by mathematical model is to identify the apparent kinetic constants k by fitting experimental

data reported in Figure 99 as a function of irradiation time. The fitting procedure was realized by using the least squares approach obtaining the following value of k: N-TiO$_2$ =0.015 L g $_{\text{N-TiO2}}^{-1}$ min-1; ZSP =0.014 L g$_{\text{N-TiO2}}^{-1}$ min^{-1}; 15N-TiO$_2$/ZSP =0.15L g$_{\text{N-TiO2}}^{-1}$ min^{-1}; 30N-TiO$_2$/ZSP =0.25 L g$_{\text{N-TiO2}}^{-1}$ min^{-1}; 50N-TiO$_2$/ZSP =0.09 L g$_{\text{N-TiO2}}^{-1}$ min^{-1}.

The pseudo-first order kinetic constant is the best parameter to compare the results of photocatalytic activity, being independent from the amount of catalyst, and only correlated to the N-TiO$_2$ active phase loaded on the ZSP surface. It is important to note that, starting from the values obtained on N-TiO$_2$ and ZSP, the kinetics constant for the photostructured photocatalysts increased of one order of magnitude or more.
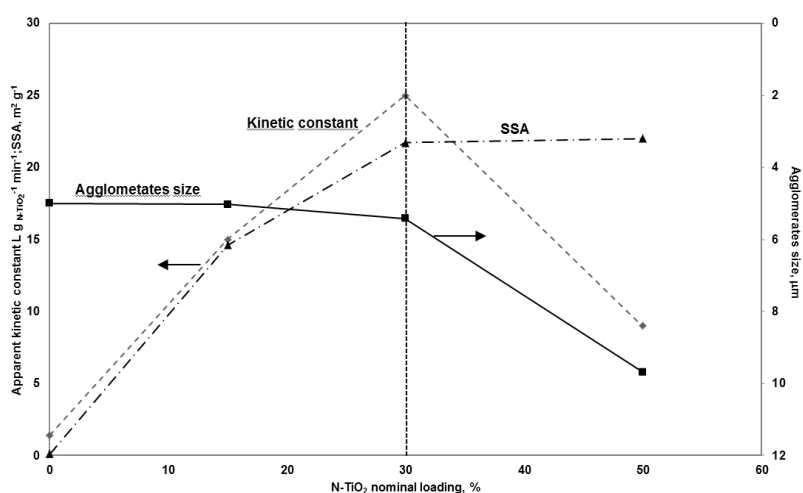
Figure 100 *Atrazine apparent kinetic constant and catalysts agglomerates size as a function of N-TiO$_2$ nominal loading*

The obtained results are summarized in Figure 100, which reports also the photocatalysts average agglomerates size as function of N-TiO$_2$ load. The apparent kinetic constant increased almost linearly up to N-TiO$_2$ loading equal to 30 wt %. In the range 0-30 wt % N-TiO$_2$ content, the average agglomerates size did not change, being almost equal to 5 μm. On the other hand, in presence of ZSP, the average size of crystallites of N-TiO$_2$ is smaller than that of pure N-TiO$_2$. As a consequence, the specific surface area (SSA), also reported in the Figure 100, follows the behavior of the kinetic constant up to the N-TiO$_2$ content of 30 wt %.

Thus, the increase of photocatalytic activity in the range 0-30 wt % is only due to the increase of specific surface area.

168

When N-TiO$_2$ loading is higher than 30 wt %, the photocatalytic activity decreased. In fact, the sample 50N-TiO$_2$/ZSP showed an apparent kinetic constant of atrazine removal equal to 0.09 L g_{N-TiO2}^{-1} min^{-1}, lower than that one obtained on 30N-TiO$_2$/ZSP, equal to 0.25 L g_{N-TiO2}^{-1} min^{-1}. In this case, the decrease of reaction rate could be related to the increase of N-TiO$_2$ agglomerates size observed by increasing N-TiO$_2$ amount from 30 to 50 wt%. From these results, it could be argued that the tendency to the agglomeration, and consequently the size of agglomerates, may influence the ability of the different N-TiO$_2$/ZSP samples to remove the atrazine, as previously observed in the E. coli inactivation on N-TiO$_2$ photocatalyst (Rizzo et al., 2014). From these results, the best catalyst is 30N-TiO$_2$/ZSP. Therefore, it was chosen to investigate the influence of catalyst dosage and initial pH of atrazine solution.

VII.5.3.3 Optimization of 30N-TiO$_2$/ZSP dosage in aqueous suspension

To study the effect of 30N-TiO$_2$/ZSP dosage, different concentrations, between 0.3 and 1.0 g L^{-1}, were used. The initial concentration of atrazine, equal to 2.5 mg L^{-1}, was kept the same in all these experiments, and in Figure 101 the effect of the amount of catalyst on the conversion of atrazine after 60 min of irradiation is reported.

It is observed that the removal rate increases proportionally up to a photocatalyst dosage of 0.5 g L^{-1}. A further increase of catalyst dosage determined a decrease of atrazine removal rate. This phenomenon may be due to the increase of agglomeration tendency (Cunningham and Sedlak, 1996) between 30N-TiO$_2$/ZSP particles in aqueous suspension, causing a decrease in the number of surface active sites.

However, a high amount of 30N-TiO$_2$/ZSP could induce the appearance of photon limitations phenomena due to the formation of agglomerated with large size that decrease the ZSP surface able to capture the UVA light emitted by the lamps. Thus, the advantage to use ZSP as support for N-TiO$_2$ particles is lost.
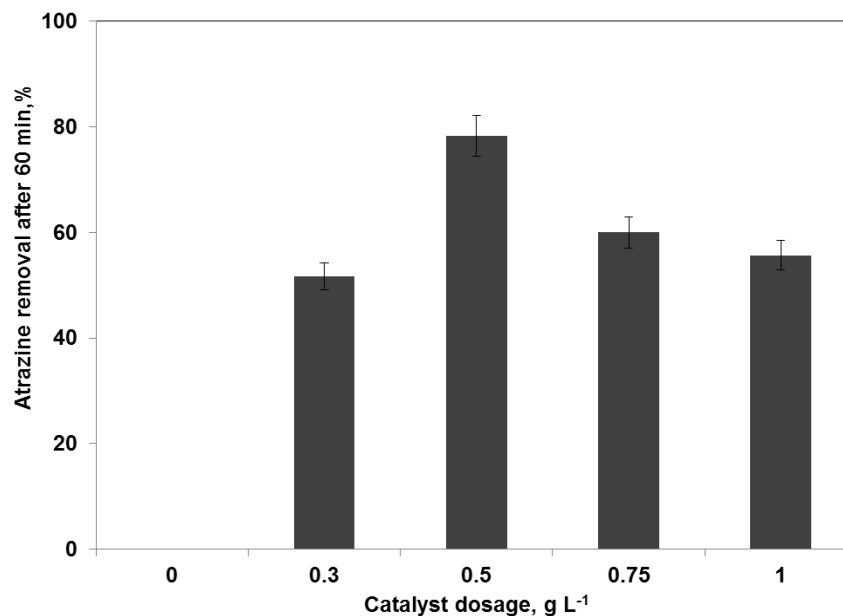
Figure 101 *Effect of 30N-TiO$_2$/ZSP dosage on the removal of atrazine.*

VII.5.3.4 Influence of pH

To study the effect of pH in the removal of atrazine, the initial pH of solution was changed in the range 3.0-9.0. The photocatalyst used was 30N-TiO$_2$/ZSP. The trend of atrazine removal in presence of different initial pH (reported in Figure 102a) showed a maximum value obtained at initial pH 5.8 in which the atrazine removal, after 90 min of irradiation, reached the value of about 94%. In contrast, a stronger acidic condition (pH = 3.0) leads to a slight low removal value, equal to 82%.

When the initial pH of solution increased, in particular at pH=7.0 and pH=9.0, the removal decreased leading to a value equal to 60% and 53%, respectively.

However, at pH=7.0, and at higher pH values, equal to 9.0, the change of surface charge of photocatalysts leads to a supplementary repulsive phenomena leading to a low removal (Parra et al., 2004). The obtained data was used for the evaluation of apparent kinetic constant that, as shown in Figure 102b increased from the value of 0.15 L g$_{N-TiO2}^{-1}$ min^{-1} to the value of 0.25 L g$_{N-TiO2}^{-1}$ min^{-1} for pH=3.0 and pH=5.8, respectively, and then decreased to a value of 0.06 L g$_{N-TiO2}^{-1}$ min^{-1} for pH= 7.0 and pH=9.0. The

170

obtained trend is in agreement with experimental data reported in literature concerning the photocatalytic removal of atrazine (Parra et al., 2004).
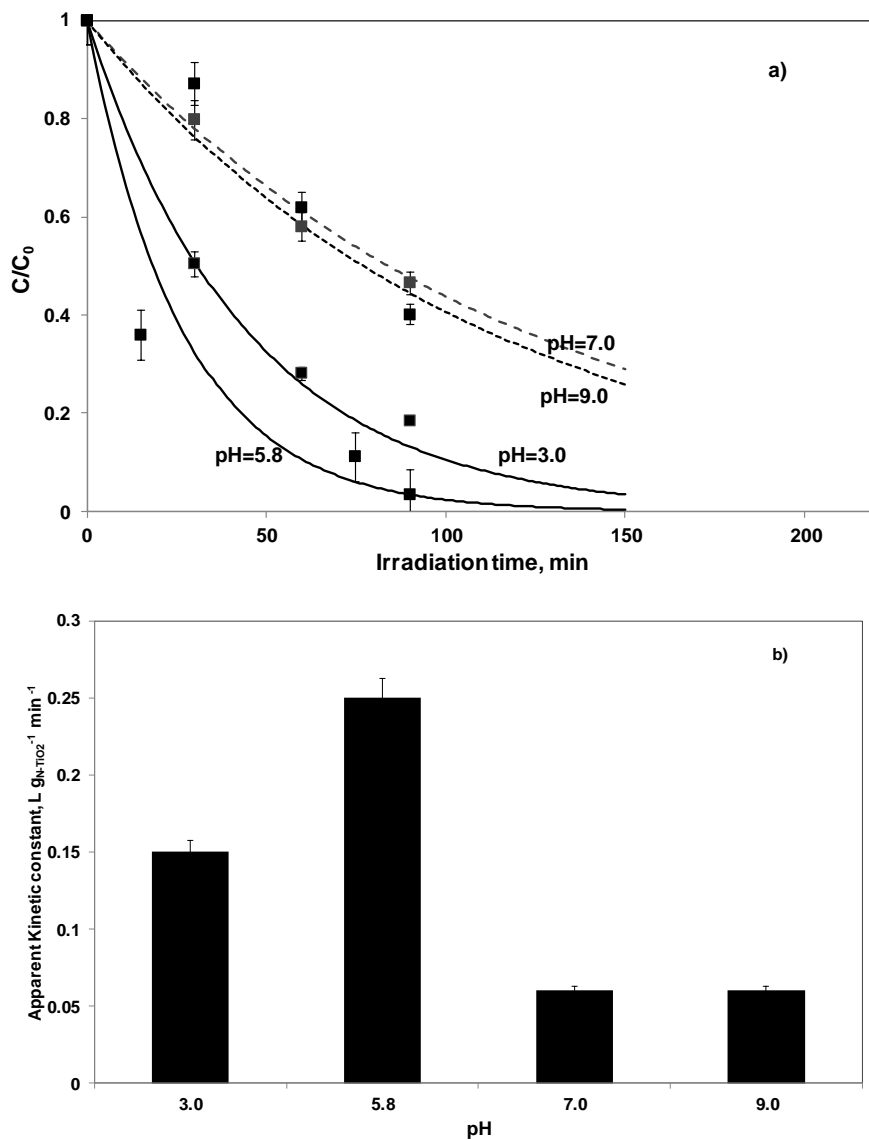
Figure 102 *a) Photocatalytic removal of atrazine on 30N-TiO$_2$/ZSP at different initial pH values, and b) apparent kinetic constant at different initial pH values.*

171

VII.5.3.5 Intermediate degradation products of atrazine

Intermediate degradation products of atrazine were observed between 5 and 30 min of irradiation using 30N-TiO$_2$/ZSP and ZSP.

Before analyzing the behavior of 30N-TiO$_2$/ZSP, the intermediates formed in presence of ZSP were analyzed. The following molecular fragments m/z were identified: 229.0733, 213.0786, 199.0623, 188.0463, 187.0619 and 173.0464. Even if ZnS-based semiconductors (ZSP) have never been studied in the photodegradation of atrazine, some of molecular fragments identified (m/z=229.0733 and m/z=173.0464) are the same as those found in the presence of TiO$_2$ (McMurray et al., 2006; Qin et al., 2010).
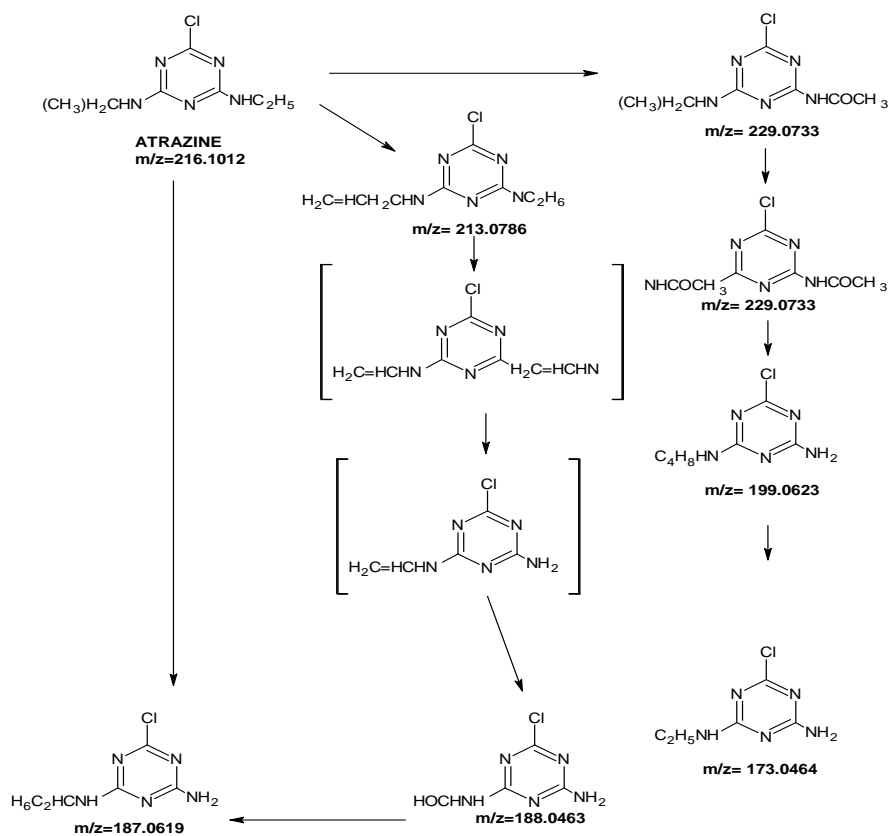
Figure 103 *Possible degradation pathway of atrazine by ZSP under UVA irradiation*

The chemical formulas for intermediates were provided by the mass accuracy of the instrument and these formulas were compared with literature

data to identify molecular structures (Andersen et al., 2013; Chen et al., 2009).All the intermediates structurally identified outline a potential degradation pathway of atrazine in presence of ZSP. Based on the structures of these intermediates detected during the degradation, the main pathways of atrazine photodegradation for ZSP is also proposed in the Figure 103. The reaction mainly involves dealkylation reactions and alkyl chain oxidation. It is important to underline that no dechlorination of aromatic structure occurred after 30 min of irradiation, meaning that cyanuric acid (1,3,5-triazine-2,4,6- triol, $C_3N_3(OH)_3$), previously reported in literature for photocatalytic degradation of atrazine using TiO_2 as photocatalysts (Qin et al., 2010), was not formed. The absence of this contaminant, which resists to the oxidation by hydroxyl radicals, is a very important issue and however, it was not detected also after long irradiation time (24 hour).
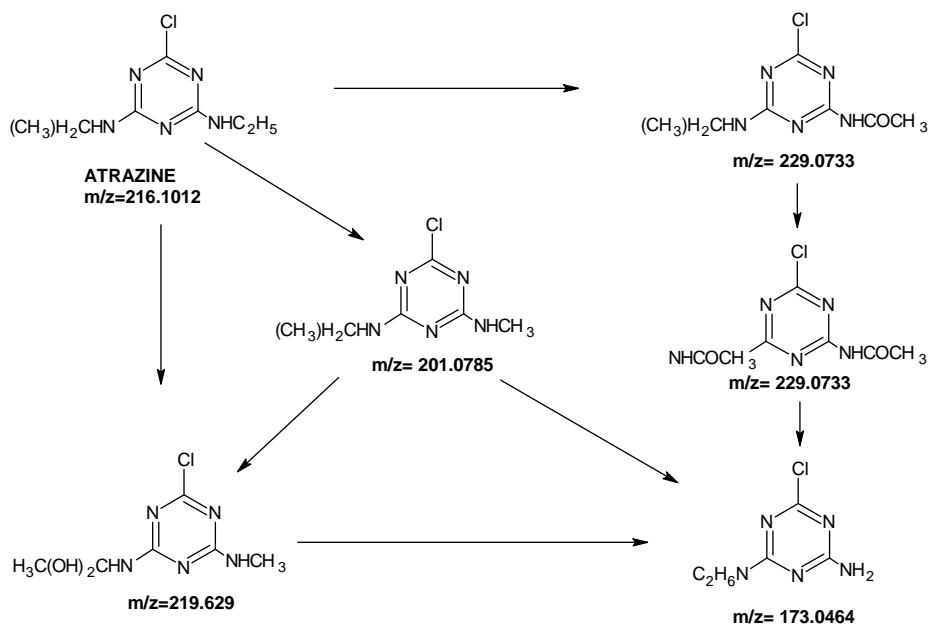
Figure 104 *Possible degradation pathway of atrazine by 30N-TiO₂/ZSP under UVA irradiation*

When N-TiO_2 is supported on ZSP, novel intermediates with m/z =201.0785 and m/z=219.629, appeared. These novel intermediates were not previously reported in literature (Andersen et al., 2013). Also in this case, the mass accuracy of the instrument is sufficient to provide chemical formulas for these intermediates and the structure was incorporated in Figure 104. Also with 30N-TiO_2/ZSP, dechlorination of atrazine was not observed and the main reactions were dealkylation and alkyl chain oxidation.

Comparing the Figure 103 and Figure 104, the first information is that the intermediates with m/z=229.0733 and m/z=173.0464 are likely formed on the ZSP surface not covered by N-TiO2 particles. However, the presence of N-TiO$_2$ particles dispersed on ZSP surface leading to a change of selectivity because on 30N-TiO$_2$/ZSP, two different compounds with m/z =201.0785 and m/z=219.629 appeared (Figure 103) inhibiting the formation of intermediates with m/z=.213.0786, 199.0623, 188.0463 and 187.0619 (Figure 104). However, it is important to underline that the presence of ZSP didn't induce the dechlorination of atrazine that leads the formation of cyanuric acid, which is, on contrary the typical final product of photocatalytic degradation of atrazine in presence of TiO$_2$.

Visible light-active N-TiO$_2$ photocatalyst was successfully deposited in a dispersed form on ZnS-based luminescent phosphor microparticles (ZSP) by a modified sol–gel method. Compared to the single materials, the synthesized composite photocatalyst exhibited enhancement in photocatalytic activity for the removal of atrazine. Anatase N-TiO$_2$ nanoparticles of small crystallite size were deposited on the surface of ZSP as a thin film of aggregated particles covering completely the support surface. With the increase of N-TiO$_2$ loading, the size of primary nanoparticles on the ZSP support increased, however being always smaller than that of pure N-TiO$_2$. From TEM images it was observed, respectively, an increase of the thickness of N-TiO$_2$ layer and its density with an increase in the N-TiO$_2$ loading. This resulted in a higher specific surface area, mainly due to N-TiO$_2$ exposed.

The results showed that N-TiO$_2$/ZSP photocatalysts are very efficient to remove atrazine under UVA illumination. This study clearly demonstrates the importance of using the ZSP as a support material for an advanced oxidation process using visible light-active TiO$_2$, due to the utilization of re-emitted radiation by ZPS after the original UVA source irradiation, thus increasing the removal rate of atrazine. The photocatalyst N-TiO$_2$/ZPS with N-TiO$_2$ loading of 30 wt % was the most active. In particular, 94% of atrazine was degraded after 90 min of UVA irradiation compared to N-TiO$_2$ only (45%). The apparent kinetic constant, estimated for all the photocatalysts with a pseudo-first order kinetic model was one order of magnitude or more higher than those of the single components, showing a "synergic" photocatalytic effect. The apparent kinetic constant trend increased with the specific surface area up to at 30 wt % of N-TiO$_2$ loading. When N-TiO$_2$ loading is higher than 30 wt %, the photocatalytic activity decreased because of the increase of N-TiO$_2$ agglomerates size, observed by increasing N-TiO$_2$ amount from 30 to 50 wt%.

The photocatalytic atrazine conversion depended strongly from the catalyst amount in the solution and from the initial pH of solution. The higher degradation degrees were found at 0.5 g L^{-1} and at slight acidic pH. A possible degradation pathway was proposed by the identification of the

174

intermediate degradation products on the 30N-TiO$_2$/ZSP and ZSP. The reaction mainly involves dealkylation reactions and alkyl chain oxidation both in presence of 30N-TiO$_2$/ZSP and ZSP. However, the presence of N-TiO$_2$ particles dispersed on ZSP surface leads to a change of selectivity, lowering the number of intermediated formed during irradiation. It is important to underline that, in presence of ZSP support, no dechlorination of aromatic structure occurred also after long time (24 hour) of irradiation, meaning that cyanuric acid was not formed during the pathway.

This study clearly demonstrates the importance of using the ZSP, as support, which increases the photodegradation of atrazine, due to both visible lights emitted by them and to the intrinsic photoactivity of ZnS because of its nature of semiconductor.

VIII Design of a continuous fixed bed photoreactor

One of the most important drawbacks of photocatalytic process is that photocatalysts are used in slurry reactors. With this type of reactor, photocatalysts must be recovered from the purified water after the treatment, and the cost of this separation stage may even invalidate economically this technique. With the aim to overcome this technical limitation the N-doped TiO_2 photocatalyst was immobilized on glass spheres to design a fixed bed continuous photoreactor

VIII.1 Immobilization of N-doped TiO_2 on glass supports

There is an important variety of materials that can be used for supporting TiO_2. The most studied are that ones based on glass, owing to their low cost and easy availability (Konstantinou et al., 2001). For supporting the photocatalysts on these materials, different techniques are developed (Kumar and Bansal, 2012). The success of these coating processes is based on the large adherence between TiO_2 and glass and to provide a high surface area of TiO_2 deposited. Only few papers regard N-TiO_2/immobilized systems mainly carried out through sputtering technique (Avisar et al., 2013). No study developed a simple sol-gel method that uses ammonia solution as the only doping source.

For this reason the aim of this section was: i) the immobilization of visible-light active N-doped TiO_2 photocatalyst (N-TiO_2) on glass spheres using a simple sol-gel method; ii) the optimization of the conditions of sol-gel synthesis for obtaining a high photo-active surface area; iii) the optimization the of N-TiO_2 amount deposited on glass spheres; iv) the evaluation of photocatalytic activity of the prepared supported photocatalysts in the removal of aqueous solution of MB and EBT both under UV and visible light irradiation.

VIII.1.1   Sol–gel synthesis

Triton X-100 (nonionic surfactant, Sigma–Aldrich) has been used as binder (Rosu et al., 2009). Triton X-100 was dissolved in isopropyl alcohol (i-PrOH, 99.8 wt %, Sigma–Aldrich) and the pH of solution was adjusted with nitric acid (HNO_3, 65 wt %, Carlo Erba) until to reach a value of about 2. Then,

titanium (IV) isopropoxide (TTIP, 97%, Sigma–Aldrich), used as titanium precursor, was added to the mixture.

The use of a low pH limits condensation reactions, imposes a repulsive charge and limits the size of precipitates (Wang et al., 2013).

In order to investigate the effect of the synthesis temperature on N-TiO_2 crystallites size, different synthesis temperatures were used. The investigated temperatures were 0°C;-5°C,-15°C; -20°C. A cryostat bath was used to control and monitor the temperature during the sol-gel synthesis. Once the solution reached the temperature conditions, an ammonia aqueous solution

Table 11 *Synthesis reaction temperature, amount of surface-active agent (Triton X-100), crystallite size, SSA (BET) of different N-TiO_2 samples*

Catalyst	Syntesis reaction Temperature (°C)	Amount Triton X-100 (g)	TiO_2 crystallites size (nm)	S.S.A (m^2/g)
N-TiO_2	0	0	17	30
0 NdTc	0	5	9	98
-5 NdTc	-5	5	8	108
-15 NdTc	-15	5	7	128
-20 NdTc	-20	5	6	147

(30 wt %, Sigma–Aldrich) was added as nitrogen precursor while the water is able to induce the hydrolysis reaction with TTIP. The molar ratio N/Ti was equal to 18.6 and corresponds to an optimized catalyst formulation found in a previous work (Sacco et al., 2012). The obtained solution was used for the immobilization of N-TiO_2. All prepared samples are reported in Table 11.

VIII.1.2   Immobilization of N-TiO_2 on glass spheres

Pyrex spheres (d_p=4.3 mm, from Microglass Heim) were used as glass substrate for the immobilization of N-TiO_2, which has been performed through dip-coating technique.

Before dip-coating, the whole surface of glass spheres was rinsed with MilliQ grade water and calcined at 450°C for 30 minutes. N-TiO_2 coating

(NdTc) was realized by immersing the glass spheres in the solution prepared as reported in the section 1.1. The glass spheres were maintained in the solution for 10 minutes and then calcined for 30 minutes at 450°C.

The dip-coating and calcination processes were repeated three, four and six times for finding the best amount N-TiO$_2$ dispersed on the glass spheres surface. All prepared samples are reported in Table 12.

Table 12 *Number of dip-coating steps; crystallites size, SSA and N-TiO$_2$ amount immobilized on glass spheres*

Catalyst	Number of dip-coating	N-TiO$_2$ amount (wt%)	S.S.A (m^2/g)
Glass spheres	0	0	0.095
3 NdTgc	3	0.22	0.27
4 NdTgc	4	0.34	0.42
6 NdTgc	6	0.77	1.2

VIII.1.3 *Photocatalytic activity tests*

Methylene blue (MB) and Eriocrome black-T (EBT) were used as model dyes .The experiments were carried out with initial concentration of MB and EBT equal to 5 mg/L, at ambient temperature and pressure. The amount of NdTc on glass spheres used during the photocatalytic test was equal to 0.4 g/L. The experiments were realized using a pyrex cylindrical photoreactor (I.D=3 cm) equipped with a peristaltic pump that continuously mix the aqueous solution. Thermocouple was inserted inside the reactor to monitor the temperature during irradiation. As visible light source, a white light LEDs strip (light intensity: 32mW/cm^2; emission spectrum in the range 400-800nm) was used and, as UV source, an UV emitting LEDs strip (light intensity: 35 mW/cm^2; emission spectrum in the range 365–400nm) was utilized. Both LEDs strips are placed surrounding the external body of the cylindrical photoreactor. The schematic picture of experimental set-up is reported in a previous paper (Vaiano et al., 2014e).

The system was left in dark until reaching MB and EBT adsorption equilibrium, and then photocatalytic reaction was initiated under UV light or visible light.

Liquid samples were analyzed in continuous by spectrophotometric measurement. In particular, a special assembly with a flow quartz cuvette and an external pump for the recirculation of liquid was used, permitting to

determine the change of MB and EBT concentration, measured with a Perkin Elmer UV-Vis spectrophotometer at $\lambda = 663$ nm and 528 nm, respectively. A standard calibration curve was obtained for different MB and EBT concentration and allowed to convert absorbance to concentration (mg/L) units. The total organic carbon (TOC) of aqueous samples was measured by the high temperature combustion method on a catalyst (Pt/Al_2O_3) in a tubular flow microreactor operating at 680 °C, with a stream of hydrocarbon free air to oxidize the organic carbon. Laboratory apparatus consisted of mass flow controllers (Brooks) operating on each gas; an injection system; a NDIR continuous analyser (Hartmann & Braun Uras 10E) for the measurements of CO_2 concentration at the combustion reactor outlet.

VIII.2 Optimization of N-TiO$_2$ sol-gel synthesis temperature for the coating process

VIII.2.1 *Samples characterization*

VIII.2.1.1 *Raman spectra*

Laser Raman spectra were obtained at room temperature with a Dispersive MicroRaman (Invia, Renishaw), equipped with 514 nm diode-laser, in the range 100-2000 cm^{-1} Raman shift on powder and structured samples.Figure 105 presents the comparison between N-TiO$_2$ synthesized by sol-gel method without the use of Triton X-100 at 0°C (a), and at 0°C in presence of Triton X-100 (b). The Raman spectra of both samples showed bands at 142, 398, 518, 641 cm^{-1} and a weak shoulder at 197 cm^{-1}, which are assigned to the E_g, B_{1g}, A_{1g} or B_{2g} and E_g modes of the anatase phase, respectively (Parker and Siegel, 1990).

From Figure 105 (insert), it is easily to see that the strongest Raman signal at 142 cm^{-1}, shifts towards higher wavenumber (144 cm^{-1}). This phenomenon means that the N-TiO$_2$ grains are smaller in size (Li et al., 2001).

It is well known that the addition of a surface-active agent such as Triton X-100 in the sol-gel synthesis may provide a convenient way to prepare small-sized particles (Wahi et al., 2006). Generally, nanoparticles are formed in two processes: first, the formation of a large crystal nucleus and secondly, the growth of the nucleus. The surface-active agent was easily adsorbed on the surface of the crystal nucleus and hence probably hindered the further

180

growth of these crystals, and in addition, the adsorption of the surface-active agent may also stabilize the nanoparticles (Li et al., 2001).

In the Figure 106, the effect of different sol-gel synthesis temperatures was also analyzed for 0NdTc and -20 NdTc samples using Triton X-100. In particular the strongest Raman peak (E_g) at 144 cm^{-1} mode of TiO_2 presents a blue shift up to 149 cm^{-1}. This data indicated that both the use of a surface-active agent and a synthesis temperature lower than 0°C lead to the formation of TiO_2 with grains smaller in size (Li et al., 2001).
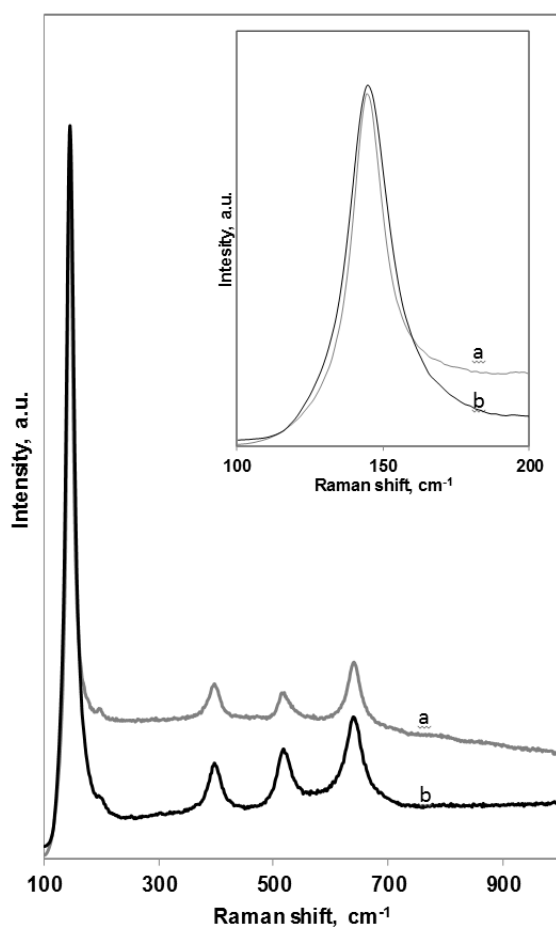
Figure 105 *Raman spectra of (a) N-TiO$_2$ synthetized by sol-gel method at 0°Cand (b) 0NDc synthetized by sol-gel method at 0°C using surface-active agent (Triton X-100); Raman shift of E$_g$ modes in the range 110-200 cm^{-1} (inset)*

VIII.2.1.2 XRD measurements

Wide-angle X-ray diffraction (WAXD) patterns with nickel filtered Cu-Kα radiation were obtained with an automatic Bruker D8 Advance diffractometer, in reflection. The results obtained from X-ray diffraction analysis showed the presence of signals typical of the titanium dioxide in the anatase form in all synthesized samples (Figure 107) (Wang et al., 2013). No signals related to rutile phase have been observed.
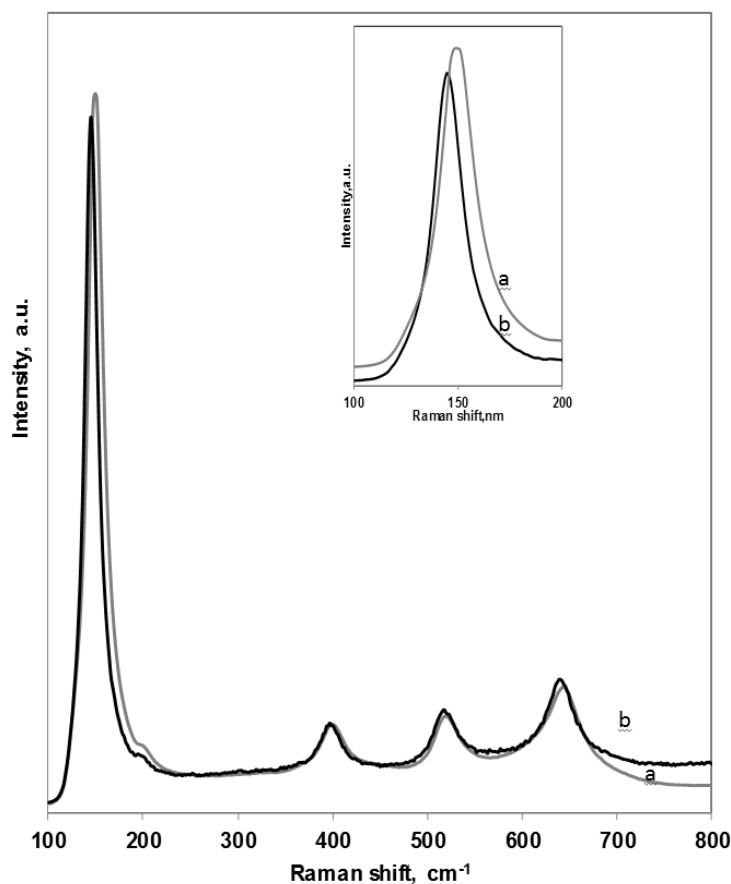
Figure 106 *Raman spectra of (a) 0NDc synthetized by sol-gel method using surface-active agent (Triton X-100) at 0°C and (b) -20NDc synthetized by sol-gel method using surface-active agent (Triton X-100) at -20°C; Raman shift of E_g modes in the range 100-200cm^{-1}(inset)*

Furthermore, the average crystallite size of N-TiO$_2$ and of all NdTc samples was calculated using the Scherrer equation on diffraction plane (101) and the obtained values are reported in Table 1. Also from XRD

182

analysis, it is possible to observe that the presence of Triton X-100 can effectively prompt the crystallization and inhibit the grain growth allowing to obtain smaller TiO_2 crystallites (Li et al., 2001).
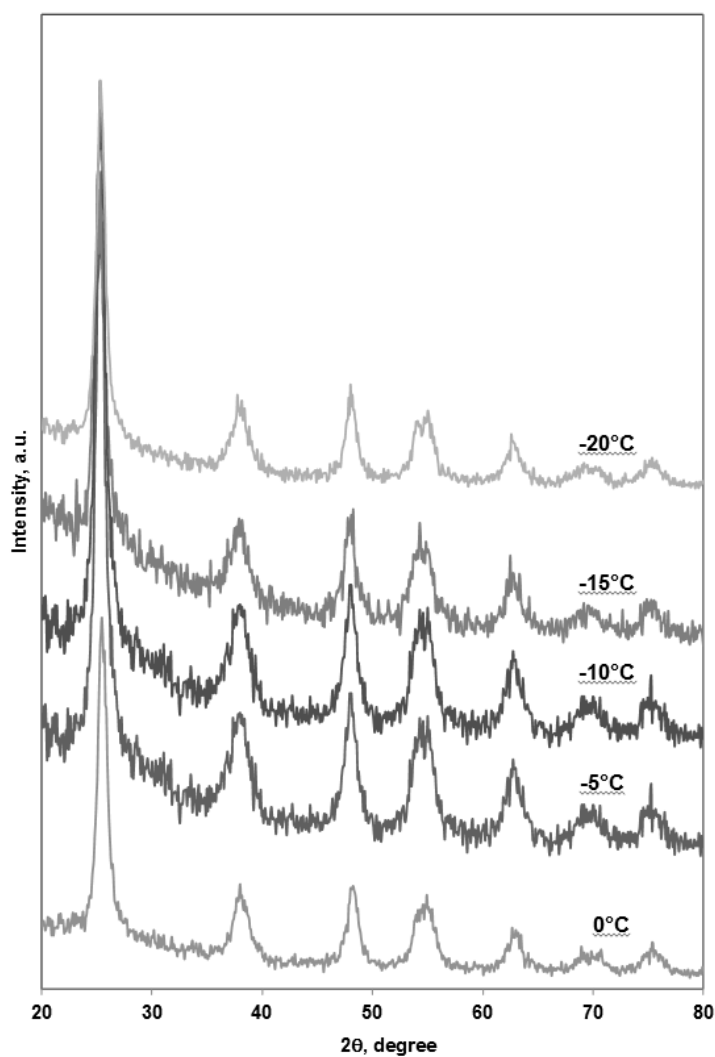
Figure 107 *XRD patters of NdTc at different synthesis reaction temperature*

In particular the use of Triton X-100 in the sol-gel synthesis reduces the average crystallites size from 17 to 9 nm.

From the Table 12 it is also evident the strong influence of sol-gel synthesis temperature on the final NdTc crystallite size.

The kinetics of the sol-gel process based on hydrolysis and condensation reactions of titanium alkoxides (TTIP) is an important parameter for the average crystallites size of final TiO_2. This process generally follows three different steps: the first stage is the formation of hydrolyzed monomers (Soloviev et al., 2001); the second step corresponds to the moment when the concentration of these monomers reached the level of critical supersaturation forming primary particles; the third step is the grow of primary particles by aggregation.

Baroša et al. showed that the reaction between TTIP and H_2O in n-propanol solution (hydrolysis) is very fast and not influenced by the synthesis temperature.
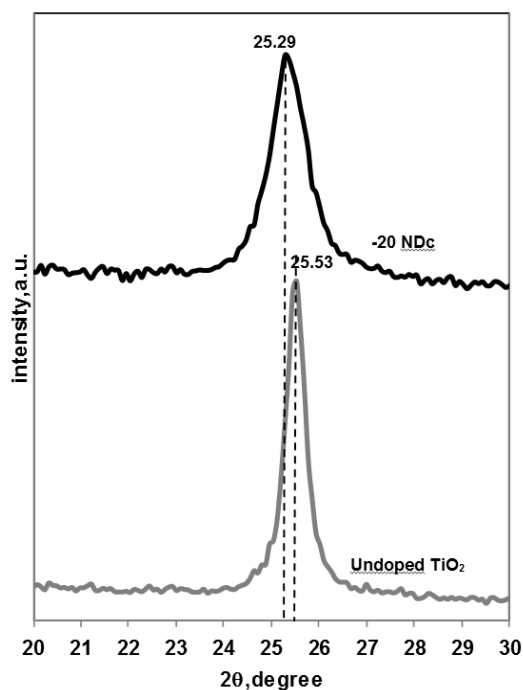
Figure 108 *XRD patters of NDc of undoped TiO_2 and -20 NDc sample in the range 20-30 degree*

The formation of titanium-oxo-alkoxy clusters through the alcoxolation reaction is instead influenced by the temperature according to Arrhenius law (Baros and Adnadevic, 2011). The rate of clusters nucleation has decreased by decreasing the temperature. As a consequence, the final size of TiO_2 nanoparticles is lower (Baros and Adnadevic, 2011). Similarly, in the present study, the effect of decreasing the sol-gel synthesis temperature shows that N-TiO_2 crystallite size decreases up to about 6 nm when the temperature was

184

equal to -20°C. Therefore, probably also in presence of ammonia aqueous solution, a lower synthesis temperature inhibited the rate of clusters nucleation.

Figure 108 illustrates the XRD patterns of -20 NDc sample and undoped TiO_2 obtained in the same synthesis conditions but without adding the ammonia aqueous solution.

The diffraction peaks related to (101) plane of -20 NDc sample shifts to a lower value of 2θ (25.29 degree) with respect to the diffraction peaks at 25.53 degree (related to the same (101) plane) of undoped TiO_2. Moreover the peak at 25.29 degree of -20 NDc becomes broader with reduced peak area. This may be because compressive strain increases as N replaces O in the TiO_2 structure due to differences in binding properties (Batzill et al., 2006). This result confirms that the crystalline structure of anatase has been doped with nitrogen.

VIII.2.1.3   Specific Surface area measurements

The catalysts were characterized by several techniques. Specific surface area (BET) was evaluated from dynamic N_2 adsorption measurement at -196°C, performed by a Costech Sorptometer 1040 after pretreatment at 150°C for 30 min in He flow.
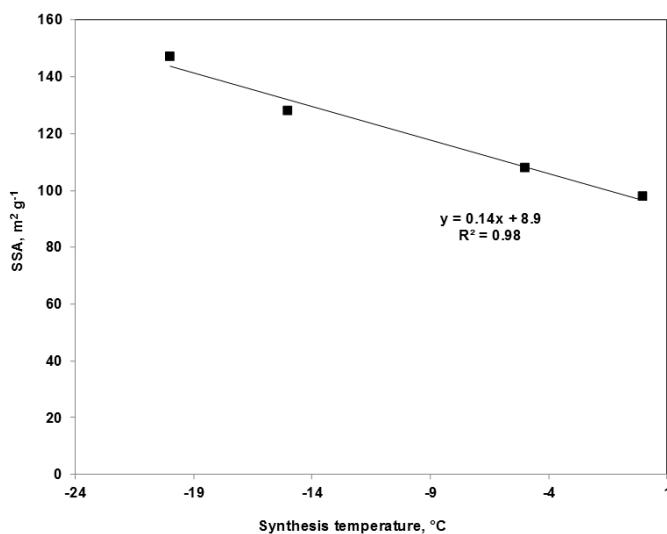
Figure 109 *Trend of NdTc specific surface area ($m^2 g^{-1}$) as a function of sol-gel synthesis reaction temperature*

The surface area of N-TiO_2 obtained at different synthesis temperature is shown in Table 11.

All the NdTgc catalysts show a higher surface area with respect to N-TiO_2. The higher surface area of NdTc catalysts is due to the lower

crystallites size caused by the use of Triton X-100. It is also observed that the surface area of the NdTc catalysts increases with the decrease of synthesis temperature (Figure 109). This can be attributed to decrease of the crystallites size, as discussed in XRD analysis (2.1.2 section).

VIII.2.2   Characterization of N-TiO$_2$ immobilized on glass spheres

VIII.2.2.1   Raman spectra

Laser Raman spectra were obtained at room temperature with a Dispersive MicroRaman (Invia, Renishaw), equipped with 514 nm diode-laser, in the range 100-2000 cm^{-1} Raman shift on powder and structured samples.
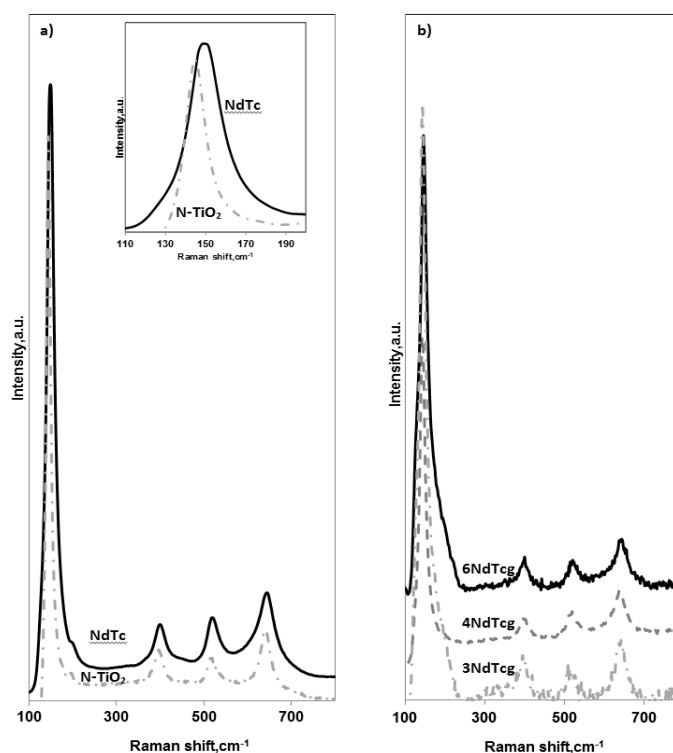
Figure 110 *a) Raman spectra of N-TiO$_2$ and NdTc samples in the range100-800cm^{-1} and Raman shift of E$_g$ modes in the range 110-200 cm^{-1}*

186

(insert); b) Raman spectra of NdTc on glass spheres in the range 100-800cm^{-1}

The structural properties of the NdTc immobilized on glass spheres (Table 12) were investigated by Raman spectroscopy. Figure 110 displays the Raman spectra of the 3NdTcg 4NdTcg and 6NdTcg respectively. All the samples exhibit the characteristic Raman-active modes of the anatase TiO_2 phase (Parker and Siegel, 1990). The presence of glass substrate did not change the Raman modes of supported N-TiO_2 that are really similar to the Raman modes founded for the -20NdTc powder.

VIII.2.2.2   SEM

Scanning electron microscopy (SEM) (Assing,mod. LEO 420) was used to characterize the morphology of NdTgc samples at an accelerating voltage of 20 kV.The surface morphology of NdTc photocatalysts immobilized on glass spheres is studied by scanning electron microscopy whose results are presented in Figure 111.
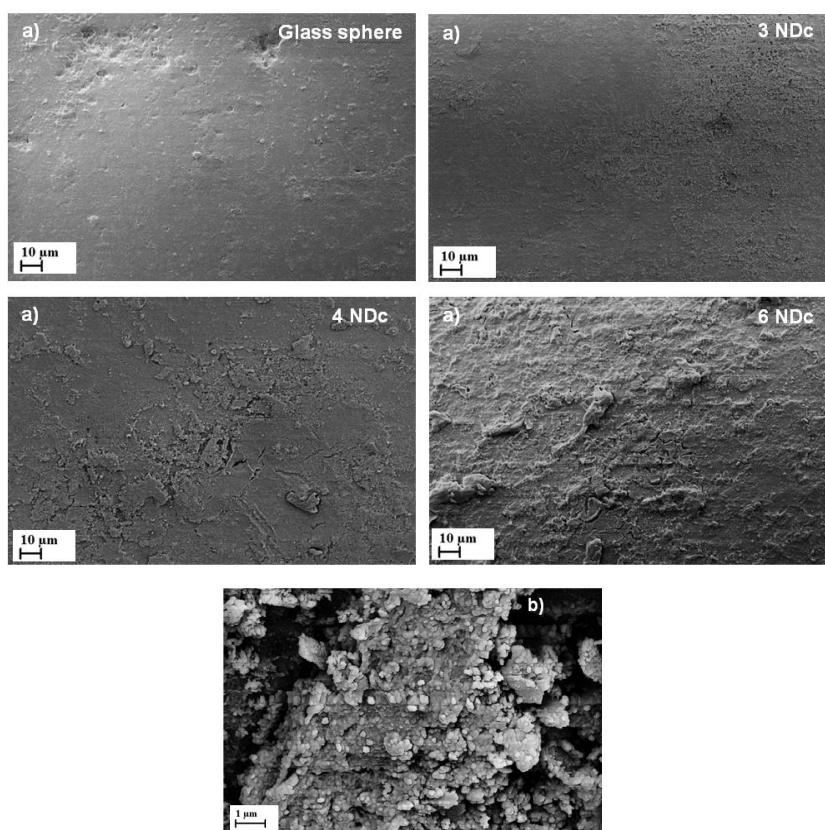
Figure 111 *a)SEM images of glass sphere, 3NdTcg, 4NdTcg and 6 NdTcg; b) SEM images of morphology of NdTc on glass spheres*

The SEM images demonstrate the presence of N-TiO$_2$ deposited on the surface of glass spheres, and rough surface of the coating, which is necessary for the good photocatalytic activity of the NdTc (Kumar and Bansal, 2013). As shown in Figure 111, the first three coating steps are not covering the entire surface but additional coats lead to a complete coverage.

It is obvious that N-TiO$_2$ is more uniformly distributed on the surface of 4 NdTgc and 6 NdTgc as compared to 3 NdTgc (Figure 111a). The morphology of N-TiO$_2$ nanoparticles seems to be as pseudo spherical (Figure 111b) in all samples and there is no considerable change in morphology for the samples 4 NdTgc and 6 NdTgc. Moreover SEM images evidence that N-TiO$_2$ is well dispersed and its distribution is homogeneous with the formation of fine and well dispersed nanoparticles.

VIII.2.2.3   Specific Surface area measurements

Table 12 presents the BET surface area values for glass spheres, 3 NdTgc, 4 NdTgc and 6 NdTgc. It can be seen that the BET surface area of coated glass spheres increased by a factor of almost 3 for 3 NdTgc and 12 for sample 6 NdTgc as compared to the uncoated glass spheres. This increase in surface area is attributed to the NdTc coating which results in a porous and rough surface, as observed from SEM analysis. Thus the increase in surface area should help in increasing the N-TiO$_2$ exposure to light which in turn would increases the photocatalytic reaction rate.

VIII.2.3   Photocatalytic activity tests

VIII.2.3.1   Dark adsorption of MB and EBT in presence of glass spheres

Prior to the photocatalytic removal, the dark adsorption and the photolysis of MB and EBT in presence of uncoated glass spheres were evaluated. The concentration of MB and EBT was 5 mg L^{-1} for both dyes.
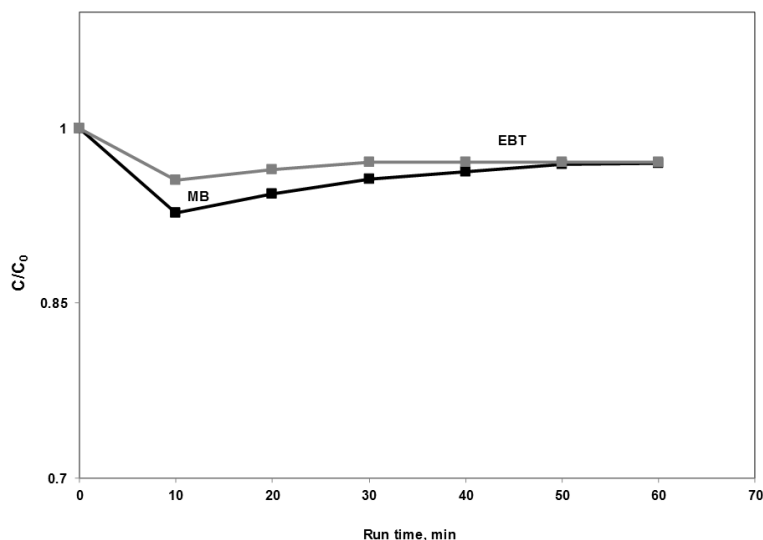
Figure 112 *Dark adsorption of MB and EBT on uncoated glass spheres*

In Figure 112 the adsorption of dyes was studied by passing each dye solution through glass spheres under dark conditions until get the constant value. After 10 minutes, it was observed a decrease of concentration of dyes, equal to 7 and 5 % for MB and EBT, respectively. Then, dyes concentration started to increase, reaching a decrease of 4 and 3% for MB and EBT respectively after 30 min and this value was almost the same up to 1 h.

The decrease in concentration of dyes was due to the adsorption of dye on the surface of glass spheres.

VIII.2.3.2   Photolysis of MB and EBT in presence of glass spheres

After the dark period, the solution was irradiated with UV light or visible light. The uncoated glass showed no decolourization activity but only a little dye desorption due to the increase of temperature up to about 35°C, caused by light sources (Figure 113).

189
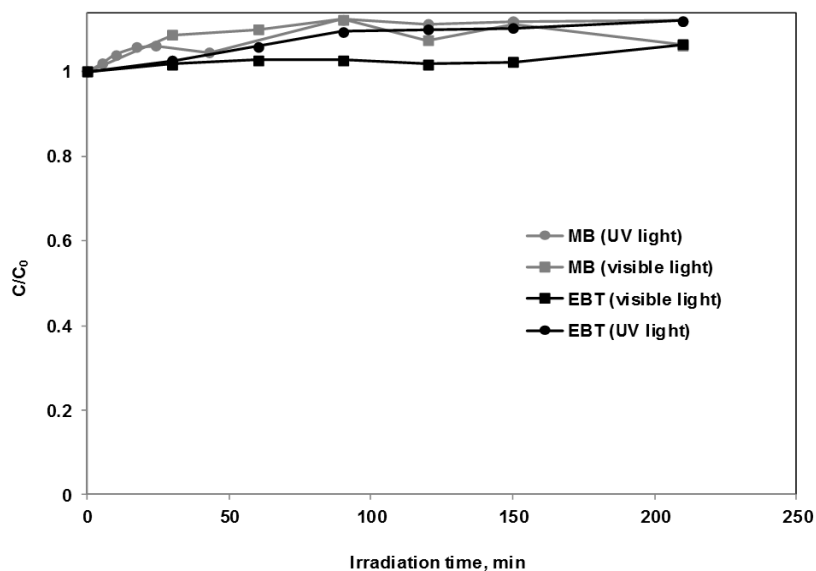
Figure 113 *Photolysis of MB and EBT in presence of uncoated glass spheres under UV and visible light irradiation*

VIII.2.3.3   Optimization of NDc amount on glass spheres

In order to define the best NDc amount deposited on glass spheres, MB dye has been chosen.

In Figure 114, the comparison of the photocatalytic activity obtained with the 3NdTcg, 4NdTcg and 6NdTcg samples is shown.

Firstly, it was evaluated the decolourization of MB due to the dark adsorption until get the constant value. All structured photocatalysts (3 NdTcg, 4 NdTcg and 6 NdTcg) have an initial step of adsorption corresponding to 20, 33 and 37% of MB decolourization respectively. After the dark period, the solution was irradiated with UV light and the reaction started to occur. Under UV light irradiation 3NDc, 4NDc and 6NDc catalysts showed a photocatalytic acitivity leading to a MB decolourization of about 20, 46 and 43 % respectively, after 107 min of irradiation time.

These results evidenced that up to NdTc amount of 0.34 wt % (4 NdTcg), photocatalytic activity markedly increased indicating that the overall of N-TiO$_2$ nanoparticles dispersed on the surface of glass spheres are effectively irradiated. For NdTc amount of 0.77 wt % (6 NdTcg), photocatalytic decolourization rate was almost the same of that one obtained with 4 NdTcg catalyst. This means that the amount of N-TiO$_2$ effectively irradiated did not change because the amount of NdTc added after four steps of dip-coating, masks the lower layers of NdTc. Thus, the best sample chosen to investigate

the stability and the ability to work with visible light irradiation and other types of dyes (EBT) was 4 NdTcg
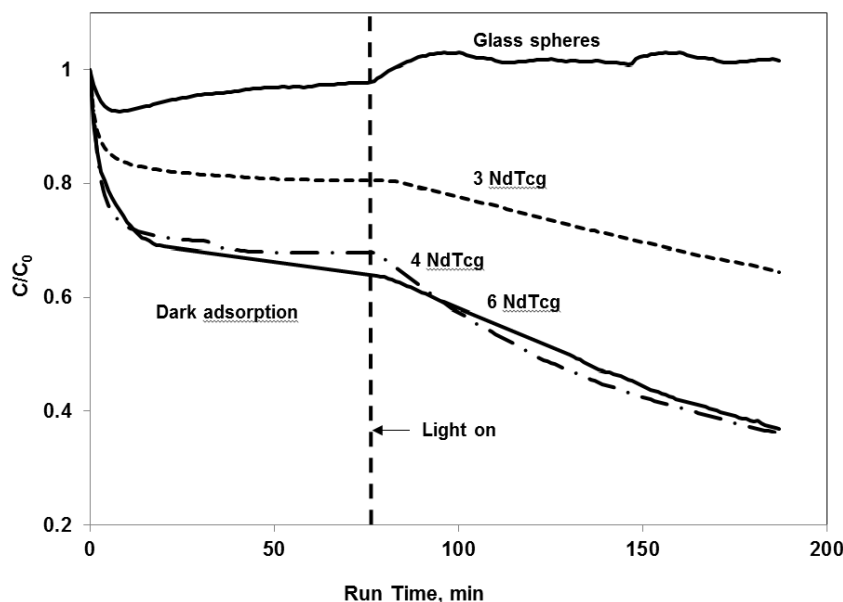
Figure 114 *Photocatalytic decolourization of MB under UV light irradiation (optimization of NdTc amount on glass sphere)*

VIII.2.3.4   Recyclability of 4NdTgc photocatalyst for

decolourization of MB

Recyclability is one of the most important factors in catalysis research. To confirm the recyclability of 4NdTcg sample, the photocatalytic decolourization reaction was repeated up to four cycles (Figure 115). The results demonstrated that there was 1–2% reduction of decolourization percentage after four cycles. The slight decrease in the decolourization rate may be due to the weakening of the dye adsorption ability. These results confirm that the photocatalytic activity of 4 NdTcg was nearly the same indicating that there is no leaching of NdTc from coated glass spheres. These results also confirm the stability of NdTc coated on glass spheres.
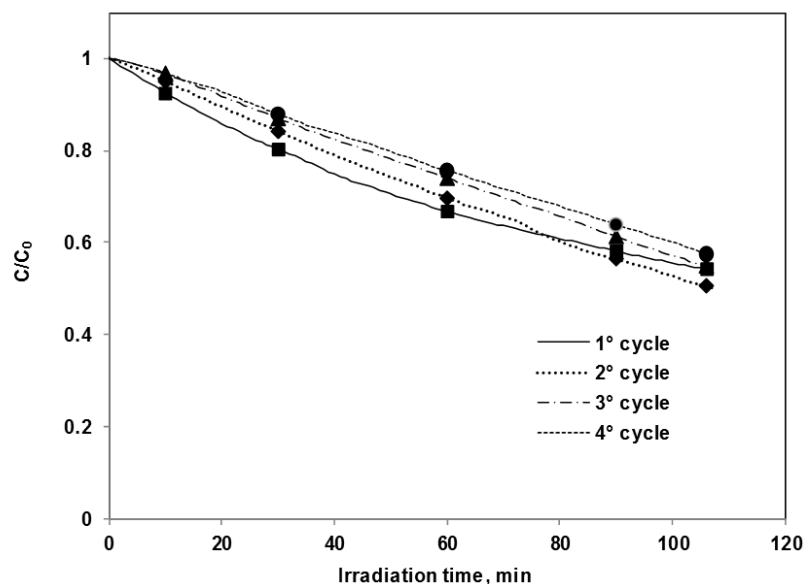
Figure 115 *Evaluation of MB decolourization performances obtained on 4NdTcg after 4 recycling experiments.*

VIII.2.3.5   *Photocatalytic activity under UV or visible light irradiation*

The 4NdTcg exhibited high photocatalytic activity also under visible light irradiation, allowing to obtain a decolourization of MB equal to 52 % after 210 min of irradiation (Figure 116). The system is also able to degrade EBT both under visible and UV light obtaining a decolourization of EBT equal to 31% and 41% under UV and visible light, respectively.

It is possible to observe that the photocatalytic MB decolourization activity was higher that one obtained for EBT. The different trend is linked to the different chemical nature of the two dyes. MB is classified as basic dyes due to cationic functional groups such as $-NH_3^+$ (Julkapli et al., 2014) while EBT is classified as an azoic dyes due to azo bonds ($-N=N-$) (Julkapli et al., 2014).The adsorptive affinity of MB on TiO_2 anatase phase is higher than an anionic azo dye, such as EBT, therefore photocatalytic decolourization activity was quicker for MB (Julkapli et al., 2014).
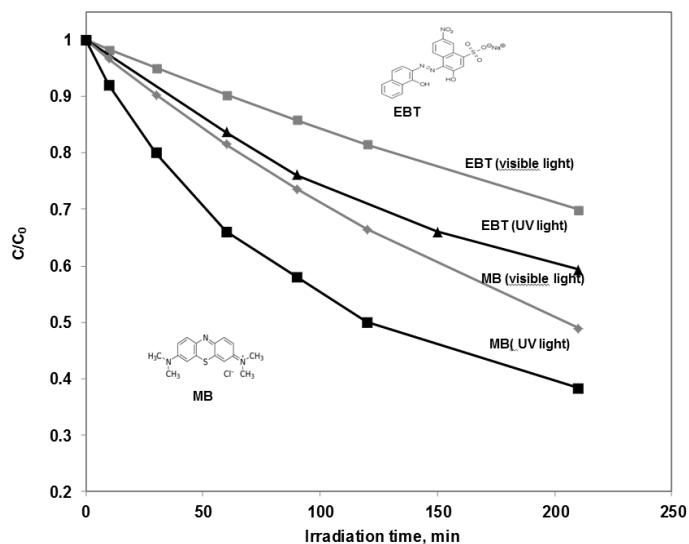
Figure 116 *Photocatalytic decolourization of MB and EBT under UV and visible light irradiation on 4NdTcg*
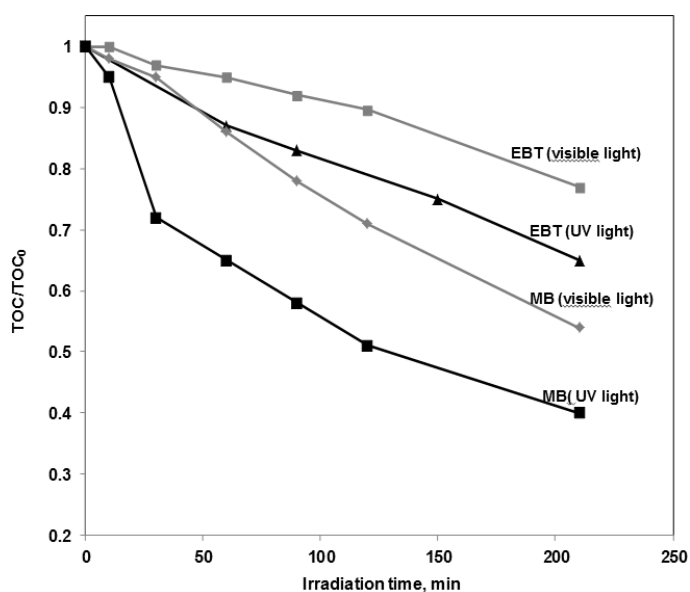
Figure 117 *Photocatalytic mineralization of MB and EBT under UV and visible light irradiation on 4 NdTcg*

The decolourization does not necessary correspond to the mineralization of the two target dyes. For this reason, the behavior of TOC has been

193

analyzed. The obtained results are reported in Figure 117. It is possible to observe a progressive decrease of TOC of aqueous sample as a function of irradiation time indicating that 4 NdTcg sample is also able to mineralize MB and EBT both under UV and visible light irradiation.

Visible active N-doped TiO_2 (NdTc) was successfully immobilized on glass spheres using sol-gel method starting from titanium isopropoxide and ammonia aqueous solution as nitrogen precursor. The first aim of the paper was to obtain the best synthesis condition for increase the specific surface area of the immobilized NdTc. It was found that the sol-gel synthesis temperature has a strong effect on crystallite size during the nucleation step. In particular, lower is the temperature lower is the value of NdTc crystallite size.

The amount of the NdTc on the surface of glass spheres increased with the number of dip-coating steps and varied from almost 0.22 wt% (three coating) to 0.77 wt% (six coatings). The efficiency of structured photocatalysts was evaluated in the decolourization of recalcitrant contaminants like methylene blue both under UV and visible light irradiation. All the samples showed high photocatalytic activity in decolourization of Methylene blue, but the optimal NdTc amount was found to be equal to 0.34 wt% obtained after four coatings. This structured photocatalysts still have great catalytic activities after four cycles and was able to remove also Erichrome black-T both in presence of UV and of visible light.

VIII.2.4   *Design of the fixed bed reactor: choice of the*

photoreactor geometry

The geometry of a photoreactor is strongly related to the source of irradiation, in particular, it has to be designed so as to collect the maximum of emitted light and to reduce the energy and investment costs. Packed bed reactors have usually an annular geometry and it is irradiated by a central lamp (Al-Ekabi et al., 1989). One of the main limits of this configuration is the uneven or partial photocatalyst's irradiation. Moreover, the uneven flow distribution also limits the amount of water in contact with the photocatalyst, negatively influencing the overall photoreactor performances (Moreira et al., 2010; Salaices et al., 2001, 2002; Serrano et al., 2010). With respect to the annular photoreactors, a flat plate geometry is scalable, and these types of reactors can be easily used with solar radiation, so they are very attractive and also provide an excellent configuration for efficient excitation of the visible light active photocatalysts (Otálvaro-Marín et al., 2014). The flat plate reactor design possesses: i) a fluid flow free from any dead or recirculation zones, obtaining a plug flow reactor; ii) ability to operate under

a wide range of liquid flow rates (flow regime should also be chosen carefully in order to avoid excessive velocities, turbulences and shear stresses that might damage the surface of the catalysts); iii) ability to be easily and efficiently integrated with an illumination system, in order to obtain the maximum model simplicity (the design of the reactor and the illumination system is aimed to deliver a high uniformity of the radiation field on the photocatalytic surface); iv) possibility to be configured for both liquid and structured catalyst side illumination (Vezzoli et al., 2013).

VIII.2.5   *Design of the fixed bed reactor: fluid dynamic*

conditions

The preliminary special domain used for the fluid dynamic modeling of the flat plate reactor system is depicted in Figure 118;
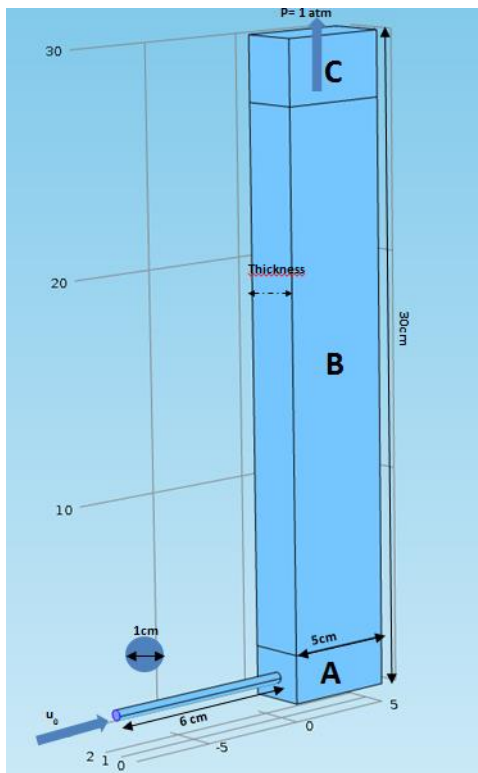
Figure 118 *Preliminary domain for the fluid dynamic model where a) is the homogenization zone; b) is the body of reactor where is settled the structured photocatalyst bed; c) the outlet zone*

because of the axial symmetry of the problem, it was studied on a semi-transversal section of the real domain. In the investigated flat plate reactor, a water flow is pumped through a 1 cm ID tube and it is send to the body of the reactor, filled by a packed bed of the structured photocatalyst. A bar is positioned over the inner zone to avoid the plug of the inlet by the structured photocatalyst. The photoreactor operates in continuous mode at steady-state condition. The modeling of the system was performed by using the software COMSOL Multiphysics 5.0 (License No.13073437,00-0f-fe-0a-73-34). The numerical simulation has been performed by COMSOL applying the finite elements method. The final mesh, after an independent study based on the knowledge of the physics indicated below, was constituted by 150849 volume elements, 16161 surface elements and 951 elements on edges. The fluid dynamics simulation was performed by assuming incompressible and isothermal flow (the temperature was set up to 293.15 K), by using the following physics:

- Free and porous media flow: modeling of the structured photocatalyst packed bed, together with the photoreactor zones free from filling components, from the point of view of a thermo-fluid problem, from which the fluid velocity components and pressure can be calculated;

In order to determine the velocity profiles for the laminar flow (Re < 15 for the system under investigation), inside the zones free from filling components, steady-state incompressible Navier–Stokes equations (Eq.48-49) are used for the momentum balance. So, the governing equations for continuity and the momentum balances could be written as follows:

$$\nabla \cdot u = 0 \qquad\qquad \text{Eq.48}$$

$$\rho(v \cdot \nabla)v = \nabla \cdot [-pI + \mu(\nabla v + (\nabla v)^T)] \qquad\qquad \text{Eq.49}$$

Where:

ρ = fluid density, kg m^{-3}

v = velocity vector, m s^{-1}

p = pressure, Pa

I = identity matrix

μ = fluid dynamic viscosity, Pa s

The boundary conditions are as follows: in the inlet section the normal average velocity was fixed (2.5 l h^{-1}); on the contrary, at the outlet section atmospheric pressure was fixed. Moreover, no slip boundary condition was considered for all walls of the photoreactor and the structured photocatalyst. The porous medium (that is the structured photocatalyst packed bed) was

196

modeled using the Brinkman equation (Eq.50), which can be written as follows:

$$\frac{\rho}{\varepsilon_p}\left((v\cdot\nabla)\frac{v}{\varepsilon_p}\right)=\nabla\cdot\left[-pI+\frac{\mu}{\varepsilon_p}(\nabla v+(\nabla v)^T)-\frac{2\mu}{3\varepsilon_p}(\nabla\cdot v)I\right]-\frac{\mu}{k}v \quad\text{Eq.50}$$

Where:

ε_p = bed porosity = 0.55

k = bed permeability, m^2

The latter can be calculated easily by the Rump-Gupte equation (Eq.51) (Fatehi and Kaviany, 1994):

$$k=\frac{\varepsilon_p^{5.5}}{5.6}d^2 \quad\text{Eq.51}$$

Where:

d = glass spheres diameter = 4.3 mm

In order to determine how the thickness of the reactor influences the velocity profiles inside the flat plate reactor, thickness was varied in the range (1<y<4 cm). The results of the mathematical modeling are shown in Figure 119. In particular, Figure 119 shows the behavior along the reactor height in terms of average velocity-maximum velocity ratio ($\bar{v}/v_{max}$), which could be related to the length of entrance, or the length at which the velocity profile is fully developed. The results demonstrated that over the inlet tube (z=1 cm) there is a zone in which the profile is continuously developing. Actually, at the bed inlet, the profile rapidly leads to a plateau value, which is sign of fully developed profile. In particular, inside the bed, the average velocity value is very close to the maximum value, so the profile ought to be almost flat. The same behavior could be observed, by varying the reactor thickness, in all cases. What varies is the velocity with which the profile is developing inside the photocatalytic bed. In fact, looking at the inset of Figure 119, which shows the $\bar{v}/v_{max}$ ratio at the bed inlet against the reactor thickness (y-direction), it could be observed that there is a maximum value at 2.5 cm, which means that at this specific thickness the approach to the fully developed profile is faster.
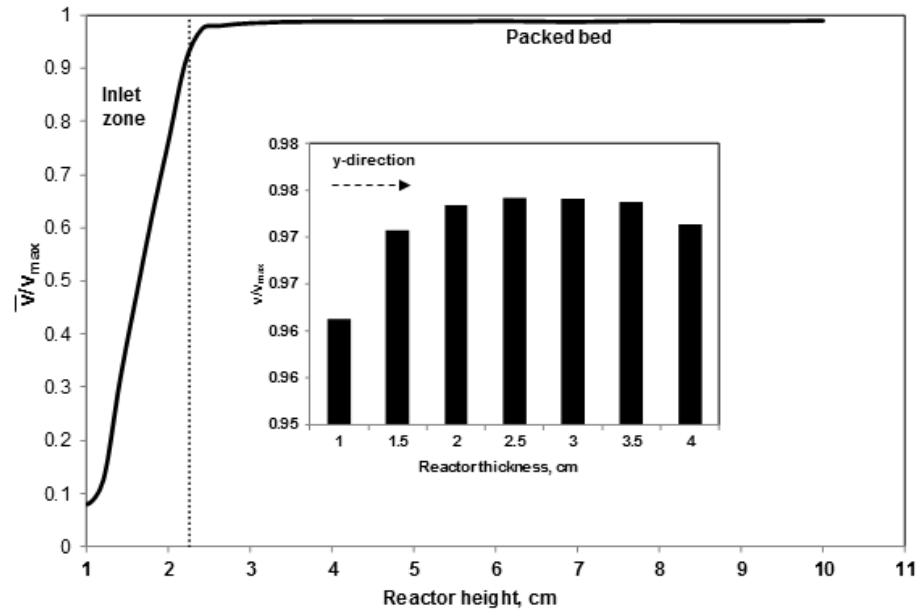
Figure 119 *Behavior of $\bar{v}/v_{max}$ as a function of reactor height (z-direction) and behavior of $\bar{v}/v_{max}$ as a function of reactor thickness at the bed inlet (inset).*

Moreover, in Figure 120a it is possible to observe the flow lines along the photoreactor, while in Figure 120b the flat profile which is developed inside the packed bed. So, this simulation demonstrates that this type of reactor configuration allows to obtain a plug flow behavior inside the photocatalytic bed, which guarantees a perfect homogenization of the fluid across the reactor width

VIII.2.6   Design of the fixed bed reactor: radiative transfer

model

The photons' distribution inside the photoreactor has been modeled by using the Helmholtz equation:

$$\nabla \cdot \left(-c\nabla I\right) + aI = f \qquad \text{Eq.52}$$

Where :

I=light intensity,W cm^{-2}

$$c = \frac{1}{3(d+a)} = \text{diffusion coefficient, cm}$$

198

a= structured catalysts absorption coefficient, cm^{-1}

d= structured catalysts scattering coefficient, cm^{-1}

f= source term=0
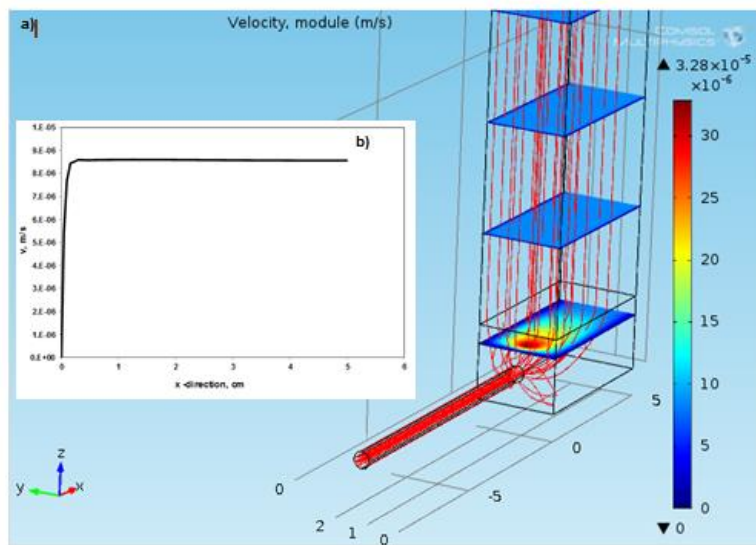
Figure 120 *a) The flow lines along the photoreactor, b) Flat profile inside the packed bed*

The source term *f* in this case is equal to zero because no light source is present inside the reactor.

The values of *a* and *d* have been estimated from UV-vis DRS spectra of the N-doped TiO_2 photocatalyst supported on glass spheres following the method reported in (Vincenzo Vaiano, 2014), that strictly depends on the emission spectrum of the light source. With this method, *a* and *d* were found equal to 78 and 22 cm^{-1}, respectively.

In order to simplify technical details of the analysis, the boundary Dirichlet condition was chosen on the external windows of the reactor. In a preliminary configuration, an 8 Watt UV-lamp provided by Philips was used. The UV-lamp has a cylindrical shape with a diameter of 1.6 cm and a height of 27 cm. This lamp has an emission spectrum centered at 365 nm (modello fotoni). The UV-light intensity at the external surface of the lamps was measured by a UV meter and it is equal to 0.023W cm^{-2}.

The lamps in this case cover the entire transparent surfaces of the reactor. So, the preliminary height of the reactor was chosen equal to the height of the UV lamps. For what regards the photoreactor thickness, taking into

account the results obtained by the fluid dynamic evaluation, it was chosen equal to 2.5 cm.

The numerical simulation has been performed by COMSOL applying the finite elements method. The final mesh, after an independent study based on the knowledge of the specific physics, was constituted by 9834 volume elements, 9834 surface elements and 1330 elements on edges.

The results of the mathematical solution of Helmholtz equation are reported in Figure 121.
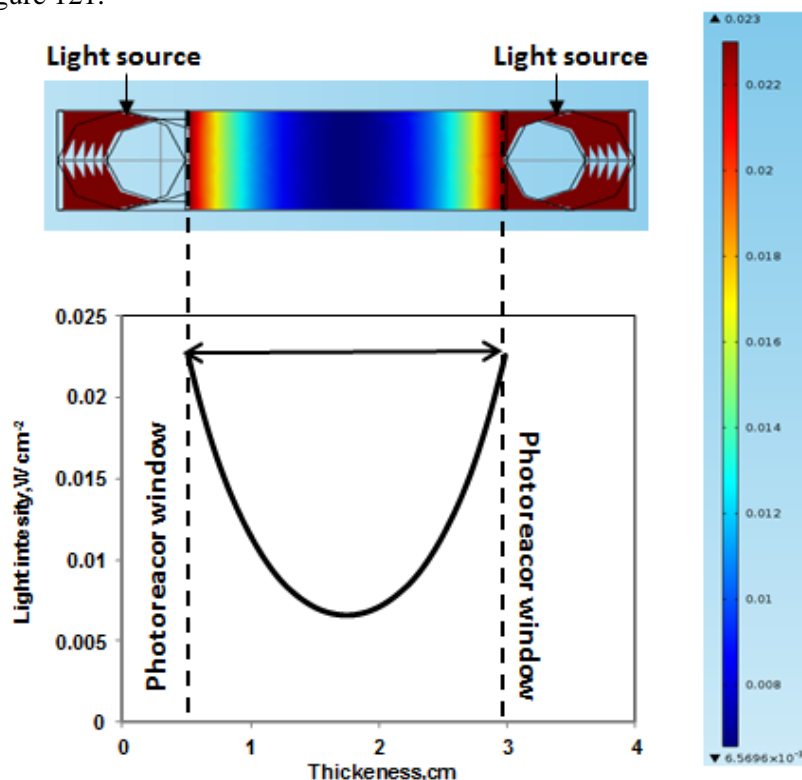
Figure 121 *The Helmholtz model of light distribution inside the reactor; Light sources: UV-lamps with intensity equal to 0.023 W cm^{-2}; Reactor thickness: 2.5 cm*

The simulation of the light distribution shows that the light profile, by using the 8 Watt UV-lamps, is characterized by a strong attenuation of the light intensity (almost 70%) inside the core of the reactor.

VIII.2.7   *Design of the fixed bed reactor: final design*

Among the types of photoreactor design, the flat plate reactor seems to be the more flexible choice for the scale-up, because it is the best compromise between construction and irradiation features. In order to optimize the design of the photoreactor, it is needed to take into account the results obtained by the fluid dynamics and the photons' distribution simulation along the reactor width. In particular, in this case the only design variable was the reactor thickness, because it is the only one that can affect significantly both the fluid dynamic behavior and the photons' distribution. So, for the final design, it was considered a reactor thickness equal to 2.5 cm, because it is the minimum thickness able to guarantee a plug flow behavior inside the structured bed, and at the same time to minimize the photons' loss inside the core of the rector.

VIII.3 Photocalytic activity tests with the designed continuous

fixed bed reactor

VIII.3.1   *Laboratory scale photoreactor*

The schematic diagram of the laboratory scale photoreactor is shown in Figure 122. The laboratory scale photoreactor geometry designed as shown in the previous sections is composed by a flat plate body with two pyrex windows irradiated by five UV (provided by Philips; nominal power: 8 Watt) or visible light (provided by Philips; nominal power: 8 Watt) sources for each window respectively (Figure 122). The photoreactor operates in continuous mode at steady-state condition. The stock solution containing the pollutant to be removed was prepared and collected in the feed tank. The feed tank is equipped with a stirrer to assure the complete homogenization of the stock solution, and an air distributor device (Q_{air}=150cm^3 min^{-1} (STP)).
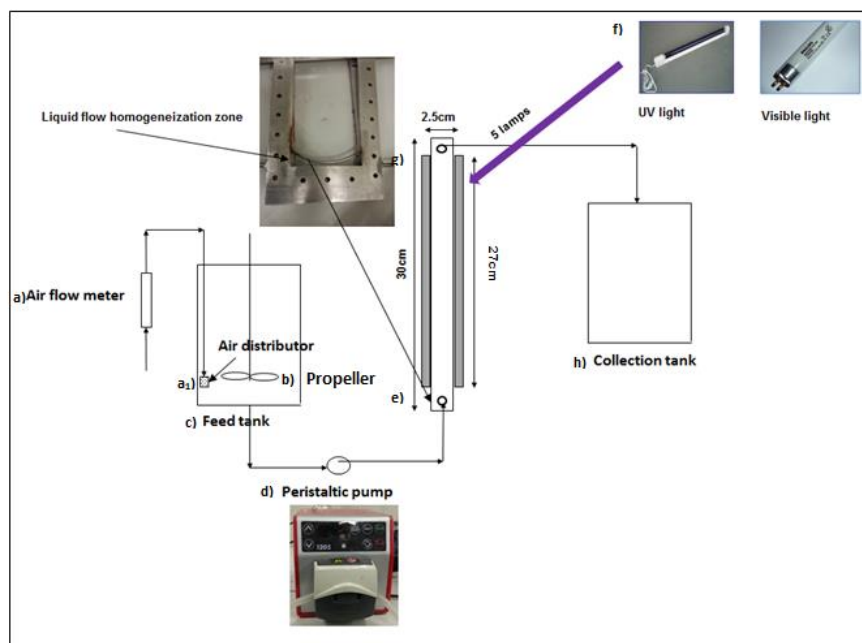
Figure 122 *Experimental set up apparatus: (a) air flow meter;(a₁) air distributor; (b) propeller; (c) feed tank; (d) peristaltic pump, (e) inlet of the flow in the reactor; (f) light sources; (g) outlet of liquid flow; (h) collection tank.*

The feed solution was pumped from the feed tank to the photoreactor using two peristaltic pumps (Watson Marlowe 120s) capable of producing a liquid flow rate in the range 0.56-2.5L h^{-1}. The overall liquid stream is fed from the bottom of the reactor by means of two stainless steel tubes with ID equal to 1 cm. The amount of structured catalyst was equal to 372 g. The liquid stream passes through the photocatalytic bed and finally comes out from the top of the reactor, being collected in a tank. The liquid sample was withdrawn on the top of the photocatalytic bed.The pH of the reaction mixture was not adjusted (natural solution pH) and the temperature was controlled before and after the flat plate body, in particular it varies from 20 to 30°C. In order to obtain the kinetic parameters using the optimized design, photocatalytic tests were carried out using methylene blue (MB) as model pollutant. Liquid samples were analyzed by spectrophotometric measurements (Perkin Elmer UV-Vis spectrophotometer at λ = 663 nm) in order to determine the changes in MB concentration.

VIII.3.2   *Experimental results using UV or visible light sources*

The photocatalytic tests were carried out using MB inlet concentration equal to 10 ppm. The light sources were switched on after the complete adsorption of MB on the structured catalysts surface. Preliminary experiments were carried out in order to verify that MB was degraded by the heterogeneous photocatalytic process. In the absence of structured catalyst, no significant decrease in MB concentration was observed during illumination, both with UV light and visible light irradiation. The MB conversion profiles, as function of contact time at steady-state conditions obtained in presence of UV and visible light irradiation, are reported in Figure 123. It can be seen that MB conversion increased with the increase of the contact time when UV light was applied, in the presence of the structured photocatalyst, in fact, MB conversion reached a value of about 75% for a contact time equal to 2.5 h.
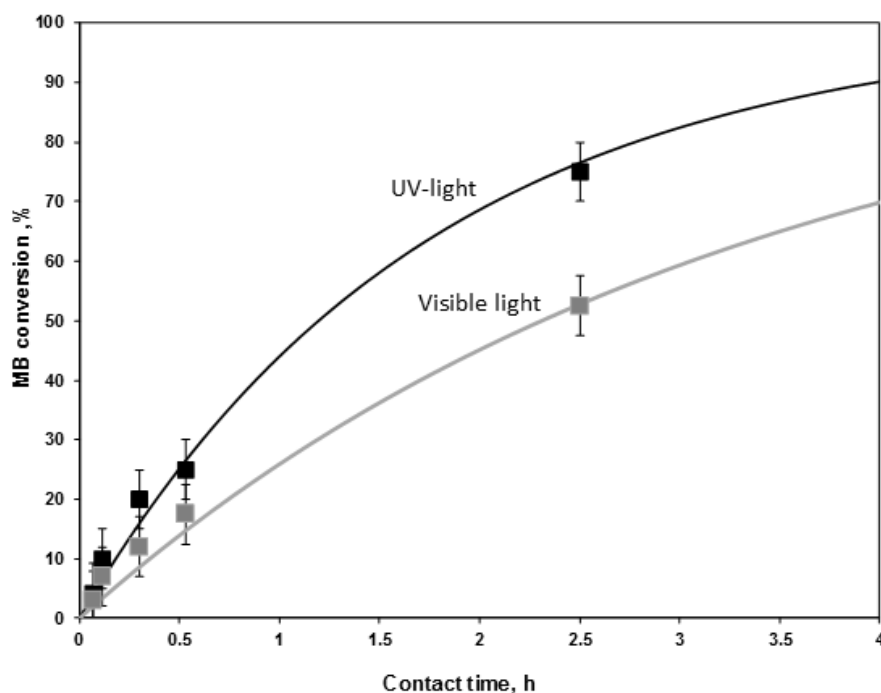
Figure 123 *MB conversion profiles as function of contact time using UV or visible light irradiation*

It was also performed visible light driven photocatalytic degradation of MB over the structured catalyst and the results are presented in Figure 123. It was observed, also in this case, that the presence of the structured catalyst led to a significant removal rate, with a MB conversion equal to 50% for a

contact time equal to 2.5 h. This is a very interesting result, in view of the implementation of a photoreactor, which would be processed also with a solar light irradiation.

VIII.3.3 *Kinetic modeling of the continuous fixed bed reactor*

irradiated by UV light

The kinetic model has been developed considering plug flow behaviour inside the packed bed, as shown by the fluid dynamic study. Therefore, the MB mass balance can be written as:

$$Q\frac{dC}{dV} = r(C,\bar{I}) \cdot \rho_{cat}$$
Eq.54

Where:

Q=Total liquid flow rate, $l\,h^{-1}$

C=MB concentration, ppm

V= reactor volume, l

$\rho_{\chi at}$=bulk density of structured catalyst, $g\,l^{-1}$

$\bar{I}$ = average light intensity inside the photoreactor, $W\,dm^{-2}$

The boundary condition for the Eq.6 is:

V=0   *C=C₀=MB inlet concentration*

The kinetic expression employed in the model is the following:

$$-r = K \cdot f_C \cdot g_I \cdot h_{C_0}$$
Eq.55

$$f_C = \frac{b \cdot C}{1 + b \cdot C}$$
Eq.56

$$g_I = \bar{I}$$
Eq.57

$$h_{C_0} = e^{-\alpha\left(\frac{b \cdot C_0}{1 + b \cdot C_0}\right)}$$
Eq.58

Where:

K=kinetic constant, $mg_{MB}\,g_{cat}^{-1}\,h^{-1}\,W^{-1}\,dm^2$

b= adsorption constant of MB, $l\,mg^{-1}$

Equation 8 is similar to the Langmuir-Hinshelwood rate law used in other studies (Sivalingam et al., 2003b).

In the hypothesis of keeping the reactant concentration constant, the dependence of reaction rate on photonic flux (Eq.9) is the same reported in literature (Camera-Roda et al., 2005; Palma et al., 2010b), which presented a simple approach for the design of photocatalytic reactors. $\bar{I}$ has been evaluated from the results of Helmholtz equation obtained from COMSOL Multiphysics (version 5.0), according to the Eq.59

$$\bar{I} = \frac{2 \cdot \int_0^{\frac{L}{2}} I(y) \cdot dy}{L} \qquad \text{Eq.59}$$

Where:

I(y)=light intensity profile as a function of photoreactor thickness,W.dm^{-2}

L= phoreactor thickness, cm

The Eq.59 allows to take into account that the light penetration inside the reactor decreases because of the strong blue colour of the structured catalyst that is a function of the amount of MB adsorbed on its surface. So, this phenomenon acts as a screening effect for the penetration of light, similar to the screening effect due to the increase of the catalyst concentration in a slurry photoreactor configuration (Konstantinou and Albanis, 2004). This effect was evaluated utilizing the parameter α, considering a first order correlation, similar to Lambert-Beer law

VIII.3.3.1   Evaluation of adsorption constant of MB on structured photocatalyst

The adsorption equilibrium was evaluated in batch conditions monitoring the concentration of MB as function of run time for different MB concentrations. The behavior of the amount of MB adsorbed on the structured catalyst (C^*) is a function of the initial MB concentration (C_0) and it is similar to a Langmuir adsorption isotherm (Sannino et al., 2013d).Thus, for the adsorption of MB on the active surface of the structured photocatalyst (Herney-Ramirez et al., 2010a), it is possible to write:

$$C^* = \frac{b \cdot C_0}{1 + b \cdot C_0} \qquad \text{Eq.60}$$

Where:

C^*: amount of MB adsorbed [g_{MB}/g_{cat}]

205

C_m: maximum absorbable value of C^*

C_0: initial concentration of MB in solution [ppm]

The Langmuir isotherm can be rearranged to give:

$$\frac{C_0}{C^*} = \frac{1}{bC_m} + \frac{1}{C_m} \cdot C_0$$ Eq.61

Plotting C_0/C^* as a function of C_0 produces a straight line with: slope=$1/C_m$ and intercept=$1/bC_m$ (Figure 124).
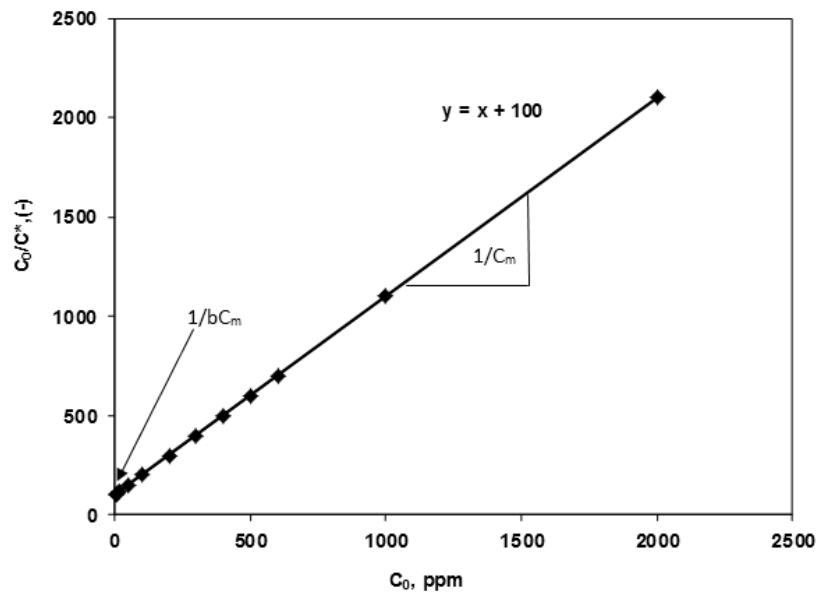
Figure 124 *Evaluation of MB adsorption constant on structured catalyst*

The value of *b* was calculated from the Eq.61, utilizing the experimental data, and it was equal to 0.01 [l mg⁻¹].

VIII.3.3.2 Evaluation of kinetic parameters

Utilizing the Eq.6 and Eq.7, MB mass balance can be written as:

$$Q \cdot \frac{dC}{dV} = -K \cdot \frac{b \cdot C}{1+b \cdot C} \cdot \bar{I} \cdot e^{-\alpha\left(\frac{b \cdot C_0}{1+b \cdot C_0}\right)} \rho_{cat}$$ Eq.62

The Eq.62, together with the boundary condition, was solved by the Euler iterative method. From the simulation made by the mathematical model, it is

possible to estimate the constants K and α by fitting the experimental data reported in Figure 125 as a function of inlet MB concentration in the range 3.6-16 ppm and with a liquid flow rate of $1.45\,l\,h^{-1}$.
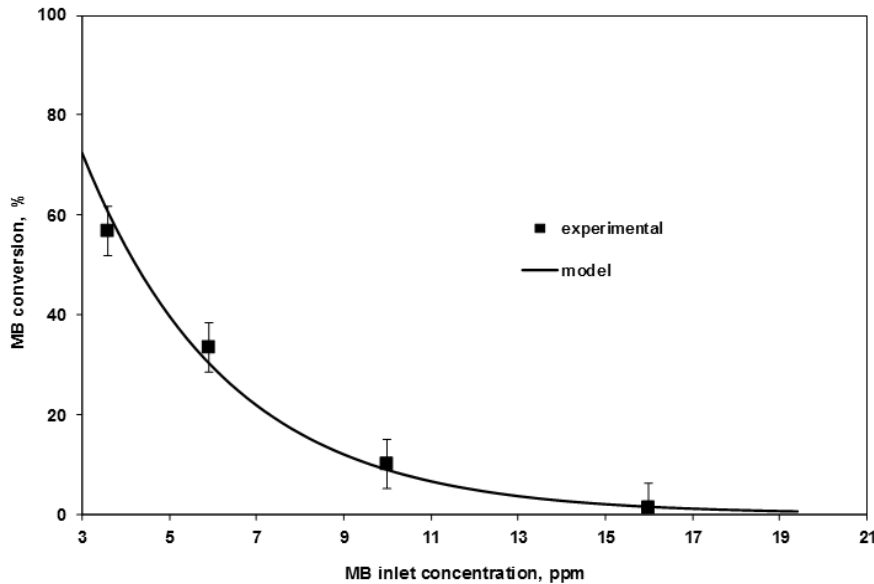
Figure 125 *MB conversion as a function of inlet concentration; comparison between model calculation and experimental data to find the model constant. Light sources: UV-lamps; liquid flow rate: 1.45l h*$^{-1}$

The fitting procedure was done by using the least squares approach obtaining the value of K: 1477 ($mg_{MB}\,g_{cat}^{-1}\,h^{-1}W^{-1}\,dm^2$) and α: 43 (-). After obtaining the kinetic parameters (K and α), the accuracy of the developed model was tested by comparing the calculated MB conversion with the experimental tests as function of contact time (Figure 125). The calculated values are in good agreement with the experimental data.
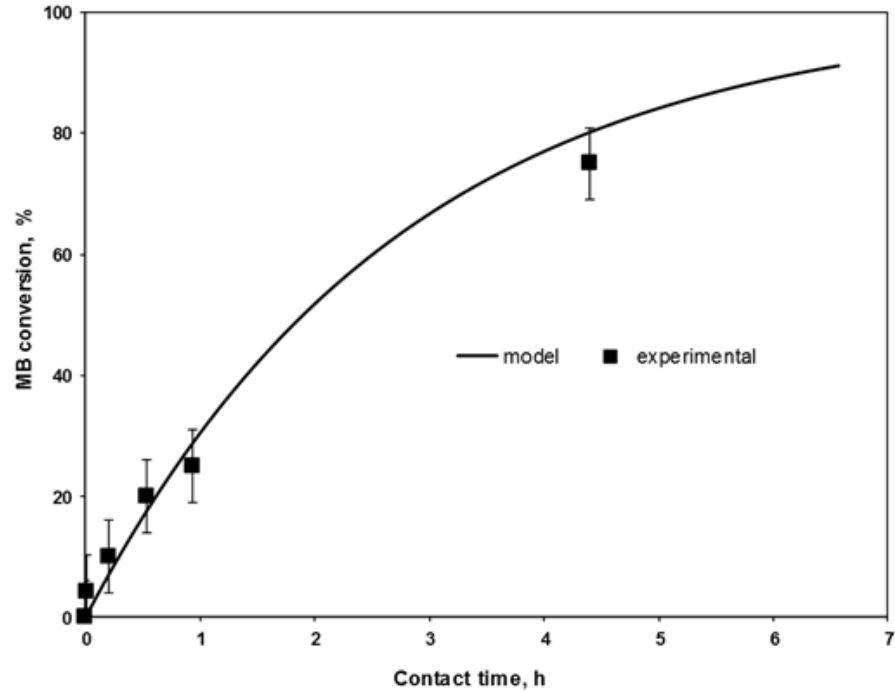
Figure 126 *Experimental and predict data at different contact times Light sources: UV-lamps; inlet MB concentration. 10ppm*

VIII.3.3.3   Influences of light distribution on photocatalytic performances

Since the light intensity strongly depends on the distance from the external irradiated windows, the simulated profile of MB conversion inside the reactor has been obtained according to the Eq.63

$$v_z(y) \cdot \frac{dC(z,y)}{dz} = -K \cdot \frac{b \cdot C(z,y)}{1+b \cdot C(z,y)} \cdot I(y) \cdot e^{-\alpha\left(\frac{b \cdot C_0}{1+b \cdot C_0}\right)} \rho_{cat} \qquad \text{Eq.63}$$

Where:

$v_z(y)$= component of velocity vector along z-direction, dm h^{-1}

In this case $v_z(y)=v_{max}$, since, as evidenced in section 2.3, the fluid dynamic conditions in the packed bed are similar to those of a plug flow, so v_{max} is the maximum velocity that is equal at any given x-direction. Since the light intensity depends on the y-direction, at any given y the MB concentration it is only a function of the z-direction. The obtained results are reported in

208

Figure 127. From the results it is evident that reaction rate is affected by the local photons' "concentration" so, the experimental data lie in the simulated profiles.
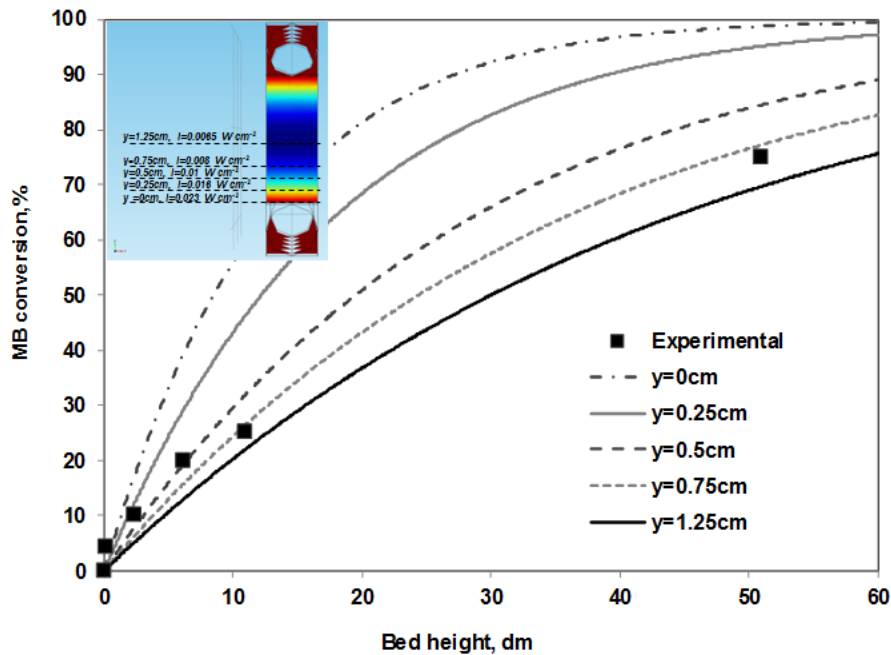
Figure 127 *MB conversion as a function of the packed- bed height (z-direction) for different distances from the irradiated window (y-direction).*

VIII.3.4   *Influences of light distribution on photocatalytic performances: possible solution for reducing the reactor volume*

The results obtained from the model and, in particular, the light intensity profiles, as function of the reactor thickness, suggest that the photoreactor performances could be enhanced by increasing the local photons' concentration. This could be achieved by changing the light sources. In particular, UV-lamps are replaced with commercial UV-LEDs (NICHIA NVSU233A(T), U365). Nowadays, LEDs are replacing traditional incandescent lamps in many applications, owing to much higher efficiency in light-electricity conversion. Further advantages of LEDs derive from the

small dimensions, robustness, and the long lasting (hundred thousands of hours compared to thousands of hours in the case of classical lamps). In this case the UV-LEDs are located directly on the photoreactor windows. Considering that the nominal UV light intensity is equal to 5.87 W cm^{-2}, the solution of the equation allows to obtain the light intensity as function of reactor y-direction (Figure 128).
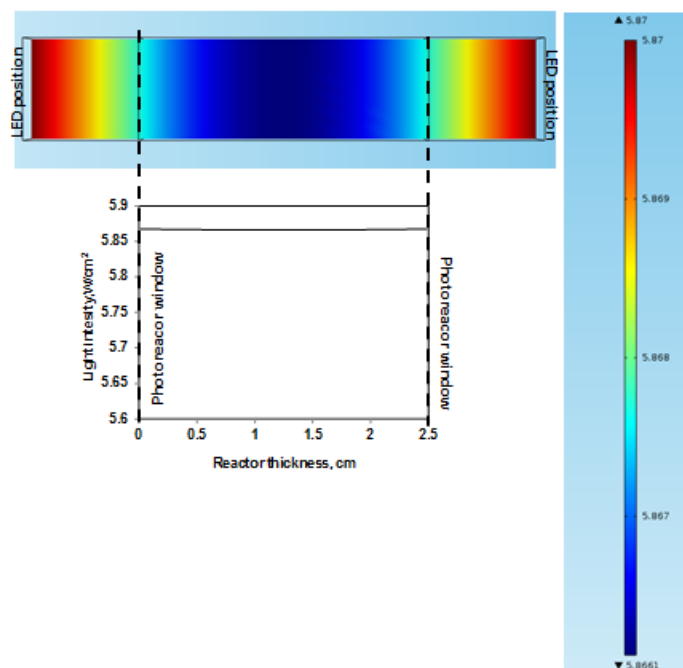
Figure 128 *The Helmholtz model of light distribution inside the reactor; Light sources: UV-LEDs with intensity equal to 5.87 W cm^{-2}; Reactor thickness: 2.5cm*

It is possible to observe that using UV-LEDs the local photons' "concentration" did not change also inside the core of the reactor. Also in this case, the mathematical model (Eq.52) was solved with the kinetic parameters previously determined with a light intensity of 5.87 W cm^{-2}. The result of the simulation is shown in Figure 129. In this case the reactor volume required for obtaining the total MB conversion could be drastically reduced. This data is very important to define a flexible design of a continuous bed photoreactor.
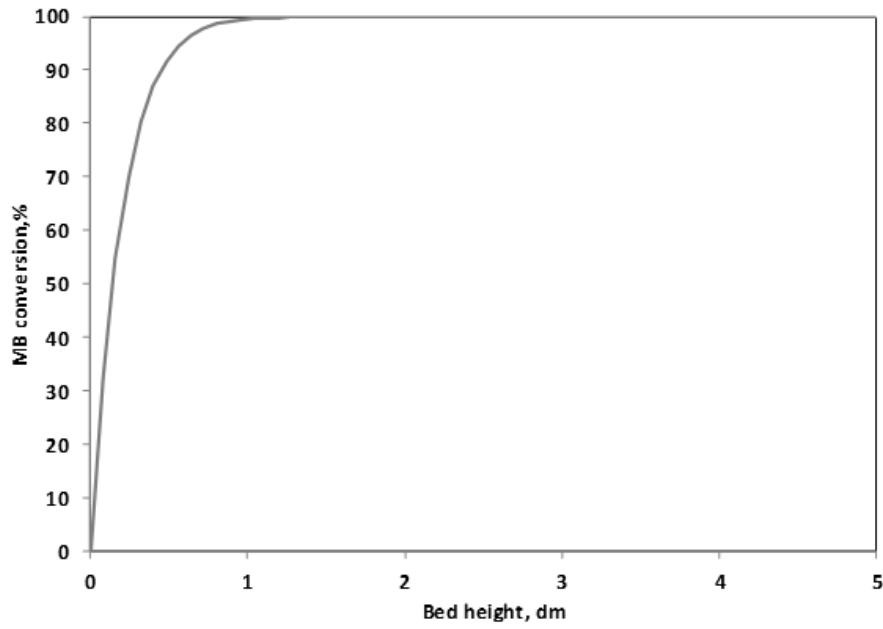
Figure 129 *Simulated MB conversion as function of z-direction, Light sources: UV-LEDs; MB concentration: 10 ppm*

IX Conclusions

N-doped titanium dioxide has been synthesized by direct hydrolysis at 0°C of titanium tetraisopropoxide with ammonia, as nitrogen source. The optimization of synthesis process was determined through a deep chemico-physical characterization of the samples.

The calcination and N/Ti molar ratio were the key parameters in the developing of N-doped TiO_2. For a calcination temperature of 450°C, the band-gap energy decreased by increasing the calcination time until 30 min. For a calcination time higher than 30 min, the value of band-gap energy increased. The N/Ti ratio has been varied until to find the catalyst with the lowest band-gap energy and the highest stablility. For all synthetized samples, X-ray diffraction analysis revealed that anatase is the only crystalline phase.

The optimized N-doped TiO_2 photocatalyst has the N-Ti molar ratio equal to 18.6 and obtained after calcination at 450 °C for 30 min. The bandgap energy of this sample is equal to 2.5 eV. This result implies that the photocatalyst is able to absorb visible light. This typical absorption is due to the electronic transition from the isolated N 2p level, which is formed by incorporation of nitrogen atoms into the TiO_2 lattice, to the conduction band.

The photocatalytic performances have been analysed in a batch photoreactor using white and blue light emitting diodes (LEDs) as visible light sources for the photocatalytic degradation of organic dyes (methylene blue and methyl orange) in liquid phase. The visible light responsive N-doped TiO_2 catalyst showed remarkable efficiencies in decolorization process and in the removal of total organic carbon. The photocatalytic behaviour of the optimized N-doped TiO_2 photocatalyst was also effective in. the degradation of emerging contaminants (spyramicin, atrazine) and in the inactivation of E. coli.

It is also important to evidence that this optimized N-doped TiO_2 photocatalyst resulted also able to reduce the total chemical oxygen demand (COD) of a highly polluted wastewater such as tannery wastewater.

To increae the quantum efficiency of N-doped TiO_2, it was coupled with other semiconductors. In particular, ZnS-based phosphors (ZSP) were

chosen. The coupling with ZSP not only reduces the charge-carriers recombination rate but also enhances the photons transfer inside the photoreactor, because ZSP emits, under UVA excitation, visible light centred at 440nm, able to photoexcite N-doped TiO_2 catalyst. Enhanced performance in comparison to either pure N-doped TiO_2 nanoparticles or bare ZSP was obtained. The photocatalyst N-doped TiO_2/ZSP at 30 wt % of N-dopedTiO_2 loading (30N-TiO_2/ZSP) exhibited the highest photocatalytic activity for the removal of methylene blue and atrazine. In the presence of ZSP support, no dechlorination of aromatic structure occurred in the degradation of atrazine, and thus no formation of cyanuric acid was observed.

The most limitation of the photocatalytic processes in slurry reactors is the low activity of N-doped TiO_2 in powder form, mainly due to the aggregation phenomena between nanoparticles. Therefore, to understand the effect of aggregation, a dispersing agent was added to the N-doped TiO_2 suspension. In particular, the effect of aggreagate size was studied in photocatalytic degradation of methylene blue. After 120 minutes of visible light irradiation, MB degradation in the presence of dispersing agent was about 80%, markedly higher than the value (about 50%) reached without the dispersing agent.

Considering this last result, a novel way to achieve high dispersion of the photocatalyst was also investigated. It consists in dispersing N-doped TiO_2 in transparent syndiotactic polystyrene monolithic aerogel (s-Ps) allowing a better dispersion of the catalysts and limiting the aggregation phenomena. These features increased the photocatalytic activity of the N-doped TiO_2 under visible light irradiation in comparison with the powder sample dispersed in solution.

Slurry reactors that employ aqueous suspension of titanium dioxide nanoparticles are not suitable due to the inconvenient and expensive separation of photocatalyst from treated wastewater. To overcome this drawback, the visible-light active N-doped TiO_2 was immobilized on glass spheres using a simple sol-gel method. The effect of sol-gel synthesis temperature was investigated on the crystallization and crystallites size of N-doped TiO_2 obtaining that the best temperature for the immobilization through dip-coating process was found at -20°C.

The removal of methylene blue and eriochrome black-T in aqueous solutions was tested to evaluate the photocatalytic activity of the immobilized photocatalyst. The optimization of N-doped TiO_2 amount on glass spheres was evaluated using methylene blue as model pollutant. In particular, it was found that until four dip-coating steps, the photocatalytic activity increased. Moreover, the N-doped TiO_2 immobilized on glass spheres can be easily separated from the reaction mixture, and maintained excellent photocatalytic activity and durability after four cycles.

With this structured catalyst, a continuous fixed bed photoreactor for wastewater treatment was firstly designed and finally implemented. Among the many different configurations of the reactor design the flat plate geometry has been chosen to maximize the exposition of catalysts to the light source. The fluid dynamic study in the flat plate fixed bed reactor was carried out using a CFD model (COMSOL Multiphysics 5.0) obtaining that the best reactor thickness to have plug flow conditions inside the photocatalytic bed is 2.5 cm. The model of light distribution inside the reactor was developed using the Helmholtz equation, set with the Dirichlet conditions on the boundary, evidencing that the use of UV-lamps determined a strong attenuation of light intensity (almost 70%) inside the core of the reactor. The result of fluid dynamic together with light intensity profile was used to implement a Laboratory scale photoreactor.

In order to obtain kinetic parameters using the optimized design, photocatalytic tests were carried out using methylene blue. The experimental results showed that dye degradation increased with contact time both using UV and visible light sources.

The Langmuir–Hinshelwood kinetic model was applied for estimating the kinetic parameters of the structured catalyst starting from experimental data collected at different methylene blue inlet concentration. The model has been validated comparing the experimental data obtained at different contact times with the values obtained from the mathematical model.

The estimated kinetic parameters are therefore used again in mass balance equation together with the spatial photons distribution, to obtain the theoretical distribution of the pollutant concentration at different distances from the irradiated window of the reactor, evidencing that reaction rate is strongly affected by local photons "concentration" and suggesting that an uniform light profile inside the reactor need to be achieved.

To determine the best irradiation condition, i.e. a light profile not affected from the attenuation and thus an optimal reactor volume, the UV-LEDs are used in the developed mathematical model. This new configuration allowed to demonstrate that the reactor volume required to obtain the total pollutant conversion could be drastically reduced. The design criteria for all type of continuous photoreactors strongly depend on fluid dynamic conditions and light sources to be used. In particular, the design of a flat plate reactor, supported by a detailed fluid dynamic study together with the light distribution in the reactor determined by the light sources, underlines that the reactor thickness must be chosen in order to have a plug flow regime while the light sources must be selected to reach a photons light distribution uniform in the core of the reactor. With these conditions a flexible criteria for the scale-up of a continuous photoreactor with the lowest volume is proposed

X References

Abinaya Subbaiyan, U.S., Ashok Sivapunniyam, Anusha Paulmani, Rajakumar Sundaram, 2013. Insilico Prediction of Toxicity in Aquatic Biota and Biodegradation Rate of Aromatic Hydrocarbons. Research and Reviews: Journal of Computational Biology 2, 6-13.

Acharya, K.P., Alabi, T.R., Schmall, N., Hewa-Kasakarage, N.N., Kirsanova, M., Nemchinov, A., Khon, E., Zamkov, M., 2009. Linker-Free Modification of TiO2 Nanorods with PbSe Nanocrystals. J. Phys. Chem. C 113, 19531-19535.

Al-Ekabi, H., Serpone, N., Pelizzetti, E., Minero, C., Fox, M.A., Draper, R.B., 1989. Kinetic studies in heterogeneous photocatalysis. 2. TiO2-mediated degradation of 4-chlorophenol alone and in a three-component mixture of 4-chlorophenol, 2,4-dichlorophenol, and 2,4,5-trichlorophenol in air-equilibrated aqueous media. Langmuir 5, 250-255.

Alemany, L.J., Lietti, L., Ferlazzo, N., Forzatti, P., Busca, G., Giamello, E., Bregani, F., 1995. Reactivity and Physicochemical Characterization of V2O5-WO3/TiO2 de-NOx catalysts. J. Catal. 155, 117-130.

Alexiadis, A., Baldi, G., Mazzarino, I., 2001. Modelling of a photocatalytic reactor with a fixed bed of supported catalyst. Catalysis Today 66, 467-474.

Alfano, O.M., Bahnemann, D., Cassano, A.E., Dillert, R., Goslich, R., 2000. Photocatalysis in water environments using artificial and solar light. Catalysis Today 58, 199-230.

Alrousan, D.M.A., Polo-Lopez, M.I., Dunlop, P.S.M., Fernandez-Ibanez, P., Byrne, J.A., 2012. Solar photocatalytic disinfection of water with immobilised titanium dioxide in re-circulating flow CPC reactors. Appl. Catal., B 128, 126-134.

Andersen, J., Pelaez, M., Guay, L., Zhang, Z., O'Shea, K., Dionysiou, D.D., 2013. NF-TiO2 photocatalysis of amitrole and atrazine with addition of oxidants under simulated solar light: Emerging synergies, degradation intermediates, and reusable attributes. Journal of Hazardous Materials 260, 569-575.

Anpo, M., 2004. Preparation, characterization, and reactivities of highly functional titanium oxide-based photocatalysts able to operate under UV-visible light irradiation: Approaches in realizing high efficiency in the use of visible light. Bull. Chem. Soc. Jpn. 77, 1427-1442.

Antoniadou, M., Vaiano, V., Sannino, D., Lianos, P., 2013. Photocatalytic oxidation of ethanol using undoped and Ru-doped titania: Acetaldehyde, hydrogen or electricity generation. Chemical Engineering Journal 224, 144-148.

Asahi, R., Morikawa, T., Ohwaki, T., Aoki, K., Taga, Y., 2001. Visible-light photocatalysis in nitrogen-doped titanium oxides. Science (Washington, DC, U. S.) 293, 269-271.

Augugliaro, V., Bellardita, M., Loddo, V., Palmisano, G., Palmisano, L., Yurdakal, S., 2012. Overview on oxidation mechanisms of organic compounds by TiO 2 in heterogeneous photocatalysis. Journal of Photochemistry and Photobiology C: Photochemistry Reviews 13, 224-245.

Augugliaro, V., Loddo, V., Marci, G., Palmisano, L., Schiavello, M., Sclafani, A., 1997. Heterogeneous photocatalysis. Fundamentals and applications. Chim. Ind. (Milan) 79, 473-481.

Avisar, D., Horovitz, I., Lozzi, L., Ruggieri, F., Baker, M., Abel, M.L., Mamane, H., 2013. Impact of water quality on removal of carbamazepine in natural waters by N-doped TiO2 photo-catalytic thin film surfaces. Journal of Hazardous Materials 244-245, 463-471.

Azhar, S.S., Liew, A.G., Suhardy, D., Hafiz, K.F., Hatim, M.D.I., 2005. Dye removal from aqueous solution by using adsorption on treated sugarcane bagasse. Am. J. Appl. Sci. 2, 1499-1503.

Barringer, E.A. and Bowen, H.K.,Formation, packing and sintering of monodispersed TiO2 poweder, 1982, J. Am.Caram. Soc., 65 C-199

Barka, N., Qourzal, S., Assabbane, A., Ait-Ichou, Y., 2010. Kinetic modeling of the photocatalytic degradation of methyl orange by supported TiO2. J. Environ. Sci. Eng. (Libertyville, IL, U. S.) 4, 1-5.

Baros, Z.Z., Adnadevic, B.K., 2011. The influence of the molar ratio [H2O]/[Ti(OR)4] on the kinetics of the titanium-oxo-alkoxy clusters nucleation. Russ. J. Phys. Chem. A 85, 2295-2298.

Batzill, M., Morales, E.H., Diebold, U., 2006. Influence of nitrogen doping on the defect formation and surface properties of TiO2 rutile and anatase. Physical Review Letters 96.

Biedrzycki, J., Livraghi, S., Giamello, E., Agnoli, S., Granozzi, G., 2014. Fluorine- and Niobium-Doped TiO2: Chemical and Spectroscopic Properties of Polycrystalline n-Type-Doped Anatase. J. Phys. Chem. C 118, 8462-8473.

Bisegna F., Gugliermetti F., Barbalace M., Monti L., Stato dell'arte dei LED (Light Emitting Diodes) 2010 Report RdS/2010/238

Blyholder, G., 1998. Infrared and Raman Spectra of Inorganic and Coordination Compounds, 5th ed., Parts A and B. By Kazuo Nakamoto (Marquette University). J. Am. Chem. Soc. 120, 5603-5604.

Bouchy, M., Zahraa, O., 2003. Photocatalytic reactors. Int. J. Photoenergy 5, 191-197.

Brinker, C.J., Scherer, G.W., 1985. Sol → gel → glass: I. Gelation and gel structure. Journal of Non-Crystalline Solids 70, 301-322.

Brucato, A., Rizzuti, L., 1997. Simplified Modeling of Radiant Fields in Heterogeneous Photoreactors. 2. Limiting "Two-Flux" Model for the Case of Reflectance Greater Than Zero. Industrial and Engineering Chemistry Research 36, 4748-4755.

Camera-Roda, G., Santarelli, F., Martin, C.A., 2005. Design of photocatalytic reactors made easy by considering the photons as immaterial reactants. Solar Energy 79, 343-352.

Carey, J.H., Lawrence, J., Tosine, H.M., 1976. Photodechlorination of PCB's in the presence of titanium dioxide in aqueous suspensions. Bull. Environ. Contam. Toxicol. 16, 697-701.

Cassano, A.E., Martín, C.A., Brandi, R.J., Alfano, O.M., 1995. Photoreactor analysis and design: Fundamentals and applications. Industrial and Engineering Chemistry Research 34, 2155-2201.

Changrani, R., Raupp, G.B., 1999. Monte Carlo simulation of the radiation field in a reticulated foam photocatalytic reactor. AIChE Journal 45, 1085-1094.

Chen, C., Yang, S., Guo, Y., Sun, C., Gu, C., Xu, B., 2009. Photolytic destruction of endocrine disruptor atrazine in aqueous solution under UV irradiation: Products and pathways. Journal of Hazardous Materials 172, 675-684.

Chen, C.C., Lu, C.S., Chung, Y.C., Jan, J.L., 2007a. UV light induced photodegradation of malachite green on TiO_2 nanoparticles. Journal of Hazardous Materials 141, 520-528.

218

Chen, H.-W., Ku, Y., Irawan, A., 2007b. Photodecomposition of o-cresol by UV-LED/TiO2 process with controlled periodic illumination. Chemosphere 69, 184-190.

Chen, X., Mao, S.S., 2007. Titanium Dioxide Nanomaterials: Synthesis, Properties, Modifications, and Applications. Chem. Rev. (Washington, DC, U. S.) 107, 2891-2959.

Churchley, J.H., 1994. Removal of dyewaste color from sewage effluent - the use of a full scale ozone plant. Water Sci. Technol. 30, 275-284.

Ciambelli, P., Sannino, D., Palma, V., Vaiano, V., 2005. Cyclohexane photocatalytic oxidative dehydrogenation to benzene on sulphated titania supported MoOx, Studies in Surface Science and Catalysis, pp. 179-187.

Ciambelli, P., Sannino, D., Palma, V., Vaiano, V., Bickley, R.I., 2008. Reaction mechanism of cyclohexane selective photo-oxidation to benzene on molybdena/titania catalysts. Applied Catalysis A: General 349, 140-147.

Ciambelli, P., Sannino, D., Palma, V., Vaiano, V., Mazzei, R.S., 2011a. Intensification of gas-phase photooxidative dehydrogenation of ethanol to acetaldehyde by using phosphors as light carriers. Photochem. Photobiol. Sci. 10, 414-418.

Ciambelli, P., Sannino, D., Palma, V., Vaiano, V., Mazzei, R.S., 2011b. Intensification of gas-phase photoxidative dehydrogenation of ethanol to acetaldehyde by using phosphors as light carriers. Photochemical and Photobiological Sciences 10, 414-418.

Cunningham, J., Sedlak, P., 1996. Kinetic studies of depollution process in TiO2 Slurries: Interdependences of adsorption and UV-intensity. Catalysis Today 29, 309-315.

Daniel, C., Alfano, D., Venditto, V., Cardea, S., Reverchon, E., Larobina, D., Mensitieri, G., Guerra, G., 2005. Aerogels with a microporous crystalline host phase. Advanced Materials 17, 1515-1518.

Daniel, C., Giudice, S., Guerra, G., 2009. Syndiotatic polystyrene aerogels with β,γ, and ϵ crystalline phases. Chemistry of Materials 21, 1028-1034.

Daniel, C., Longo, S., Ricciardi, R., Reverchon, E., Guerra, G., 2013. Monolithic nanoporous crystalline aerogels. Macromolecular Rapid Communications 34, 1194-1207.

de Caprariis, B., Di Rita, M., Stoller, M., Verdone, N., Chianese, A., 2012. Reaction-precipitation by a spinning disc reactor: Influence of

hydrodynamics on nanoparticles production. Chemical Engineering Science 76, 73-80.

De Lasa, H., Serrano, B., Salaices, M., 2005. Photocatalytic reaction engineering.

Di Valentin, C., Finazzi, E., Pacchioni, G., Selloni, A., Livraghi, S., Paganini, M.C., Giamello, E., 2007. N-doped TiO2: Theory and experiment. Chem. Phys. 339, 44-56.

Dimitrakopoulou, D., Rethemiotaki, I., Frontistis, Z., Xekoukoulotakis, N.P., Venieri, D., Mantzavinos, D., 2012. Degradation, mineralization and antibiotic inactivation of amoxicillin by UV-A/TiO2 photocatalysis. J. Environ. Manage. 98, 168-174.

Donaldson, A.A., Ye, A., McEvoy, J.G., Zhang, Z., 2013. Rotating corrugated photoreactor design: Experimental and computational analysis of TiO2-based photocatalysis. AIChE Journal 59, 560-570.

Emeline, A.V., Kuznetsov, V.N., Rybchuk, V.K., Serpone, N., 2008. Visible-light-active titania photocatalysts: the case of N-doped TiO2s-properties and some fundamental issues. Int. J. Photoenergy, No pp. given.

EUCAST, European Committee on Antimicrobial Susceptibility Testing, http://www.eucast.org/.

Fatehi, M., Kaviany, M., 1994. Adiabatic reverse combustion in a packed bed. Combustion and Flame 99, 1-17.

Fazio, S., Guzman, J., Colomer, M.T., Salomoni, A., Moreno, R., 2008. Colloidal stability of nanosized titania aqueous suspensions. J. Eur. Ceram. Soc. 28, 2171-2176.

Fegley B.Jr, Barringer E.A. and Bowen H.K., Synthesis and characterization of monosized doped TiO2 powders 1984 Journal of the American Ceramic Society, Vol.67, 113-116

Fernandez, P., Blanco, J., Sichel, C., Malato, S., 2005. Water disinfection by solar photocatalysis using compound parabolic collectors. Catal Today 101, 345-352.

Fox, M.A., Dulay, M.T., 1993. Heterogeneous photocatalysis. Chemical Reviews 93, 341-357.

Francisco, M.S.P., Mastelaro, V.R., 2002. Inhibition of the Anatase-Rutile Phase Transformation with Addition of CeO2 to CuO-TiO2 System: Raman Spectroscopy, X-ray Diffraction, and Textural Studies. Chem. Mater. 14, 2514-2518.

Franco, L.M.A., Zambrano, G., Gomez, M.E., Camps, E., Escobar-Alarcon, L., 2012. Photocatalytic activity of nitrogen-doped and

undoped titanium dioxide sputtered thin films. Superficies Vacio 25, 161-165.

Gao, X., Bare, S.R., Fierro, J.L.G., Banares, M.A., Wachs, I.E., 1998. Preparation and in-situ spectroscopic characterization of molecularly dispersed titanium oxide on silica. Journal of Physical Chemistry B 102, 5653-5666.

Grampp, G., Landgraf, S., 2002. The blue laser diode the complete story, 2nd edition by Shuji Nakamura, Stephen Pearton, and Gerard Fasol. Adv. Mater. (Weinheim, Ger.) 14, 170.

Greenwood, R., Kendall, K., 1999. Selection of suitable dispersants for aqueous suspensions of zirconia and titania powders using acoustophoresis. J. Eur. Ceram. Soc. 19, 479-488.

Guo, W., Shen, Y., Boschloo, G., Hagfeldt, A., Ma, T., 2011. Influence of nitrogen dopants on N-doped TiO_2 electrodes and their applications in dye-sensitized solar cells. Electrochim. Acta 56, 4611-4617.

Hajaghazadeh, M., Vaiano, V., Sannino, D., Kakooei, H., Sotudeh-Gharebagh, R., Ciambelli, P., 2014. Heterogeneous photocatalytic oxidation of methyl ethyl ketone under UV-A light in an LED-fluidized bed reactor. Catalysis Today 230, 79-84.

Han, C., Pelaez, M., Likodimos, V., Kontos, A.G., Falaras, P., O'Shea, K., Dionysiou, D.D., 2011. Innovative visible light-activated sulfur doped TiO_2 films for water treatment. Appl. Catal., B 107, 77-87.

Hansen, H.K., Nunez, P., Raboy, D., Schippacasse, I., Grandon, R., 2007. Electrocoagulation in wastewater containing arsenic: Comparing different process designs. Electrochim. Acta 52, 3464-3470.

Harris, C., Kamat, P.V., 2009. Photocatalysis with CdSe nanoparticles in confined media: Mapping charge transfer events in the subpicosecond to second timescales. ACS Nano 3, 682-690.

Herney-Ramirez, J., Vicente, M.A., Madeira, L.M., 2010a. Heterogeneous photo-Fenton oxidation with pillared clay-based catalysts for wastewater treatment: A review. Applied Catalysis B-Environmental 98, 10-26.

Herney-Ramirez, J., Vicente, M.A., Madeira, L.M., 2010b. Heterogeneous photo-Fenton oxidation with pillared clay-based catalysts for wastewater treatment: A review. Appl. Catal., B 98, 10-26.

Hoffmann, M.R., Martin, S.T., Choi, W., Bahnemann, D.W., 1995. Environmental Applications of Semiconductor Photocatalysis. Chem. Rev. (Washington, D. C.) 95, 69-96.

221

Houas, A., Lachheb, H., Ksibi, M., Elaloui, E., Guillard, C., Herrmann, J.M., 2001. Photocatalytic degradation pathway of methylene blue in water. Appl. Catal., B 31, 145-157.

Huang, Y., Sun, F., Wu, T., Wu, Q., Huang, Z., Su, H., Zhang, Z., 2011. Photochemical preparation of CdS hollow microspheres at room temperature and their use in visible-light photocatalysis. Journal of Solid State Chemistry 184, 644-648.

Ihara, T., Miyoshi, M., Iriyama, Y., Matsumoto, O., Sugihara, S., 2003. Visible-light-active titanium oxide photocatalyst realized by an oxygen-deficient structure and by nitrogen doping. Appl. Catal., B 42, 403-409.

Irie, H., Watanabe, Y., Hashimoto, K., 2003. Nitrogen-Concentration Dependence on Photocatalytic Activity of TiO2-xNx Powders. J. Phys. Chem. B 107, 5483-5486.

Jassby, D., Farner-Budarz, J., Wiesner, M., 2011. Impact of aggregate size and structure on the photocatalytic properties of TiO2 and ZnO nanoparticles. American Chemical Society, pp. GEOC-60.

Jassby, D., Farner Budarz, J., Wiesner, M., 2012. Impact of aggregate size and structure on the photocatalytic properties of TiO2 and ZnO nanoparticles. Environmental Science and Technology 46, 6934-6941.

Jones, O.A., Lester, J.N., Voulvoulis, N., 2005a. Pharmaceuticals: a threat to drinking water? Trends Biotechnol. 23, 163-167.

Jones, O.A.H., Voulvoulis, N., Lester, J.N., 2005b. Human pharmaceuticals in wastewater treatment processes. Crit. Rev. Environ. Sci. Technol. 35, 401-427.

Julkapli, N.M., Bagheri, S., Abd Hamid, S.B., 2014. Recent advances in heterogeneous photocatalytic decolorization of synthetic dyes. Sci. World J., 692307/692301-692307/692326, 692326.

Karvaly, B., Hevesi, I., 1971. Diffuse reflectance spectra of vanadium pentoxide powder. Z. Naturforsch. A 26, 245-249.

Kim, J., Kang, M., 2012. A newly designed a TiO2-loaded spherical ZnS nano/micro-composites for high hydrogen production from methanol/water solution photo-splitting. Bull. Korean Chem. Soc. 33, 2133-2139.

Kim, Y.J., Gao, B., Han, S.Y., Jung, M.H., Chakraborty, A.K., Ko, T., Lee, C., Lee, W.I., 2009. Heterojunction of FeTiO3 Nanodisks and TiO2 Nanoparticle for a Novel Visible Light Photocatalyst. J. Phys. Chem. C 113, 19179-19184.

Konstantinou, I.K., Albanis, T.A., 2004. TiO$_2$-assisted photocatalytic degradation of azo dyes in aqueous solution: kinetic and mechanistic

investigations - A review. Applied Catalysis B-Environmental 49, 1-14.

Konstantinou, I.K., Sakellarides, T.M., Sakkas, V.A., Albanis, T.A., 2001. Photocatalytic degradation of selected s-triazine herbicides and oganophosphorus insecticides over aqueous TiO2 suspensions. Environmental Science and Technology 35, 398-405.

Kudo, A., Miseki, Y., 2009. Heterogeneous photocatalyst materials for water splitting. Chem. Soc. Rev. 38, 253-278.

Kumar, J., Bansal, A., 2012. Photodegradation of amaranth in aqueous solution catalyzed by immobilized nanoparticles of titanium dioxide. Int. J. Environ. Sci. Technol. 9, 479-484.

Kumar, J., Bansal, A., 2013. Comparative study of immobilization techniques for photocatalytic degradation of Rhodamine B using nanoparticles of titanium dioxide. Water, Air, Soil Pollut. 224, 1-11.

Labiadh, H., Ben Chaabane, T., Balan, L., Becheik, N., Corbel, S., Medjahdi, G., Schneider, R., 2014. Preparation of Cu-doped ZnS QDs/TiO2 nanocomposites with high photocatalytic activity. Appl. Catal., B 144, 29-35.

Lam, S.W., Soetanto, A., Amal, R., 2009. Self-cleaning performance of polycarbonate surfaces coated with titania nanoparticles. Journal of Nanoparticle Research 11, 1971-1979.

Larry L.Hench, Jon K.West, The sol-gel process, 1990, Chem. Rev. 90,33-72

Lazar, M.A., Varghese, S., Nair, S.S., 2012. Photocatalytic water treatment by titanium dioxide: recent updates. Catalysts 2, 572-601.

Lea, J., Adesina, A.A., 1998. The photo-oxidative degradation of sodium dodecyl sulphate in aerated aqueous TiO_2 suspension. Journal of Photochemistry and Photobiology a-Chemistry 118, 111-122.

Li Puma, G., 2005. Dimensionless analysis of photocatalytic reactors using suspended solid photocatalysts. Chemical Engineering Research and Design 83, 820-826.

Li Puma, G., Brucato, A., 2007. Dimensionless analysis of slurry photocatalytic reactors using two-flux and six-flux radiation absorption-scattering models. Catal. Today 122, 78-90.

Li Puma, G., Yue, P.L., 1998. A laminar falling film slurry photocatalytic reactor. Part I - model development. Chem. Eng. Sci. 53, 2993-3006.

Li Puma, G., Yue, P.L., 2001. A Novel Fountain Photocatalytic Reactor for Water Treatment and Purification: Modeling and Design. Ind. Eng. Chem. Res. 40, 5162-5169.

Li, W.S., Shen, Z.X., Li, H.Y., Shen, D.Z., Fan, X.W., 2001. Blue shift of Raman peak from coated TiO2 nanoparticles. Journal of Raman Spectroscopy 32, 862-865.

Linsebigler, A.L., Lu, G., Yates, J.T., Jr., 1995. Photocatalysis on TiO2 Surfaces: Principles, Mechanisms, and Selected Results. Chem. Rev. (Washington, D. C.) 95, 735-758.

Liu, Y., Guan, Y., Gao, B., Yue, Q., 2012. Antioxidant responses and degradation of two antibiotic contaminants in Microcystis aeruginosa. Ecotoxicol. Environ. Saf. 86, 23-30.

Liu, Y., Li, J., Qiu, X., Burda, C., 2006. Novel TiO_2 nanocatalysts for wastewater purification: tapping energy from the sun. Water Science and Technology 54, 47-54.

Longo, S., Vitillo, J.G., Daniel, C., Guerra, G., 2013. Monolithic aerogels based on poly(2,6-diphenyl-1,4-phenylene oxide) and syndiotactic polystyrene. ACS Applied Materials and Interfaces 5, 5493-5499.

Ma, B., Wang, L., Dong, H., Gao, R., Geng, Y., Zhu, Y., Qiu, Y., 2011. Photocatalysis of PbS quantum dots in a quantum dot-sensitized solar cell: Photovoltaic performance and characteristics. Physical Chemistry Chemical Physics 13, 2656-2658.

Malato, S., Fernandez-Ibanez, P., Maldonado, M.I., Blanco, J., Gernjak, W., 2009. Decontamination and disinfection of water by solar photocatalysis: Recent overview and trends. Catal Today 147, 1-59.

Margolin J. The Road to the Transistor, September 2005. URL (http://www.jmargolin.com/history/trans.htm)

Martin, C.A., Camera-Roda, G., Santarelli, F., 1999. Effective design of photocatalytic reactors: influence of radiative transfer on their performance. Catal. Today 48, 307-313.

Matijevic E., Preparation and properties of uniform size colloids. 1993, Chem. Mater., 5,412-426

Matthews, R.W., 1989. Photocatalytic oxidation and adsorption of methylene blue on thin films of near-ultraviolet-illuminated titania. J. Chem. Soc., Faraday Trans. 1 85, 1291-1302.

McMurray, T.A., Dunlop, P.S.M., Byrne, J.A., 2006. The photocatalytic degradation of atrazine on nanoparticulate TiO2 films. Journal of Photochemistry and Photobiology A: Chemistry 182, 43-51.

Michael, I., Rizzo, L., McArdell, C.S., Manaia, C.M., Merlin, C., Schwartz, T., Dagot, C., Fatta-Kassinos, D., 2013. Urban wastewater

treatment plants as hotspots for the release of antibiotics in the environment: A review. Water Res. 47, 957-995.

Milow, B., Blanco, J., Fernandez, P., Malato, S., Richter, C., Funken, K.H., Sattler, C., 1999. Photocatalytic detoxification of contaminated water. Minerals, Metals & Materials Society, pp. 1989-1998.

Miranda-García, N., Maldonado, M.I., Coronado, J.M., Malato, S., 2010. Degradation study of 15 emerging contaminants at low concentration by immobilized TiO2 in a pilot plant. Catalysis Today 151, 107-113.

Moreira, J., Serrano, B., Ortiz, A., De Lasa, H., 2010. Evaluation of photon absorption in an aqueous TiO2 slurry reactor using Monte Carlo simulations and macroscopic balance. Industrial and Engineering Chemistry Research 49, 10524-10534.

Morikawa, T., Asahi, R., Ohwaki, T., Aoki, K., Taga, Y., 2001. Band-gap narrowing of titanium dioxide by nitrogen doping. Jpn. J. Appl. Phys., Part 2 40, L561-L563.

Munir, M., Wong, K., Xagoraraki, I., 2011. Release of antibiotic resistant bacteria and genes in the effluent and biosolids of five wastewater utilities in Michigan. Water Res. 45, 681-693.

Murcia, J.J., Hidalgo, M.C., Navío, J.A., Vaiano, V., Ciambelli, P., Sannino, D., 2012. Photocatalytic ethanol oxidative dehydrogenation over Pt/TiO 2: Effect of the addition of blue phosphors. International Journal of Photoenergy 2012.

Murcia, J.J., Hidalgo, M.C., Navío, J.A., Vaiano, V., Sannino, D., Ciambelli, P., 2013. Cyclohexane photocatalytic oxidation on Pt/TiO2 catalysts. Catalysis Today 209, 164-169.

Nie, G., Cai, T., Zhang, S., Hou, J., Xu, J., Han, X., 2007. Low potential electrosyntheses of high quality freestanding polyazulene films. Materials Letters 61, 3079-3082.

Nilsen, W.G., 1969. Second-order Raman spectra of some zinc blende and wurtzite crystals. Springer-Verlag New York Inc., pp. 129-137.

Noh, J.S., Schwarz, J.A., 1989. Estimation of the point of zero charge of simple oxides by mass titration. J. Colloid Interface Sci. 130, 157-164.

Nohynek, G.J., Dufour, E.K., 2012. Nano-sized cosmetic formulations or solid nanoparticles in sunscreens: A risk to human health? Arch. Toxicol. 86, 1063-1075.

Otálvaro-Marín, H.L., Mueses, M.A., Machuca-Martínez, F., 2014. Boundary layer of photon absorption applied to heterogeneous photocatalytic solar flat plate reactor design. International Journal of Photoenergy 2014.

225

Othman, S.H., Abdul Rashid, S., Mohd Ghazi, T.I., Abdullah, N., 2012. Dispersion and stabilization of photocatalytic TiO2 nanoparticles in aqueous suspension for coatings applications. J. Nanomater., 718214, 718210 pp.

Pacheco, J.E., Prairie, M.R., Yellowhorse, L., 1993. Photocatalytic destruction of chlorinated solvents in water with solar energy. J. Sol. Energy Eng. 115, 123-129.

Pagliaro, M., Ciriminna, R., Palmisano, G., 2008. Flexible solar cells. ChemSusChem 1, 880-891.

Palma, V., Sannino, D., Vaiano, V., Ciambelli, P., 2010a. Fluidized-bed reactor for the intensification of gas-phase photocatalytic oxidative dehydrogenation of cyclohexane. Industrial and Engineering Chemistry Research 49, 10279-10286.

Palma, V., Sannino, D., Vaiano, V., Ciambelli, P., 2010b. Fluidized-Bed Reactor for the Intensification of Gas-Phase Photocatalytic Oxidative Dehydrogenation of Cyclohexane. Industrial & Engineering Chemistry Research 49, 10279-10286.

Palmisano, G., Loddo, V., Nazer, H.H.E., Yurdakal, S., Augugliaro, V., Ciriminna, R., Pagliaro, M., 2009. Graphite-supported TiO2 for 4-nitrophenol degradation in a photoelectrocatalytic reactor. Chemical Engineering Journal 155, 339-346.

Parker, J.C., Siegel, R.W., 1990. Raman microprobe study of nanophase titania and oxidation-induced spectral changes. J. Mater. Res. 5, 1246-1252.

Parra, S., Stanca, S.E., Guasaquillo, I., Ravindranathan Thampi, K., 2004. Photocatalytic degradation of atrazine using suspended and supported TiO2. Applied Catalysis B: Environmental 51, 107-116.

Periyathamby, U., Ray, A.K., 1999. Computer simulation of a novel photocatalytic reactor using distributive computing environment. Chem. Eng. Technol. 22, 881-888.

Porel, M., Klimczak, A., Freitag, M., Galoppini, E., Ramamurthy, V., 2012. Photoinduced Electron Transfer Across a Molecular Wall: Coumarin Dyes as Donors and Methyl viologen and TiO2 as Acceptors. Langmuir 28, 3355-3359.

Pozzo, R.L., Baltanás, M.A., Cassano, A.E., 1997. Supported titanium oxide as photocatalyst in water decontamination: State of the art. Catalysis Today 39, 219-231.

Prados-Joya, G., Sanchez-Polo, M., Rivera-Utrilla, J., Ferro-garcia, M., 2011. Photodegradation of the antibiotics nitroimidazoles in aqueous solution by ultraviolet radiation. Water Res. 45, 393-403.

Qin, C., Yang, S., Sun, C., Zhan, M., Wang, R., Cai, H., Zhou, J., 2010. Investigation of the effects of humic acid and H2O2 on the photocatalytic degradation of atrazine assisted by microwave. Frontiers of Environmental Science and Engineering in China 4, 321-328.

Quincy, R.B., Houalla, M., Hercules, D.M., 1987. Quantitative Raman characterization of molybdenum/titania catalysts. J. Catal. 106, 85-92.

Rengifo-Herrera, J.A., Pierzchala, K., Sienkiewicz, A., Forro, L., Kiwi, J., Pulgarin, C., 2009. Abatement of organics and Escherichia coli by N, S co-doped TiO2 under UV and visible light. Implications of the formation of singlet oxygen (1O2) under visible light. Appl. Catal., B 88, 398-406.

Rengifo-Herrera, J.A., Pulgarin, C., 2010. Photocatalytic activity of N, S co-doped and N-doped commercial anatase TiO_2 powders towards phenol oxidation and E. coli inactivation under simulated solar light irradiation. Solar Energy 84, 37-43.

Rizzo, L., Fiorentino, A., Anselmo, A., 2013a. Advanced treatment of urban wastewater by UV radiation: Effect on antibiotics and antibiotic-resistant E. coli strains. Chemosphere 92, 171-176.

Rizzo, L., Sannino, D., Vaiano, V., Sacco, O., Scarpa, A., Pietrogiacomi, D., 2013b. Effect of solar simulated N-doped TiO2 photocatalysis on the inactivation and antibiotic resistance of an E. coli strain in biologically treated urban wastewater. Applied Catalysis B: Environmental 144, 369-378.

Rizzo, L., Sannino, D., Vaiano, V., Sacco, O., Scarpa, A., Pietrogiacomi, D., 2014. Effect of solar simulated N-doped TiO2 photocatalysis on inactivation and antibiotic resistance of E. coli strain in biologically treated urban wastewater. Appl. Catal., B 144, 369-378.

Rosu, M.C., Suciu, R.C., Kasco, I., Dreve, S.V., Indrea, E., Silipas, T.D., 2009. A spectroscopic study of dyes decomposition by irradiated nanocrystalline TiO2. Journal of Physics: Conference Series 182.

Rouquerol, J., Avnir, D., Fairbridge, C.W., Everett, D.H., Haynes, J.H., Pernicone, N., Ramsay, J.D.F., Sing, K.S.W., Unger, K.K., 1994. Recommendations for the characterization of porous solids. Pure Appl. Chem. 66, 1739-1758.

Sacco, O., Stoller, M., Vaiano, V., Ciambelli, P., Chianese, A., Sannino, D., 2012. Photocatalytic degradation of organic dyes under visible light on n-doped TiO2 photocatalysts. International Journal of Photoenergy 2012.

Salaices, M., Serrano, B., De Lasa, H.I., 2001. Photocatalytic conversion of organic pollutants extinction coefficients and quantum efficiencies. Industrial and Engineering Chemistry Research 40, 5455-5464.

Salaices, M., Serrano, B., De Lasa, H.I., 2002. Experimental evaluation of photon absorption in an aqueous TiO2 slurry reactor. Chemical Engineering Journal 90, 219-229.

Sannino, D., Vaiano, V., Ciambelli, P., 2013a. Innovative structured VOx/TiO2 photocatalysts supported on phosphors for the selective photocatalytic oxidation of ethanol to acetaldehyde. Catalysis Today 205, 159-167.

Sannino, D., Vaiano, V., Ciambelli, P., Carotenuto, G., Di Serio, M., Santacesaria, E., 2013b. Enhanced performances of grafted VOx on titania/silica for the selective photocatalytic oxidation of ethanol to acetaldehyde. Catalysis Today 209, 159-163.

Sannino, D., Vaiano, V., Ciambelli, P., Eloy, P., Gaigneaux, E.M., 2011. Avoiding the deactivation of sulphated MoOx/TiO2 catalysts in the photocatalytic cyclohexane oxidative dehydrogenation by a fluidized bed photoreactor. Appl. Catal., A 394, 71-78.

Sannino, D., Vaiano, V., Ciambelli, P., Isupova, L.A., 2013c. Mathematical modelling of the heterogeneous photo-Fenton oxidation Of acetic acid on structured catalysts. Chemical Engineering Journal 224, 53-58.

Sannino, D., Vaiano, V., Sacco, O., Ciambelli, P., 2013d. Mathematical modelling of photocatalytic degradation of methylene blue under visible light irradiation. Journal of Environmental Chemical Engineering 1, 56-60.

Sannino, D., Vaiano, V., Sarno, G., Ciambelli, P., 2013e. Smart tiles for the preservation of indoor air quality. Chemical Engineering Transactions 32, 355-360.

Sato, K., Li, J.-G., Kamiya, H., Ishigaki, T., 2008. Ultrasonic dispersion of TiO2 nanoparticles in aqueous suspension. J. Am. Ceram. Soc. 91, 2481-2487.

Sato, S., 1986. Photocatalytic activity of NOx-doped TiO2 in the visible light region. Chemical Physics Letters 123, 126-128.

Schiavello, M., 1997. Heterogeneous Photocatalysis. Wiley.

Schwartz, T., Kohnen, W., Jansen, B., Obst, U., 2003. Detection of antibiotic-resistant bacteria and their resistance genes in wastewater, surface water, and drinking water biofilms. FEMS Microbiol. Ecol. 43, 325-335.

Sczechowski, J.G., Koval, C.A., Noble, R.D., 1995. A Taylor vortex reactor for heterogeneous photocatalysis. Chemical Engineering Science 50, 3163-3173.

Segneanu A. E., Orbeci C., Lazau C., Sfirloaga P., Vlazan P., Bandas C. and Grozescu I., Waste Water Treatment Methods Chapter 4, Intech, 2013 http://dx.doi.org/10.5772/53755

Sentein, C., Guizard, B., Giraud, S., Ye, C., Tenegal, F., 2009. Dispersion and stability of TiO2 nanoparticles synthesized by laser pyrolysis in aqueous suspensions. J. Phys.: Conf. Ser. 170, No pp. given.

Serpone, N., 1997. Relative photonic efficiencies and quantum yields in heterogeneous photocatalysis. Journal of Photochemistry and Photobiology A: Chemistry 104, 1-12.

Serrano, B., Ortíz, A., Moreira, J., De Lasa, H.I., 2010. Photocatalytic thermodynamic efficiency factors. Practical limits in photocatalytic reactors. Industrial and Engineering Chemistry Research 49, 6824-6833.

Shi, H., Magaye, R., Castranova, V., Zhao, J., 2013. Titanium dioxide nanoparticles: A review of current toxicological data. Particle and Fibre Toxicology 10.

Shi, X., Zhang, S., Fawcett, J.P., Zhong, D., 2004. Acid catalysed degradation of some spiramycin derivatives found in the antibiotic bitespiramycin. J. Pharm. Biomed. Anal. 36, 593-600.

Singh, S., Mahalingam, H., Singh, P.K., 2013. Polymer-supported titanium dioxide photocatalysts for environmental remediation: A review. Applied Catalysis A: General 462-463, 178-195.

Sivalingam, G., Nagaveni, K., Hegde, M.S., Madras, G., 2003a. Photocatalytic degradation of various dyes by combustion synthesized nano anatase TiO2. Appl. Catal., B 45, 23-38.

Sivalingam, G., Nagaveni, K., Hegde, M.S., Madras, G., 2003b. Photocatalytic degradation of various dyes by combustion synthesized nano anatase TiO$_2$. Applied Catalysis B-Environmental 45, 23-38.

Socrates, G., 2004. Infrared and Raman Characteristic Group Frequencies: Tables and Charts, 3rd Edition. John Wiley & Sons.

Soloviev, A., Tufeu, R., Sanchez, C., Kanaev, A.V., 2001. Nucleation Stage in the Ti(OPri)4 Sol-Gel Process. J. Phys. Chem. B 105, 4175-4180.

Sopyan, I., Watanabe, M., Murasawa, S., Hashimoto, K., Fujishima, A., 1996. A film-type photocatalyst incorporating highly active TiO2 powder and fluororesin binder: Photocatalytic activity and long-term stability. Journal of Electroanalytical Chemistry 415, 183-186.

Sorrentino, A., Rega, S., Sannino, D., Magliano, A., Ciambelli, P., Santacesaria, E., 2001. Performances of V2O5-based catalysts obtained by grafting vanadyl tri-isopropoxide on TiO2-SiO2 in SCR. Applied Catalysis A: General 209, 45-57.

Stoller, M., Chianese, A., 2006. Optimization of membrane batch processes by means of the critical flux theory. Desalination 191, 62-70.

Tayade, R.J., Natarajan, T.S., Bajaj, H.C., 2009. Photocatalytic Degradation of Methylene Blue Dye Using Ultraviolet Light Emitting Diodes. Ind. Eng. Chem. Res. 48, 10262-10267.

Tsao J. Y., Solid-state lighting, 2004 MAY/JUNE, IEEE CIRCUITS & DEVICES MAGAZINE.

Vaiano, V., Sacco, O., Sannino, D., Ciambelli, P., 2014a. Photocatalytic removal of spiramycin from wastewater under visible light with N-doped TiO2 photocatalysts. Chemical Engineering Journal.

Vaiano, V., Sacco, O., Sannino, D., Ciambelli, P., Longo, S., Venditto, V., Guerra, G., 2014b. N-doped TiO2/s-PS aerogels for photocatalytic degradation of organic dyes in wastewater under visible light irradiation. Journal of Chemical Technology and Biotechnology.

Vaiano, V., Sacco, O., Sannino, D., Ciambelli, P., Longo, S., Venditto, V., Guerra, G., 2014c. N-doped TiO2/s-PS aerogels for photocatalytic degradation of organic dyes in wastewater under visible light irradiation. Journal of Chemical Technology and Biotechnology 89, 1175-1181.

Vaiano, V., Sacco, O., Sannino, D., Ciambelli, P., Longo, S., Venditto, V., Guerra, G., 2014d. N-doped TiO2/s-PS aerogels for photocatalytic degradation of organic dyes in wastewater under visible light irradiation. J. Chem. Technol. Biotechnol., Ahead of Print.

Vaiano, V., Sacco, O., Stoller, M., Chianese, A., Ciambelli, P., Sannino, D., 2014e. Influence of the photoreactor configuration and of different light sources in the photocatalytic treatment of highly polluted wastewater. International Journal of Chemical Reactor Engineering 12.

Verhoeven, J.W., 1996. Glossary of terms used in photochemistry. Pure Appl. Chem. 68, 2223-2286.

Vezzoli, M., Farrell, T., Baker, A., Psaltis, S., Martens, W.N., Bell, J.M., 2013. Optimal catalyst thickness in titanium dioxide fixed film reactors: Mathematical modelling and experimental validation. Chemical Engineering Journal 234, 57-65.

Vincenzo Vaiano, O.S., Marco Stoller, Angelo Chianese, Paolo Ciambelli, and Diana Sannino, 2014. Influence of the Photoreactor Configuration and of Different Light Sources in the Photocatalytic Treatment of Highly Polluted Wastewater. International Journal of Chemical Reactor Engineering 12, 1-13.

Wahi, R.K., Liu, Y., Falkner, J.C., Colvin, V.L., 2006. Solvothermal synthesis and characterization of anatase TiO2 nanocrystals with ultrahigh surface area. Journal of Colloid and Interface Science 302, 530-536.

Wang, F., Lai, Y.-H., Kocherginsky, N.M., Kosteski, Y.Y., 2003. The First Fully Characterized 1,3-Polyazulene: High Electrical Conductivity Resulting from Cation Radicals and Polycations Generated upon Protonation. Org. Lett. 5, 995-998.

Wang, Y., Xie, Y., Yuan, J., Liu, G., 2013. Controlled synthesis and photocatalytic activity of TiO2 nanoparticles by a novel gel-network precipitation method. Asian Journal of Chemistry 25, 739-744.

Ward, M.D., White, J.R., Bard, A.J., 1983. Electrochemical investigation of the energetics of particulate titanium dioxide photocatalysts. The methyl viologen-acetate system. J. Am. Chem. Soc. 105, 27-31.

Welte, A., Waldauf, C., Brabec, C., Wellmann, P.J., 2008. Application of optical absorbance for the investigation of electronic and structural properties of sol-gel processed TiO2 films. Thin Solid Films 516, 7256-7259.

Xekoukoulotakis, N.P., Drosou, C., Brebou, C., Chatzisymeon, E., Hapeshi, E., Fatta-Kassinos, D., Mantzavinos, D., 2011. Kinetics of UV-A/TiO2 photocatalytic degradation and mineralization of the antibiotic sulfamethoxazole in aqueous matrices. Catal. Today 161, 163-168.

Yin, L., Shen, H., 2001. Structures and photocatalysis of nanocrystalline TiO2 powders and thin films derived by sol-gel process, Proceedings of the International Conference on Energy Conversion and Application (ICECA'2001), pp. 173-176.

Yogi, C., Kojima, K., Takai, T., Wada, N., 2009. Photocatalytic degradation of Methylene blue by Au-deposited TiO2 film under UV irradiation. J. Mater. Sci. 44, 821-827.

Yu, X., Wu, Q., Jiang, S., Guo, Y., 2006. Nanoscale ZnS/TiO2 composites: Preparation, characterization, and visible-light photocatalytic activity. Mater. Charact. 57, 333-341.

Zaleska, A., 2008. Doped-TiO2: a review. Recent Pat. Eng. 2, 157-164.

Zhao, A., Masa, J., Xia, W., Maljusch, A., Willinger, M.-G., Clavel, G., Xie, K., Schloegl, R., Schuhmann, W., Muhler, M., 2014. Spinel Mn-Co Oxide in N-Doped Carbon Nanotubes as a Bifunctional Electrocatalyst Synthesized by Oxidative Cutting. J. Am. Chem. Soc. 136, 7551-7554.

Zhao, C., Pelaez, M., Duan, X., Deng, H., O'Shea, K., Fatta-Kassinos, D., Dionysiou, D.D., 2013. Role of pH on photolytic and photocatalytic degradation of antibiotic Oxytetracycline in aqueous solution under visible/solar light: Kinetics and mechanism studies. Appl. Catal., B 134-135, 83-92.

Zhou, H., Smith, D.W., 2002. Advanced technologies in water and wastewater treatment. J. Environ. Eng. Sci. 1, 247-264.